Dielectric Metasurfaces from Fundamentals to Applications

Thesis by
Seyedeh Mahsa Kamali

In Partial Fulfillment of the Requirements for the
Degree of
Doctor of Philosophy

CALIFORNIA INSTITUTE OF TECHNOLOGY
Pasadena, California

2019
Defended May 3, 2019

Seyedeh Mahsa Kamali
ORCID: 0000-0002-6968-811X

To Ehsan

and

to my parents.

ACKNOWLEDGEMENTS

It is hard to believe that almost five years have passed since I first joined Caltech; five years of education, new experiences, and opportunities which broadened and deepened my vision and perspective, and helped me in my personal and career development. These experiences and developments were made possible by the presence and support of wonderful colleagues, mentors, family, and friends. I have enjoyed every moment of my graduate school journey, and it is my pleasure to acknowledge those who made this journey possible and joyful for me.

First and foremost, I would like to acknowledge my advisor Professor Andrei Faraon. Andrei's enthusiasm and passion for science with real-life applications, his caring and cheerful character, and his leadership have always been very inspiring. I thank Andrei for providing me this great opportunity to pursue my passion, supporting me and giving me the freedom of exploring new ideas, and most importantly, for helping me develop as a researcher by being a great role model. I will always be grateful for all Andrei taught me over the past five years.

I have been fortunate to have had the great opportunity to interact and collaborate with great colleagues and mentors from across Caltech, UIUC, USC, and Stanford University. The works presented in this thesis would not have been possible without the help of Professors Julia Greer and Austin Minnich at Caltech, Paul Braun at UIUC, and Alan Willner at USC. I thank them and also their students who worked hard and patiently with me on different projects. Moreover, I would like to deeply thank Austin, Julia, and Paul for being great mentors as well as collaborators; I thank them for all their guidance in helping me define my future career path. I am also very grateful to Professor Jennifer Dionne at Stanford for always providing me with great advice and perspective about my research. I thank Jen and express my appreciation to all her help and guidance, and for being a great female role model for me.

I would also like to express my sincere gratitude to my thesis committee members Professors Harry Atwater, Azita Emami, Austin Minnich, and Lihong Wang for their time, and providing guidance and thoughtful advices. I would also like to thank Professor Axel Scherer for serving on my candidacy exam committee.

I have been very fortunate to be involved in a multi-institutional grant, LMI-EFRC, which provided a friendly and collaborative ambient between scientific leaders from Caltech, Stanford, UC Berkeley, and UIUC. I would like to thank all the LMI-EFRC

members and the agency members who all together provided this great opportunity for me. I specifically would like to thank Professors Ralph Nuzzo, Harry Atwater, Mark Brongersma, and Eli Yablonovitch for the fruitful discussions and conversations in which they provided guidance and perspective.

I have been super fortunate to be part of NFugue, a venture backed startup from Kairos Ventures. I would like to thank Jim Demetriades, Dr. Travis Blake, and Dr. Jakob van Zyl for their great help, support, and fruitful discussions. I would also like to thank students who worked hard and patiently with me on this interdisciplinary project. Specifically, I would like to thank Phillippe Pearson, Daniel Bacon-Brown, Ryan Ng, and Luizetta Navrazhnykh.

I would like to express my great appreciation to the whole Faraon group, as they all contributed in generating a collaborative and friendly research environment. In particular, I am grateful to Amir for being a great mentor during the first years of my PhD. His insightful advices and guidance helped me in ways well beyond the bounds of this short acknowledgment. I am thankful for all his help and being a great example of a scientist and researcher for me. I owe a tremendous debt of gratitude to Ehsan, who has been the best colleague, supporter, friend, and husband! I am the most fortunate to have his tireless support and help. I would also like to thank Yu, who helped me a lot with my research while he was at Caltech and even after his graduation. I would like to thank Evan, Jon, John, Tian, Ioana, Chuting, Han, and Jake for their critical advice and help. Also, thank Philip, Conner, Sadegh, Greg, Tianzhe, Andrei, Daniel, Mi, and Tian for the fruitful discussions during our meetings. I would also like to thank our collaborators from Samsung Electronics, specifically Dr. Seunghoon Han and Dr. Duhyun Lee for the insightful discussions and collaborations on various ideas.

I owe much gratitude to the KNI staff, and everyone who helped train me; specifically thanks to Dr. Guy DeRose, Melissa Melendes, Neils, Dr. Matthew Sullivan Hunt, Steven Martinez, Bert Mendoza, Alex Wertheim, Nathan S. Lee, Tiffany Kimoto, Jennifer Palmer, and Mary Sikora. I would also like to thank Max and William from Scherer group for their generous advice on nanofabrication techniques. Moreover, I would like to thank Dr. Andres Collazo from Caltech Biological Imaging Facility, for patiently training me on various microscopy setups.

I would like to thank everyone at Caltech who gave me support outside the lab, starting with Christine Jenstad, Cecilia Gamboa, Tanya Owen, and Jonathan Gross, who helped so many of us to focus on the research. I would like to thank Dr.

Carrie Hofmann, Tiffany Kimoto, Jennifer Blankenship, and Lyann Lau for their tireless support and help in organizing great meetings and workshops as part of the LMI-EFRC grant. I would like to thank Dr. Kate McAnulty, Natalie Gilmore, and Angelica Medina-Cuevas from the Graduate Studies Office for all their hard work and passion for helping us to get the most out of our graduate experiences. I would also like to thank Tess Legaspi from the Registrar's Office and Daniel Yoder from International Office for being super helpful and friendly, speeding everything up and assisting in every aspect they could.

My graduate journey had about one semester detour through UIUC before I joined Caltech. I owe much gratitude to my first advisor, Professor Lynford Goddard, not only for his mentoring and advising, but also for his caring and how kindly he accepted the fact that I would like to follow my passion at Caltech. I am always thankful and respectful to Lynford for helping me in following my passion.

I would also like to thank all my undergraduate instructors and advisors who were my first teachers and inspiration. I specifically would like to thank Professors Mahmoud Shahabadi, Karim Mohammad Pour Aghdam, and Mojtaba Dehmollaian, who fostered the passion for science and research in me.

Sometimes individuals leave lasting impressions regardless of the the brevity of the interactions; life lessons that help to be more determined and be ambitious enough in achieving the goals. I have been fortunate, over the past few years, to learn from such individuals who inspired me to work hard toward achieving my goals at the most critical of times. I thank Professors Stefanie Mueller, Vivienne Sze, Viviana Gradinaru, Farnaz Niroui, Negar Reiskarimian, Mona Eskandari, Hossein Taheri, and also Debby McWhinney from the board of trustees at Caltech for their inspiration.

This thesis would not have been possible without the unconditional support of my family and friends. I thank my parents (Soheila and Reza), my only sister (Sana), my brother-in-law (Abbas), and my little niece (Ala) for always being there for me, reminding me about our goals and responsibilities as human beings, encouraging me, and inspiring me even from thousands of miles away. I am forever thankful and cheer-full for having the best ever family. For sure, the hardest part of the graduate school journey for me, was being far away from them for five consecutive years. I am very fortunate to have friends who helped me feel at home and provided me a memorable graduate experience. I thank all my friends and in particular Hanieh, Zahra, Marzieh, Fahimeh, Sahar, Fatemeh, Mohammad, Ali, Hassan, Mostafa, Pouya, Jalil, and Masoud, who were always there for me just like my family.

My graduate journey has been filled with invaluable learning experiences, new perspectives, and friendships that I will always fondly remember as I move towards future adventures with great motivation and excitement. I am forever thankful to all God's unending blessings.

Seyedeh Mahsa Kamali
Pasadena, California
May 3, 2019

ABSTRACT

In the past few decades, the advancements in nanotechnology have significantly altered many fields of science and technology, especially electronics and integrated photonics. Free-space optics, on the other hand, has remained mostly unaffected, and even today "optics" reminds us of carefully shaped and polished pieces of various types of glasses and crystals lumped into lenses and beam shapers. Several of these devices are then combined into more complicated optical systems like microscopes and pulse shapers that are expensive, bulky, sensitive to various environmental factors, and require several alignment steps. This thesis contains my work on designing and utilizing structures engineered at the nano-scale, which are called metasurfaces, to implement compact optical elements and systems with capabilities beyond those of conventional refractive and diffractive optics. My contributions to this field are two-fold: I have developed and contributed to the development of new concepts that take metasurfaces beyond conventional difractive optics in various aspects, in addition to paradigm changing platforms for optical element and system design. Here, I first give an overview and a brief history about optical metasurfaces. Next I discuss the unprecedented capabilities of metasurfaces in controlling light based on its degrees of freedom like illumination angle and polarization. Then, I will focus on various novel metasurface platforms of conformal and tunable metasurfaces, 3D metasurface beam shapers, and integrated metasurfaces. I conclude with an outlook on future potentials and challenges that need to be overcome for realizing their wide-spread applications.

Thesis supervisor:

- Andrei Faraon
  Professor of Applied Physics and Electrical Engineering

Thesis committee:

- Andrei Faraon
  Professor of Applied Physics and Electrical Engineering
- Harry A. Atwater
  Howard Hughes Professor of Applied Physics and Materials Science
- Azita Emami (Chair)
  Andrew and Peggy Cherng Professor of Electrical Engineering and Medical Engineering
- Austin Minnich
  Professor of Mechanical Engineering and Applied Physics
- Lihong Wang
  Bren Professor of Medical Engineering and Electrical Engineering

PUBLISHED CONTENT AND CONTRIBUTIONS

[1] S. M. Kamali*, E. Arbabi*, A. Arbabi, and A. Faraon, "A review of dielectric optical metasurfaces for wavefront control", Nanophotonics **7**, 1041–1068 (2018) DOI: 10.1515/nanoph-2017-0129,

S.K. and E.A contributed equally in this work. S.K. participated in the collection and analysis of the data and writing of this review paper.

[2] S. M. Kamali, E. Arbabi, A. Arbabi, Y. Horie, M. Faraji-Dana, and A. Faraon, "Angle-multiplexed metasurfaces: encoding independent wavefronts in a single metasurface under different illumination angles", Phys. Rev. X **7**, 041056 (2017) DOI: 10.1103/PhysRevX.7.041056,

S.K. participated in the conception of the project, design, fabrication, and characterization of the devices, analysis of the data, and writing the manuscript.

[3] E. Arbabi, S. M. Kamali, A. Arbabi, and A. Faraon, "Full-stokes imaging polarimetry using dielectric metasurfaces", ACS Photonics **5**, 3132–3140 (2018) DOI: 10.1021/acsphotonics.8b00362,

S.K. participated in the fabrication and measurement of the samples, analysis of the data, and writing the manuscript.

[4] E. Arbabi, S. M. Kamali, A. Arbabi, and A. Faraon, "Vectorial holograms with a dielectric metasurface: ultimate polarization pattern generation", Submitted,

S.K. participated in the fabrication and measurement of the samples, analysis of the data, and writing the manuscript.

[5] S. M. Kamali, A. Arbabi, E. Arbabi, Y. Horie, and A. Faraon, "Decoupling optical function and geometrical form using conformal flexible dielectric metasurfaces", Nat. Commun. **7**, 11618 (2016) DOI: doi.org/10.1038/ncomms11618,

S.K. participated in the conception of the project, design, fabrication, and characterization of the devices, analysis of the data, and writing the manuscript.

[6] S. M. Kamali, E. Arbabi, A. Arbabi, Y. Horie, and A. Faraon, "Highly tunable elastic dielectric metasurface lenses", Laser Photon. Rev. **10**, 1062–1062 (2016) DOI: 10.1002/lpor.201600144,

S.K. participated in the conception of the project, design, fabrication, and characterization of the devices, analysis of the data, and writing the manuscript.

[7] S. M. Kamali, E. Arbabi, H. Kwon, and A. Faraon, "Metasurface-mask-assisted 3d beam shaping: a new route for 3d fabrication of exotic periodic structures", Submitted,

S.K. participated in the conception of the project, design, fabrication, and characterization of the devices, analysis of the data, and writing the manuscript.

[8] S. M. Kamali*, E. Arbabi*, and A. Faraon, “Metasurface-based compact light engine for ar headsets”, in Spie photon. west (2019), p. 11040, DOI: doi.org/10.1117/12.2523720,

S.K. and E.A contributed equally in this work. S.K. participated in the conception of the ideas, design of the devices, performing the simulations, analysis of the data, and writing the manuscript.

OTHER PUBLICATIONS

[1] A. Arbabi, E. Arbabi, S. M. Kamali, Y. Horie, S. Han, and A. Faraon, "Miniature optical planar camera based on a wide-angle metasurface doublet corrected for monochromatic aberrations", Nat. Commun. **7**, 13682 (2016) DOI: 10.1038/ncomms13682.

[2] E. Arbabi, A. Arbabi, S. M. Kamali, Y. Horie, and A. Faraon, "Multiwavelength polarization-insensitive lenses based on dielectric metasurfaces with meta-molecules", Optica **3**, 628–633 (2016) DOI: 10.1364/OPTICA.3.000628.

[3] Y. Horie, A. Arbabi, E. Arbabi, S. M. Kamali, and A. Faraon, "Wide bandwidth and high resolution planar filter array based on DBR-metasurface-DBR structures", Opt. Express **24**, 11677–11682 (2016) DOI: 10.1364/OE.24.011677.

[4] Y. Ren, L. Li, Z. Wang, S. M. Kamali, E. Arbabi, A. Arbabi, Z. Zhao, G. Xie, Y. Cao, N. Ahmed, Y. Yan, C. Liu, A. J. Willner, S. Ashrafi, M. Tur, A. Faraon, and A. E. Willner, "Orbital angular momentum-based space division multiplexing for high-capacity underwater optical communications", Sci. Rep. **6**, 33306 (2016) DOI: doi.org/10.1038/srep33306.

[5] Y. Horie, A. Arbabi, E. Arbabi, S. M. Kamali, and A. Faraon, "High-speed, phase-dominant spatial light modulation with silicon-based active resonant antennas", ACS Photonics **5**, 1711–1717 (2018) DOI: 10.1021/acsphotonics.7b01073.

[6] Y. Horie, S. Han, J.-Y. Lee, J. Kim, Y. Kim, A. Arbabi, C. Shin, L. Shi, E. Arbabi, S. M. Kamali, H.-S. Lee, S. Hwang, and A. Faraon, "Visible wavelength color filters using dielectric subwavelength gratings for backside-illuminated CMOS image sensor technologies", Nano Lett. **17**, 3159–3164 (2017) DOI: 10.1021/acs.nanolett.7b00636.

[7] E. Arbabi, A. Arbabi, S. M. Kamali, Y. Horie, and A. Faraon, "Multiwavelength metasurfaces through spatial multiplexing", Sci. Rep. **6**, 32803 (2016) DOI: 10.1038/srep32803.

[8] E. Arbabi, A. Arbabi, S. M. Kamali, Y. Horie, and A. Faraon, "High efficiency double-wavelength dielectric metasurface lenses with dichroic birefringent meta-atoms", Opt. Express **24**, 18468–18477 (2016) DOI: 10.1364/OE.24.018468.

[9] M. Faraji-Dana*, E. Arbabi*, A. Arbabi, S. M. Kamali, H. Kwon, and A. Faraon, "Compact folded metasurface spectrometer", Nat. Commun. **9**, 4196 (2018) DOI: 10.1038/s41467-018-06495-5.

[10] E. Arbabi, J. Li, R. J. Hutchins, S. M. Kamali, A. Arbabi, Y. Horie, P. Van Dorpe, V. Gradinaru, D. A. Wagenaar, and A. Faraon, "Two-photon microscopy with a double-wavelength metasurface objective lens", Nano Lett. **18**, 4943–4948 (2018) DOI: 10.1021/acs.nanolett.8b01737.

[11] E. Arbabi, A. Arbabi, S. M. Kamali, Y. Horie, and A. Faraon, "Controlling the sign of chromatic dispersion in diffractive optics with dielectric metasurfaces", Optica **4**, 625–632 (2017) DOI: 10.1364/OPTICA.4.000625.

[12] H. Kwon, E. Arbabi, S. M. Kamali, M. Faraji-Dana, and A. Faraon, "Computational complex optical field imaging using a designed metasurface diffuser", Optica **5**, 924–931 (2018) DOI: 10.1364/OPTICA.5.000924.

[13] H. Kwon, E. Arbabi, S. M. Kamali, M. Faraji-Dana, and A. Faraon, "Quantitative phase gradient microscopy using a system of multifunctional metasurfaces", Submitted.

[14] M. Faraji-Dana, E. Arbabi, H. Kwon, S. M. Kamali, A. Arbabi, J. G. Bartholomew, and A. Faraon, "Miniaturized metasurface hyperspectral-imager", Submitted.

[15] E. Arbabi, A. Arbabi, S. M. Kamali, Y. Horie, M. Faraji-Dana, and A. Faraon, "Mems-tunable dielectric metasurface lens", Nat. Commun. **9**, 812 (2018) DOI: 10.1038/s41467-018-03155-6.

[16] A. Arbabi, E. Arbabi, Y. Horie, S. M. Kamali, and A. Faraon, "Planar metasurface retroreflector", Nat. Photon. **11**, 415–420 (2017) DOI: 10.1038/nphoton.2017.96.

[17] M. Jang, Y. Horie, A. Shibukawa, J. Brake, Y. Liu, S. M. Kamali, A. Arbabi, H. Ruan, A. Faraon, and C. Yang, "Wavefront shaping with disorder-engineered metasurfaces", Nat. Photon. **12**, 84–90 (2018) DOI: 10.1038/s41566-017-0078-z.

TABLE OF CONTENTS

LIST OF FIGURES

ABBREVIATIONS

2D	two-dimensional.
DOE	diffractive optical element.
NA	numerical aperture.
HCA	high-contrast transmit/reflect array.
α-Si	amorphous silicon.
EMT	effective medium theory.
TiO_2	titanium dioxide.
NIR	near infrared.
FOV	field of view.
AR	augmented reality.
SiO_2	silicon dioxide.
TE	transverse electric.
Al_2O_3	aluminum oxide.
TM	transverse magnetic.
RCWA	rigorous coupled-wave analysis.
PECVD	plasma-enhanced chemical vapor deposition.
SF_6	sulfur hexafluoride.
C_4F_8	octafluorocyclobutane.
NH_4OH	ammonium hydroxide.
H_2O_2	hydrogen peroxide.
RHCP	right-hand circular polarization.
LHCP	left-hand circular polarization.
DoFP-PC	division of focal plane polarization camera.
LED	light emitting diode.
HWP	half waveplate.
QWP	quarter waveplate.
H/V	horizontal/vertical.
PBS	polarizing beamsplitter.
LP	linear polarizer.
DoFP	division of focal plane.
FWHM	full width at half maximum.
GS	Gerchberg-Saxton.
RGB	red-green-blue.
EBL	electron beam lithography.

CCD	charge-coupled device.
PDMS	polydimethylsiloxane.
OPD	optical path difference.
Ge	Germanium.
SEM	scanning electron microscope.
DI water	deionized water.
ND	neutral density.
3D	three-dimensional.
cSi	crystalline silicon.
PWE	plane wave expansion.
RMS	root mean square.
DUV	deep ultraviolet.
SLM	spatial light modulator.

Chapter 1

INTRODUCTION

The material in this chapter was in part presented in

> S. M. Kamali*, E. Arbabi*, A. Arbabi, and A. Faraon, "A review of dielectric optical metasurfaces for wavefront control", Nanophotonics **7**, 1041–1068 (2018) DOI: 10.1515/nanoph-2017-0129,

During the past few years, optical metasurfaces have gained a great deal of attention as a promising category of thin optical elements based on new operation principles that provide capabilities beyond conventional optical elements in many aspects. In this chapter I start with an introduction of metasurfaces and a brief historical review of them. Then, I discuss recent advancements and developments of different optical metasurface platforms, and explain the operation principles of the high-contrast dielectric metasurface platform which is the basis for all the works presented in the following chapters. At the end, I provide a short outline of the thesis content.

1.1 Introduction and historical review of metasurfaces

Optical metasurfaces are two-dimensional (2D) arrays of subwavelength scatterers that are designed to modify different characteristics of light such as its wavefront, polarization distribution, intensity distribution, or spectrum [1–13]. The subwavelength scatterers (referred to as meta-atoms in this context), capture and reradiate (or scatter) the incident light. Depending on the meta-atom design, the scattered light might have different characteristics compared to the incident light. For instance, it might have a different phase, polarization ellipse, angular distribution, intensity, and/or spectral content. For most metasurfaces, the output is either the scattered light or the interference between the scattered and the incident light. By proper selection of the meta-atoms and their locations in the array, the characteristics of light interacting with the metasurface can be engineered. As a result, different conventional optical components such as gratings, lenses, mirrors, holograms, waveplates, polarizers, and spectral filters may be realized. Furthermore, a single metasurface might provide a functionality that may only be achieved by a combination of conventional optical components [14] or an entirely novel functionality [15]. Typically metasurface

optical components are subwavelength thick, have a planar form factor, and can be batch-fabricated at potentially low cost using the standard micro and nano-fabrication processes. In the past few years, the efficiency of the optical metasurfaces has improved significantly by switching from metallic (or plasmonic) meta-atoms to high refractive index dielectric ones. The combination of the relatively high efficiency, potentially low cost, and the planar and thin form factor has generated significant interest in metasurface optical components, and attracted a large number of researchers from different disciplines and with various backgrounds. The result has been the rapid expansion of the field. Here we discuss the recent progress in the development of optical metasurfaces, focusing on dielectric metasurfaces that modify the wavefront and/or polarization distribution of light.

Optical metasurfaces are conceptually similar and technically closely related to the reflectarrays and transmitarrays which have been studied for decades in the microwave community [16]. For example, the idea of using elements (or meta-atoms) with different sizes and shapes has been used as early as 1993 in that community for creating spatially varying phase profiles [17]. Early demonstrations of optical metasurfaces which used metallic meta-atoms are similar to their microwave counterparts [18]. Another example is the use of the geometric (or Pancharatnam-Berry) phase for controlling the wavefront of circularly polarized waves that also has been used before in the microwave community [19, 20]. In addition, many of the properties, design techniques, and models for metasurface components are similar to those used in the context of diffractive optical elements (DOEs). The recognition of these similarities can be beneficial in the design and development of metasurfaces. An example of the results that are similarly applicable to metasurfaces and DOEs is the ray optics treatment of the refraction, reflection, and transmission of rays upon interaction with surfaces that impart a spatially varying phase. This topic has been well studied in diffractive optics and the resulting relation is known as the grating equation. A general treatment of this problem when the phase imparting surface has an arbitrary curved shape can be found in [21]. Depending on how they are realized, DOEs have different categories including kinoforms [22], holographic optical elements, computer-generated holograms [23], and effective medium structures [24, 25], and are realized using structures that are different from metasurfaces. However, similar to metasurfaces, they impart spatially varying phase excursion and are modeled as spatially varying phase masks. As a result, many of the techniques, theories, and designs developed for and using DOEs are directly applicable and transformable to metasurfaces. Some of the examples include the algorithms for the design of

phase profiles that project desired intensity patterns [23], estimations of diffraction efficiency for quantized phase levels [26], elimination of the spherical aberrations by proper selection of the phase profile [27], elimination of coma aberration of a phase profile by applying it on a curved spherical surface [28], and removal of other monochromatic aberrations by using a stop [29] or multiple cascaded elements [29].

One of the advantages of recognizing the relation of the metasurfaces to other DOEs, is the identification of the potential advantages of the metasurfaces over conventional DOEs. For instance, low-cost, efficient, and relatively wideband diffractive lenses can be realized using conventional DOEs [30], but their performance degrades significantly with increasing their numerical apertures (NAs). As we discuss in section 1.3, properly designed metasurfaces can outperform conventional DOEs.

1.2 Recent developments

In the past few years, the advances and the wider accessibility of micro and nano-fabrication technologies, along with an increased interest in dielectric high-contrast [31, 36, 37] and plasmonic structures [18, 38–41] for manipulation of optical wavefronts, have caused a surge in the research field of metasurfaces. Two of the early works using high contrast mirrors and plasmonic scatterers are shown in Figs. 1.1a and 1.1b, respectively. The ultrathin form factor of plasmonic structures, and the great interest in the field of plasmonics itself, resulted in most of the earlier works using a single metallic layer to manipulate light using resonance phase, geometric phase, or their combination [3, 40, 42–47]. However, material losses and fundamental limitations of single layer thin plasmonic metasurfaces (especially in the transmission mode) [48–50] significantly limit their performance. Dielectric geometric phase elements based on nano-beam half waveplates (similar to the example shown in Fig. 1.1c) have also been investigated [32, 51] for wavefront shaping. These elements are designed to work with one polarization, and achieving simultaneously both high efficiency and large deflection angles is challenging because of significant coupling between the elements.

To overcome the fundamental limitations of ultra-thin metasurfaces, Huygens' metasurfaces were introduced [33] that allow for simultaneous excitation of modes with equal electric and magnetic dipole moments. These structures do not have a deep subwavelength thicknesses, as shown in Fig. 1.1d where the wavelength is 30 mm. Despite their success in lower frequencies [52–57], in the optical domain metallic Huygens' metasurfaces are still limited by material losses and

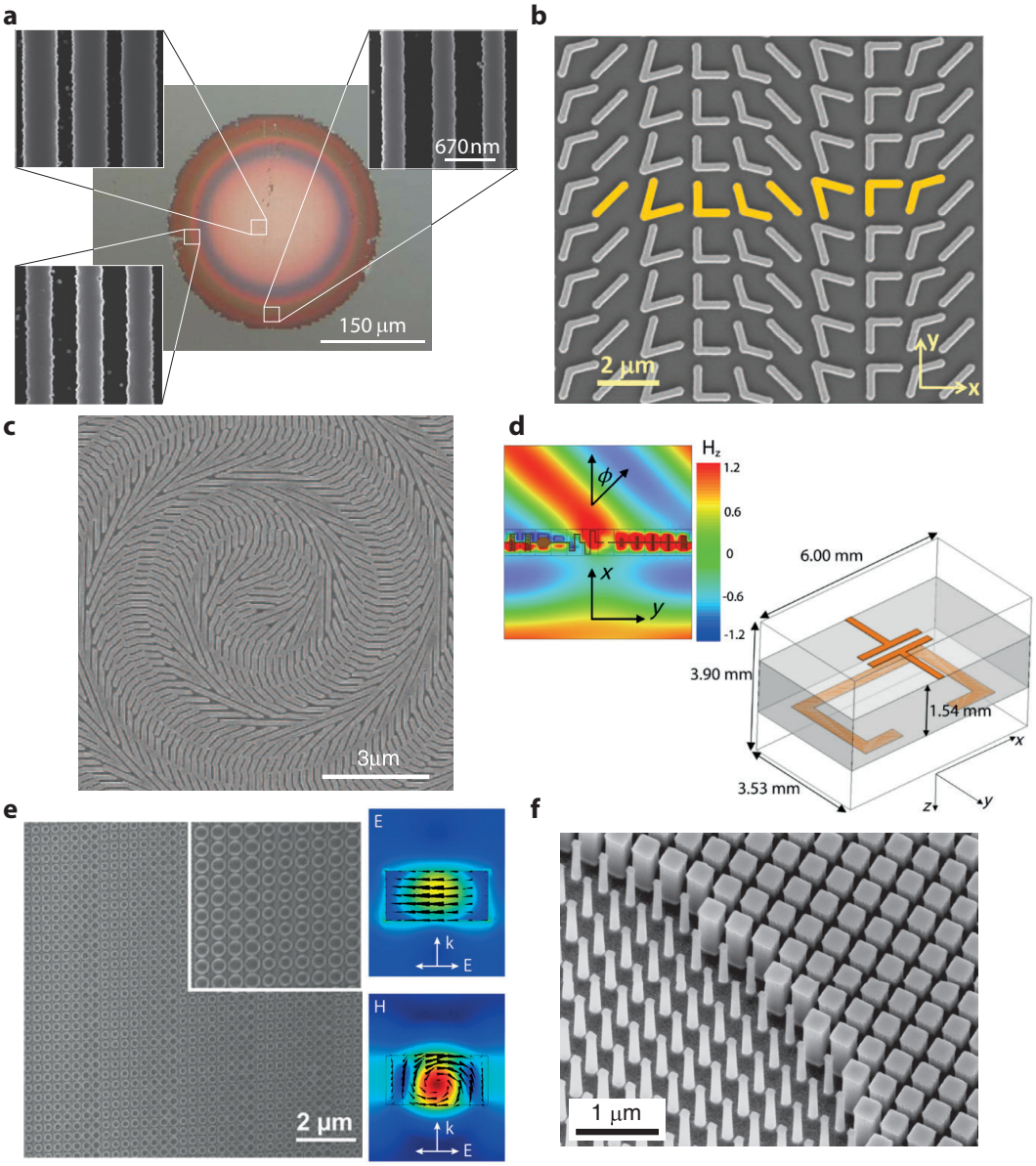

Figure 1.1: **Recent advances in metasurfaces**. **a**, Optical and scanning electron micrographs of a high-contrast grating mirror with focusing ability [31]. **b**, Scanning electron micrograph of a plasmonic metasurface beam deflector [18]. **c**, A geometric phase axicon with dielectric microbars [32]. **d**, Microwave beam deflection with a metallic Huygens' metasurface along with unit cell of the beam deflector [33]. **e**, Scanning electron micrograph of a dielectric Huygens' beam deflector. Simulated field intensities are plotted on the right [34]. **f**, Scanning electron micrograph of a portion of a high-contrast transmitarray lens [35].

often require complicated fabrication. As a result, dielectric Huygens' metasurfaces were explored [34, 58–63] that allowed for two longitudinal resonance modes with dominant electric and magnetic dipole moments with the same frequency to circumvent material losses [Fig. 1.1e]. There are, however, some challenges that limit the practicality of dielectric Huygens' metasurfaces. First, full 2π phase coverage at a single wavelength, which is what matters for wavefront manipulation, while keeping a high transmission requires changing all sizes of the resonators (including their heights) which is challenging to achieve with the conventional planar microfabrication technology. Second, the coupling between adjacent meta-atoms is considerable in Huygens' metasurfaces, and this significantly degrades the performance of devices with large deflection angles as they require fast varying structures [34]. As a result, more groups started investigating the high-contrast transmit/reflect arrays (HCAs) structures (similar to the one shown in Fig. 1.1f) that use thicker (about 0.5λ to λ) high-index layers to pattern the metasurface [14, 37, 64–73]. These structures are very similar to the blazed binary optical elements that are at least two decades old [74–77]; nevertheless, they outperform other classes of metasurfaces in many wavefront manipulation applications. In the following section, we will briefly discuss their operation principles, and review the recent findings and achievement of metasurfaces for controlling the wavefront of light.

We should note here that the applications of optical metasurfaces in the general sense of the word (i.e., patterned thin layers on a substrate) go beyond spatial wavefront manipulation. Thin light absorbers [78–92], optical filters [93–105], nonlinear [106–113], and anapole metasurfaces [114, 115] are a few examples of such elements. This review is focused on applications of metasurfaces in wavefront manipulation, and therefore it doesn't cover these other types of metasurfaces.

1.3 High-contrast reflect/transmit arrays

Since HCAs are central to the most of the discussions of this section, we first briefly discuss their operation. We are primarily interested in the two-dimensional HCAs, and therefore we consider their case here, although much of the discussions are also valid for the one-dimensional case. In general, these devices are based on high-refractive-index dielectric nano-scatterers surrounded by low-index media [14, 37, 64, 66, 69–71, 75, 77]. The structure can be symmetric (i.e., with the substrate and capping layers having the same refractive indices) [35] or asymmetric [65, 66, 75, 77]. Depending on the materials and the required phase coverage, the

thickness of the high-index layer is usually between $0.5\lambda_0$ and λ_0, where λ_0 is the free space wavelength. Typically, these structures are designed to be compatible with conventional microfabrication techniques; therefore, they are composed of nano-scatterers made from the same material structure and with the same thickness over the device area. Various scatterers can have different cross-sections in the plane of the metasurface, but the cross-section of any single scatterer is usually kept the same along the layer thickness to facilitate its fabrication using binary lithography techniques. For wavefront shaping, the nano-scatterers should be on the vertices of a subwavelength lattice that satisfies the Nyquist sampling criterion [35] in order to avoid excitation of unwanted diffraction orders. For simplicity, the lattices are usually selected to be periodic. Figure 1.2a shows two typically used structures with triangular and square lattices [37, 77]. For polarization-independent operation (in the case of normal incidence with small deflection angle) the nano-scatterers should have symmetric cross-sections such as circles, squares, regular hexagons, etc. (Fig. 1.2a). Similar to high-contrast gratings [31, 36, 116], these structures can also be used in reflection mode by backing them with a metallic or dielectric reflector [117–119] [Fig. 1.2a, bottom], or by properly selecting their thicknesses [120, 121].

The first HCA diffractive devices demonstrated by Lalanne et al. (referred to as blazed binary diffractive devices at the time) were designed to operate in an effective medium theory (EMT) regime where only one transverse mode could be excited in the HCAs layer [75, 77]. In 2011, it was suggested by Fattal et al. [37], and later demonstrated [64–66] that using higher index materials (Si or amorphous silicon (α-Si) instead of titanium dioxide (TiO_2)) can result in devices with higher efficiency for large deflection angles, despite a departure from the EMT regime (where the lattice constant is larger than the structural cut-off [77], yet it is small enough to avoid unwanted diffraction [64, 65]). It is worth noting that even for the lower index materials like TiO_2, the optimal operation regime seems to be where the lattice is designed just below the structural cut-off [76]. It is worth noting that depending on the design parameters, higher index devices (such as silicon ones) can operate in the EMT regime [122]. One example of such devices is shown in Fig. 1.2b, where a graded index lens was etched into a silicon wafer to focus light inside the wafer [122]. The ability of the EMT blazed binary structures to significantly outperform the conventional échelette gratings is dominantly attributed to the waveguiding effect of the nano-posts that results in a sampling of the incoming and outgoing waves with small coupling between adjacent nano-posts [76]. In devices using higher refractive index materials like silicon, the coupling between adjacent nano-posts remains small

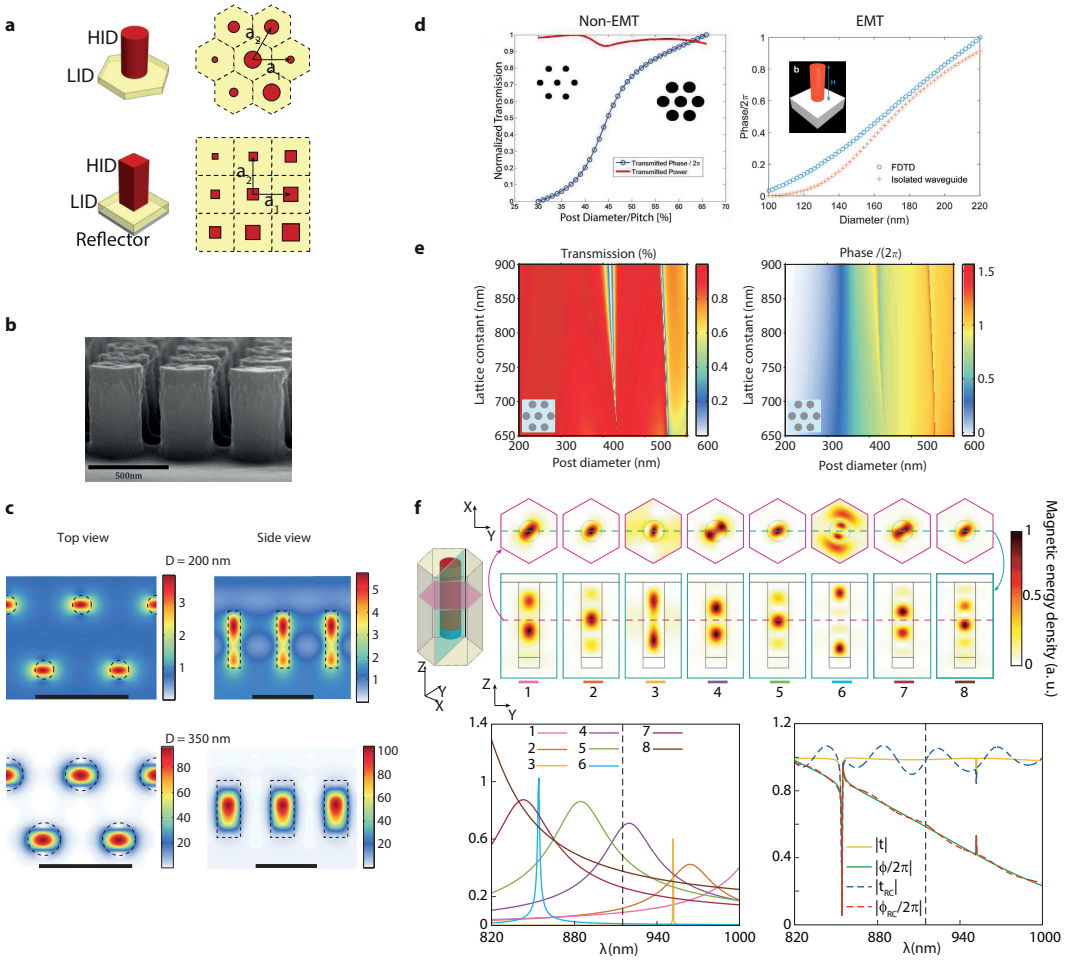

Figure 1.2: **Operation principles of HCAs**. **a**, Schematic illustration of some possible HCA configurations with different nano-post shapes and lattice structures. HID: high-index dielectric, LID: low-index dielectric. **b**, Scanning electron micrograph of a graded index lens, etched directly into a silicon wafer [122].**c**, Simulated magnetic energy density in a periodic array of α-Si nano-posts plotted in cross sections perpendicular to (left), and passing through (right) the nano-posts' axes. For larger nano-posts, the field is highly confined inside the nano-posts. The scale bars are 1 μm [66]. **d**, Simulated transmission phase for α-Si nano-posts operating beyond the EMT regime (left, [65]), and TiO_2 nano-posts operating within the EMT regime (right, [123]). **e**, Simulated transmission amplitude and phase of a periodic array of circular α-Si nano-posts versus posts diameter and lattice constant [66]. **f**, Top: Magnetic energy distribution of optical resonances inside an α-Si nano-post that contribute to the transmission amplitude and phase of the structure around 900 nm [124]. Bottom: Reconstruction of the nano-post transmission and phase using the frequency responses of the resonance modes. The left figure shows relative contributions of the different modes.

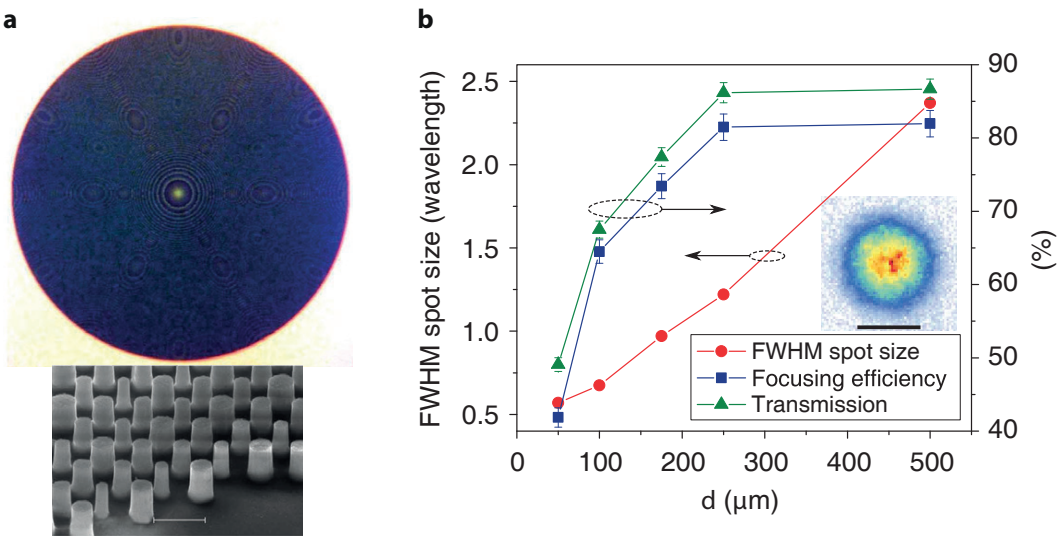

Figure 1.3: **High efficiency high-NA lenses based on α-Si HCA**. **a**, Optical image (top) and scanning electron micrograph (bottom) of a portion of a near infrared (NIR) lenses fabricated with α-Si HCAs. **b**, Performance of the fabricated HCA lenses. The lenses are designed to focus light emitted by a single-mode optical fiber to a diffraction-limited spot. The lenses have NAs from ~0.5 to ~0.97, and measured focusing efficiencies of 82% to 42%. Scale bar: $1\mu m$.

even above the structural cut-off. In Fig. 1.2c, the simulated magnetic energy density is plotted for α-Si nano-posts, showing that the field is highly confined inside the silicon nano-posts which reduces the coupling between nanoposts. In this case, there are multiple propagating transverse modes inside the layer [66]. In addition, due to the larger number of resonances, the transmission phase for the nano-posts with the higher refractive index is a steeper function of the nano-post's size (compared to the EMT structures) as shown in Fig. 1.2d [65, 123]. This relieves the requirements of the nano-posts aspect ratio and makes their fabrication more feasible [65].

A second effect of the high field confinement is that the behavior of the structure becomes more insensitive to the lattice parameters, as shown in Fig. 1.2e [66]. More importantly, this means that the transmission phase of a nano-post is largely insensitive to its neighboring posts; therefore, adjacent nano-posts can have significantly different sizes without much degradation of their performance. This is in contrast to the dielectric Huygens metasurfaces [34, 58, 60, 117, 125, 126], where the coupling between neighboring scatterers results in significant performance degradation if the size of the neighboring scatterers changes too abruptly. In addition, unlike the Huygens metasurfaces, the high transmission amplitude and full 2π-phase-coverage of the HCAs result from the contributions of multiple resonances. Such resonances

are shown for a typical α-Si nano-post in Fig. 1.2f [124]. An expansion of the optical scattering of the nano-posts to electric and magnetic multipoles is also possible [69]. However, capturing the full physics requires the use of higher order multipoles, and the expansion does not give much direct information about the contribution of each resonance to each of the multipole terms, or how they can be tailored for a specific application.

In recent years, multiple groups have demonstrated high-efficiency high-numerical aperture (NA) lenses using the HCA platform [65, 66, 68, 71, 123, 127]. Figure 1.3, shows one of the early demonstrations where lenses with NAs ranging from ~0.5 to above 0.95 were demonstrated, with measured absolute focusing efficiencies from 82% to 42% depending on the NA, while keeping a close to diffraction limited spot.

In both EMT and non-EMT regimes, the standard design method for optical phase masks (lenses in particular) has been to extract the transmission (reflection) coefficient for a periodic array of nano-posts and use them directly to design aperiodic devices that manipulate the phase profile [37, 64–66, 77]. This design process is based on the assumptions that the sampling is local, there is not much coupling between the nano-posts, and the transmission phase and amplitude remain the same for different scattering angles. The validity of these assumptions starts to break at large deflection angles and contributes to the lower efficiency of the devices at such angles. More recently, a few methods have been proposed and demonstrated potential for increasing the efficiency of these devices [128–130]. While periodic devices (i.e., blazed gratings) with measured efficiencies as high as 75% at 75-degree deflection angles have been demonstrated, the case for non-periodic devices is more challenging, and to the best of our knowledge, the absolute measured focusing efficiencies for lenses with NAs about 0.8 have been limited to slightly above 75% [129]. Proper measurement and reporting of the efficiency is a very important parameter in phase control devices with high-gradients. A proper definition of efficiency for lenses is the power of light focused to a small area around the focal point (for instance a disk with a diameter that is two to three times the diffraction limited Airy diameter). With this definition, it is essential in experiments that a pinhole be used around the focal spot to block the light outside this area; otherwise, the measured value would be the transmission efficiency. It is also important to identify the illuminating beam size when measuring efficiencies. Using a beam smaller than the clear aperture of the lens will effectively reduce the NA of the lens and lead to an overestimation of the device efficiency. The type of power detector used may also significantly bias the

efficiency measurements. The light focused by a high NA device has a wide angular spectrum and many detectors are sensitive to the incident angle of light. Ideally, a detector with a wide acceptance angle such as an integrating sphere should be used in the efficiency measurements.

The discussed capabilities of metasurfaces and in particular HCAs in shaping the wavefront of light and deflecting beam to large angles with high efficiencies have been the main motivation and advantage of metasurfaces over conventional DOEs. However, a more important property of metasurfaces beyond conventional DOEs is their capabilities to control light independently based in its various degrees of freedom such as polarization [14, 131–133], angle [15, 134], and wavelength [118, 135–137]. Furthermore, metasurfaces compact and two-dimensional form factors enable paradigm changing platforms for optical element and system design. For example, we have developed conformal and tunable optical elements based on metasrufaces encapsulated in flexible substrates [35, 124], wide field of view (FOV) cameras and retroreflectors using vertically cascaded metasurfaces [119, 138], micro-electro-mechanically tunable lenses [139], compact folded optical systems like spectrometers and hyper-spectral imagers [140, 141], and 3D beam shapers 6. These capabilities are what truly set metasurfaces in general, and HCAs in particular, apart from conventional diffractive and refractive optics. As such, my doctoral work has been focused on the development of HCAs with these capabilities.

1.4 Thesis outline

The main goal of this thesis is to showcase the unprecedented capabilities of optical metasurfaces and in particular HCAs, Chapters 2 and 3 are focused on metasurfaces based on new underlying concepts of controlling light based on its illumination angle and polarization degrees of freedom. Chapters 4, 5, 6, and 7 are focused on new metasurface platforms of conformal and tunable metasurfaces, 3D metasurface beam shapers, and integrated metasurfaces.

More specifically, Chapter 2 introduces the concept of angle-multiplexed metasurfaces through designing nanostructures that independently control the phases imparted onto light impinging from two directions (i.e., with different transverse momenta). As a result, it enables dramatically different embedded optical functions in a single metasurface, separately accessible under different illumination angles. Chapter 3 discusses a metasurface platform with simultanous polarization and phase control based on birefringent nanoposts, which enables imaging and generation of various

states of polarization. Chapter 4 introduces the concept and demonstration of conformal metasurfaces to alter the optical properties of any arbitrarily shaped object with a properly designed thin and flexible metasurface. Chapter 5 discusses high-performance tunable metasurface lenses through stretching their elastic substrate. Chapter 6 introduces the metasurface assisted 3D beam shaping platform in order to fabricate three-dimensional exotic periodic lattices, like gyroid and diamond structures. Chapter 7 introduces the concept of optical systems through monolithic integration of multiple metasurface elements. Projection optics in compact augmented reality (AR) headsets are discussed as an example of optical systems. Chapter 8 concludes the thesis with a discussion about potentials and challenges, and future outlook and vision.

Chapter 2

METASURFACES WITH PHASE AND ANGLE CONTROL

The material in this chapter was in part presented in

> S. M. Kamali, E. Arbabi, A. Arbabi, Y. Horie, M. Faraji-Dana, and A. Faraon, "Angle-multiplexed metasurfaces: encoding independent wavefronts in a single metasurface under different illumination angles", Phys. Rev. X **7**, 041056 (2017) DOI: 10.1103/PhysRevX.7.041056,

The angular response of thin DOEs is highly correlated. For example, the angles of incidence and diffraction of a grating are locked through the grating momentum determined by the grating period. Other diffractive devices, including conventional metasurfaces, have a similar angular behavior due to the fixed locations of the Fresnel zone boundaries and the weak angular sensitivity of the meta-atoms. To alter this fundamental property, in this chapter, we introduce *angle-multiplexed metasurfaces*, composed of reflective high-contrast dielectric U-shaped meta-atoms, whose response under illumination from different angles can be controlled independently. This enables flat optical devices that impose different and independent optical transformations when illuminated from different directions, a capability not previously available in diffractive optics.

2.1 Motivation

The concept of angular correlation is schematically depicted in Fig. 2.1a for a diffraction grating. In gratings, the diffraction angle θ_m of order m is related to the incident angle θ_{in} by the relation $d(\sin(\theta_m) - \sin(\theta_{\text{in}})) = m\lambda$, where λ is the wavelength, and d is the grating period, determined solely by the geometry. Therefore, a grating adds a fixed "linear momentum", dictated by its period, to the momentum of the incident light regardless of the incident angle. Similarly, a regular hologram designed to project a certain image when illuminated from a given angle will project the same image (with possible distortions and efficiency reduction) when illuminated from a different angle (Fig. 2.1c). The concept that we introduce here is shown schematically in Fig. 2.1b for an angle-multiplexed grating that adds a different

"linear momentum" depending on the angle of incidence, and Fig. 2.1d for an angle-multiplexed hologram that displays a different image depending on the angle of incidence. Breaking this fundamental correlation and achieving independent control over distinct incident angles is conceptually new and results in the realization of a new category of compact multifunctional devices which allow for embedding several functions into a thin single metasurface.

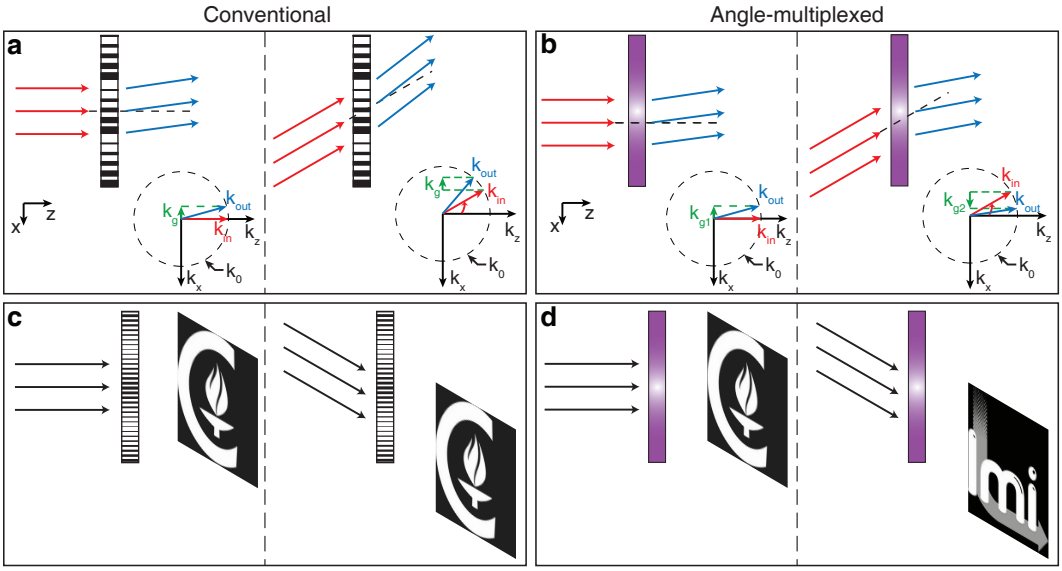

Figure 2.1: **Angle-multiplexed metasurface concept**. **a**, Schematic illustration of diffraction of light by a grating. A grating adds a fixed linear momentum ($\hbar k_g$) to the incident light, independent of the illumination angle. If the illumination angle deviates from the designated incident angle, light is deflected to a different angle which is dictated by the grating period. **b**, Illustration of the angle-multiplexed metasurface platform. This platform provides different responses according to the illumination angle. For instance, two gratings with different deflection angles (different grating momenta) can be multiplexed such that different illumination angles acquire different momenta. **c**, Illustration of a typical hologram that creates one specific image (Caltech logo) under one illumination angle (left). The same hologram will be translated laterally (and distorted) by tilting the illumination angle (right). **d**, Schematic illustration of an angle-multiplexed hologram. Different images are created under different illumination angles. For ease of illustration, the devices are shown in transmission while the actual fabricated devices are designed to operate in reflection mode.

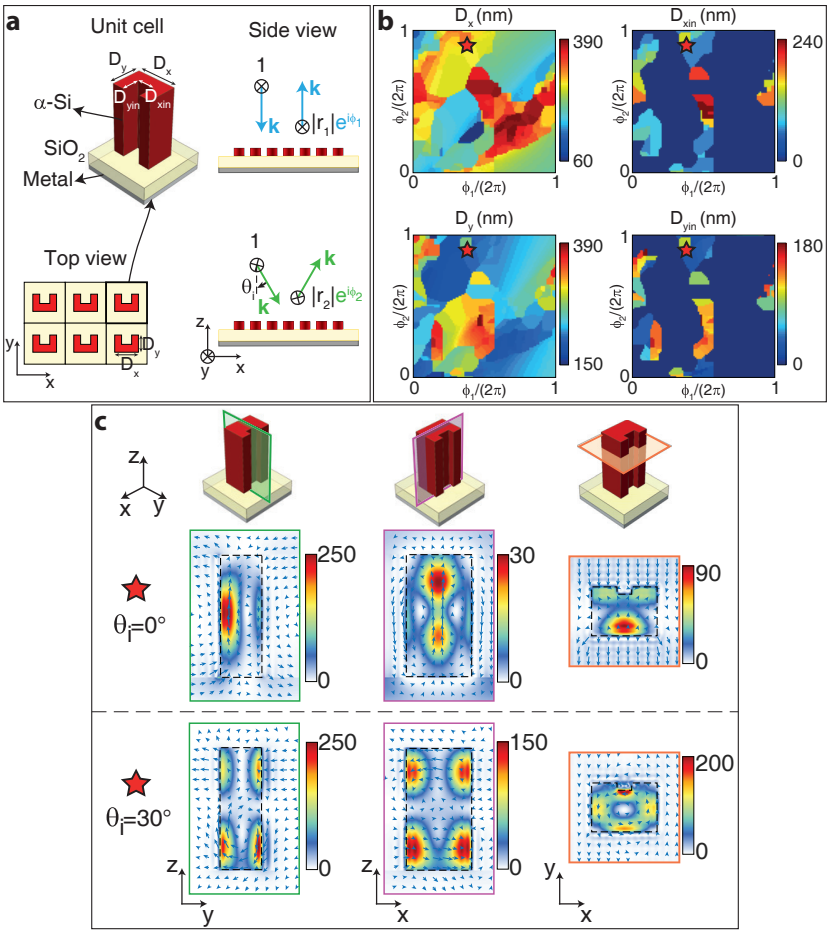

Figure 2.2: **The meta-atom structure and the design graphs.** **a**, Schematic drawing of various views of a uniform array of U-shaped cross-section α-Si meta-atoms arranged in a square lattice resting on a thin SiO_2 spacer layer on a reflective surface (i.e., a metallic mirror). The array provides angle-dependent response such that TE-polarized light at 0° and 30° illumination angles undergo different phase shifts as they reflect from the array. **b**, Simulated values of the U meta-atom dimensions (D_x, D_y, $D_{x\text{in}}$, and $D_{y\text{in}}$) for achieving full 2π phase shifts for TE-polarized light at 0° and 30° illumination angles, respectively. One can find the values of the four dimensions of a meta-atom which imposes ϕ_1 and ϕ_2 reflection phase shifts onto TE-polarized normal and 30° incident angle optical waves from (b). **c**, Electric energy density inside a single unit cell in a periodic uniform lattice for a typical meta-atom (shown in (b) with a star symbol) at 0° and 30° illumination angles is plotted in three cross sections. Blue arrows indicate in-plane electric field distributions excitepd at each illumination angle. Different field distributions at normal and 30° incidence are an indication of excitation of different resonant modes under different incident angles. In all parts of the figure, the meta-atoms are 500 nm tall. The silicon dioxide and aluminum layers are 125 nm and 100 nm thick respectively, the lattice constant is 450 nm, and all simulations are performed at the wavelength of 915 nm.

2.2 Operation theory and design of angle-multiplexed meta-atoms

A meta-atom structure capable of providing independent phase control under transverse electric (TE)-polarized light illumination with 0° and 30° incident angles is shown in Fig. 5.2a. The α-Si meta-atoms have a U-shaped cross section (we will call them U meta-atoms from here on) and are located at the vertices of a periodic square lattice on a low refractive index silicon dioxide (SiO_2) and aluminum oxide (Al_2O_3) spacer layers backed by an aluminum reflector. Since the electric field is highly localized in the nano-posts, the low-loss low-index dielectric spacer between the nano-posts and the metallic reflector is necessary to avoid the high losses from metal. In addition, the spacer layer allows for efficient excitation of the resonance modes under both angles of illumination through a constructive interference between the incident and reflected fields inside the nano-posts. Therefore, the nano-posts act as one-sided multi-mode resonators [118, 119, 124]. For the wavelength of 915 nm, the meta-atoms are 500 nm tall, the SiO_2 layer, the Al_2O_3 layer, and the aluminum reflector are 125 nm, 30 nm, and 100 nm thick, respectively, and the lattice constant is 450 nm. A uniform array of U meta-atoms provides an angle-dependent response such that TE-polarized light waves incident at 0° and 30° undergo different phase shifts (ϕ_1 and ϕ_2, respectively) as they are reflected from the array. A periodic array of U meta-atoms was simulated to find the reflection amplitude and phase at each incident angle (see Sec. 4.7 for simulation details). Any combination of ϕ_1 and ϕ_2 from 0 to 2π can be simultaneously obtained by properly choosing the in-plane dimensions of the meta-atoms (i.e., D_x, D_y, $D_{x\text{in}}$, and $D_{y\text{in}}$ as shown in Fig. 5.2b). Therefore, any two arbitrary and independent phase profiles for TE-polarized 0° and 30° illumination angles can be designed simultaneously (see Sec. 4.7 for design procedure details). The corresponding reflection amplitudes ($|r_1|$ and $|r_2|$) and achieved phase shifts are shown in Fig. 2.5 in section 4.7. The independent control of phase at different incident angles is a result of exciting different modes of the U meta-atom under two distinct illumination angles. Figure 5.2c shows the excited electric energy density for a typical meta-atom in a periodic array at three different cross-sections under 0° and 30° incident angles (top and bottom receptively). The example meta-atom dimensions and corresponding phases at each illumination angle are shown in Fig. 5.2b by a star symbol. Modes that are excited under 30° illumination angle are different from the excited modes at normal illumination as seen in Fig. 5.2c. There are two categories of symmetric and antisymmetric

resonant modes. In normal incidence only symmetric modes are excited, while in oblique illumination both the symmetric and antisymmetric modes are excited. This is a key factor in realizing this independent control for different angles in a local metasurface platform. As the metasurface is still assumed to be local (i.e., the coupling between adjacent meta-atoms is neglected in the design), any two arbitrary different wavefronts can be simultaneously designed for the two different illumination angles by using the design graphs shown in Fig. 5.2b. In addition, due to the symmetry of the nano-posts (and also as verified from simulation results) the polarization conversion of the metasurface platform from TE to TM is negligible.

2.3 Experimental results of the angle-multiplexed grating and hologram

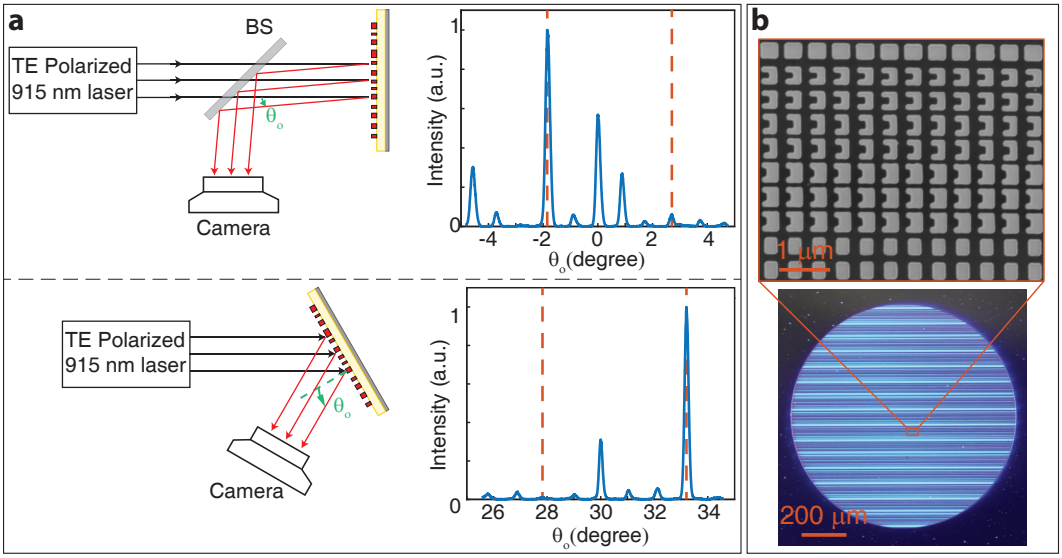

Figure 2.3: **Angle-multiplexed grating**. **a**, Simplified schematic of the measurement setup (left), and measured reflectance of the angle-multiplexed grating under normal illumination of TE-polarized light as a function of the observation angle θ_0 (right). The grating deflects 0° and 30° TE-polarized incident light to -1.85° and +33.2° respectively. Orange dashed lines indicate the designed deflection angles (-1.85° and +33.2° under 0° and 30° incidence respectively), and the deflection angles corresponding to regular gratings with fixed grating periods (2.7° under normal and 27.88° under 30° illumination angle assuming grating periods of 21λ and 31λ, respectively). See Sec. 4.7 and Fig. 2.6 for measurement details. **b**, Optical image of the angle-multiplexed grating. The inset shows a scanning electron micrograph of the top view of meta-atoms composing the metasurface. See 4.7 for fabrication details. BS: beam splitter.

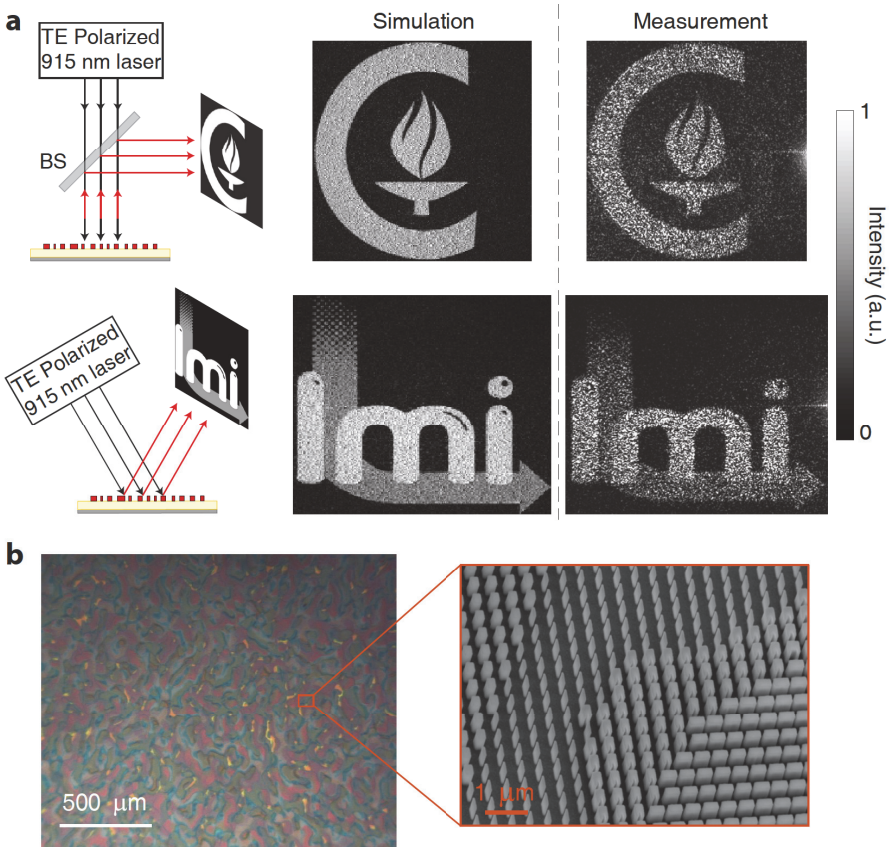

Figure 2.4: **Angle-multiplexed hologram a**, Simplified drawing of the measurement setups under normal and 30° illumination angles (left). The angle-multiplexed hologram is designed to create two different images under different incident angles (Caltech and LMI logos under 0° and 30°, respectively). Simulated and measured reflected images captured under 915-nm TE-polarized light at 0° and 30° illumination angles are shown on the right. See Sec. 4.7 and Fig. 2.7 for measurement details. **b**, Optical image of a portion of the angle-multiplexed hologram. The inset shows a scanning electron micrograph under oblique view of meta-atoms composing the metasurface. See Sec. 4.7 for fabrication details. BS: beam splitter.

The freedom provided by the proposed platform to simultaneously control the phase of light at two distinct incident angles allows for the implementation of a variety of new compact optical components. To demonstrate the versatility of this platform, we fabricated and characterized two examples of angle-multiplexed metasurfaces. First, an angle-multiplexed grating was designed to operate at 0° and 30° incident angles with two different effective grating periods. The angle-multiplexed grating has a diameter of 1 mm and deflects 915-nm TE-polarized light incident at 0° and 30° into -1.85° and +33.2° respectively. The corresponding effective periods are 31λ (blazed for -1 diffraction order) and 21λ (blazed for +1 diffraction order) for 0° and 30°

illuminations, respectively (λ =915 nm is the free space wavelength). The designed devices were fabricated using standard semiconductor fabrication techniques as described in Sec. 4.7. Optical and scanning electron microscope images of the fabricated angle-multiplexed grating are shown in Fig. 2.3b. Figure 2.3a shows the measured diffracted light intensities versus angle under 0° (top) and 30° (bottom) TE-polarized illuminations, as well as the simplified measurement setup schematics. The measured reflectance as a function of observation angle shows a dominant peak at the designed angles (i.e., -1.85° under normal illumination and +33.2° under 30° incident angle). Orange dashed lines show deflection angles corresponding to both effective periods, which are 31λ (blazed for -1 diffraction order) and 21λ (blazed for +1 diffraction order). A regular grating with a 31λ period, blazed for -1 diffraction order, would deflect normal incidence into -1.85°, and 30° incident angle into 27.88°. Similarly, another regular grating with 21λ period, blazed for +1 diffraction order, would deflect normal incidence into +2.7° and 30° incident angle into 33.2°. The angle-multiplexed grating, on the other hand, deflects 0° and 30° incident angles into -1.85° and +33.2° respectively, with no strong deflection peaks at the angle corresponding to the other grating periods (which are, +2.7° and 27.88°). The deflection efficiency of the grating at each incident angle is defined as the power deflected by the grating to the desired order, divided by the power reflected from a plain aluminum reflector (see Sec. 4.7 for measurement details and Fig. 2.6 for measurement setups). Deflection efficiencies of 30% and 41% were measured under 0° and 30° incident angles, respectively. For comparison, we simulated the central ~200 μm-long portion of the grating with a finite difference time domain full-wave electromagnetic solver [142] (see Sec. 4.7 and Fig. 2.7 for simulation results). The simulated deflection efficiencies are 63% and 54% for 0° and 30° operation, respectively. To consider the possible fabrication errors, we also simulated the grating with a random error added to the all in-plane sizes of the meta-atoms. The error is normally distributed with a zero mean, a 4-nm standard deviation, and a forced maximum of 8 nm. The simulated deflection efficiencies with the added errors are 46% and 39% under 0° and 30° incident angles. We attribute the remaining difference between simulated and measured efficiencies to two factors: first, the deposited aluminum reflected layer has a significant surface roughness. This may result in existence and excitation of local surface plasmon resonances that contribute to both increased loss and reflection phase error. Second, to counter the effects of systematic fabrication errors, an array of gratings with different biases added to each size of the meta-atoms is fabricated. In the measurements, one of the devices with

good performance under both illumination angles is selected and characterized (i.e., there are other fabricated gratings that demonstrate higher efficiencies for one of the angles). As a result, the characterized device might differ from the one with sizes closest to design values. This may justify the different balances between measured and simulated values for efficiencies under the two illumination angles.

As a second example, an angle-multiplexed hologram which projects two different images under 0° and 30° illumination angles was designed, fabricated, and characterized. The hologram covers a 2 mm by 2 mm square, and projects the Caltech and LMI logos when illuminated by TE-polarized light at 915 nm at 0° and 30° incident angles. Optical and scanning electron microscope images of a portion of the fabricated hologram are shown in Fig. 2.4b. Simulated and measured intensity profiles for two different illumination angles (top and bottom) are shown in Fig. 2.4a, along with simplified schematics of the measurement setups. The Caltech logo is created under normal illumination. By scanning the incident angle from 0° to 30°, the projected image changes from the Caltech logo to the LMI logo. The change in the recorded image with the incident angle is shown in this supplemental movie. The good agreement between the simulation and measurement results confirms the independent control of this platform over distinct incident angles. In order to avoid an overlap between the holographic image and the zeroth-order diffraction, the holograms are designed to operate off axis (see Sec. 4.7 for details of hologram design).

2.4 Discussion

The angle-multiplexed metasurface platform allows for devices that perform completely independent functions (i.e., grating, lens, hologram, orbital angular momentum generator, etc.) for different angles of illumination. It is worth noting that the concept and implementation of the angle-multiplexed metasurfaces are fundamentally different from multi-order gratings. While the multi-order gratings can be designed such that the efficiencies of different diffraction orders vary with the incident angle [143, 144], the grating momentum corresponding to each order (which is locked to the period of the grating) remains fixed. This difference becomes much clearer when considering the case of holograms. Unlike in the demonstrated platform, it is not possible to encode two completely independent phase profiles corresponding to two completely independent functions in a multi-order holographic optical element (i.e., the generalized case of the multi-order gratings).

2.5 Summary and outlook

In conclusion, we developed optical metasurfaces that break the angular correlation of thin diffractive components, and enable devices where independent phase masks can be embedded in a single thin layer and accessed separately under different illumination angles. Here, the shape of the meta-atom was chosen intuitively, and we expect that by utilizing more advanced optimization procedures the independent control can be extended to more angles and the device performance can be improved significantly. From a technological point of view, this is a novel class of metasurfaces that opens the path towards ultracompact multifunctional flat devices not feasible otherwise. This is complementary to the previously demonstrated independent control over different polarizations [14, 145] or wavelengths of the incident light [136, 137, 146, 147], and thus significantly expands the range of applications for nano-engineered metasurfaces.

2.6 Appendix

Simulation and Design

To find the reflection amplitude and phase of a uniform array of meta-atoms, the rigorous coupled-wave analysis (RCWA) technique was used [148]. A normal and a 30° incident plane wave at 915 nm wavelength were used as the excitation, and the amplitude and phase of the reflected wave were extracted. The subwavelength lattice for both normal and oblique illumination angles results in the excitation of only the zeroth order diffracted light. This justifies the use of only one reflection value at each illumination angle for describing the optical behavior of the meta-atom at each illumination angle. The α-Si layer was assumed to be 500 nm thick. The SiO_2 and aluminum layers were assumed to be 125 nm and 100 nm thick, respectively. Refractive indices at 915 nm wavelength were assumed as follows: α-Si: 3.558, SiO2: 1.44, Al2O3: 1.7574, and Al: 1.9183-i8.3447. The meta-atom in-plane dimensions (D_x, D_y, $D_{x\mathrm{in}}$, and $D_{y\mathrm{in}}$) are swept such that the minimum feature size remains larger than 50 nm for relieving fabrication constraints.

The optimum meta-atom dimensions for each lattice site at the two incident angles were found by minimizing the total reflection error, which is defined as $\epsilon = |\exp(\mathrm{i}\phi_1) - \mathrm{r}_1|^2 + |\exp(\mathrm{i}\phi_2) - \mathrm{r}_2|^2$, where r_1 and r_2 are the complex reflection coefficients of the unit-cell at the two incident angles. Therefore, for any desired combination of phases ϕ_1 and ϕ_2 in the 0 to 2π range at the two incident angles, there

is a corresponding meta-atom (i.e., D_x, D_y, $D_{x\text{in}}$, and $D_{y\text{in}}$ values) that minimizes the reflection error. To limit the rapid jumps in dimensions shown in Fig.5.2b, some modification terms were added to the reflection error in order to ensure that adjacent dimensions are preferred for the adjacent phases. The modification terms were defined as an exponential function of the Euclidean distance between the in-plane dimensions of the meta-atoms for adjacent phase values.

The holograms of different incident angles were designed individually using the Gerchberg-Saxton (GS) algorithm with $\sim 3^\circ$ deflection angles. The simulation results presented in Fig. 2.4 were computed by assuming that the coupling among adjacent meta-toms is negligible, such that each meta-atom imposes the exact complex reflection amplitude found from simulations of the periodic structure. The hologram area was assumed to be illuminated uniformly with 0° and 30° incident angle plane waves, and the projected holographic images were found by taking the Fourier transform of the field after being reflected from the phase mask.

Sample fabrication and Measurement procedure

A ~100-nm aluminum layer was evaporated on a silicon wafer, followed by a ~30-nm Al_2O_3 layer. A 125-nm-thick SiO_2 and a 500-nm-thick α-Si layer were subsequently deposited using the plasma-enhanced chemical vapor deposition (PECVD) technique at 200°C. A Vistec EBPG5200 e-beam lithography system was used to define the pattern in a ~300 nm thick layer of ZEP-520A positive electron-beam resist (spin coated at 5000 rpm for 1 min). The pattern was developed in the resist developer (ZED-N50 from Zeon Chemicals) for 3 minutes. A ~50-nm-thick Al_2O_3 layer was evaporated on the sample, and the pattern was then transferred to the Al_2O_3 layer by a lift off process. The patterned Al_2O_3 hard mask was then used to dry etch the α-Si layer in a mixture of sulfur hexafluoride (SF_6) and octafluorocyclobutane (C_4F_8) plasma. Finally, the Al_2O_3 mask was removed in a 1:1 solution of ammonium hydroxide (NH_4OH) and hydrogen peroxide (H_2O_2) at 80°C.

The angle-multiplexed grating was measured using the setup shown schematically in Fig. 2.6 in Sec. 4.7. A 915-nm fiber-coupled semiconductor laser was used for illumination and a fiber collimation package (Thorlabs F220APC-780) was used to collimate the incident beam. A polarizer (Thorlabs LPVIS100-MP2) was inserted to confirm the TE polarization state of the incident light. An additional lens with a focal length of 10 cm (Thorlabs AC254-100-B-ML) was placed before the grating at a distance of ~8 cm to partially focus the beam and reduce the beam divergence

after being deflected by the grating in order to decrease the measurement error. The light deflected from the device was imaged using a custom built microscope. The microscope consists of a 10X objective lens (Mitutoyo M Plan Apo 10X, NA= 0.28) and a tube lens (Thorlabs LB1945-B-ML) with a focal distance of 20 cm, which images the object plane onto a camera (CoolSNAP K4 from Photometrics). A rotation stage was used to adjust the illumination angle and a 50/50 beamsplitter (Thorlabs NIR Non-Polarizing Cube Beamsplitter) was inserted before the grating for measurements under normal illumination. For efficiency measurements of the grating, an iris was used to select the desired diffraction order and block all other diffraction orders. A power meter (Thorlabs PM100D) with a photodetector (Thorlabs S122C) was used to measure the deflected power off the grating, as well as the reflected power from a plain aluminum reflector (from an area adjacent to the grating). The grating efficiency was calculated by dividing the power deflected to the desired order to the power reflected by the aluminum reflector. Neutral density (ND) filters (Thorlabs ND filters, B coated) were used to adjust the light intensity and decrease the background noise captured by the camera.

The angle-multiplexed hologram was characterized using the setup shown schematically in Fig. 2.7. The setup is similar to the grating measurement setup with some modifications. The 10 cm focal distance lens used to partially focus light to the grating was removed to obtain a relatively uniform illumination of the hologram area. The input beam being larger than the device in addition to fabrication imperfections results in a strong zeroth-order diffraction. The zeroth-order diffraction is cropped in Fig.2.4a, as it is outside the holographic image of interest due to the off-axis design of the hologram. The custom-built microscope was also altered as follows: the objective lens was used to generate a Fourier transform of the hologram plane in its back focal plane. The tube lens was replaced by a lens with a focal length of 6 cm, which images the back focal plane of the objective into the camera. Two rotation stages were used in order to be able to independently rotate the device and the illumination beam. The camera and the imaging setups were not on the rotation stages.

Full-wave simulation of the angle-multiplexed grating

The central ~200-μm-long portion of the grating presented in the main text, was simulated for comparison. The simulated grating is 445 lattice constants long in the x direction and 1 lattice constant long in the y direction. Periodic boundary condition was considered in the y direction. The grating was simulated at the wavelength of

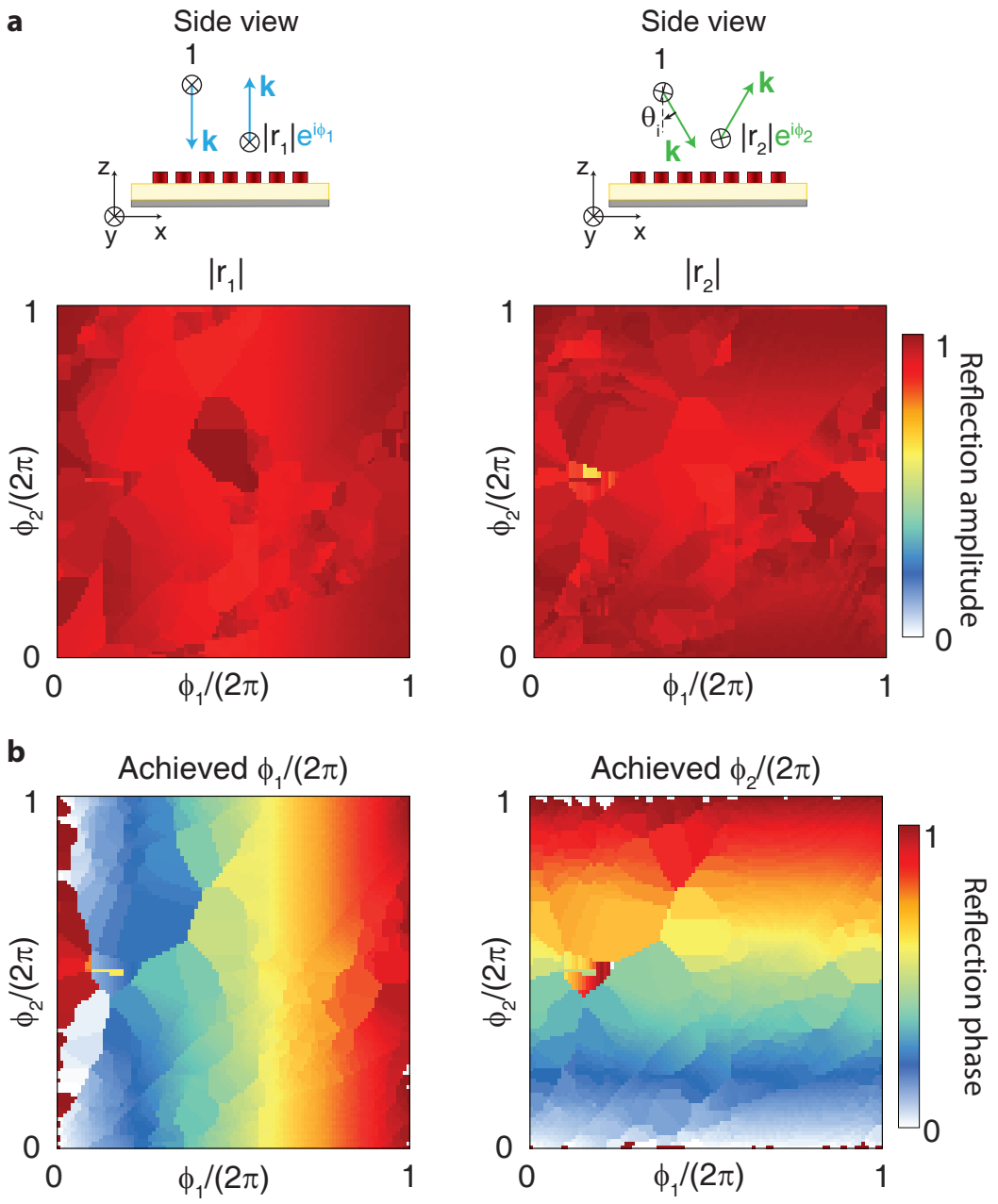

Figure 2.5: **Simulated achieved reflection amplitudes and phases for the selected meta-atoms. a**, Simulated reflection amplitudes at 0° and 30° incident angles as a function of required phase shifts for the periodic array of selected meta-atoms that can span the full 2π by 2π phases for both incident angles. **b**, Simulated achieved phase shifts of the chosen nano-posts versus the required phase shift values.

915 nm in MEEP [**oskooi2010meep**] and normal and 30° incident y-polarized (TE) plane-waves were used as the excitation. Angular distribution of the reflected power at 0° and 30° incident angles are shown in Fig. 2.7a and 2.7b, respectively. The far

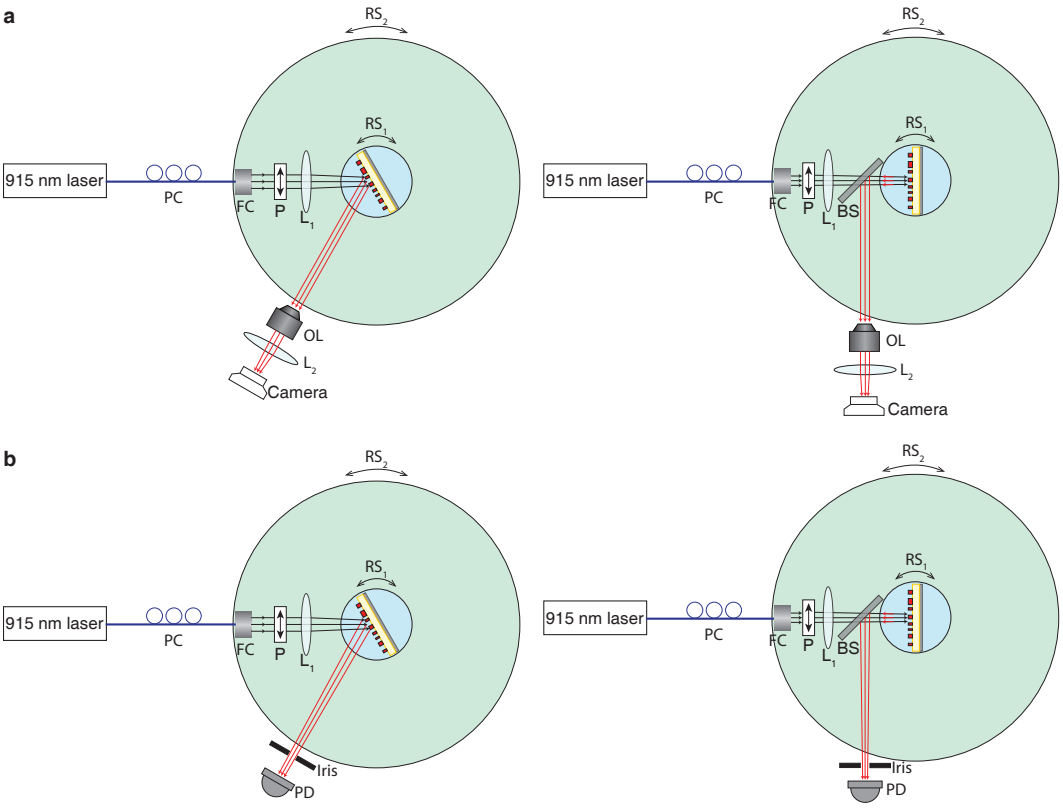

Figure 2.6: **Measurement setup used to characterize the grating. a**, Schematic drawing of the measurement setup used for characterization of the grating under oblique (left) and normal (right) illumination angles. **b**, Schematic illustration of the measurement setup used for characterization of deflection efficiency for oblique (left) and normal (right) illuminations. BS: beam splitter, L: lens, PC: polarization controller, FC: fiber collimator, P: polarizer, PD: photodetector. RS: rotation stage. OL: objective lens. The focal lengths of lenses L_1 and L_2 are $f_1 = 10$ cm and $f_2 = 20$ cm, respectively.

field reflected power was analyzed by taking the Fourier transform of the reflected field above the meta-atoms. The deflection efficiency was calculated by dividing the deflected power to the desired order by the total input power. The simulated deflection efficiency for 0° and 30° incident angles were 63% and 54% respectively. Existence of no other strong diffraction order in Fig. 2.7a and 2.7b, and the high deflection efficiencies achieved demonstrate the independent control of the platform at each incident angle. To consider the possible fabrication errors, the grating with a random error added to all the in-plane sizes of the meta-atoms is also simulated. The error is normally distributed with a zero mean, a 4-nm standard deviation, and a forced maximum of 8 nm. Angular distribution of the reflected power at 0° and 30° incident angles for the grating with a random error is shown in Fig. 2.7c and 2.7d,

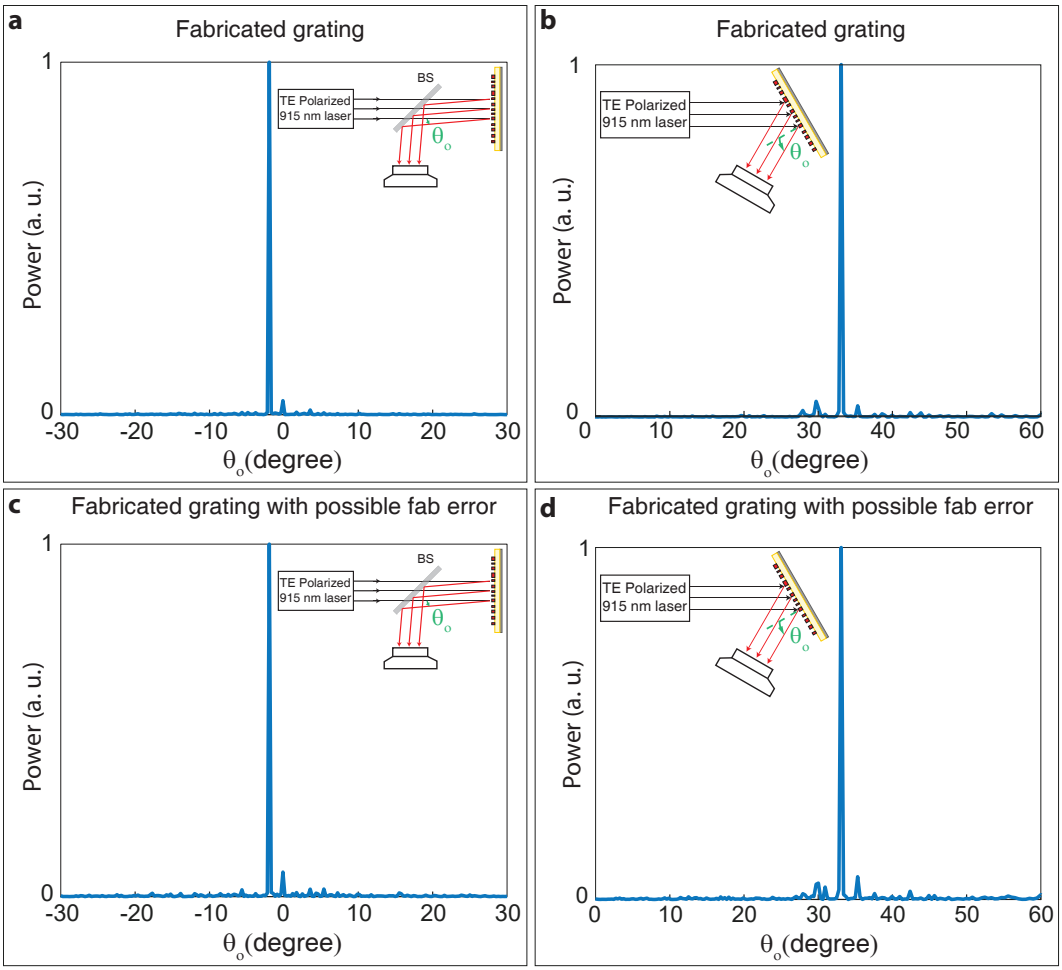

Figure 2.7: **Simulation results of the angle-multiplexed grating. a** and **b**, Distribution of reflected power versus observation angle under 0° (a) and 30° (b) incident angles for a ~200-μm-long portion of the fabricated grating. **c** and **d**, The same graphs as (a) and (b), but with a random error added to the all in-plane sizes of the meta-atoms. The error is normally distributed with a zero mean, a 4-nm standard deviation, and a forced maximum of 8 nm.

respectively. The simulated deflection efficiencies with the added errors are 46% and 39% under 0° and 30° incident angles. Although the deflection efficiency of the grating drops by adding a random random, its general functionality remains the same according to Fig. 2.7c and 2.7d.

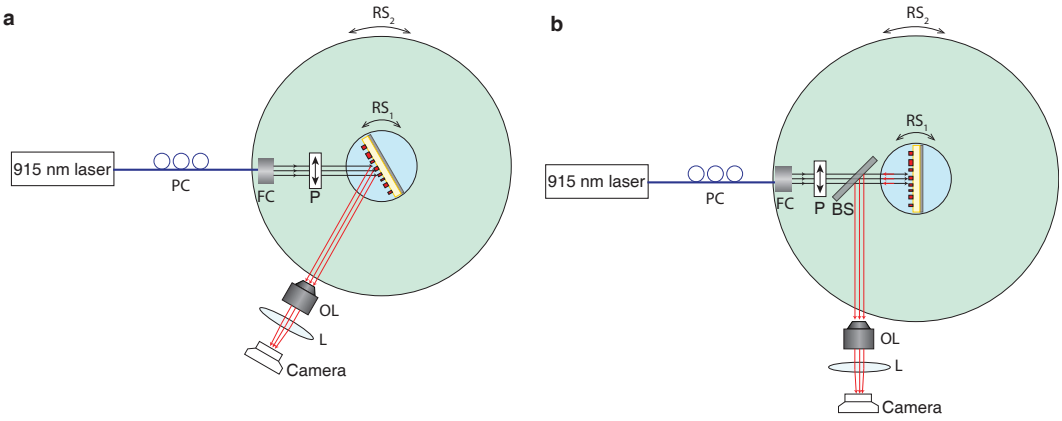

Figure 2.8: **Measurement setup used for the hologram.** **a** and **b**, Schematic drawing of the measurement setup used for characterization of the hologram under oblique (a) and normal (b) illumination angles. BS: beam splitter, L: lens, PC: polarization controller, FC: fiber collimator, P: polarizer, PD: photodetector. RS: rotation stage. OL: objective lens. The focal length of lens L is $f_1 = 6$ cm.

Chapter 3

METASURFACES WITH POLARIZATION AND PHASE CONTROL

The material in this chapter was in part presented in

E. Arbabi, S. M. Kamali, A. Arbabi, and A. Faraon, "Full-stokes imaging polarimetry using dielectric metasurfaces", ACS Photonics **5**, 3132–3140 (2018) DOI: 10.1021/acsphotonics.8b00362,

E. Arbabi, S. M. Kamali, A. Arbabi, and A. Faraon, "Vectorial holograms with a dielectric metasurface: ultimate polarization pattern generation", Submitted,

Spatially varying polarization and phase control is one of the unprecedented capabilities of HCAs. In this chapter, we introduce and explain this capability, and its underlying operation principle. Then, we discuss the two different manifestations of this control, and present an example application for each manifestation. First, we demonstrate polarimetric imaging, which exploits this capability of metasurfaces in independent phase control for orthogonal polarizations to split and focus light in different polarization bases. Second, we demonstrate vectorial holograms that can store and project the color image data in the polarization state of a monochromatic hologram through generating arbitrary polarization patterns.

3.1 Motivation

Polarization is a degree of freedom of light carrying important information that is usually absent in the intensity and spectral content. Its control has been of great interest for various applications in display systems [149, 150], particle trapping [151, 152], laser materials processing [153, 154], and polarized Raman spectroscopy [155, 156]. Polarization has conventionally been manipulated using naturally birefringent materials. In refractive optics, polarization and phase control are generally performed with different types of devices. DOEs, on the other hand, have the ability to simultaneously control polarization and phase. For instance, polarization-gratings have been fabricated and used to deflect light based on its state of polarization [157–159]. Spatially varying polarization control (along with the associated geometric phase)

was demonstrated about two decades ago with computer-generated holograms [51, 160–166]. For example, using the geometric phase (that changes sign with changing the incident light helicity), Hasman et al. demonstrated polarization dependent focusing, where the lens demonstrates positive optical power for one incident helicity, and an equal but negative optical power for the other one [51]. Dielectric metasurfaces that used geometric phase for beam shaping were also introduced around the same time [163, 164]. In 2015, Arbabi et al. reported a generalization of this concept to achieve independent and simultaneous control of phase and polarization of light [14]. The idea is based on birefringent elements with the ability to completely and independently control the phase of two orthogonal linear polarizations, and freely choose the orientation of those directions (i.e., the optical axis directions). In this chapter, we discuss the two different manifestations of this control through two different examples of polarization camera and polarization holograms. We use birefringent HCA nano-posts platform to provide this control.

3.2 Polarimetric imaging

Polarization is a degree of freedom of light carrying important information that is usually absent in intensity and spectral content. Imaging polarimetry is the process of determining the polarization state of light, either partially or fully, over an extended scene. While spectral and hyperspectral imaging techniques provide information about the molecular and material composition of a scene [167, 168], polarimetric imaging contains information about the shape and texture of reflecting surfaces, the orientation of light emitters, or the optical activity of various materials [169, 170]. This additional information has led to many applications for imaging polarimetry ranging from astronomy and remote sensing to marine biology and medicine [169, 171–177]. Therefore, several methods have been developed over the past decades to enable mapping of the polarization state over an extended scene [177–184].

Generally, polarimetric imaging techniques can be categorized into three groups: division of amplitude, division of aperture, and division of focal plane [169]. All of these techniques are based on measuring the intensity in different polarization bases and using them to estimate the full Stokes vector or a part of it. DoFP-PCs are less expensive, more compact, and require less complicated optics compared to the two other categories of polarimetric imaging systems [169, 182–184]. In addition, they require much less effort for registering images of different polarizations as the registration is automatically achieved in the fabrication of the polarization

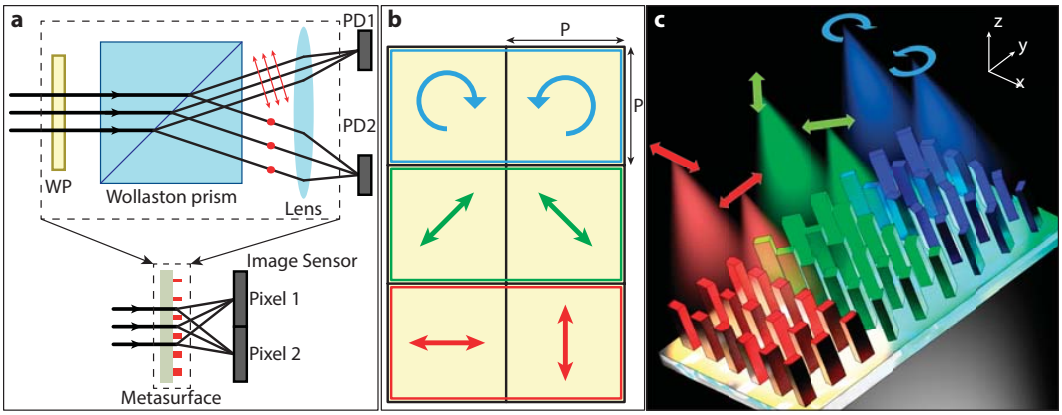

Figure 3.1: **Concept of a metasurface polarization camera. a**, Top: Schematics of a conventional setup used for polarimetry: a waveplate (quarter or half) followed by a Wollaston prism and a lens that focuses light on detectors. Bottom: A compact metasurface implements the functionality of all three components combined, and can be directly integrated on an image sensor. WP: waveplate; PD: photodetector. **b**, A possible arrangement for a superpixel of the polarization camera, comprising six image sensor pixels. Three independent polarization basis (H/V, ±45°, and RHCP/LHCP) are chosen to measure the Stokes parameters at each superpixel. **c**, Three-dimensional illustration of a superpixel focusing different polarizations to different spots. The colors are used only for clarity of the image and bear no wavelength information.

sensitive image sensors. The advances in micro/nano-fabrication have increased the quality of DoFP-PCs and reduced their fabrication costs, making them commercially available. DoFP-PCs either use a birefringent crystal to split polarizations [185, 186], or thin-film [183, 187] or wire-grid [177, 182, 188] polarization filters. To enable the measurement of degree of circular polarization, form-birefringent quarter waveplates were integrated with linear polarizers in the mid-IR [189]. Recently, liquid crystal retarders have been integrated with linear polarization filters to enable full Stokes polarimetric imaging by implementing circular [190] and elliptical polarization filters [191, 192]. An issue with the previously demonstrated DoFP-PCs is that they all have a theoretical efficiency limit of 50% due to using polarization filters [169], or spatially blocking half of the aperture [186].

Optical metasurfaces have enabled high-efficiency phase and polarization control with large gradients [14, 66, 70, 71, 74, 75]. In addition, their compatibility with conventional microfabrication techniques allows for their integration into optical metasystems [119, 138, 139, 193] or with optoelectronic components. They have also been used for polarimetry [97, 194–201], but not polarimetric imaging. An important

capability of HCA based metasurfaces is the simultaneous control of polarization and phase [14]. Here, we show how this capability can be utilized to demonstrate a dielectric metasurface mask for DoFP-PCs with the ability to fully measure the Stokes parameters, including the degree of circular polarization and helicity. In addition, since the mask operates based on polarization splitting and focusing instead of polarization filtering, it overcomes both the 50% theoretical efficiency limit, and the one-pixel registration error (resulting from distinct physical areas of the polarization filters) of the previously demonstrated DoFP-PCs [169]. In addition, unlike the previously demonstrated full Stokes DoFP-PCs, the metasurface is fabricated in a single dielectric layer and does not require integration of multiple layers operating as retarders and polarization filters. For the experimentally demonstrated metasurface mask designed for an 850-nm center wavelength, the polarization cross-talk ranges from 10% to 15% for pixel sizes from 7.2 μm to 2.4 μm when using an 850-nm light emitting diode (LED) as the light source. In addition, we use a polarization mask to demonstrate that the metasurface DoFP-PC can be used to form polarization images over extended scenes.

There are several representations for the polarization of light [202]. Among them, the Stokes vector formalism has some conceptual and experimental advantages since it can be used to represent light with various degrees of polarization, and can be directly determined by measuring the power in certain polarization bases [202]. Therefore, most imaging polarimetry systems determine the Stokes vector $\mathbf{S} = [S_0, S_1, S_2, S_3]$ [169], where the components are defined as $S_0 = I$, $S_1 = I_x - I_y$, $S_2 = I_{45} - I_{-45}$, and $S_3 = I_R - I_L$. Here I is the total intensity, I_x, I_y, I_{45}, and I_{-45} are the intensity of light in linear polarization bases along the x, y, +45-degree, and -45-degree directions, respectively. I_R and I_L denote the intensities of the right-hand and left-hand circularly polarized light. Usually, S_1, S_2, and S_3 are normalized to S_0 such that their value changes between -1 and +1. To fully characterize the state of polarization, all these intensities should be determined. A conventional setup used to measure the full Stokes vector is shown in Fig. 3.1**a**: a waveplate (half or quarter), followed by a Wollaston prism and a lens that focuses the beams on photodetectors. One can determine the four Stokes parameters [202] from the detector signals acquired under three different conditions: without a waveplate, with a half waveplate (HWP) inserted, and with a quarter waveplate (QWP) inserted in the setup. An optical metasurface with the ability to fully control phase and polarization of light [14] can perform the same task over a much smaller volume and without changing any optical components. The metasurface can split any two orthogonal

states of polarization and simultaneously focus them to different points with high efficiency and on a micron-scale. This is schematically shown in Fig. 3.1**a**. Such a metasurface can be directly integrated on an image sensor for making a polarization camera. To fully measure the Stokes parameters, the projection of the input light on three different polarization basis sets should be measured. A typical choice of basis is horizontal/vertical (H/V), ±45° linear, and right-hand-circular/left-hand-circular (RHCP/LHCP) that can be used to directly measure the Stokes parameters. Figure 3.1**b** shows a possible configuration where the three metasurface polarizing beamsplitters (PBSs) are multiplexed to make a superpixel, comprising of six image sensor pixels. Each image sensor pixel can then be used to measure the power in a single polarization state. A schematic illustration of a superpixel is shown in Fig. 3.1**c**. The colors are only used to distinguish different parts of the super pixel more easily, and do not correspond to actual wavelengths. The blue nano-posts separate and focus RHCP/LHCP, and the green ones and the red ones do the same for ±45° and H/V, respectively.

3.3 Simultaneous control of polarization and phase

As seen in Fig. 3.2**a**, the metasurface is composed of α-Si nano-posts with rectangular cross-sections on a low-index fused silica substrate. With a proper choice of the α-Si layer thickness and lattice constant (650 nm and 480 nm respectively for an operating wavelength of 850 nm), the nano-posts can provide full and independent 2π phase control over x and y-polarized light, where x and y are aligned with the nano-post axes (see Fig. 3.10) [14]. Using the phase versus dimension graphs, one could calculate the nano-post dimensions required to provide a specific pair of phase values, ϕ_x and ϕ_y, as shown in Fig. 3.2**b**. This allows for designing a metasurface that controls x and y-polarized light independently. With a simple generalization, the same can be applied to any two orthogonal linear polarizations using nano-posts that are rotated around their optical axis with the correct angle to match the new linear polarizations (e.g., the $x' - y'$ axis in Fig. 3.2**c**). An important and interesting point demonstrated in [14] is that this can be done on a point-by-point manner, where the polarization basis is different for each nano-post. This property allows us to easily design the metasurface PBS for the two linear bases of interest. Moreover, as demonstrated in [14], an even more interesting property of this seemingly simple structure is that the independent control of orthogonal polarizations can be generalized to elliptical and circular polarizations as well (with a small drawback that the output and input

polarizations will have the opposite handedness). To see this, here we reiterate the results presented in the supplementary material of [14], as it is important to make the design process clear.

The operation of a nano-post can be modeled by a Jones [203] matrix relating the input and output electric fields (i.e., $\mathbf{E}^{\text{out}} = \mathbf{T}\mathbf{E}^{\text{in}}$). For the rotated nano-post shown in Fig. 3.2**c**, the Jones matrix can be written as:

$$\mathbf{T} = \begin{bmatrix} T_{xx} & T_{xy} \\ T_{yx} & T_{yy} \end{bmatrix} = \mathbf{R}(\theta) \begin{bmatrix} e^{i\phi_{x'}} & 0 \\ 0 & e^{i\phi_{y'}} \end{bmatrix} \mathbf{R}(-\theta), \tag{3.1}$$

where $\mathbf{R}(\theta)$ denotes the rotation matrix by an angle θ in the counter-clockwise direction. Here we have assumed a unity transmission since the nano-posts are highly transmissive. We note here that the right hand side of Equation 3.1 is a unitary and symmetric matrix. Using only these two conditions (i.e., unitarity and symmetry), we find $T_{xy} = T_{yx}$, $|T_{yx}| = \sqrt{1 - |T_{xx}|^2}$, and $T_{yy} = -\exp(\mathrm{i}2\angle T_{yx})T_{xx}$. As one could expect, these reduce the available number of controllable parameters to three ($|T_{xx}|$, $\angle T_{xx}$, and $\angle T_{yx}$), corresponding to the three available physical parameters ($\phi_{x'}$, $\phi_{y'}$, and θ). Using these relations to simplify $\mathbf{E}^{\text{out}} = \mathbf{T}\mathbf{E}^{\text{in}}$, we can rewrite it to find the Jones matrix elements in terms of the input and output fields:

$$\begin{bmatrix} E_x^{\text{out}*} & E_y^{\text{out}*} \\ E_x^{\text{in}} & E_y^{\text{in}} \end{bmatrix} \begin{bmatrix} T_{xx} \\ T_{yx} \end{bmatrix} = \begin{bmatrix} E_x^{\text{in}*} \\ E_x^{\text{out}} \end{bmatrix}, \tag{3.2}$$

where $*$ denotes complex conjugation. Equation 3.2 is important as it shows how one can find the Jones matrix required to transform any input field with a given phase and polarization, to any desired output field with a different phase and polarization. This is the first application of the birefringent meta-atoms, i.e., *complete and independent polarization and phase control*. This capability is what allows us to design and implement the vectorial holograms discussed in the following sections.

The Jones matrix is uniquely determined by Eq. 3.2, unless the determinant of the coefficients matrix on the left hand side is zero. In this case, the matrix rows (i.e., $\mathbf{E}^{\text{out}*}$ and $\mathbf{E}^{\text{in}}$) will be proportional. Since the Jones matrix is unitary (i.e., the input and output powers are equal), the proportionality coefficient must have a unit amplitude: $\mathbf{E}^{\text{out}*} = \exp(\mathrm{i}\phi)\mathbf{E}^{\text{in}}$. This equation means that $\mathbf{E}^{\text{out}}$ and $\mathbf{E}^{\text{in}}$ have the same polarization ellipse, but an opposite handedness. Now, this input/output field set imposes only one equation on the Jones matrix elements. To uniquely determine the Jones matrix, a second equation is required. To get this second equation, we use a second set of input/output fields that satisfy the same condition as the first

set: $\mathbf{E}_2^{\text{out}*} = \exp(\mathrm{i}\phi_2)\mathbf{E}_2^{\text{in}}$. Here we are using the numeral subscripts to distinguish between the two input/output field sets. This way, the equation for the first set becomes $\mathbf{E}_1^{\text{out}*} = \exp(\mathrm{i}\phi_1)\mathbf{E}_1^{\text{in}}$. If ϕ_1 and ϕ_2 can be independently controlled, one can see using a conservation of energy argument that $\mathbf{E}_1^{\text{in}}$ and $\mathbf{E}_2^{\text{in}}$ (as well as $\mathbf{E}_1^{\text{out}}$ and $\mathbf{E}_2^{\text{out}}$) should be orthogonal to each other. Thus, we can write the final equation as:

$$\begin{bmatrix} E_{1,x}^{\text{in}} & E_{1,y}^{\text{in}} \\ E_{2,x}^{\text{in}} & E_{2,y}^{\text{in}} \end{bmatrix} \begin{bmatrix} T_{xx} \\ T_{yx} \end{bmatrix} = \begin{bmatrix} E_{1,x}^{\text{out}} \\ E_{2,x}^{\text{out}} \end{bmatrix} = \begin{bmatrix} \exp(\mathrm{i}\phi_1)E_{1,x}^{\text{in}*} \\ \exp(\mathrm{i}\phi_2)E_{2,x}^{\text{in}*} \end{bmatrix}. \tag{3.3}$$

This is the second important application of the method, *polarization controlled phase manipulation*: given *any* two orthogonal input polarizations (denoted by $\mathbf{E}_1^{\text{in}}$ and $\mathbf{E}_2^{\text{in}}$), their phase can be independently controlled using the Jones matrix given by Equation 3.3. For instance, Arbabi et. al. [14], demonstrated a metasurface that focuses RHCP input light to a tight spot, and LHCP input light to a doughnut shape. The cost is that the output orthogonal polarizations have the opposite handedness compared to the input ones. This second capability allows for the design and implementation of the metasurface polarization camera. Once the Jones matrix is calculated from Eq. 3.3 (or 3.2, depending on the function), the two phases, $\phi_{x'}$ and $\phi_{y'}$, and the rotation angle θ can be calculated from Eq. 3.1. Let us emphasize here that since this is a point-by-point design, all the steps can be repeated independently for each nano-post, meaning that the polarization basis can be changed from one nano-post to the next.

3.4 Metasurface polarization camera: design, fabrication, and characterization

Based on the concept and technique just described, the first design step is identifying the input polarizations at each point. For the DoFP-PC, three different sets of H/V, ±45°, and RHCP/LHCP are chosen, corresponding to the three distinct areas in the superpixel shown in Fig. 3.1**b**. Then, the required phase profiles are determined to split each two orthogonal polarizations and focus them to the centers of adjacent pixels on the image sensor as shown schematically in Fig. 3.1**c**. For a pixel size of 4.8 μm, the calculated phase profiles are shown in Fig. 3.2**d**, where the focal distance is assumed to be 9.6 μm. Since each polarization basis covers two image sensor pixels, the phases are defined over the area of two pixels. In addition, the calculated phases are the same for the three different polarization bases, and therefore only one basis is shown in Fig. 3.2**d**. Using these phases and knowing the desired polarization

basis at each point, we calculated the rotation angles and nano-post dimensions from Eqs. 3.3 and 3.1 along with the data shown in Fig. 3.2**b**.

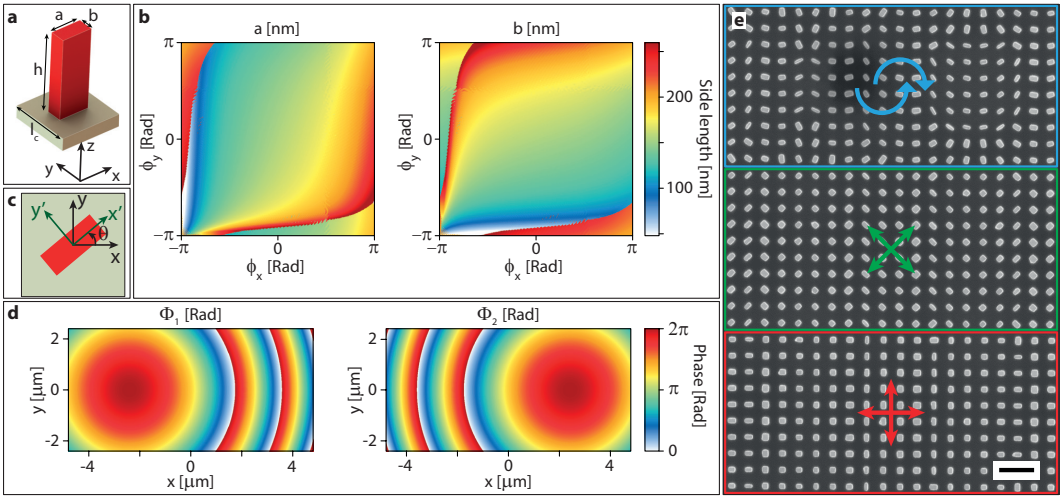

Figure 3.2: **Meta-atom and pixel design. a**, An α-Si nano-post with a rectangular cross section resting on a glass substrate provides full polarization and phase control. **b**, Design graphs used for finding the in-plane dimensions of a nano-post. Given a pair of transmission phases ϕ_x and ϕ_y, one can find the corresponding nano-post dimensions a and b from the two graphs. The nano-posts are 650 nm tall, and the lattice constant is 480 nm. **c**, Schematic illustration of a rotated nano-post, showing the rotation angle and the old and the new optical axis sets. **d**, Required phase profiles for a metasurface that does both polarization beam splitting and focusing at two orthogonal polarizations. These can be any set of orthogonal polarizations, linear or elliptical. The focal distance for these phase profiles is 9.6 μm, equal to the width of the superpixel in the x direction. The lateral positions of the focal spots are x= ±2.4 μm and y=0. **e**, Scanning electron micrograph of a fabricated superpixel. The polarization basis for each part is shown with the colored arrows. Scale bar: 1 μm.

The metasurface mask was then fabricated in a process explained in more detail in Sec. 4.7. A 650-nm-thick layer of α-Si was deposited on a fused silica wafer. The metasurface pattern was defined using electron-beam lithography, and transferred to the α-Si layer through a lift-off process used to form a hard etch-mask, followed by dry etching. Fig. 3.2**e** shows a scanning electron micrograph of a fabricated superpixel, with the polarization bases denoted by arrows for each section. In addition to the metasurface mask corresponding to a pixel size of 4.8 μm that is mentioned above and shown in Fig. 3.2**e**, two other masks with pixel sizes of 7.2 μm and 2.4 μm were also fabricated with focal distances of 14.4 μm and 4.8 μm, respectively. We used these to study the effect of pixel size on performance.

To characterize the metasurface mask we illuminated it with light from an 850-nm LED filtered by a 10-nm bandpass filter with different states of polarization. We then imaged the plane corresponding to the image sensor location using a custom-built microscope (see Fig. 3.11 for measurement details and the setup). Figure 3.3 summarizes the superpixel characterization results for the 4.8-μm pixel design. The measured Stokes parameters are plotted in Fig. 3.3**a** for different input polarizations, showing a $< 10\%$ cross-talk between polarizations and high similarity between different superpixels. The measurements were averaged over the field of view of the microscope that corresponds to about 120 superpixels. The standard deviations are shown in the graph as error bars. In addition, the intensity distribution over a sample superpixel area is shown in Fig. 3.3**b**. The graphs show the clear ability of the metasurface mask to route light as desired for various input polarizations. Similar characterization results without a bandpass filter, corresponding to a bandwidth of about 5%, are presented in Fig. 3.12. Slight performance degradation is observed with a maximum cross-talk of $\sim 13\%$ since the metasurface efficiency decreases with changing the wavelength. In addition, similar measurement results for metasurface masks with pixel sizes of 7.2 μm and 2.4 μm are presented in Figs. 3.13 and 3.14, respectively. The results show a degradation of performance with reducing the pixel size as the cross-talk is smaller than 7.5% and 13% for 7.2-μm and 2.4-μm pixels, respectively. To show the ability of the metasurface mask to characterize the polarization state of unpolarized light, we repeated the same measurements with the polarization filter removed from the setup. Figure 3.3**c** summarizes the results of this measurement that determines the polarization state of light emitted by the LED. The data given in Fig. 3.7**a** is used to estimate the calibration matrix. As expected, the emitted light has a low degree of polarization (<0.08). We also characterized the polarization state of the emitted LED light using a QWP and a linear polarizer (LP), and found the degree of polarization to be equal to zero up to the measurement error.

In addition, we measured the transmission efficiency of the metasurface mask and found it to be in the range of 60% to 65% for all pixel size designs and input polarizations. The lower than expected transmission is mainly due to a few factors. First, the metasurface has a maximum deflection angle larger than 50°, which results in lower transmission efficiency [66, 129]. Second, the relatively large metasurface lattice constant of 480 nm does not satisfy the Nyquist sampling theorem for the large-deflection-angle transmission masks inside the fused silica substrate [35]. This results in spurious diffraction of light inside the substrate. Finally, the mask is periodic with a larger-than-wavelength period equal to the superpixel dimensions.

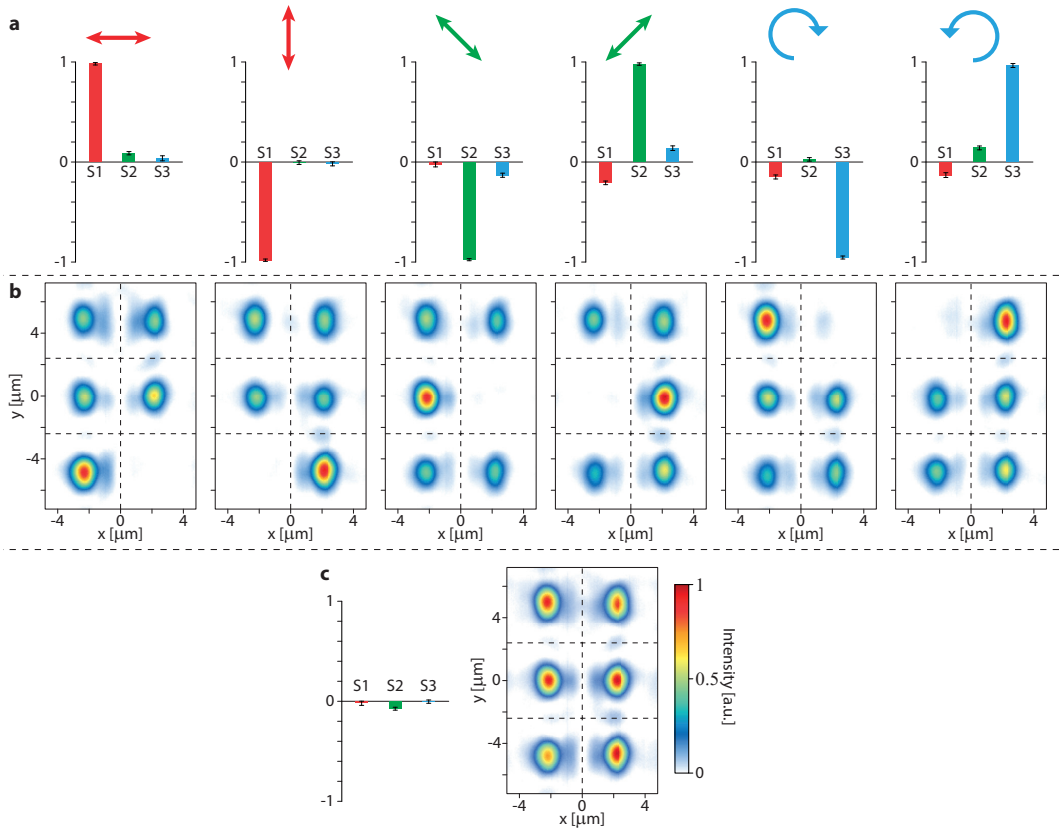

Figure 3.3: **Characterization results of the superpixels of the DoFP metasurface mask. a**, Measured average Stokes parameters for different input polarizations (shown with colored arrows), and **b**, the corresponding intensity distributions for a sample superpixel. The Stokes parameters are averaged over about 120 superpixels (limited by the microscope field of view), and the error bars represent the statistical standard deviations. **c**, Measured average Stokes parameters and the corresponding intensity distribution for the LED light source without any polarization filters in the setup. All the measurements are performed with an 850-nm LED filtered by a bandpass filter (center: 850 nm, full width at half maximum (FWHM): 10 nm) as the light source.

This results in excitation of higher diffraction orders especially inside the substrate that has a higher refractive index. It is worth noting that the achieved $\sim$ 65% efficiency is still higher than the 50% theoretical limit of a polarimetric camera that is based on polarization filtering.

3.5 Polarimetric imaging: experimental results and discussion

Finally, we show polarimetric imaging using the DoFP metasurface mask. We designed and used a custom dielectric metasurface polarization mask as the imaging target. We utilized the polarization-phase control method described above, and a

fabrication process similar to the DoFP metasurface mask for the imaging target as well. The mask converts x-polarized input light to an output polarization state characterized by the polarization ellipses and the Stokes parameters shown in Figs. 3.4**a** and 3.4**b**, respectively. Each Stokes parameter is +1 or -1 in an area of the image corresponding to the specific polarization. For instance, S_3 is +1 in the right half circle, -1 in the left half circle, and 0 elsewhere. Using a second custom-built microscope, the image of the polarization mask was projected onto the DoFP metasurface mask (see Fig. 3.11 for the measurement setup and the details). First, we removed the metasurface mask and performed a conventional polarimetric imaging of the projected image using a LP and a QWP. To this end, six different images were captured with different rotations of the LP and the QWP to determine the Stokes parameters. The results are shown in Fig. 3.4**c**. Second, we removed the LP and the QWP and inserted the DoFP metasurface mask. The Stokes parameters were extracted from a single image captured at the focal plane of the DoFP metasurface mask. The results are shown in Fig. 3.4**d**, and are in good agreement with the results of regular polarimetric imaging. The lower quality of the metasurface polarimetric camera image is mainly due to the limited number of superpixels that fit inside a single field of view of the microscope. The field of view is limited by the microscope magnification and image sensor size which are $\times$22 and $\sim$15 mm, respectively. This results in a low resolution of 70-by-46 points for the metasurface polarimetric image versus a $\sim$2000-by-2000 point resolution for the regular polarimetric image. In addition, to form the final image, we need to know the coordinates of each superpixel a priori. The existing errors in estimating these coordinates that result from small tilts in the setup, aberrations of the custom-built microscope, and etc. cause a degraded performance over some superpixels. In a polarization camera made using the DoFP metasurface mask, both of these issues will be resolved as the resolution can be much higher, and the mask and image sensor are lithographically aligned.

To extract the polarization information of the image we integrated the intensity inside the area of two adjacent DoFP mask pixels. Then, we calculated the corresponding Stokes parameters simply by dividing the difference between the two measured intensities by their sum. While straightforward, this is not the optimal method to perform this task as there is non-negligible cross-talk between different polarization intensities measured by the pixels (Fig. 3.3). The issue becomes more pronounced moving toward smaller pixel sizes as seen for the 2.4-μm case (Fig. 3.14). To address this issue, a better polarization extraction method is to form a calibration matrix that relates the actual intensities to the corresponding measured values for a specific

DoFP metasurface mask design (for instance using the data in Fig. 3.3). This allows one to reduce the effect of the cross-talk and measure the polarization state more precisely.

The designed small focal distances (e.g., 9.6 μm for the 4.8-μm pixel) result in an upper limit of 40% for the operation bandwidth of the device due to diffractive chromatic dispersion. To get this upper limit we assumed a constant phase profile that doesn't change with wavelength and used the criterion given in [138]. Therefore, the actual bandwidth of the device is limited by the focusing and polarization control efficiencies that drop with detuning from the design wavelength. In addition, it is expected that the same level of performance achieved from the 2.4-μm pixel in this work, can be achieved from a ~1.7-μm pixel if the material between the mask and the image sensor has a refractive index of 1.5, which is the case when the DoFP mask is separated from the image sensor by an oxide or polymer layer as in a realistic device. To achieve smaller pixel sizes, better performance, and larger operation bandwidths one could use more advanced optimization [130] or chromatic-dispersion control techniques [118], especially since the size of a single superpixel is small and allows for a fast simulation of the forward problem. In addition, a spatial multiplexing scheme [136, 147, 204, 205] can be used to interleave multiple superpixels corresponding to different optical bands, and therefore make a color-polarization camera.

Using the polarization-phase control method and the platform introduced in [14], we demonstrated a metasurface mask for DoFP-PCs. The mask is designed to split and focus light to six different pixels on an image sensor for three different polarization bases. This allows for complete characterization of polarization by measuring the four Stokes parameters over the area of each superpixel which corresponds to the area of six pixels on an image sensor. We experimentally demonstrated the ability of the metasurface masks to correctly measure the polarization state for different input polarizations. In addition, we used the DoFP metasurface mask to form an image of a complicated polarization object, showing the ability to make a polarization camera. Many of the limitations faced here can be overcome using more advanced optimization techniques or better data extraction methods. We anticipate that polarization cameras based on metasurface masks will be able to replace the conventional polarization cameras for many applications, as they enable measurement of the full polarization state including the degree of circular polarization and handedness.

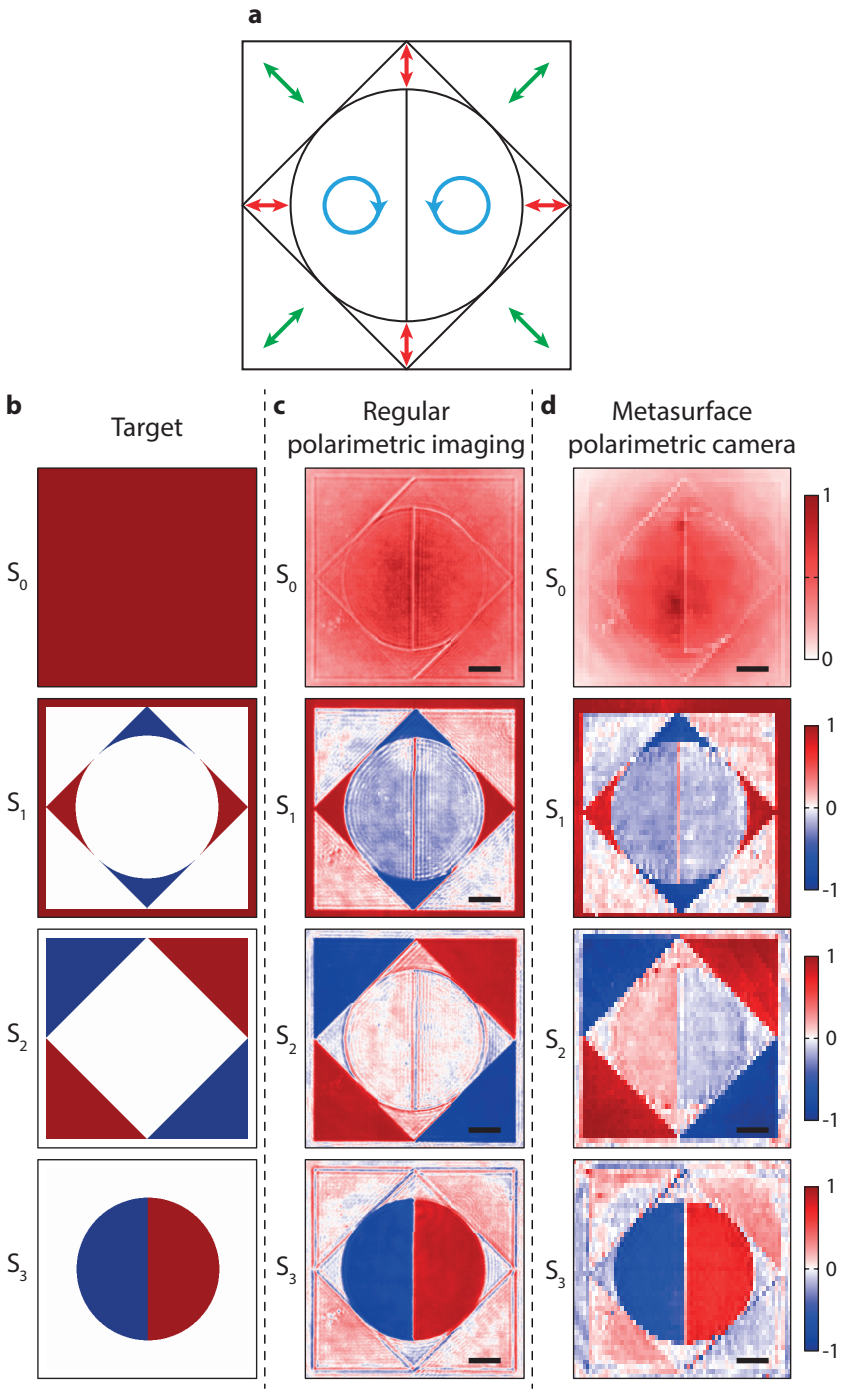

Figure 3.4: **Polarimetric imaging.** **a**, Schematic illustration of target polarization ellipse in different parts of the polarization sample. Stokes parameters of the polarization sample: **b**, the targeted polarization mask, **c**, the fabricated mask imaged using conventional polarimetry, and **d**, the same mask imaged using the metasurface polarimetric camera. The scale bars denote 100 μm in the metasurface polarization camera mask plane.

3.6 Vectorial holograms

Polarization holograms are in general two or three dimensional holograms with a spatially varying degree or direction of birefringence [157, 206–208], encoding phase, polarization, and/or amplitude data. Computer generated polarization holograms have mostly been utilized to store phase information using the geometric phase and perform as polarization dependent gratings, lenses, and holograms [159, 207, 209, 210]. While polarization holograms can in principle be used to control the phase and amplitude [211], or phase and polarization simultaneously [212], limited phase control levels, complex fabrication, and large pixel sizes significantly limit their applicability for these purposes.

Computer generated polarization holograms implemented using structural birefringence and fabricated using conventional micro-fabrication techniques [32, 161, 163, 166, 213, 214] overcome some of the limitations of conventional polarization holograms, but the level of control over polarization and phase is limited in these structures. Metasurface HCAs [1, 7, 11, 124, 215–217], on the other hand, enable full and simultaneous control of polarization and phase on a subwavelength lattice and with high efficiency [14]. While most demonstrations so far have either focused on solely controlling the polarization [69, 131, 218] or independent control of phase for two orthogonal polarizations [132, 145, 219–221], another important application of the concept and platform demonstrated in [14] and discussed in the previous sections is the simultaneous control of polarization and phase. Although this ability has been partially utilized to demonstrate metasurfaces that shape the beam and work as half-wave plates simultaneously [117, 222], its full potential has not been explored yet.

In these sections, we use the simultaneous polarization and phase control capability to demonstrate a new category of vectorial (polarization) holograms, where the electric field vector is controlled independently on each point of the mask. The holograms project vectorial images in which the data is stored in the state of polarization. We propose and employ a modified Gerchberg-Saxton (GS) algorithm that enables the design of these vectorial holograms. Given the existence of three independent degrees of freedom in the polarization of light for fully polarized beams, we experimentally show that these vectorial holograms can store and project the data in complicated red-green-blue (RGB) full-color images. It is worth noting that diatomic plasmonic as well as high-contrast dielectric metasurfaces were recently used to demonstrate vectorial holograms [223, 224]. However, the vectorial holograms demonstrated in [223,

224] are basically spatial superpositions of multiple holograms that have specific output polarizations (e.g., the metasurface consists of a few spatially multiplexed holograms projecting images with different polarization states). In contrast, the metasurface holograms demonstrated in the following sections act as a whole to create polarization patterns of arbitrary complexity as evidenced by the encoded RGB images.

3.7 Polarization hologram: concept and design

Figure 3.5 shows a schematic of the metasurface, and the color-encoded polarization hologram generated. The metasurface is illuminated by a beam with known wavelength and polarization state. The dielectric metasurface, made up of high index nano-posts, enables simultaneous and independent control of the output phase and polarization [14]. Since each nano-post operates almost independently, this full control can be implemented on a subwavelength lattice. This allows for an unprecedented control of the vectorial electric field on the output side of the metasurface. As we show in the following, this control can be utilized to encode the data of a color image into the polarization state of light which the metasurface can generate and project.

As discussed above, polarization of light can be fully characterized using the Stokes parameters S_0, S_1, S_2, and S_3, usually defined as $S_0 = I$, $S_1 = I_x - I_y$, $S_2 = I_{45} - I_{-45}$, and $S_2 = I_R - I_L$. Here, I denotes the total light intensity, I_x and I_y are the partial intensities of light linearly polarized along the x and y axes, I_{45} and I_{-45} are the intensity in the linear bases along +45 and -45 degree axes, and I_R and I_L denote the right hand and left hand circular intensities, respectively. For fully polarized light, the four parameters are related through the relation $S_0 = \sqrt{{S_1}^2 + {S_2}^2 + {S_3}^2}$. This, reduces the number of independent parameters to three, which in a different representation correspond to the amplitude of the electric field along the x and y axes and their phase difference.

As shown in Figs. 3.6**a** and 3.6**b**, the red, green, and blue components of a color image can be mapped to the Stokes parameters S_1, S_2, and S_3 through a simple linear transformation that maps the color ranges to the [-1,1] interval. Figure 3.6**c** shows the distribution of the pixels of the image shown in Fig. 3.6**a** on the Poincare sphere. This shows that the points cover a very large portion of possible polarization states, denoting the capability of the method to generate images with arbitrarily complex polarization distributions. Finally, for the actual hologram design process it is more

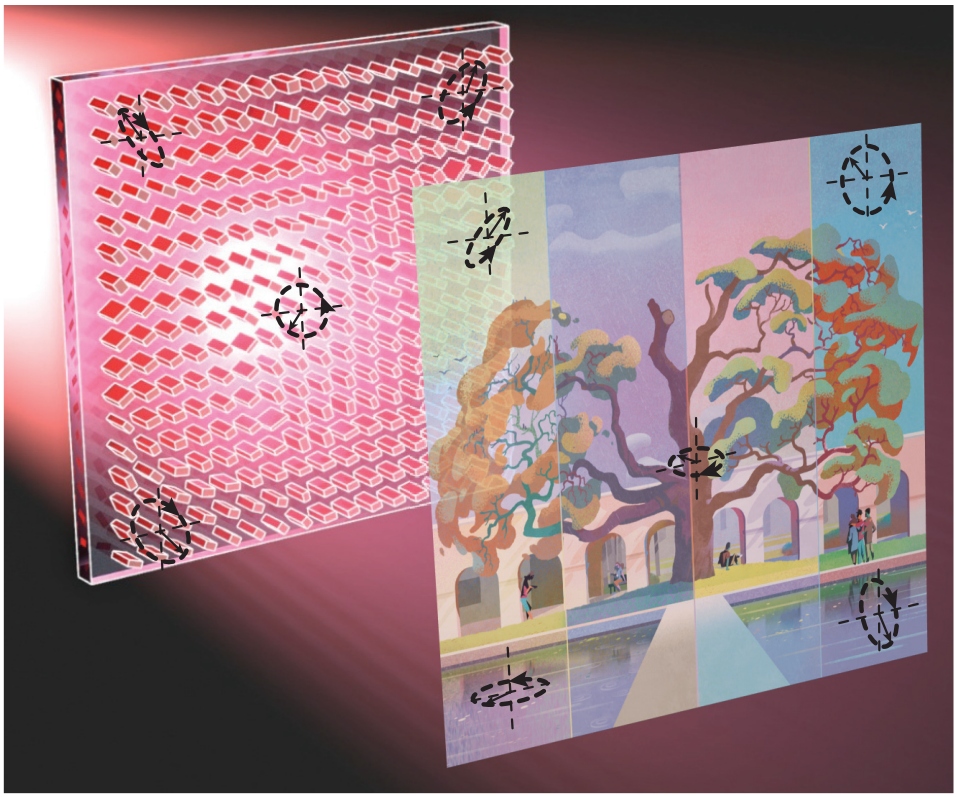

Figure 3.5: **Schematic illustration of a metasurface polarization hologram, projecting a polarization pattern encoding an RGB image.** The metasurface is illuminated with a beam of known wavelength and polarization. Each dielectric nano-post is designed to control the polarization and phase of the output light at the corresponding lattice site.

helpful to use the electric field representation of polarization, which is possible as the light is fully polarized. Figure 3.6**d** shows the amplitudes of the electric field along the x and y axes, $|E_x|$ and $|E_y|$, and their phase difference, $\phi = \angle E_y - \angle E_x$, which are calculated form the Stokes parameters plotted in Fig. 3.6**b**.

To design the metasurface, we developed and used a modified GS algorithm. As shown in Fig. 3.7, the field right before the metasurface has an amplitude of one and is polarized along the x axis. The field right after the metasurface can have any arbitrary polarization and phase distributions, however, it has a unity amplitude, i.e., $\sqrt{|{E_x}^m|^2 + |{E_y}^m|^2} = 1$. On the hologram plane (infinity), polarization and amplitude distributions, $|{E_x}^h|$, $|{E_y}^h|$, and ϕ are set, while the relative phases between different points, $\angle {E_x}^h$, are available degrees of freedom. We start the process by assigning a uniform phase to the field in the hologram plane, and setting the initial hologram

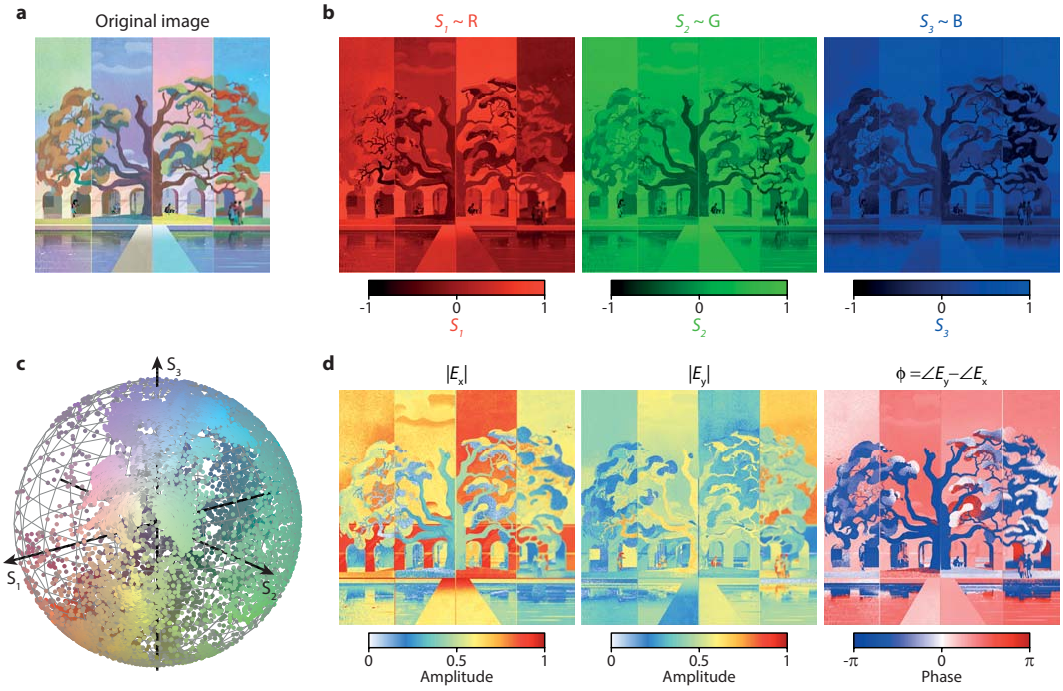

Figure 3.6: **Mapping an RGB image data to polarization.** **a**, The original RGB image. **b**, The red, green, and blue components of the image in **a**, corresponding to the Stokes parameters characterizing the polarization pattern. **c**, A Poincare sphere representation of the polarization pattern corresponding to the image in **a**. The position of each point and its color demonstrate the polarization and intensity of light at one point in the image. For the data to be more clear, only about two percent of the original image pixels are used. **d**, The electric field amplitudes along the x and y axes and their phase difference, calculated from the Stokes parameters in **b**. This data is directly used in the metasurface hologram design algorithm through a modified GS algorithm.

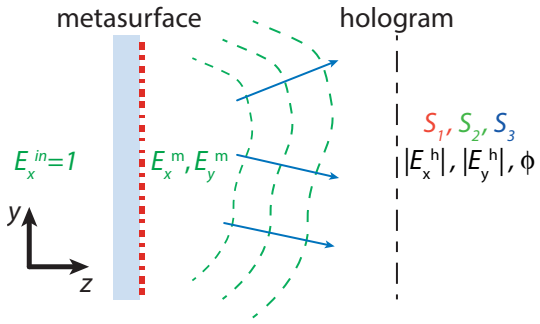

Figure 3.7: **Vectorial hologram design schematic.** Schematic of the metasurface generating the desired polarization pattern. The required electric field vector on the metasurface, E_x^m and E_y^m, is calculated directly from the modified GS algorithm.

fields as follows:

$$\begin{aligned} {E_{\mathrm{x}}}^{h}(1) &= |{E_{\mathrm{x}}}^{h}| \\ {E_{\mathrm{y}}}^{h}(1) &= |{E_{\mathrm{y}}}^{h}|\mathrm{e}^{j\phi} \end{aligned}. \tag{3.4}$$

At each subsequent step, the metasurface field is calculated through the following Fourier transform relations:

$$\begin{aligned} {E_{\mathrm{x}}}^{m}(i) &= \frac{\mathcal{F}[{E_{\mathrm{x}}}^{h}(i)]}{I(i)} \\ {E_{\mathrm{y}}}^{m}(i) &= \frac{\mathcal{F}[{E_{\mathrm{y}}}^{h}(i)]}{I(i)} \\ I(i) &= \sqrt{\mathcal{F}[{E_{\mathrm{x}}}^{h}(i)]^2 + \mathcal{F}[{E_{\mathrm{y}}}^{h}(i)]^2} \end{aligned}, \tag{3.5}$$

where i is the iteration step, $\mathcal{F}[\cdot]$ represents the Fourier transform operator, and $I(i)$ is the total intensity used to normalize the field as it should have an almost unity amplitude. The hologram fields in the next iterations should satisfy $\phi = \angle {E_{\mathrm{y}}}^{h} - \angle {E_{\mathrm{x}}}^{h}$. Therefore, in each step we can only set the phase of one polarization from the GS algorithm, and the phase of the other polarization should be calculated using the known phase difference, ϕ. To make the process symmetric for the two polarizations, we alternate between them in each pair of iterations, i.e.,

$$\begin{aligned} i \text{ is even}: &\begin{cases} {E_{\mathrm{x}}}^{h}(i) = |{E_{\mathrm{x}}}^{h}|\exp(j\angle\mathcal{F}^{-1}[{E_{\mathrm{x}}}^{m}(i-1)]) \\ {E_{\mathrm{y}}}^{h}(i) = |{E_{\mathrm{y}}}^{h}|\exp(j\angle\mathcal{F}^{-1}[{E_{\mathrm{x}}}^{m}(i-1)]+j\phi) \end{cases} \\ i \text{ is odd}: &\begin{cases} {E_{\mathrm{x}}}^{h}(i) = |{E_{\mathrm{x}}}^{h}|\exp(j\angle\mathcal{F}^{-1}[{E_{\mathrm{y}}}^{m}(i-1)]-j\phi) \\ {E_{\mathrm{y}}}^{h}(i) = |{E_{\mathrm{y}}}^{h}|\exp(j\angle\mathcal{F}^{-1}[{E_{\mathrm{y}}}^{m}(i-1)]) \end{cases} \end{aligned}. \tag{3.6}$$

In the examples used in this work, the modified algorithm converged to the final designs in less than twenty iterations.

After determining the required field distributions on the metasurface, we need to design a metasurface structure that can generate these field distributions with high efficiency. As shown in Figs. 3.8**a**, 3.8**b**, and 3.8**d**, the metasurface is based on high-index cuboid nanoposts with different dimensions along the x and y axes, a and b, respectively. For proper choices of the nanoposts height and distance, the transmission phases can be controlled independently from 0 to 2π, while keeping the transmission amplitude close to 1. For the operation wavelength of 850 nm, here we have used α-Si nanoposts that are 682 nm tall and located on a square lattice with a 420-nm long lattice constant. Figure 3.8**c** shows the nanopost side lengths, a and b, versus the transmission phases for x- and y-polarized light.

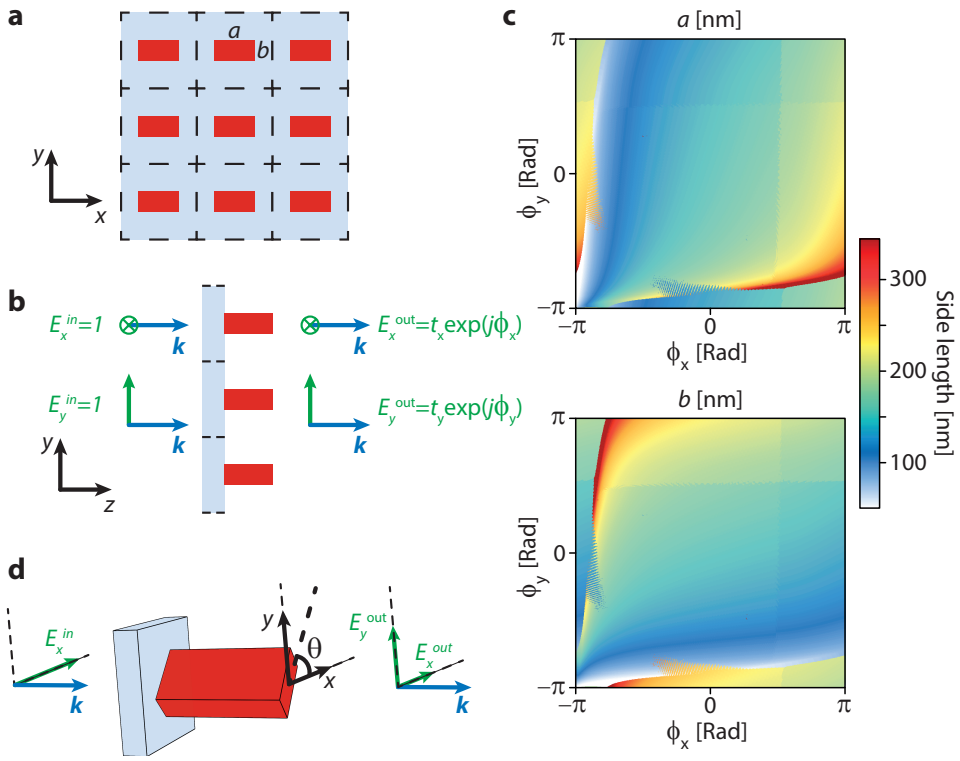

Figure 3.8: **Metasurface structure and design graphs. a**, Schematics of a uniform lattice of dielectric nano-posts showing the post dimensions. **b**, Side-view of the uniform array of nano-posts, showing the transmission parameters along the x and y axes. With a proper choice of the material, lattice constant, and post height, ϕ_x and ϕ_y can be fully and independently controlled to cover the whole 0–2π range. **c**, Chosen values of a and b as functions of ϕ_x and ϕ_y. **d**, Simultaneous control of the output polarization and phase through rotating the nano-post with correspondingly chosen dimensions. The nano-post can generate an output field with any arbitrary polarization and phase from any given input polarization.

As discussed above, the metasurface structure of Fig. 3.8, has the ability to control the phase and polarization of output light independently on a subwavelength lattice. Specifically, when the transmittance of the metasurface is close to unity, the transmission of the nanopost shown in Fig. 3.8**d** can be modeled as $\mathbf{E}^{\text{out}} = \mathbf{T}\mathbf{E}^{\text{in}}$, where the Jones matrix $\mathbf{T}$ is given by Eq. 3.1. Once the input and output electric field vectors are known at each point on the metasurface, the corresponding Jones matrix can be calculated from Eq. 3.2. Then, the required rotation angle θ and phase pairs, $\phi_{x'}$ and $\phi_{y'}$, can be calculated using Eq. 3.1. The data in Fig. 3.8**c** can then be used to find the nanopost that provides the required phases.

3.8 Polarization hologram: experimental results and discussion

In order to experimentally investigate the capability of the proposed method and structure to generate polarization holograms, we designed and fabricated two different polarization holograms that project the data in two color images. The original, simulated, and measured color images are shown in Figs. 3.9**a** and 3.9**b** for the two images. Both holograms are about 30 degrees in height, corresponding to a diagonal NA of 0.36 for the hologram in Fig. 3.9**a**. The design process was exactly similar for the two images, and started by calculating the Stokes parameters from the RGB data, as shown in Figs. 3.6**a** and 3.6**b**, which correspond to the hologram of Fig. 3.9**a**. The initial electric field distribution on the hologram was then calculated from the Stokes parameters [Fig. 3.6**d**], and the modified GS algorithm was used to calculate the required metasurface electric field distributions as well as the simulated polarization holograms, shown in Figs. 3.9**a** and 3.9**b**, middle. Assuming an input electric field polarized along the x axis, the corresponding nanoposts were found through the process explained in the previous paragraph.

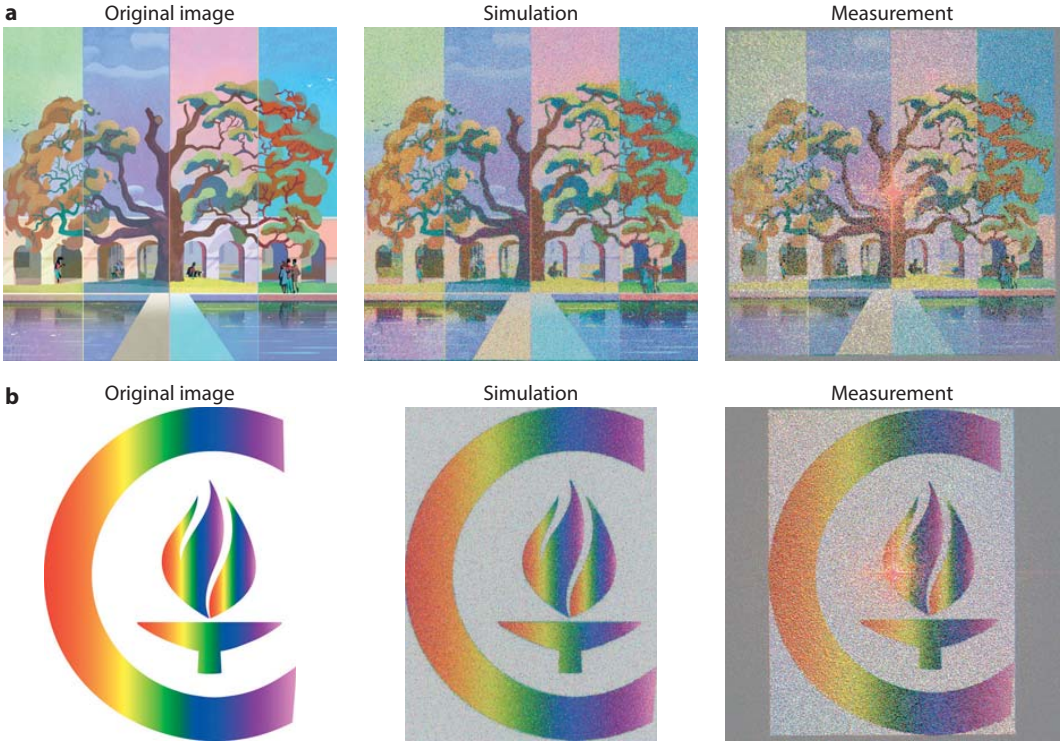

Figure 3.9: **Simulation and measurement results a** and **b**, The original target image along with simulated and measured polarization holograms converted to false-color images. Both holograms are about 30-degrees tall, corresponding to a diagonal NA of 0.36 for the holograms in panel **a**.

The process used to fabricate the devices is mostly similar to the fabrication process of the polarization camera, and it is explained in Sec. 4.7 in more detail. In short, a layer of α-Si was deposited on the fused silica substrate. The metasurface pattern was defined using electron-beam lithography and reversed through evaporation and lift-off of an aluminum oxide (Al_2O_3) layer. This layer was used as a hard mask in dry etching of α-Si and was dissolved after the etch step.

To measure the hologram, we used a custom-built microscope that imaged the back-focal plane of the objective lens on the image sensor, using a simple 4-f system. We used an LP to set the input polarization along the x axis. In addition, a polarization analyzer composed of a QWP and an LP was used inside the 4-f system to measure the hologram Stokes parameters. The measured Stokes parameters were then converted back to RGB data and combined to form the measured holograms plotted in Figs. 3.9**a** and 3.9**b**, right.

It is worth noting here that a free normalization parameter exists in the conversion of the Stokes parameters to the RGB data that determines the light intensity corresponding to *white* color. In addition, different linear transformations might be used for the conversion to map specific colors to specific intensities. Here, using 8-bit color images where the RGB values change from 0 to 255 for each color, we simply used the linear relation $S_i = (X - 128)/128$, where i can be 1, 2, or 3 and X denotes R, G, or B, respectively. However, one might want to have a different color mapping, for instance converting black to an intensity of zero. This might simply be possible either through using only half of the possible existing polarization states, i.e., by setting $S_i \geq 0$, or using a more complicated mapping.

An alternative design method is possible where all the nanoposts have the same rotation axis (i.e., all nano-posts have $\theta = \theta_0$. In that design, there is no conversion between the two linear polarizations along the two axes of the nanoposts, which we can call x and y without loss of generality. As a result, the input and output x-polarized (as well as y-polarized) powers should be equal, which means that the input polarization should be chosen based on the axes directions and the desired hologram. In addition, the normalization step in the hologram design algorithm would be slightly different for this method. We simulated the same polarization holograms using this alternative method as well, and didn't observe any significant difference in their performance.

The unprecedented capabilities of dielectric metasurfaces in simultaneous control of phase and polarization allow for implementation of new categories of devices with

no conventional counterparts. Here, we discussed vectorial holograms that generate polarization patterns of almost arbitrary complexity, designed using a modified GS algorithm. The devices operate in the near infrared and are based on an α-Si birefringent metasurface. The same method and structure can readily be used in other wavelength ranges using various materials [67, 221, 225]. While the demonstrated concepts and methods can be used to make holograms with enhanced security and added data storage capabilities, we expect that they spur more important applications in advanced structured illumination schemes or vectorial beam generation.

3.9 Appendix

Simulation and design of polarization camera

To design the DoFP metasurface mask, we first calculated the two phase profiles required for the two polarization states [Fig. 3.2**d**]. The phase profiles correspond to decentered aspheric lenses that focus each polarization at the center of one image sensor pixel. These phases are then used in Eq. 3.3 along with the known input polarization states to calculate the Jones matrix. To find the nano-post corresponding to each Jones matrix, the matrix is diagonalized according to Eq. 3.1, and the two phases, $\phi_{x'}$ and $\phi_{y'}$, and the rotation angle θ are then extracted. The dimensions of the nano-post providing the required pair of phases is then found using the data in Fig. 3.2**b**.

The polarization target used for the imaging experiments in Fig. 3.4 was designed in a slightly different manner since in this case only the output polarization is of interest. Assuming an x-polarized input light, the output polarization at each point on the mask was chosen according to Fig. 3.4**a**. In the general case, the mask can then be designed using the Jones matrix found from Equation 3.2. In this special case, however, the device is a set of nano-posts acting as quarter or half wave-plates. Therefore, we designed the nano-posts in a manner similar to [131] to make it robust to fabrication errors.

To find the transmission amplitude and phase for the nano-posts [Fig. 3.10] we simulated a uniform array of nano-posts with rectangular cross-sections under normally incident x- and y-polarized light using the rigorous coupled-wave analysis (RCWA) technique [148]. The resulting complex transmissions were then used to find the best nano-post that provides each required phase pair through minimizing the Euclidean distance between $[e^{i\phi_x}, e^{i\phi_y}]$ and $[t_x, t_y]$, where ϕ_x and ϕ_y are the desired phase values, and t_x and t_y are complex nano-post transmissions. The optimized

nano-post dimensions are plotted in Fig. 3.2**b**.

Fabrication of polarization camera

The fabrication process is the same for both the DoFP metasurface mask and the polarization imaging target. The fabrication started with deposition of a 650-nm-thick layer of α-Si on a 500-µm-thick fused silica substrate. The metasurface pattern is defined in a ~300-nm-thick ZEP-520A positive electron-beam resist using EBL. After development of the resist, a ~70-nm-thick layer of Al_2O_3 is deposited on the sample using electron-beam evaporation and lifted off to invert the pattern. The Al_2O_3 is then used as a hard mask in the reactive ion etching of the α-Si layer. Finally, the Al_2O_3 mask is removed in a solution of H_2O_2 and NH_4OH.

Measurement of polarization camera

The measurement setups (including part models) are schematically illustrated in Fig. 3.11 for different parts of the characterization process. To characterize the DoFP super-pixel performance, light from an LED was passed through an LP and a QWP to set the input polarization state. The six different polarization states [Fig. 3.3**a**] were generated using this combination. The intensity distribution patterns at the focal plane after the DoFP metasurface mask were then imaged using a custom-built microscope. The data was analyzed by calculating the Stokes parameters measured by each super-pixel, and averaging over all the super-pixels that fit within the field of view. A 10-nm bandwidth filter with a center wavelength of 850 nm was inserted in the path to characterize the narrow-band operation, and was then removed to acquire the results for a wider-bandwidth source.

The imaging polarimetry experiments were performed in a similar way. For these experiments, the polarization target was illuminated by x-polarized light out of a supercontinuum laser source (filtered by the same 10-nm bandwidth filter). The target was imaged onto the DoFP metasurface mask plane using a secondary custom-built microscope (operating as relay optics). The intensity distribution at the focal plane after the DoFP metasurface mask was then imaged and analyzed to generate the polarization images plotted in Fig. 3.4**d**. For comparison, the DoFP metasurface mask was removed and a polarization analyzer (i.e., a QWP and an LP) was inserted into the system to form the reference polarization images plotted in Fig. 3.4**c**.

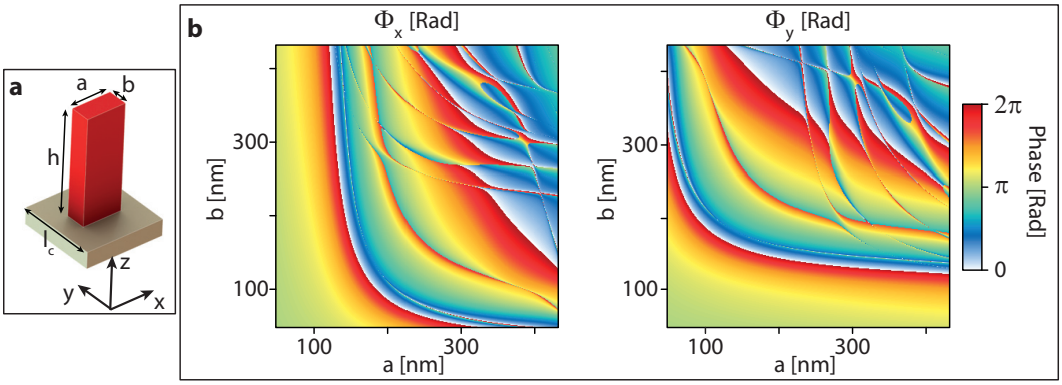

Figure 3.10: **Transmission phase of the birefringent nano-posts. a**, Schematic illustration of an α-Si nano-post showing its dimensions. **b**, Simulated transmission phases for the x- and y-polarized light at the wavelength of 850 nm. The posts are 650 nm tall, and the lattice constant is 480 nm.

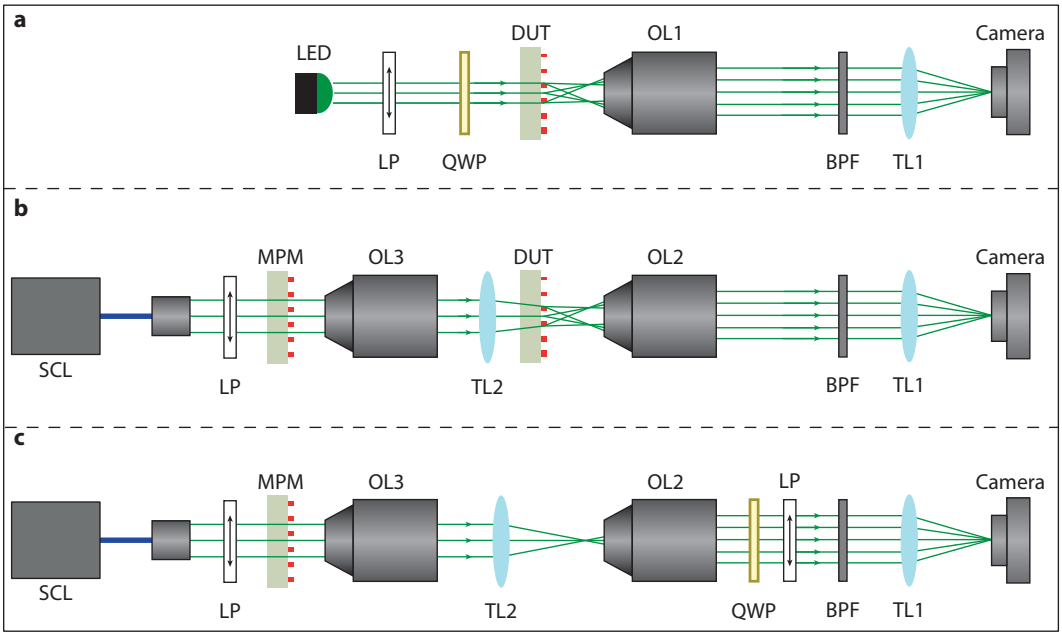

Figure 3.11: **Measurement setups for polarization camera. a**, Schematics of the measurement setup used to characterize the superpixels of the DoFP metasurface mask. **b**, Schematics of the measurement setup used to capture polarimetric images using the DoFP metasurface mask. **c**, Schematics of the measurement setup used to capture polarimetric images using the conventional method. LP: Linear polarizer; QWP: Quarter wave-plate; DUT: Device under test; OL: Objective lens; BPF: Bandpass filter; TL: Tube lens; SCL: Supercontinuum laser; MPM: Metasurface polarization mask. (OL1: Olympus UMPlanFl 100×, NA=0.95; OL2: LMPlanFl 20×, NA = 0.4; OL3: Mitutoyo M Plan Apo 10, NA=0.28; BPF: Thorlabs FL850-10; TL1: Thorlabs AC254-200-B-ML; TL2: Thorlabs LB1723-B; LP: Thorlabs LPVIS100-MP2; QWP: Thorlabs AQWP10M-980; SCL: Fianium WhiteLase micro.)

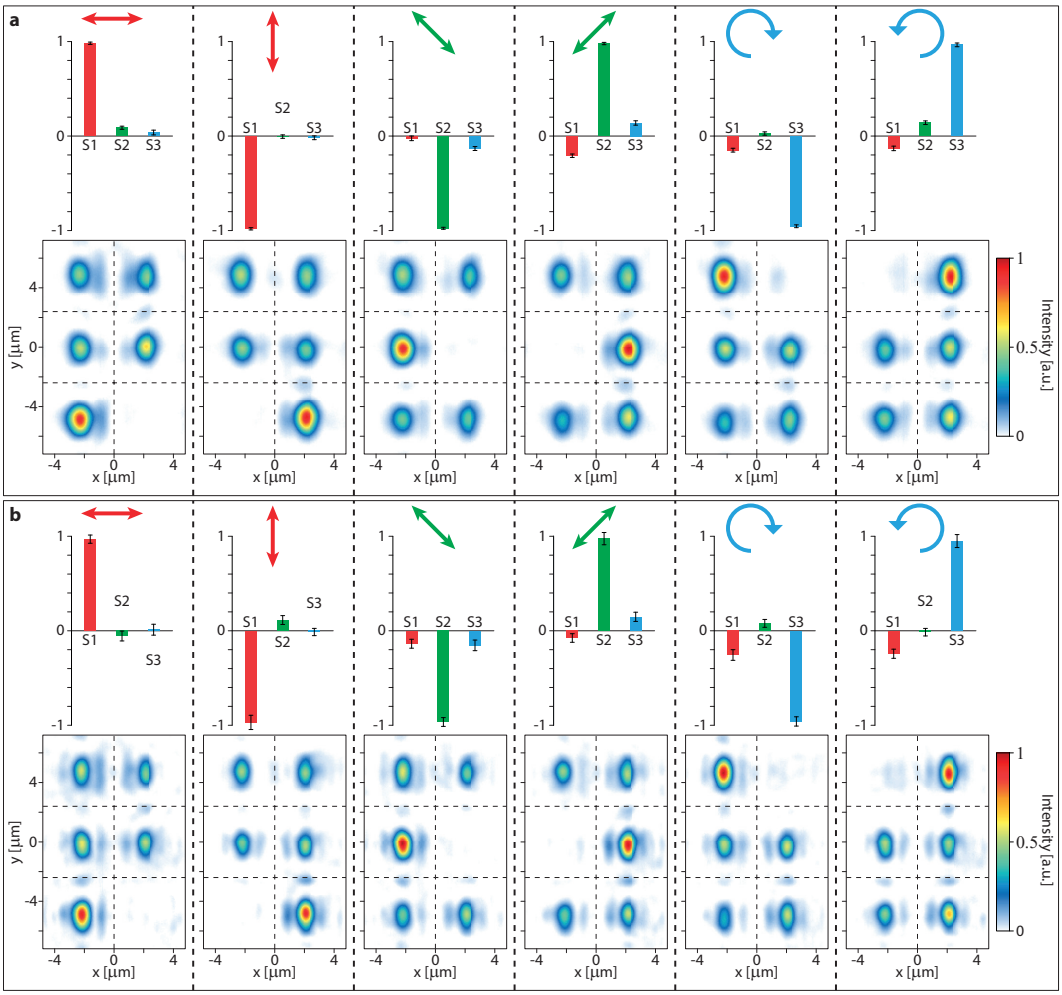

Figure 3.12: **Superpixel characterization of the DoFP metasurface mask with 4.8-μm pixels.** **a**, Calculated average Stokes parameters for different input polarizations (top) and the corresponding intensity distributions of a sample superpixel (bottom). The Stokes parameters are averaged over about 120 superpixels (limited by the microscope field of view), and the error bars demonstrate the statistical standard deviations. The measurements are performed with an 850-nm LED filtered by a bandpass filter (center: 850 nm, FWHM: 10 nm) as the light source. **b**, Same as **a**, with the bandpass filter removed from the setup. The results shown in **a** are the same as the ones presented in Figs. 3.3**a** and 3.3**b** and are shown here for comparison with the results shown in **b**. When using the band-pass filter, the iris in front of the LED has a larger diameter to compensate for the lower power of the filtered light. This results in the focal spots being tighter without the band-pass filter.

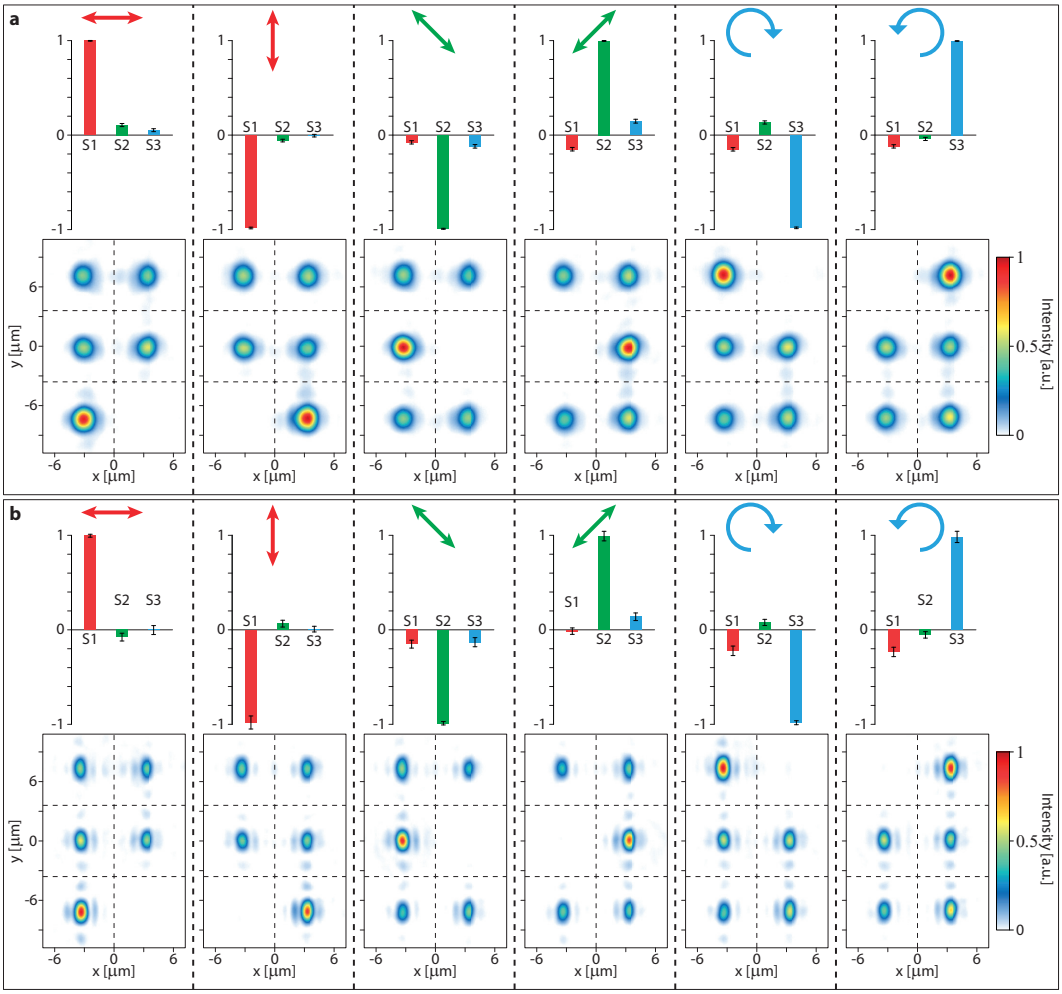

Figure 3.13: **Superpixel characterization of the DoFP metasurface mask with 7.2-μm pixels.** **a**, Calculated average Stokes parameters for different input polarizations (top) and the corresponding intensity distributions of a sample superpixel (bottom). The Stokes parameters are averaged over more than 50 superpixels (limited by the microscope field of view), and the error bars demonstrate the statistical standard deviations. The measurements are performed with an 850-nm LED filtered by a bandpass filter (center: 850 nm, FWHM: 10 nm) as the light source. **b**, Same as **a**, with the bandpass filter removed from the setup.

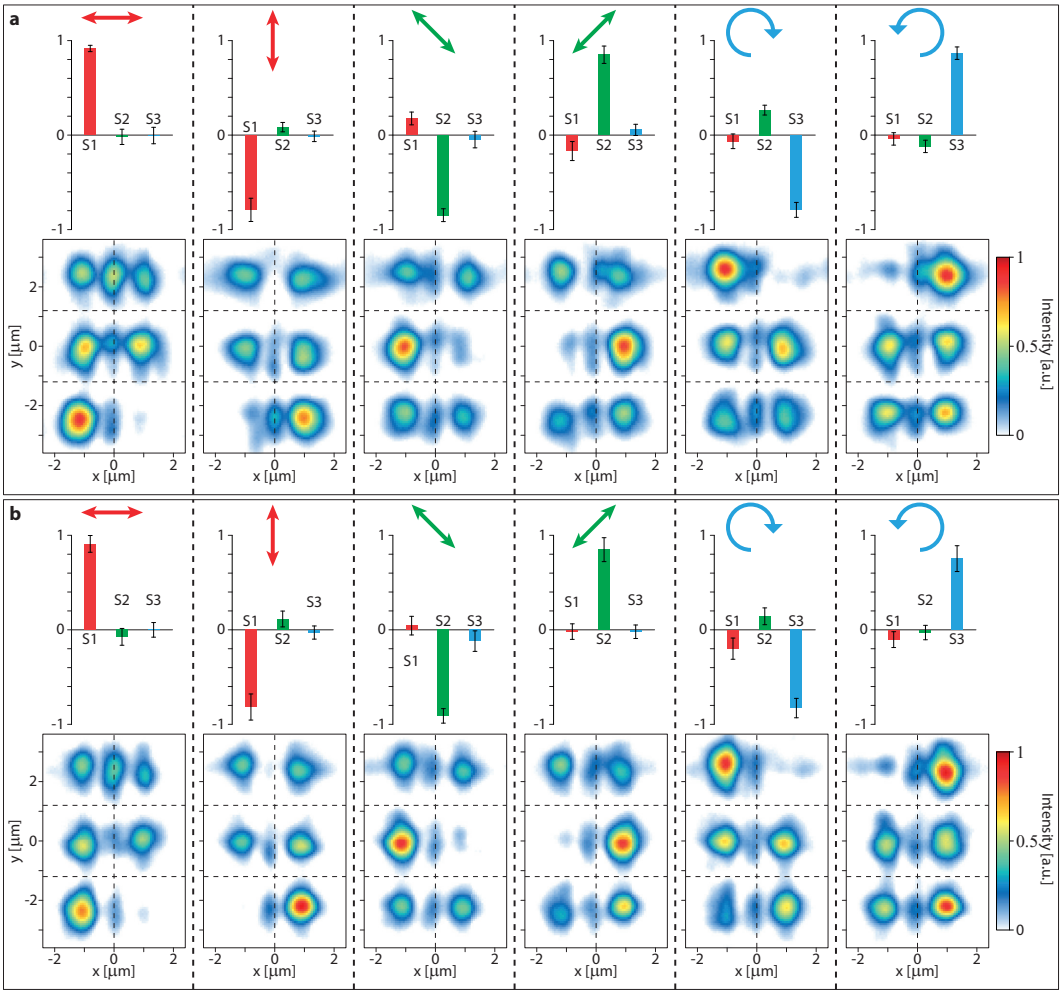

Figure 3.14: **Superpixel characterization of the DoFP metasurface mask with 2.4-μm pixels.** **a**, Calculated average Stokes parameters for different input polarizations (top) and the corresponding intensity distributions of a sample superpixel (bottom). The Stokes parameters are averaged over about 370 superpixels (limited by the microscope field of view), and the error bars demonstrate the statistical standard deviations. The measurements are performed with an 850-nm LED filtered by a bandpass filter (center: 850 nm, FWHM: 10 nm) as the light source. **b**, Same as **a**, with the bandpass filter removed from the setup.

Simulation of polarization holograms

The RCWA technique [148] was used to calculate the transmission amplitude and phase of the rectangular nanoposts. The refractive indices of α-Si and fused silica were assumed to be 3.6 and 1.45 at the operation wavelength of 850 nm. The sizes of nanoposts that provide a specific phase pair plotted in Fig. 3.8**c** are found through minimizing the total complex error $|t_x - \exp(i\phi_x)|^2 + |t_2 - \exp(i\phi_y)|^2$. The holograms are designed using Eqs. 3.4-3.6, where the fast Fourtier transform technique is used to calculate the discrete Fourier transforms. The algorithm converged to the final designs in less than 20 iterations in all cases.

Fabrication of polarization holograms

The α-Si layer was deposited on the fused silica substrate using the plasma enhanced chemical vapor deposition to a final thickness of 682 nm. The metasurface pattern was generated using an EBPG5200 electron beam lithography machine in a positive electron resist (ZEP-520A). An electron beam evaporated Al_2O_3 layer was used to reverse the generated pattern with a lift-off process, and was then used as a hard mask for dry etching the α-Si layer. The Al_2O_3 layer was then dissolved in a mixture of hydrogen peroxide and amunioum hydroxide.

Measurement procedure of polarization holograms

The metasurface was illuminated by an x-polarized collimated beam from an ~850-nm laser diode. An objective lens (LMPlanFl 20×, NA=0.4; Olympus) was used to form a Fourier transform of the metasurface hologram in its back focal plane. A $4f$ system (LB1471-B, f=50 mm and LB1437-B, f=150 mm; Thorlabs Inc.) was then used to image the back focal plane onto a charge-coupled device (CCD) image sensor (CoolSNAP K4; Photometrics). A polarization state analyzer formed from a QWP (AQWP10M-980; Thorlabs Inc.) and an LP (LPVIS100-MP2; Thorlabs Inc.), placed inside the $4f$ system was used to measure the Stokes parameters of the holograms. The measured Stokes parameters were numerically combined and converted to color data to form the final false-color holograms.

Chapter 4

CONFORMAL FLEXIBLE METASURFACES

The material in this chapter was in part presented in

> S. M. Kamali, A. Arbabi, E. Arbabi, Y. Horie, and A. Faraon, "Decoupling optical function and geometrical form using conformal flexible dielectric metasurfaces", Nat. Commun. **7**, 11618 (2016) DOI: doi.org/10.1038/ncomms11618,

Physical geometry and optical properties of objects are generally correlated: cylinders focus light to a line, spheres to a point, and arbitrarily shaped objects introduce optical aberrations. Multi-functional components with decoupled geometrical form and optical function are needed when specific optical functionalities must be provided while the shapes are dictated by other considerations like ergonomics, aerodynamics, or esthetics. In this chapter, we introduce conformal metasurface platform for decoupling optical properties of objects from their physical shape through thin and flexible dielectric metasurfaces. The conformal metasurfaces, which are based on HCA, are composed of silicon nano-posts embedded in a polymer substrate that locally modify NIR (λ= 915 nm) optical wavefronts. As proof of concept, we show that cylindrical lenses covered with metasurfaces can be transformed to function as aspherical lenses focusing light to a point. The conformal metasurface concept is highly versatile for developing arbitrarily shaped multi-functional optical devices.

4.1 Motivation

The correlation between the geometry of an object and its optical functionality [226] has introduced long-standing design challenges to optical engineers developing multi-functional components [227]. The traditional solution has been to compromise and optimize the component material and geometry by considering all the physical requirements. This was originally studied in the context of conformal and freeform optics where optical components with non-standard surfaces were developed for integration of optics into flying objects with specific aerodynamic shapes [228, 229]. More recently, this issue has attracted new attention due to its application in integration of optics into various consumer electronic products and medical equipment with stringent packaging and design requirements. Furthermore, controlling optical

properties of objects without physically modifying them can enable the visual blending of an object with its background [230–233] or changing its appearance through generation of a holographic virtual image [234, 235]. In the context of conformal optics, the conventional solution is to stack several bulky optical elements with non-standard surface profiles underneath the outermost surface of the object [229]. Such solutions usually have challenging fabrication processes requiring custom-made fabrication equipment, are bulky, and do not provide a unified and versatile approach that can be applied to arbitrary geometries. Conformal metasurface approach can provide a solution for decoupling the geometric shape and optical characteristics of arbitrary objects. In this chapter, we introduce flexible metasurfaces based on HCA platform that can be conformed to a non-planar arbitrarily shaped object to modify its optical properties at will. We present a general design procedure and a high yield fabrication process for the conformal flexible metasurface platform. As a proof of principle, we experimentally demonstrate flexible metasurfaces that wrap over cylindrical surfaces and convert them to aspherical lenses.

4.2 Conformal metasurfaces platform

Figure 4.1a shows a schematic illustration of a non-planar arbitrarily shaped transparent object wrapped by a flexible metasurface based on this platform. The metasurface layer is composed of an array of dissimilar cylindrical α-Si nano-posts with different diameters placed on a subwavelength periodic hexagonal lattice, and embedded in polydimethylsiloxane (PDMS) as a flexible substrate (Fig. 4.1a, inset). The arbitrary shape of the object's surface distorts the wavefront of the transmitted light in an undesirable way (Fig. 4.1b). By conforming the metasurface onto the object's outermost surface, the distortion can be compensated and the wavefront of the transmitted light can be shaped to a desired form, similar to phase compensating antenna arrays employed in the microwave regime [236]. For example, the metasurface can be designed to correct the distortions introduced by the arbitrarily shaped object and make it act similar to an aspherical lens that focuses light to a point as schematically shown in Fig. 4.1c.

4.3 Operation principle and design procedure

The desired phase profile of the conformal metasurface is found with the knowledge of the geometry of the transparent object over which it is wrapped, and the desired optical response. First, the object without the metasurface is considered, and the

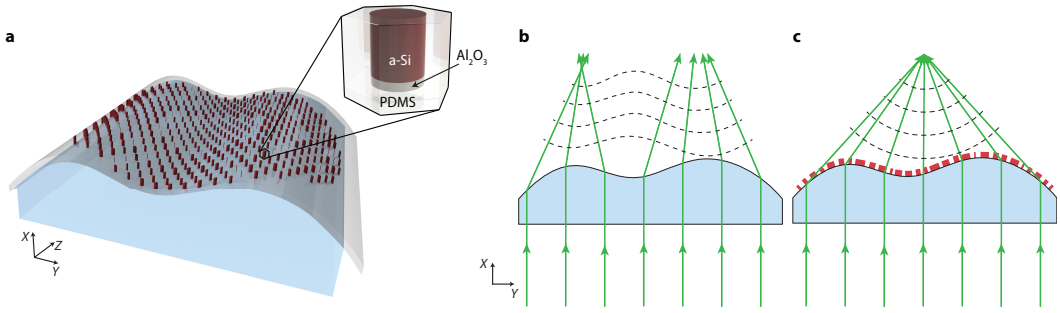

Figure 4.1: **Conformal optics with optical dielectric metasurfaces. a**, A schematic illustration of a dielectric metasurface layer conformed to the surface of a transparent object with arbitrary geometry. (Inset) The building block of the metasurface structure: an α-Si nano-post on a thin layer of Al_2O_3 embedded in a low index flexible substrate PDMS for instance). **b**, Side view of the arbitrarily shaped object showing how the object refracts light according to its geometry and generates an undesirable wavefront. **c**, The same object with a thin dielectric metasurface layer conformed to its surface to change its optical response to a desired one.

phase profile of the optical waves transmitted through the object is computed along the surface of the object. For objects with dimensions significantly larger than the optical wavelengths, this phase profile can be found using ray optics approximation and by computing the optical path length and the corresponding optical path difference (OPD) of the rays passing through different points along the outermost surface of the object with respect to the chief ray. Then, using a similar OPD-based approach, the phase profile required to achieve the desired specific functionality is obtained along the surface of the object. For example, if we want the object to focus light to a point, a converging spherical wavefront is desired, which is sampled along the arbitrary surface of the object. The metasurface layer, when wrapped on the surface of the object, should locally impose an additional optical phase shift equal to the difference between the original phase of the object and the desired phase profile. Therefore, the desired metasurface phase profile is expressed as a function of two coordinate values defining the non-planar surface of the object. To obtain the appropriate phase profile of the metasurface before its transfer to the non-planar surface, an appropriate coordinate transformation should be applied. For example, if the flexible substrate of the metasurface is under no stress after being mounted on the object's surface, then the appropriate coordinate transformation conserves length along the surface of the object.

Using this design procedure, we computed two sets of conformal metasurface phase profiles for both a convex and a concave cylindrical glass. The metasurfaces modify

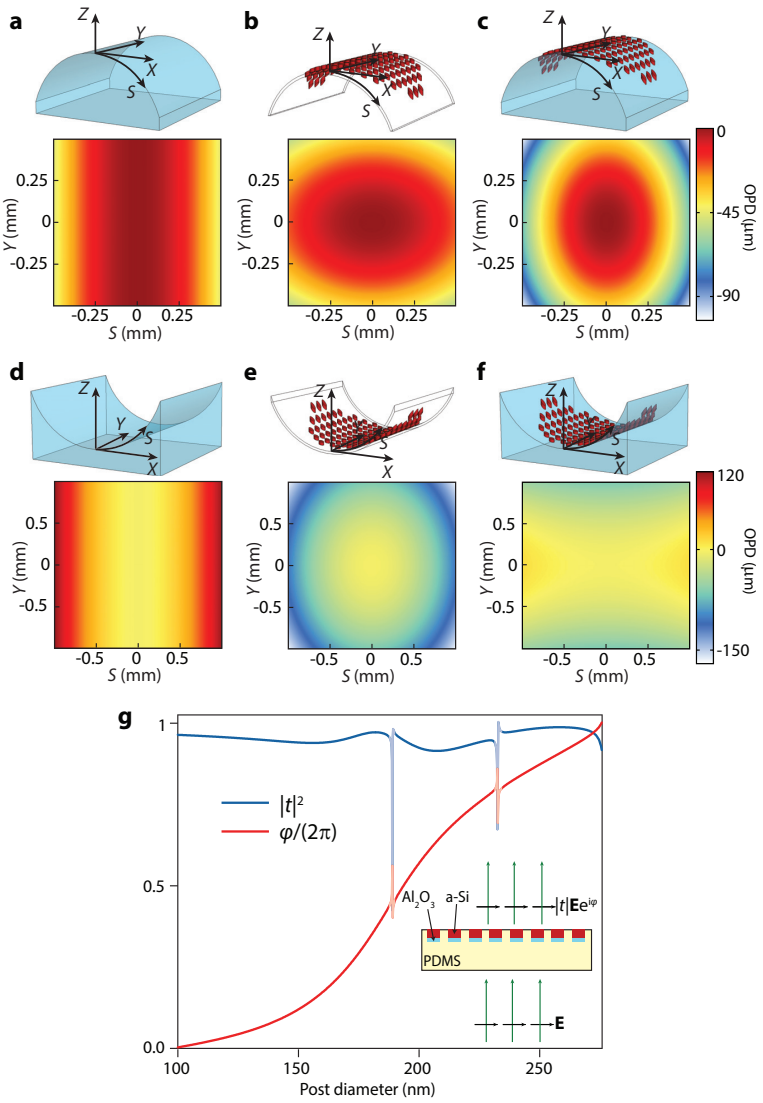

Figure 4.2: **Design procedure of conformal metasurfaces.** **a**, The OPD (in μm) of the rays passing through a converging cylindrical object. **b**, The difference OPD needed at the surface of the convex cylindrical object compensated by the conformal metasurface. **c**, Desired OPD at the surface of the object which is provided by the object and conformal metasurface combination. **d**, **e**, and **f** show similar plots for a diverging cylinder. "S" is the arch length on the cylinder surface in a plane perpendicular to the Y axis. **g**, Simulated intensity transmission and phase of the transmission coefficient for a periodic array of α-Si nano-posts embedded in PDMS as shown in the inset. The nano-posts are composed of 720 nm α-Si on 100 nm Al_2O_3, and are arranged in a hexagonal lattice. The simulation wavelength is 915 nm. This graph is used to relate the phase shift values (and the respective OPDs) needed at different points on the conformal metasurface to the nano-post diameters. See section 4.7 for simulation details.

the wavefronts of the cylindrical objects to make them behave as aspherical lenses. Figure 4.2a (4.2d) shows the OPD of the rays passing through the convex (concave) cylinder at its top surface. Considering the desired converging spherical wavefront, the desired OPD of the rays at the surface of the convex (concave) cylinder is calculated and shown in Fig. 4.2c (4.2f). The difference between the OPDs of the convex (concave) cylindrical object and the converging spherical phase profile is shown in Fig. 4.2b (4.2e). The conformal metasurfaces should impose phase shifts equivalent to these OPDs at the operation wavelength (see Sec. 4.7 for simulation details). Since the cylindrical surfaces are isometric with a plane, the metasurfaces can be mounted on them under negligible stress. Therefore, only a simple geometric transformation (*XY* to *SY* in Fig. 4.2a) is used to map the coordinates on a cylinder surface to a plane.

The optical coupling among the nano-posts is weak in the HCA metasurface platform, and each nano-post scatters light almost independent of its neighboring nano-posts. The weak coupling is due to the high index contrast between the nano-posts and their surroundings, and it is manifested in the localization of the optical energy inside the nano-posts and the weak dependence of the transmission of the nano-post arrays to their spacing (i.e., lattice constant) as has been previously discussed [66] in more detail. This simplifies the design by allowing to directly relate the local transmission coefficient to the diameter of the nano-post at each unit cell of the metasurface. Figure 4.2g shows the simulated intensity transmission coefficient and phase of the transmission coefficient for periodic arrays of 720 nm tall nano-posts embedded in PDMS with diameters ranging from 100 nm to 275 nm (see Sec. 4.7 for simulation details). The nano-posts are arranged in a hexagonal lattice with 550 nm lattice constant, and the simulation wavelength is 915 nm. Refractive indices of α-Si and PDMS are 3.56 and 1.41 at the simulation wavelength, respectively. The whole 0 to 2π phase range can be covered by changing the nano-post diameters while keeping the intensity transmission coefficient above 91%. These results are obtained assuming normal incidence.

To get more insight into the operation mechanism, each nano-post can be considered as a truncated circular cross-section waveguide [76]. Because of the truncation of both ends, the nano-post supports multiple low quality factor Fabry-Perot resonances which interfere and lead to high transmission of the nano-post array (see Sec. 4.7 and Fig. 4.5). We also note that in contrast to Huygens' metasurfaces where only two resonant modes are employed (one with a significant electric dipole and

one with significant magnetic dipole) [60], the resonant modes of the nano-posts contain dipole, quadrupole, and higher order electric and magnetic multipoles in their multipole expansion. Although the modal expansion approach provides some intuitive understanding of the operation principle, it does not offer guidelines for designing of the nano-post arrays. Moreover, an effective medium method does not capture the underlying physics of the periodic structures that support more than one propagating mode [65, 75, 76]. Therefore it is not applicable to most of the nano-posts widths we used in designing the metasurface, as a periodic array of nano-posts with diameters greater than 180 nm would be multimode. Considering these, and the limited number of design parameters (i.e., nano-post height and the lattice constant), we prefer the direct approach of finding the transmission of the nano-post arrays (as shown in Fig. 4.2g) over the modal expansion technique.

Low sensitivity to the incident angle is a necessary property for a conformal metasurface since the incident angle would be varying across the metasurface when it is wrapped over a non-planar object. For the metasurface platform considered here, the transmission coefficient of TE polarized light is weakly dependent on the incidence angle, and transmission coefficient of TM polarized light shows some angle dependent resonances (Sec. 4.7 and Fig. 4.6). These resonances introduce a small phase error and lower transmission, but as we experimentally show, they only slightly reduce the metasurface efficiency for TM polarization. For very steep angles, the metasurface efficiency decreases as analyzed in our previous work [66]. The general metasurface design procedure is as follows. First, the coordinate-transformed desired metasurface phase was sampled at the lattice sites of the periodic hexagonal lattice. Then, the diameter of the nano-post at each site was obtained using the corresponding sampled phase value at that site and the phase-diameter relation shown in Fig. 4.2g. To ensure a one to one relationship between the phase and nano-post diameters, and to keep the transmission high, nano-post diameters corresponding to the sharp resonances in Fig. 4.2g were not used. Using this procedure, metasurfaces with phase profiles shown in Fig. 4.2b and 4.2e were designed to be conformed to convex and concave cylindrical objects. These metasurfaces modify the optical response of the cylinders such that they behave as aspherical lenses and focus light to single points (see Sec. 4.7 for the details of designed lenses and cylindrical surfaces).

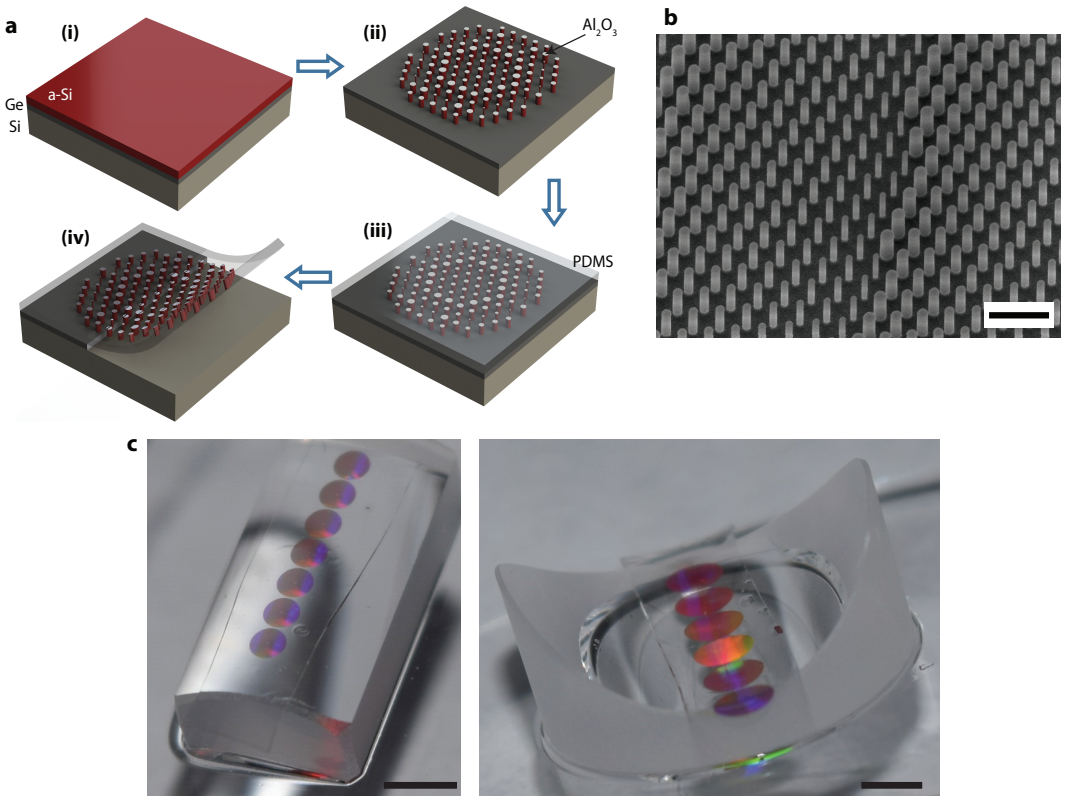

Figure 4.3: **Overview of the fabrication process and images of the fabricated metasurface.** **a**, Steps involved in the fabrication of conformal metasurfaces: (**i**) Germanium (Ge) and α-Si are deposited on a silicon wafer. (**ii**) α-Si nano-posts are patterned and dry etched using an Al_2O_3 hard mask. (**iii**) PDMS is spin coated on the substrate. (**iv**) The sacrificial Ge layer is dissolved to release the nano-posts which are embedded in the flexible PDMS layer. **b**, A SEM image of the silicon nano-posts with the Al_2O_3 mask before spin coating PDMS. Scale bar, 1 μm. **c**, Optical images of two flexible metasurfaces conformed to a convex glass cylinder (left) and a concave glass cylinder (right). In both cases, the metasurfaces make cylinders behave like converging aspherical lenses. Scale bars, 2 mm.

4.4 Fabrication and characterization of conformal metasurfaces.

Figure 4.3a schematically illustrates the key steps in fabricating thin, flexible, and conformable metasurfaces. A Ge sacrificial layer is deposited on a silicon wafer and then an α-Si layer is deposited over the Ge (Fig. 4.3a, (i)). The α-Si layer is patterned using electron-beam lithography followed by dry etching using an Al_2O_3 hard mask (Fig. 4.3a, (ii)). The sample is subsequently spin coated with two layers of PDMS (a diluted thin layer followed by a thicker layer (Fig. 4.3a, (iii)). Then,

the sample is immersed in a diluted NH_4OH solution which dissolves the Ge layer and releases the flexible metasurface with minimal degradation of the metasurface and the PDMS layer (Fig. 4.3a, (iv)). A SEM image of the fabricated device before spin coating the PDMS layer is shown in Fig. 4.3b. Optical images of metasurfaces conformed to the convex and concave glass cylinders are shown in Fig. 4.3c. The whole fabrication process has a near unity yield, with almost all of the metasurfaces retaining a large majority of the nano-posts (Sec. 4.7 and Fig. 4.7). Moreover, it does not degrade the optical quality of the metasurface layer. The optical quality of the flexible metasurface layer was tested by transferring a flat metasurface lens to a flat substrate. See Fig. 4.8 for the measurement results and focusing efficiency of the transferred flat metasurface lens. To demonstrate the capabilities of this platform, two different conformal metasurfaces operating at the NIR wavelength of 915 nm were fabricated and characterized. The first 1-mm-diameter metasurface conforms to a converging cylindrical lens with a radius of 4.13 mm. The cylinder by itself focuses light to a line 8.1 mm away from its surface (Fig. 4.4a). The presence of the metasurface modifies the cylinder to behave as an aspherical lens focusing light to a point 3.5 mm away from the surface of the cylinder (Fig. 4.4a). The second device is a 2-mm diameter metasurface conforming to a diverging glass cylinder with a radius of 6.48 mm and a focal length of -12.7 mm (Fig. 4.4b). With the metasurface on top, the concave cylinder focuses light to a point 8 mm away from the cylinder surface (Fig. 4.4b).

The devices were characterized under 915 nm collimated laser beam illumination by recording intensity profiles at different planes parallel to their focal planes. Figure 4.4 also shows the measured intensity profiles. The focal plane intensity profiles are shown as insets. A tight focus is observed at the designed focal length. Focusing efficiencies of 56% and 52% under TE illumination (i.e., electrical field parallel to the cylinder axis) were measured for the two devices, respectively. The focusing efficiency is defined as the ratio of the power focused by the device to the incident power on the device (see Sec. 4.7 for the measurement details). Under TM illumination, numerical estimations based on the angular response of a uniform array shown in Fig. 4.6 indicate a slight degradation of the device performance for larger angles between the metasurface and the incident beam. The devices were measured with TM input beam polarizations and, as expected, showed similar behavior as under TE illumination with focusing efficiencies of 56% and 50%. The difference in TE and TM polarization efficiencies increases as the incidence angle becomes steeper (Fig. 4.9); the focus pattern, however, remains almost the same under both

polarizations (Fig. 4.10). The corresponding measured FWHM of the focal spots are approximately 3.5 μm and 5 μm comparable to diffraction limited FWHM of 3.2 μm and 3.7 μm, respectively. Slight aberrations observed in the focal plane intensity profiles are mostly due to imperfections in the alignment of the metasurface to the non-planar substrates. Reduction of efficiency in conformal metasurfaces compared to the transferred flat metasurfaces (Fig. 4.8) is mostly due to the imperfections in the alignment, slight movements of the nano-posts within the flexible substrate during the substrate handling, and the difference between the actual non-planar substrate profile and the profile assumed for design.

4.5 Discussion

Although here we have used cylindrical substrates as proof of principle, this platform is not limited to surfaces that can be projected to a plane using isometric transformations. Conformal metasurfaces can be designed for other types of objects (for instance spheres where the metasurface needs to be stretched for conforming) with a similar method. High stretchability and flexibility of thin PDMS layers (~50 μm) make them suitable for conforming to non-isometric surfaces. In such cases, however, a mechanical analysis of the metasurface deformation upon mounting on the object should be carried out. The coordinate transformation that projects the conformal lattice to the planar one should also account for this deformation. Besides, in the case of objects with steep angles (where the incident collimated beam is far from normal to the metasurface at some points), further considerations should be taken in choosing the lattice constant to avoid excitation of higher order diffractions. Moreover, since the design procedure is local (i.e., each nano-post at each lattice site is chosen independently), the incident angle of the beam at each lattice point can be taken into account in designing the respective nano-post.

Conformal dielectric metasurfaces operate based on spatially varying nano-structured diffractive scatterers. The behavior of the device is wavelength dependent because both the optical response of the scatterers and their arrangement is optimized for a given wavelength. The performance of the proposed devices has a wavelength dependence similar to other HCA lenses recently demonstrated [66] where good performance is maintained over a bandwidth of a few percent around the design wavelength.

The proposed platform is relatively robust to systematic and random errors. Fabrication errors do not affect the device functionality and only reduce its efficiency (5 nm

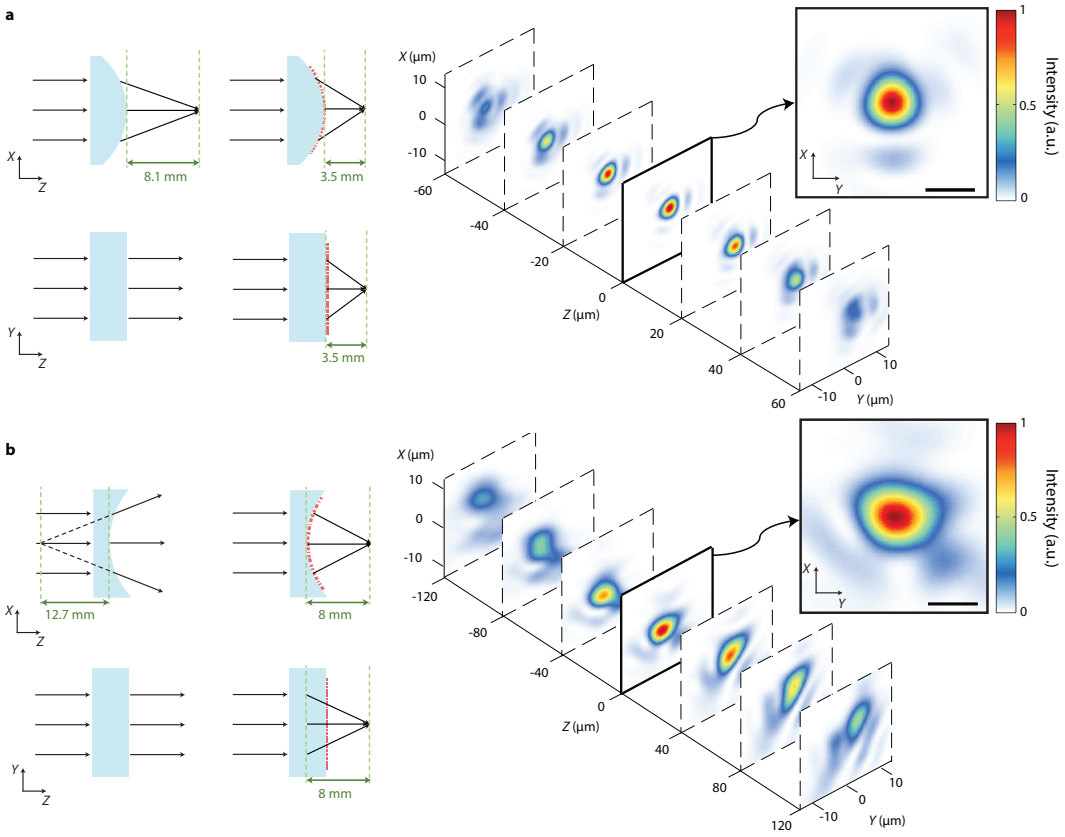

Figure 4.4: **Measurement results of conformal dielectric metasurfaces.** **a**, A converging cylindrical lens with a radius of 4.13 mm and a focal distance of 8.1 mm is optically modified using a conformal metasurface with a diameter of 1 mm. The cylinder plus the metasurface combination behaves as an aspherical lens with a focal length of 3.5 mm. The coordinate system is the same as in Fig. 2. **b**, A different metasurface is mounted on a concave glass cylinder with a radius of 6.48 mm and a focal distance of −12.7 mm, which makes it focus to a spot 8 mm away from its surface (as an aspherical lens). Schematic illustrations (side and top views) are shown on the left, and intensities at planes parallel to the focal plane and at different distances from it are shown on the right. Intensities at the focal plane are depicted in the insets. Measurements are performed at the wavelength of 915 nm. For the measurement details see Sec. 4.7. Scale bars, 5 μm.

error in nano-post diameters results in ∼3% reduction of efficiency [14]). Alignment imperfections (extra stretch or angular rotation) results in focal distance mismatch between the nonplanar object and the metasurface. Microlens focal distance has second order dependence on the substrate stretch ratio. For instance, for the devices shown in Fig. 4.4, having 1% strain in the flexible metasurface results in a 2% error in focal distance, and a 1 degree rotation misalignment results in 0.06% mismatch between the horizontal and vertical focal distances. Also, fractional wavelength error

is equal to the fractional error of the focal distance [66] (i.e., 1% error in wavelength results in 1% error in focal distance of the flexible metasurface).

The developed fabrication process has a near unity yield (more than 99.5%) and we are able to transfer almost all of the nano-posts into the PDMS with good accuracy. Nevertheless, the proposed platform is very robust to the fabrication deficiencies; various imperfections including deviations between designed and fabricated nano-post sizes (~5 nm in the diameter and (or) height of the nano-posts), rough side walls, and missing nano-posts (~10%) only result in small reductions in the efficiency of the device, and do not alter the functionality significantly.

4.6 Summary and outlook

In conclusion, we demonstrated flexible dielectric metasurfaces and showed their applications for conformal optics. As proof of concept, the optical properties of glass cylinders have been changed to behave like aspherical lenses focusing light to a point. The design paradigm can be applied to any other system where conformal optical design is required. In addition, flexible electronics is a well-established field of research, with the aim of transferring conventional systems to flexible and non-planar substrates. Very promising results have been achieved during the last decade with various applications in wearable electronics, electronic skins, and medical devices [237–239]. The flexible and conformal metasurface platform proposed here can be merged with conformal electronics, leading to versatile flexible optoelectronic technologies.

4.7 Appendix

Design procedure

The optical path length and the corresponding OPD of light passing through the cylinders were computed using ray optics approximation. For simulations, the convex and concave cylinders were assumed to have radii of 4.13 mm and 6.48 mm, respectively, and a refractive index of 1.507. The PDMS layer was modeled as a 50-μm-thick layer with a refractive index of 1.41. In both cases, the object OPDs were calculated at the outermost surface of the PDMS, considering light propagation through the PDMS layer and refraction at the glass-PDMS interface. The desired OPDs were also calculated at the same surfaces, assuming focal distances of 3.5 mm and 8 mm for the convex and concave lenses, respectively. Two different metasurfaces

of diameters 1 mm and 2 mm were designed for the convex and concave cylinders to impose the phase shifts equivalent to the difference of the cylinders' and the desired OPDs.

The planar periodic metasurfaces were simulated using the RCWA technique to find the complex transmission coefficients corresponding to all nano-post diameters for normal incident plane waves (Fig. 4.2g) [148]. The lattice constant is chosen such that the array is non-diffractive at the simulation wavelength. Simulation results shown in Fig. 4.6 were also obtained using the RCWA technique. All of the simulations and calculations were performed at the wavelength of 915 nm.

Sample fabrication

A 300-nm-thick Ge sacrificial layer was deposited by electron-beam evaporation on a silicon wafer, and 720 nm hydrogenated α-Si was deposited on the Ge layer using PECVD with a 5% mixture of silane in argon at $200^{\circ}C$. The refractive index of the α-Si layer was measured using variable angle spectroscopic ellipsometry and was found to be 3.56 at the wavelength of 915 nm. The metasurface pattern was defined in ZEP-520A positive resist (~300 nm, spin coated at 5000 rpm for 1 min) using a Vistec EBPG5000+ electron-beam lithography system. The pattern was developed in a resist developer (ZED-N50 from Zeon Chemicals). After developing the resist, the pattern was transferred into a ~100-nm-thick Al_2O_3 layer deposited by electron-beam evaporation through a lift-off process. The patterned Al_2O_3 served as a hard mask for dry etching of the α-Si layer in a mixture of SF_6 and C_4F_8 plasma. The PDMS polymer (RTV-615 A and B mixed with a 10:1 mass ratio) was diluted in toluene in a 2:3 weight ratio as a thinner. The mixture was spin coated at 3000 rpm for 1 min on the fabricated metasurface to fill the gaps between the nano-posts and to form a thin PDMS film (Fig. 4.7). The sample was degassed and cured for more than 30 mins. The second layer of PDMS without a thinner was spin coated on the sample to form a ~50-μm-thick PDMS film (spin coated at 1000 rpm for 1 min). The sample was degassed and cured for more than 1 hr. Finally, immersion in a 1:1:30 mixture of NH_4OH, H_2O_2, and deionized water (DI water) at room temperature removed the sacrificial Ge layer releasing the PDMS substrate and the embedded nano-posts (~one day). The released metasurface is then mounted manually on the cylinders (Edmund Optics 43-856 and 47-748). To compensate for the misalignment of the substrate and metasurface, multiple lenses with slightly different rotations were fabricated in each sample (Fig. 4.3c). This way, the best aligned microlens should have a rotation error of less than or equal to one degree (the rotation step

between two successive metasurface lenses).

Measurement procedure

Devices were characterized using the setups shown schematically in Fig. 4.11. A 915 nm fiber coupled semiconductor laser was used as the source and a fiber collimation package (Thorlabs F220APC-780) was used to collimate the beam. Intensity at different planes was captured by using a 50× objective lens (Olympus LMPlanFL N, NA=0.5), a tube lens (Thorlabs LB1945-B) with focal distance of 20 cm, and a camera (CoolSNAP K4 from Photometrics) as shown in Fig. 4.11a. Moreover, neutral density (ND) filters (Thorlabs ND filters, B coated) were used to adjust the light intensity and decrease the background noise captured by the camera. The overall microscope magnification was measured by imaging a calibration sample with known feature sizes. To measure the efficiencies, an additional lens (Thorlabs LB1945-B with focal length of 20 cm) was used to partially focus the collimated beam, so that more than 99% of the beam power falls inside the device under test. The beam radius was adjusted by changing the distance between the lens and the sample. A 15 μm diameter pinhole (approximately three times the measured FWHM) was placed at the focal plane of the sample to only allow the light focused inside the pinhole area to pass through. The focusing efficiency was then determined as the ratio of measured optical power after the pinhole (i.e., the power in focus) to the measured power right before the sample (the incident power). The measurement setup used for efficiency characterization is shown in Fig. 4.11b. For polarization sensitivity measurement, a polarizer (Thorlabs LPNIR050-MP) was added before the sample to set the polarization state of the incident beam.

Resonant modes of the nano-posts

To get more insight into the resonant modes contributing to the transmission coefficient, we consider the amplitude and phase of the transmission coefficient of a periodic array of the nano-posts as a function of wavelength around 915 nm (yellow and green solid curves in Fig. 4.5e). The nano-posts diameter was chosen to be 200 nm, in the middle of our parameter scale. The resonant modes of such an array that have resonant frequencies within the desired bandwidth are found using the finite element method in COMSOL Multiphysics. The magnetic energy density for these resonant modes is shown in Fig. 4.5b in two horizontal and vertical cross sections indicated in Fig. 4.5a. Total transmission of the nano-posts array is determined by the interference between the incident light and these dominant resonant modes. We

have reconstructed the amplitude and phase of the transmission coefficient in the bandwidth of interest using these resonant curves. Figure 4.5d shows the resonant curves with their corresponding amplitudes used in the reconstruction, along with the reconstructed transmission amplitude. Figure 4.5e compares the actual transmission amplitude and phase of the nano-posts array with the reconstructed ones. Using more resonant modes (with frequencies outside the bandwidth of interest) it is possible to reconstruct the transmission with even higher accuracy.

Angular dependence of transmission coefficient for TE and TM polarizations

Figure 4.6a shows a schematic illustration of a uniform array of nano-posts embedded in PDMS (left), and its simulated transmission amplitude (top) and phase (bottom) as a function of nano-posts diameter and incident beam angle for TE polarization. Similar plots for TM polarization are shown in Fig. 4.6b. These results show weak angular dependence of the high contrast transmitarray metasurfaces for TE polarization in the range of angles involved in their operation. The larger angular dependence for the TM polarization results in slight degradation of the device performance in this polarization. The maximum angle between the metasurface normal and the incident beam for the two metasurfaces discussed in the main text are 7° and 9°. The angular dependence increases for larger incident angles, indicating that angular dependence should be considered in the design of conformal metasurfaces with steep local incident angles. Moreover, for the lattice used here, higher diffraction orders are present for incident angles larger than ~25°, and a smaller lattice constant should be used for metasurfaces with larger incident angles. Magnetic energy density distributions for a uniform nano-posts array with the diameter of 258 nm illuminated with a plane wave with incident angle of θ=9° for TE and TM polarizations are shown in Figs. 4.6c and 4.6e, respectively. The corresponding diameter/angle points are indicated by solid squares on the transmission plots presented in Figs. 4.6a and 4.6b. Similar plots of the magnetic energy density distributions for an incident angle θ=1° are shown in Figs. 4.6d and 4.6f (indicated by solid circles on the transmission plots in Fig. 4.6a and 4.6b). The magnetic energy density of the incident beam is chosen to be 1. For obliquely incident beams the symmetry between the TE and TM waves is broken, and this results in various modes in the nano-posts being excited with different amplitudes for the two polarizations. This in turn results in dissimilar behavior for the TE and TM polarizations as a function of the incident angle. Comparing Figs. 4.6c and 4.6d, we can observe that the magnetic energy density inside the nano-posts is very similar for TE wave with

different incident angles. From Figs. 4.6e and 4.6f, however, we can see that the magnetic energy density distribution changes significantly with incident angle for TM wave. This change in excited modes of the nano-posts for the TM waves as a function of angle, which is a consequence of the axial component of the electric field becoming important, results in the stronger angular dependence of the TM transmission observed here.

High fidelity of the nano-post transfer process

To preserve the high efficiency and the diffraction limited optical performance of the metasurfaces through the transfer process to the PDMS substrate, it is essential that a large majority of the nano-posts are transferred, and the gaps between the nano-posts are uniformly filled with PDMS. The efficiency of the metasurface decreases and wavefront aberrations are introduced if some of the nano-posts are not transferred because the portion of the light passing through the areas with missing nano-posts does not undergo the proper phase shift. Air voids between the nano-posts also degrade the efficiency and cause wavefront aberrations by disturbing the near-field optical distributions of the nano-posts which in turn leads to a lower local transmission efficiency and an incorrect phase shift. To verify that all the nano-posts are transferred to the flexible substrate, after the transfer process, the metasurfaces were examined using an optical microscope. We observed that all the nano-posts were successfully transferred as it is shown in Fig. 4.7a, which shows an optical microscope image of a portion of a flexible metasurface. The void-free filling of the gaps between the nano-posts with PDMS was verified using scanning electron microscope (SEM). A thin layer of gold (~15 nm) was deposited on the top surface of the flexible metasurface to avoid charge accumulation during SEM imaging. An SEM image of the metasurface taken at a tilt angle of 30 degrees with respect to the metasurface normal is shown in Fig. 4.7b. The cracks seen in this SEM image at the location of the nano-posts are in the gold layer. They did not initially exist and were slowly appeared as the imaged area was exposed to the electron beam and the sample was charged. As Fig. 4.7b shows, no void is present between the nano-posts, and the same conclusion was made when a larger area of the metasurface was inspected with SEM. According to all different SEM images, the yield of the entire fabrication process is more than 99.5% with a 95% confidence interval [240].

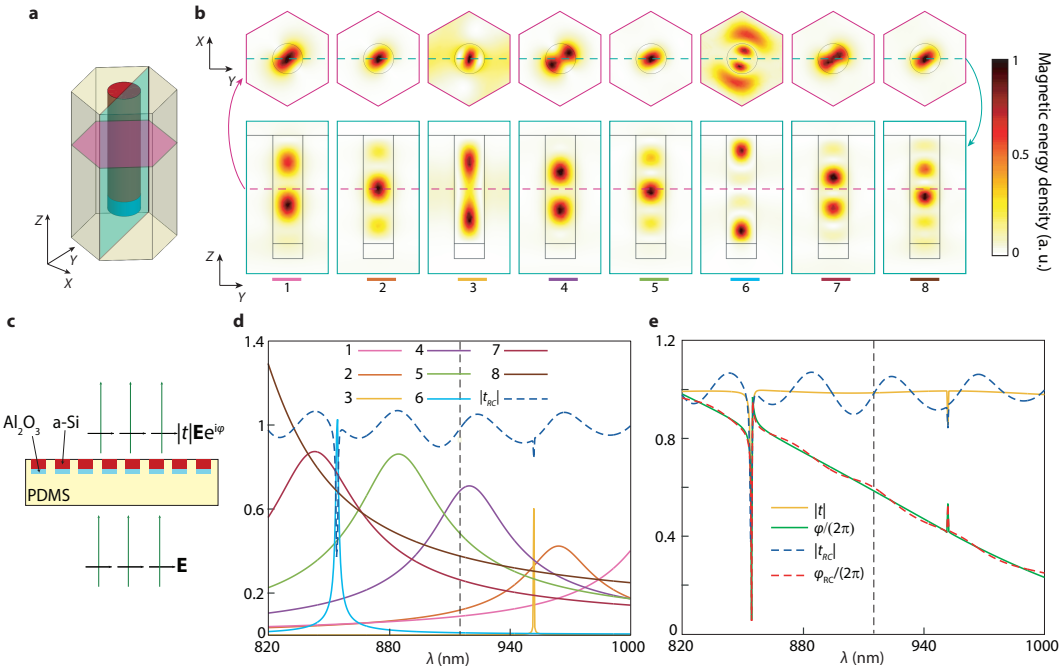

Figure 4.5: **Resonant modes of the nano-posts and their contribution to transmission.** **(a)** Schematic illustration of the metasurface unit cell. **(b)** Magnetic energy density distribution of 8 dominant resonant modes in the bandwidth from 820 nm to 1000 nm, at horizontal (top) and vertical (bottom) cross sections shown in **a**. **(c)** Schematic illustration of a uniform array of nano-posts illuminated with a normally incident plane wave. The amplitude of the transmission coefficient ($|t|$) and its phase (φ) are indicated in the illustration. **(d)** Weighted resonance curves demonstrating contribution of 8 dominant resonant modes to the transmission of a periodic array of nano-posts with diameter of 200 nm, as well as the reconstructed transmission amplitude from these 8 modes. **(e)** Transmission amplitude and phase of the periodic array of nano-posts, and reconstructed transmission amplitude and phase using the 8 dominant resonant modes. $|t_{\mathrm{RC}}|$: reconstructed transmission amplitude, φ_{RC}: reconstructed transmission phase.

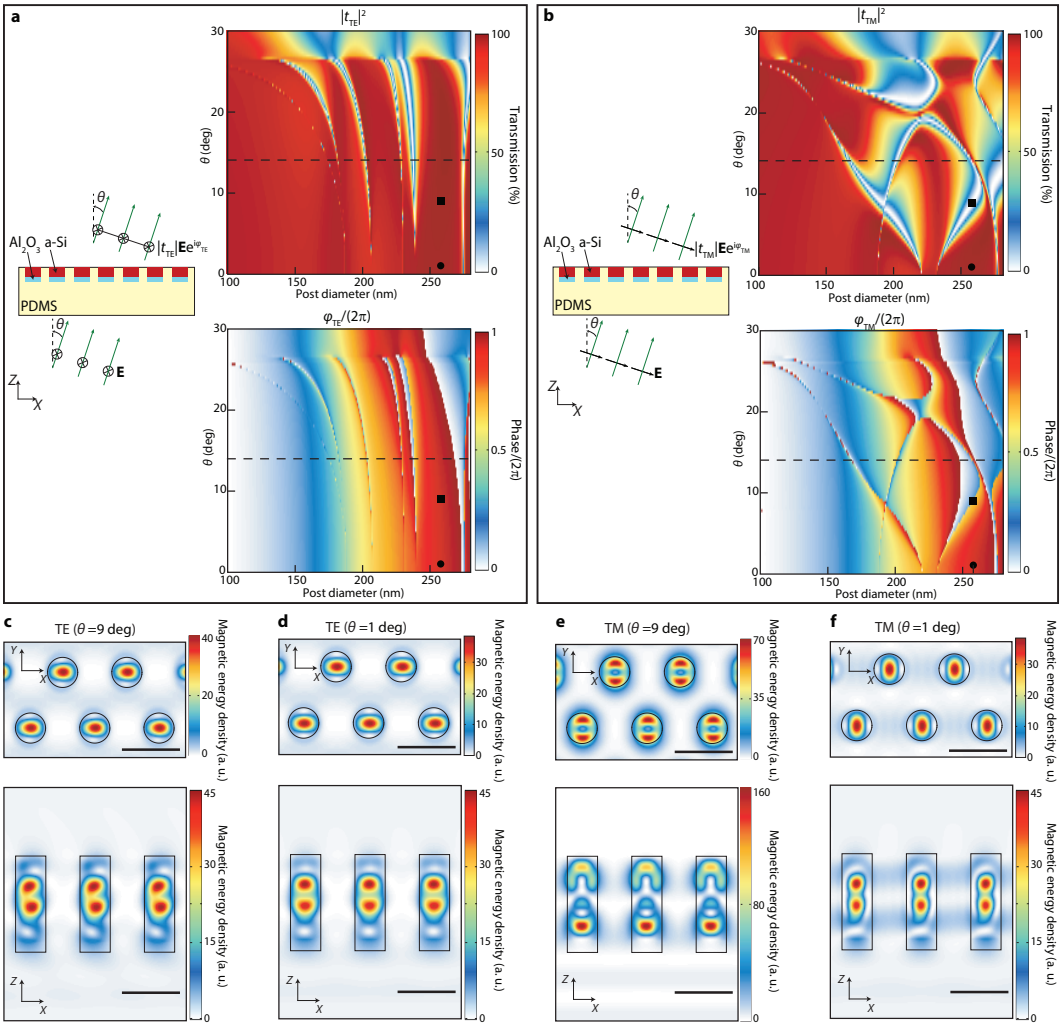

Figure 4.6: **Angular dependence of the transmission coefficient.** **(a)** Schematic illustration of a uniform array of nano-posts embedded in PDMS illuminated by an obliquely incident plane wave (left), and its simulated transmission amplitude and phase as a function of nano-post diameter and incident beam angle for TE and TM (**b**) polarizations. Black dashed lines indicate the largest angle between the metasurface normal and the incident beam used in this manuscript. **(c)** Top and side views of magnetic energy density distribution for TE polarization under an oblique incident plane wave with θ=9°(solid squares in **a**) and **(d)** θ=1°(solid circles in **a**). **(e)** Top and side views of magnetic energy density distribution for TM polarization under an incident plane wave with θ=9° (solid squares in **b**) and **(f)** θ=1° (solid circles in **b**). Black solid lines show the boundaries of the nano-posts. The magnetic energy density of the incident plane wave is chosen to be 1. Scale bars, 500 nm. TE: transverse electric, TM: transverse magnetic.

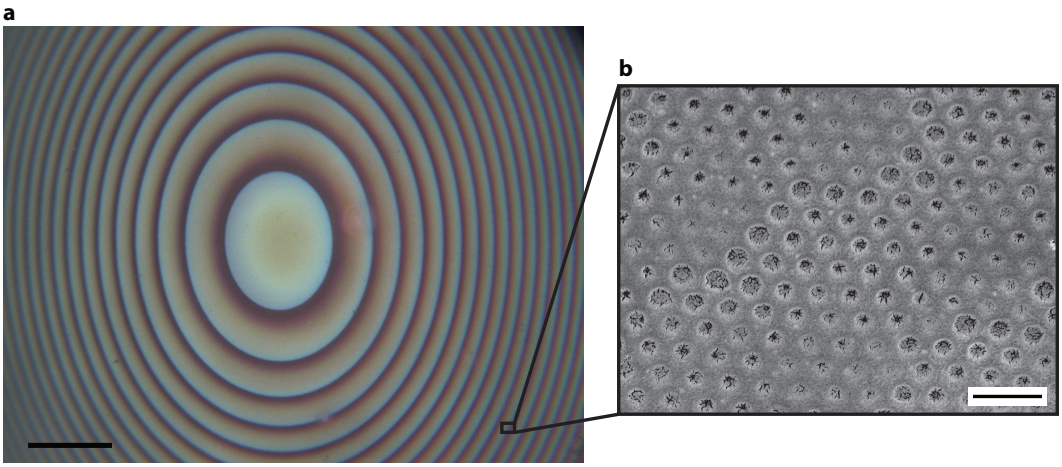

Figure 4.7: **Complete embedding of amorphous silicon nano-posts in PDMS. (a)** Optical microscope image of a portion of a fabricated conformal metasurface lens after transferring to a flexible substrate. This image shows that almost all of the nano-posts are retained in the transfer process. Scale bar, 100 μm. **(b)** SEM image of a portion of the flexible metasurface, taken at a tilt angle of 30 degrees. The image shows silicon nano-posts are entirely embedded in the flexible substrate PDMS), and void-free filling of the gaps between the nano-posts with PDMS. To dissipate charge accumulation during scanning electron imaging, a ~15-nm-thick gold layer was deposited on the sample prior to imaging. The cracks seen in the gold layer at the position of the nano-posts were not present initially and were gradually formed as the sample was exposed to the electron beam. Scale bar, 1 μm.

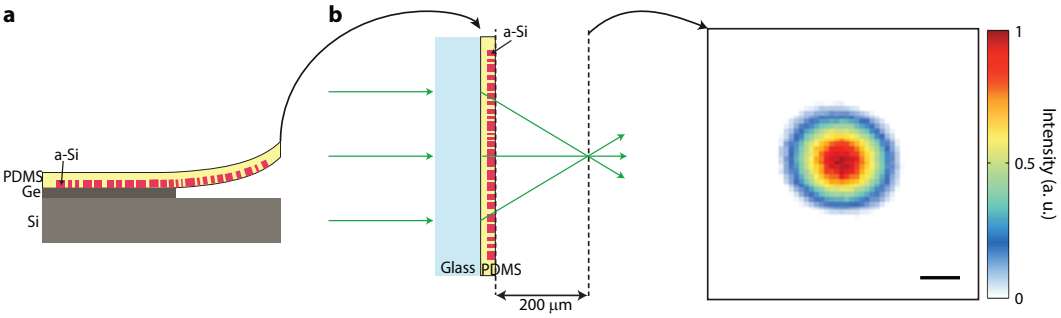

Figure 4.8: **Preservation of high efficiency and diffraction limited optical performance of the metasurfaces through the transfer process. (a)** A metasurface lens designed to operate as an aspherical lens when mounted on a flat substrate is transferred to a PDMS substrate. The metasurface lens has a diameter of 200 μm and a focal distance of 200 μm. **(b)** Measured focal plane intensity profile when the flexible metasurface is mounted on a flat glass substrate and illuminated with a collimated beam (as shown in the inset). The measured FWHM spot size of ~ 1 μm agrees well with the diffraction limited FWHM spot size of 1 μm. The focusing efficiency of the lens was measured as 70%. The diffraction limited spot size and the relatively high focusing efficiency verifies the fidelity of the fabrication process in preserving optical properties of metasurfaces. Measurements are performed at the wavelength of 915 nm (see section 4.7 for measurement details). Scale bar, 1 μm.

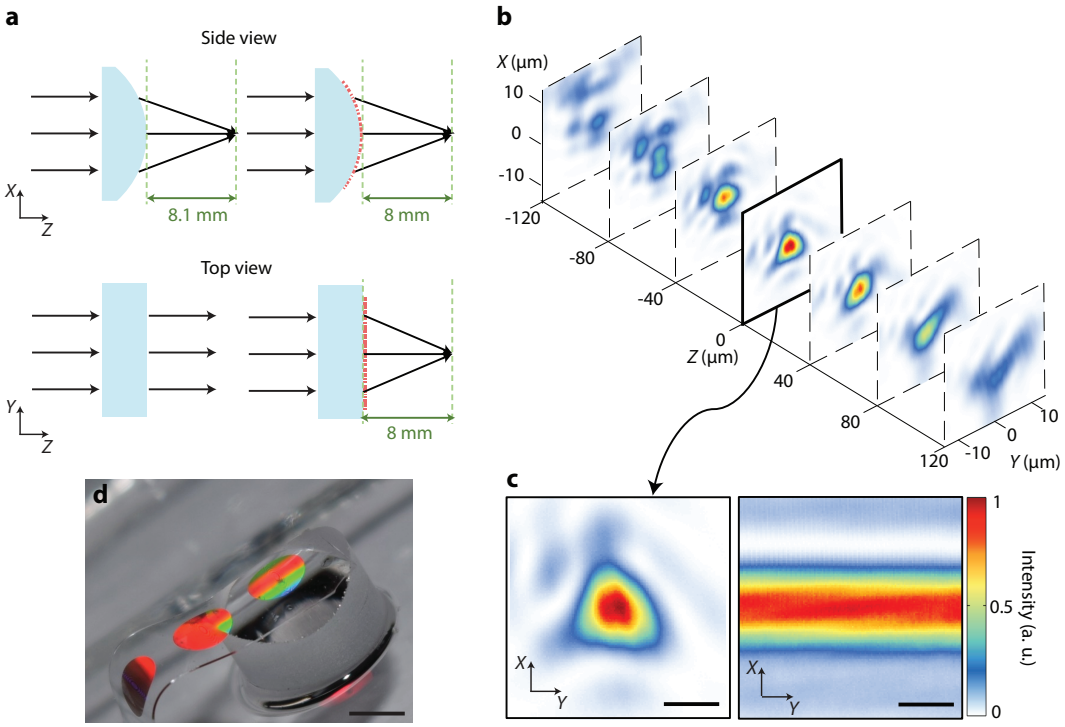

Figure 4.9: **Conformal metasurface with steep incident angles. (a)** Schematic illustration of a metasurface which converts a cylindrical lens to an aspheric lens. The metasurface diameter is 2 mm, and the largest angle between the metasurface normal and the incident beam is 14°. **(b)** Intensities measured at different planes parallel to the focal plane of the cylinder metasurface combination. **(c)** Measured intensities for the glass cylinder (right) and cylinder plus metasurface combination (left) at their respective focal planes. The measured FWHM spot size at the focal plane is approximately 4.5 μm, which is comparable to the diffraction limited FWHM spot size of 3.7 μm. For the metasurface cylinder combination, by using a setup shown in Fig. 4.11b, focusing efficiencies of 68% and 64% were measured for TE and TM polarizations, respectively. All the measurements are performed at the wavelength of 915 nm. Scale bars, 5 μm. **(d)** Optical image of the fabricated metasurface mounted on the glass cylinder. Scale bar, 2 mm.

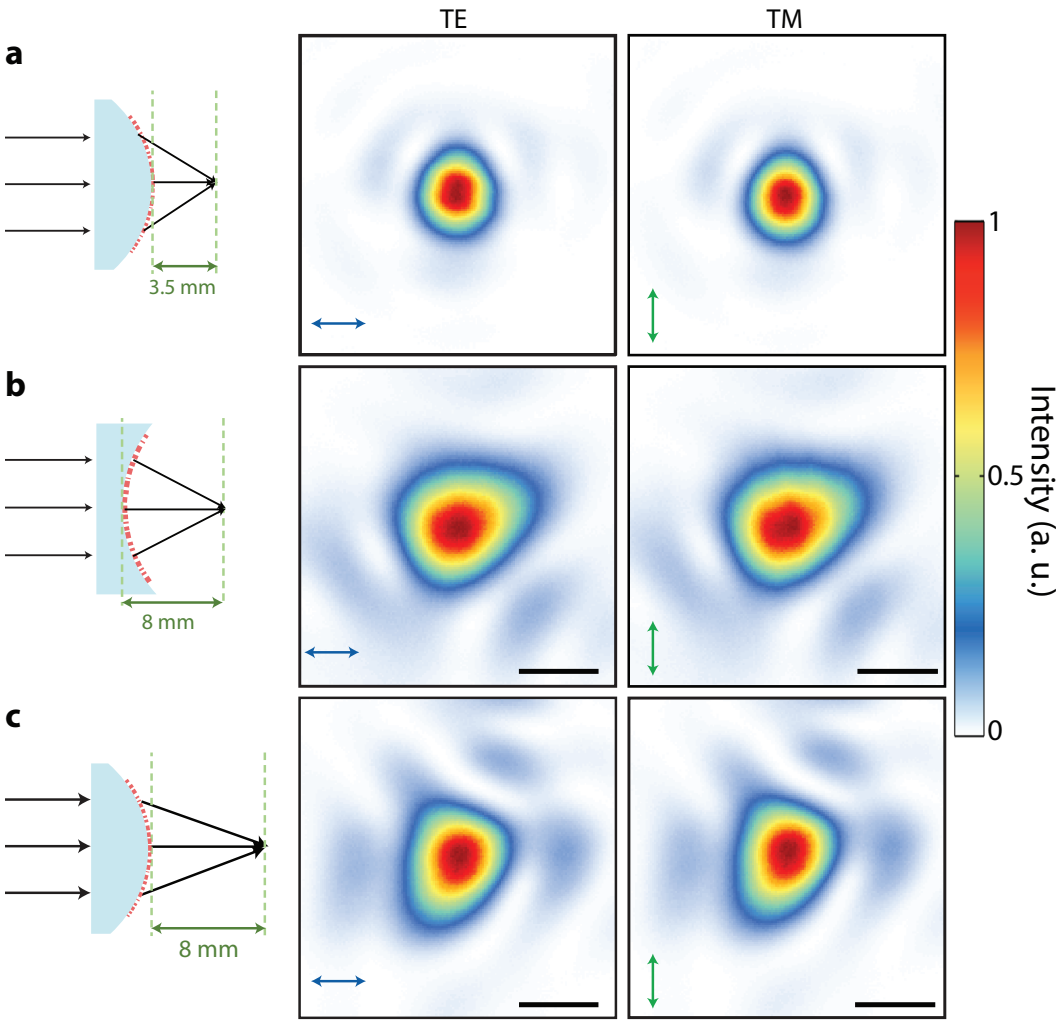

Figure 4.10: **Effect of the input beam polarization on device performance.** Intensity pattern measured at the focal plane of three different conformal metasurfaces with TE (left) and TM (right) polarizations. **(a)** A 1 mm-diameter metasurface on a convex cylinder with a 3.5 mm focal distance, **(b)** A 2-mm-diameter metasurface on a concave cylinder with an 8 mm focal distance, and **(c)** A 2-mm-diameter metasurface on a convex cylinder with an 8 mm focal distance. Focus pattern shows very negligible polarization dependence for all of the devices. The measured efficiencies, however, are more sensitive to polarization. The 1-mm-diameter metasurface with a maximum beam incident angle of 7° has an efficiency of 56% for both polarizations, while for the 2-mm-diameter metasurface lens on convex cylinder with maximum incident angle of 14° the efficiency drops from 68% for TE polarization to 64% for TM polarization. Besides, the metasurface lens on the concave cylinder with a maximum beam incident angle of 9° has efficiencies of 52% and 50% for TE and TM polarizations, respectively. This is in accordance with the angular dependence of transmission coefficient as shown in Fig. 4.6. The device efficiency for TM polarization degrades as the angle between metasurface normal and incident beam increases. However, this does not considerably affect the focus shape for any of the devices. Scale bars, 5 μm. TE: transverse electric, TM: transverse magnetic.

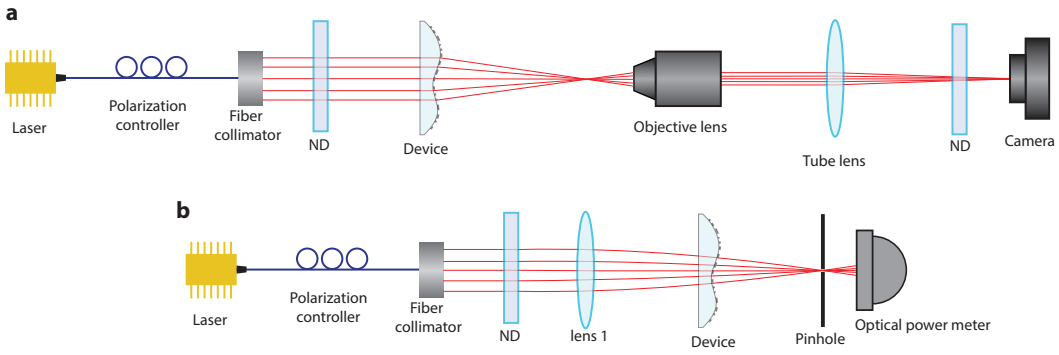

Figure 4.11: **Measurement setup**. **(a)** Schematic illustration of the measurement setup used for characterization of the conformal metasurfaces. ND: neutral density filter. **(b)** Schematic diagram of the experimental setup used for measuring the efficiencies of conformal metasurfaces.

Chapter 5

TUNABLE ELASTIC DIELECTRIC METASURFACES

The material in this chapter was in part presented in

S. M. Kamali, E. Arbabi, A. Arbabi, Y. Horie, and A. Faraon, "Highly tunable elastic dielectric metasurface lenses", Laser Photon. Rev. **10**, 1062–1062 (2016) DOI: 10.1002/lpor.201600144,

In this chapter, we report highly tunable dielectric metasurface platform based on subwavelength thick silicon nano-posts encapsulated in a thin transparent elastic polymer. As a proof of concept, we demonstrate a metasurface microlens operating at 915 nm, with focal distance tuning from 600 μm to 1400 μm (over 952 diopters change in optical power) through radial strain, while maintaining a diffraction limited focus and a focusing efficiency above 50%. The demonstrated tunable metasurface concept is highly versatile for developing ultra-slim, multi-functional, and tunable optical devices with widespread applications ranging from consumer electronics to medical devices and optical communications.

5.1 Motivation

The two dimensional nature and the subwavelength thickness of metasurfaces make them suitable for tunable and reconfigurable optical elements. Recent examples include frequency response tuning using substrate deformation [241, 242], refractive index tuning via thermo-optic effects [243, 244], phase change materials [245, 246], and electrically driven carrier accumulation [247, 248].

Stretchable substrates have also been used to demonstrate tunable diffractive and plasmonic metasurface components [249–252], but they suffer from limited efficiency and polarization dependent operation [252]. In this chapter, we present mechanically tunable dielectric metasurfaces based on elastic substrates, simultaneously enabling a large tuning range, polarization independent operation, and high transmission. As a proof of principle, we experimentally demonstrate a microlens with over 130% focal distance tuning (from 600 μm to 1400 μm) while keeping high efficiency and diffraction limited focusing.

5.2 Theory of Tunable Elastic Metasurface Lenses

Figure 5.1a shows a schematic of a metasurface microlens encapsulated in an elastic substrate with radius r and focal distance f. The paraxial phase profile of the lens has the following form [253], and is drawn in Fig. 5.1c (solid blue curve):

$$\phi(\rho, \lambda) \approx \frac{\pi\rho^2}{\lambda f}, \tag{5.1}$$

where ρ is the distance to the center of the lens and λ is the working wavelength.

Uniformly stretching the substrate with a stretch ratio of $1 + \epsilon$, and assuming that the local phase transformation does not depend on the substrate deformation, the phase initially applied at radius ρ is now applied at radius $\rho(1 + \epsilon)$; therefore, the under strain phase profile becomes $\phi'(\rho, \lambda) = \pi\rho^2/(\lambda(1 + \epsilon)^2 f)$ (shown in Fig. 5.1c, solid red curve). This indicates that stretching the elastic metasurface microlens with stretching ratio of $1 + \epsilon$ scales its focal length by a factor of $(1 + \epsilon)^2$, as shown schematically in Fig. 5.1b.

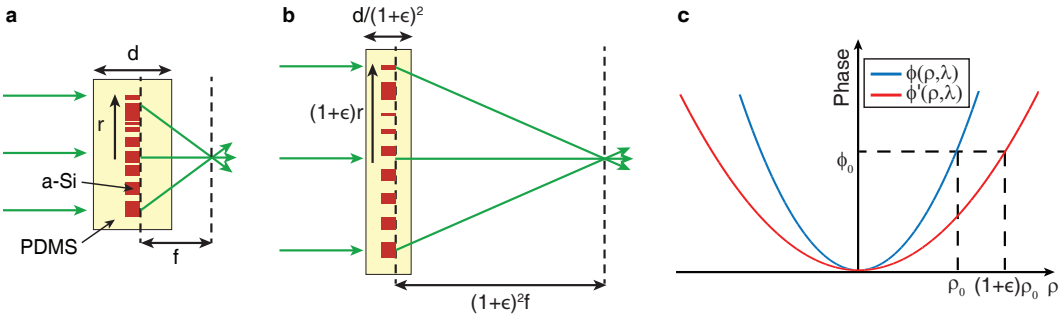

Figure 5.1: **Principle of tunable elastic metasurface lenses.** **a**, A side view schematic illustration of a dielectric metasurface microlens with focal distance of f encapsulated in a low index elastic membrane. **b**, By stretching the metasurface microlens with a stretch ratio of $1 + \epsilon$, its focal distance changes by $(1 + \epsilon)^2$, providing a large tunability. The membrane thickness decreases according to its Poisson ratio (ν), considered to be 0.5 here. **c**, Phase of the metasurface microlens before (solid blue curve) and after (solid red curve) stretching. α-Si: amorphous silicon, PDMS: Polydimethylsiloxane.

For implementation, we used a metasurface platform based on HCA with meta-atoms placed on a subwavelength periodic lattice in a low index medium. The building blocks of the metasurface are α-Si square cross-section nano-posts on a thin layer of Al_2O_3 encapsulated in PDMS as a low index elastic membrane (Fig. 5.2a, inset).

A key characteristic of this platform differentiating it from Huygens' metasurfaces [34, 60, 125, 242], is the weak optical coupling between the nano-posts, which simplifies the metasurface design by allowing local sampling of the phase profile using different widths for the nano-posts placed on the vertices of a square lattice. This weak coupling is due to the high index contrast between the nano-posts and their surrounding medium, and is manifested in the high localization of energy density inside the nano-posts [66, 124]. An important consequence of the weak coupling is that the phase transformation mainly depends on the nano-posts width and not on the distance between them, leading to the same local phase shift almost independent of the stretch factors of the substrate. Figures 5.2c and 5.2d show the simulated transmittance and phase of the transmission coefficient for a periodic square lattice of encapsulated nano-posts in PDMS with strain values from 0% to 50%. The nano-posts are assumed to be 690 nm tall, and the lattice constant at 0% strain is 380 nm. Nano-posts height must be chosen such that the whole 0 to 2π phase range is covered at all strains of interest by changing the nano-posts width, while keeping high transmission values. The lattice constant should be selected such that the lattice is subwavelength and satisfies the Nyquist sampling criterion simultaneously for all strain values (see Sec. 6.7 and Fig. 5.5). The simulation results are obtained assuming normal incidence at the wavelength of 915 nm. The weak dependence of the transmission of the nano-post array on different strain values, which can be seen in Figs. 5.2c and 5.2d, is another evidence for the weak coupling between the nano-posts.

Since the transmission coefficient is almost independent of the strain, we can design the metasurface at one specific strain. Figure 5.2b shows the intensity and phase of the transmission coefficient at the middle strain value ($\epsilon = 25\%$) as a function of the nano-post width, that is used for designing the tunable metasurface. Considering the desired phase profile $\phi(\rho)$ at 25%, the corresponding nano-post width at each lattice site was found by minimizing the transmission error $\Delta T = |e^{i\phi} - |t|e^{i\angle t}|$, where t is the complex transmission coefficient. An aspheric phase profile is assumed as the desired phase profile. Minimizing ΔT at each lattice site results in selecting the nano-post with the closest complex transmission value to the desired one ($e^{i\phi}$) and automatically excludes the two high quality factor resonances observed in Fig. 5.2b around 171 nm and 214 nm nano-post widths. The nano-posts can be considered as truncated square cross-section waveguides with multiple low quality factor Fabry-Perot resonant modes. These multiple resonances are excited and contribute to the scattered field with various strengths [124]. In addition, the high quality factor

resonances observed in Fig. 5.2b are formed because of the extended lattice modes of the periodic arrangement of the nano-posts. Total transmission of the nano-posts array is determined by the superposition of the scattered fields of these resonant modes and the incident light, which results in high transmittance and a full 2π range for the phase shift of the transmission coefficient [124].

Using the proposed platform, a tunable metasurface microlens is designed to operate at the wavelength of 915 nm. The microlens has a diameter of 200 μm under no strain, and its focal distance changes from 600 μm to more than 1400 μm (optical power from 1667 to 714 diopters) when the strain value varies from 0% to 53%.

5.3 Design Procedure of Tunable Metasurface Lenses

To find the transmittance and phase values (Fig. 5.2b-d), a periodic array of square nano-posts on a square lattice was simulated at 915 nm with a normally incident plane wave using RCWA [148]. Refractive indices of 3.56 and 1.41 were used for α-Si and PDMS. The lattice constant was chosen to be 380 nm at 0% strain and linearly scaled with the stretch ratio. It was chosen such that the array remains non-diffractive with enough sampling unit cells for reconstructing the wavefront at all the strain values of interest (see Sec. 6.7 for the details). The metasurface microlens was designed for the middle strain (25% strain), for which the lattice constant is 475 nm. The lattice constant was then scaled down to 380 nm for device fabrication.

The intensity distributions shown in Figs. 5.6 and 5.7 were found by modeling the microlens as a phase mask. The transmission coefficient of the phase mask was calculated through interpolation of the complex transmission coefficients of the nano-posts. The effect of the strain was considered in both the position and the transmission coefficient of the nano-posts. A plane wave was used to illuminate the phase mask. The fields after the phase mask were propagated through the top PDMS layer (~50 μm thick at zero strain) and air to the focal plane and beyond using plane wave expansion technique. For efficiency calculations, a Gaussian beam with more than 99% of its power inside the device was used. The Gaussian beam radius was linearly scaled with the stretch ratio. Intensity profiles in the focal plane for different strain values were found using the same plane wave expansion technique. The focusing efficiencies were calculated by dividing the power passing through a disk around the focal point to the total incident power. The diameter of the disk for each strain value was set to be ~3 times the analytical FWHM. In order to verify the accuracy of the described simulation method, a four times smaller version of

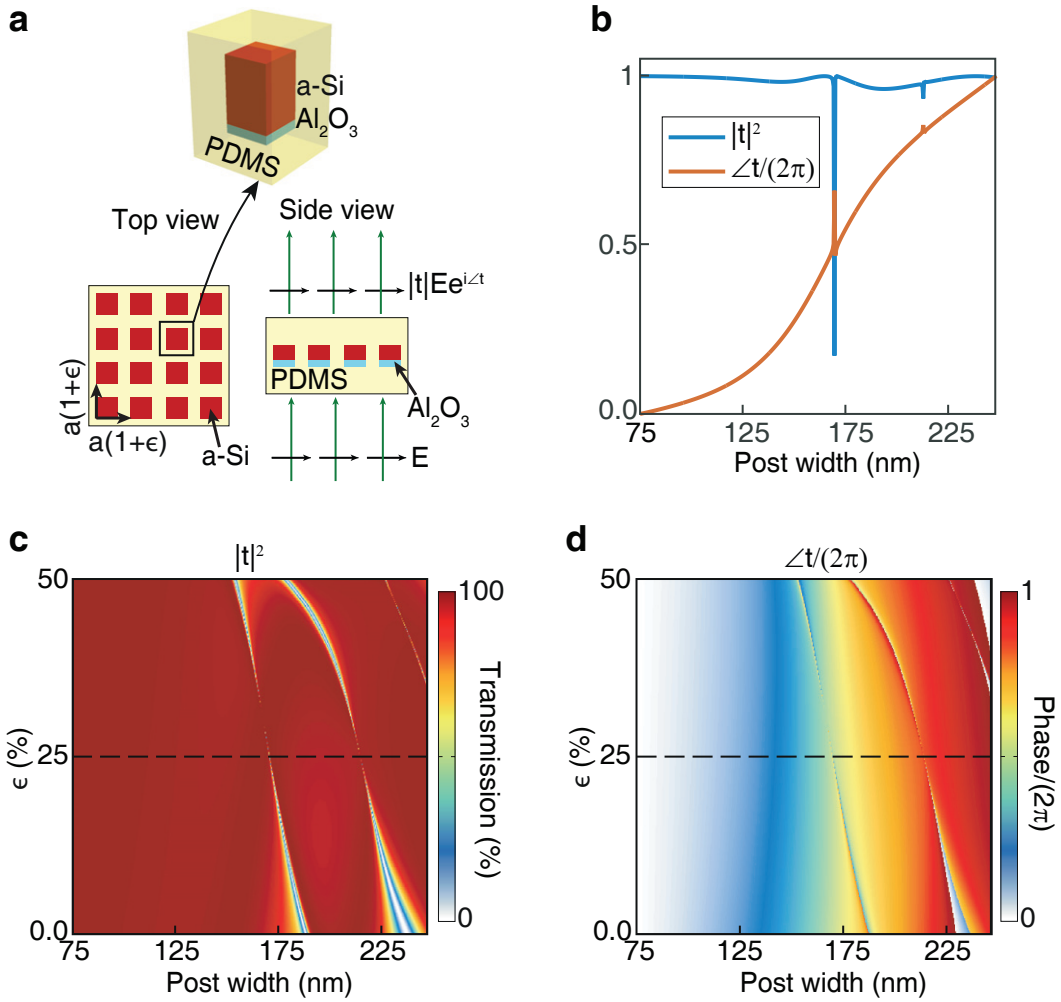

Figure 5.2: **Design procedure of tunable metasurfaces. a**, Schematic drawing of the top and side views of a uniform array of square cross-section nano-posts arranged in a square lattice and encapsulated in PDMS. The inset shows the building block of the array: an α-Si nano-post on a thin layer of Al_2O_3. **b**, Simulated intensity and phase of the transmission coefficient for $\epsilon = 25\%$ (corresponding to the dashed lines shown in **c** and **d**) used to map the transmission values to the nano-post widths.**c**, Simulated intensity and **d**, phase of the transmission coefficient for the array shown in **a**, as a function of the nano-post width and the substrate strain. The nano-posts are 690 nm tall, Al_2O_3 layer is ~100 nm thick, and the simulation wavelength is 915 nm. α-Si: amorphous silicon, PDMS: Polydimethylsiloxane.

the actual device (50 μm diameter, 150 μm focal distance in relaxed state) with the same NA was simulated at different strain values (0% to 50% with 10% steps) using the 3D finite difference time domain method [254]. Intensity distributions and the focusing efficiencies were in good agreement with the described simulation method based on the plane wave expansion technique.

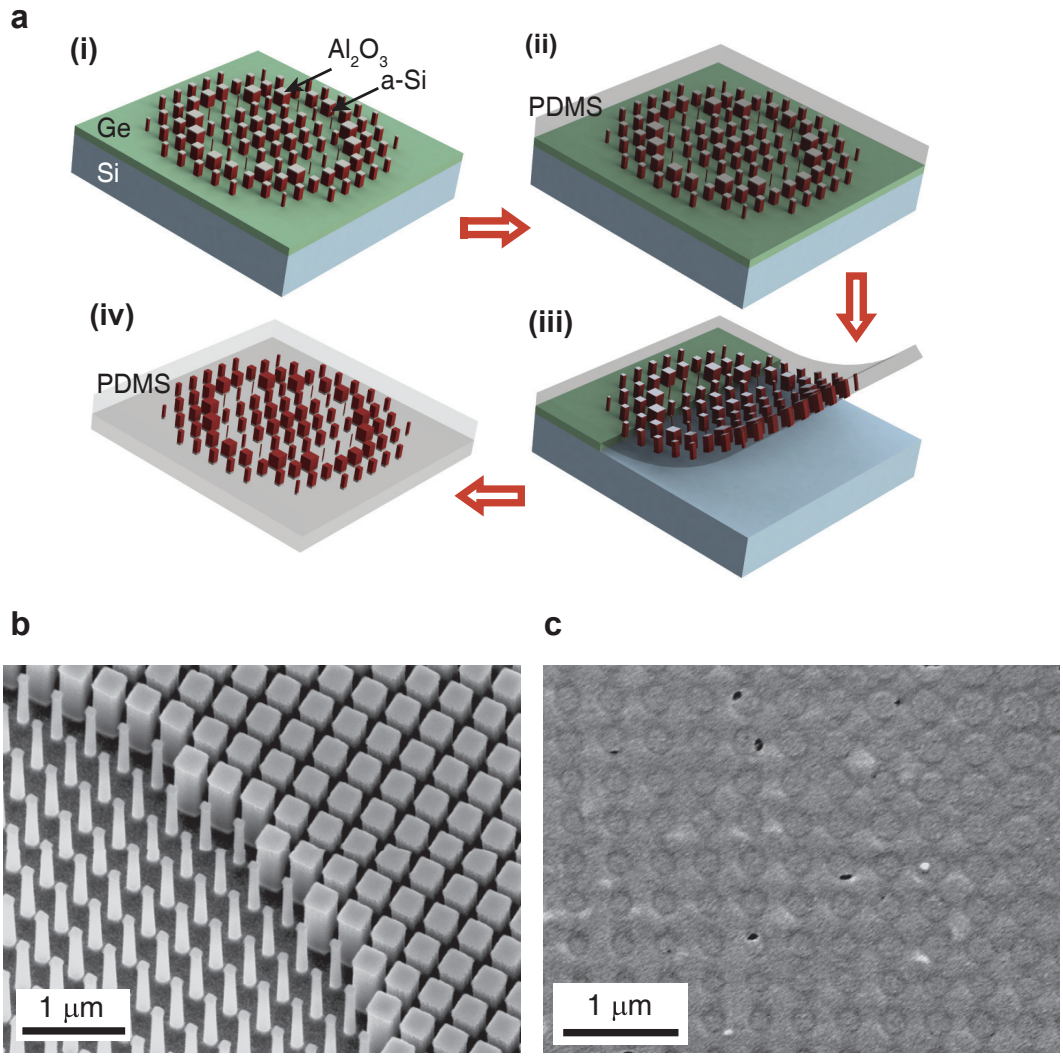

Figure 5.3: **Overview of the fabrication steps and images of the device at different steps. a**, Major steps involved in fabricating tunable metasurfaces: (i) α-Si nano-posts are patterned and dry etched using an Al_2O_3 hard mask. The nano-posts rest on a Ge sacrificial layer on a silicon wafer. (ii) PDMS is spin coated on the metasurface structure. (iii) The sacrificial Ge layer is dissolved to release the nano-posts which are now embedded in the flexible and stretchable PDMS layer. (iv) A second PDMS layer is spin coated on the side containing the metasurface to provide a fully encapsulated microlens. **b**, Scanning electron micrograph of the nano-posts before spin coating the first PDMS layer (step (i)). **c**, Scanning electron micrograph of the nano-posts embedded in PDMS (step (iii)), taken at a tilt angle of 30 degrees. To dissipate the electric charge accumulated during scanning electron microscopy, a ~20-nm-thick gold layer was deposited on the sample prior to imaging. Small holes observed around the nano-posts are in the deposited gold layer. α-Si: amorphous silicon, PDMS: Polydimethylsiloxane.

5.4 Fabrication Process of Elastic Metasurfaces

Figure 5.3a schematically illustrates the key steps in fabricating a metasurface encapsulated in a thin elastic membrane. A Ge sacrificial layer (~300 nm) was evaporated on a silicon wafer, followed by a 690-nm-thick hydrogenated PECVD α-Si layer (5% mixture of silane in argon at 200 $^{\circ}C$). The refractive index of the α-Si layer was found to be 3.56 at the wavelength of 915 nm, using variable angle spectroscopic ellipsometry. A Vistec EBPG5000+ e-beam lithography system was used to define the pattern in ZEP-520A positive resist (~300 nm, spin coated at 5000 rpm for 1 min). A resist developer (ZED-N50 from Zeon Chemicals) was used to develop the pattern for 3 minutes. A ~100-nm-thick Al_2O_3 layer was deposited on the sample by e-beam evaporation. The pattern was then transferred into Al_2O_3 by lifting off the resist. The patterned Al_2O_3 hard mask was used for dry etching the α-Si layer in a mixture of SF_6 and C_4F_8 plasma (Fig. 5.3a, (i)). The PDMS (10:1 mixing ratio of Sylgard 184 base and curing agent) was diluted in toluene in a 2:3 weight ratio as a thinner. The diluted PDMS mixture was spin coated (at 3000 rpm for 1 min) on the fabricated metasurface to fill the gaps between the nano-posts and to form a thin PDMS film. The sample was then degassed and cured at 80 $^{\circ}C$ for more than 30 mins. The second layer of PDMS without a thinner (~50 μm, spin coated at 1000 rpm for 1 min) was likewise degassed and cured at 80 $^{\circ}C$ for more than 1 hr (Fig. 5.3a, (ii)). The sample was then immersed in a 1:1:30 mixture of ammonium hydroxide, hydrogen peroxide, and DI water at room temperature to remove the sacrificial Ge layer and release the embedded nano-posts in the PDMS substrate (Fig. 5.3a, (iii)). Another layer of PDMS without a thinner was then spin coated on the microlens side of the sample (at 1000 rpm for 1 min) to fully encapsulate the nano-posts in PDMS (Fig. 5.3a, (iv)). The sample was again degassed and cured at 80 $^{\circ}C$ for more than 1 hr. The total PDMS thickness was ~100 μm. Encapsulation of nano-posts in PDMS is a crucial step in preserving the metasurface shape and minimizing defects when the device is highly strained (see Fig. 5.8 in Sec. 6.7). A scanning electron micrograph of the nano-posts on Ge layer before spin coating the first PDMS layer is shown in Fig. 5.3b. The nano-post transfer process has a near unity yield in retaining almost all the nano-posts at their positions [124]. Void-free filling of the gaps between the nano-posts was confirmed by inspecting nano-posts embedded in PDMS before spin coating the PDMS cladding (Fig. 5.3c). To compensate for systematic fabrication errors, an array of devices with all the nano-post widths biased uniformly in steps of 3 nm was fabricated (Fig. 5.4b).

5.5 Measurement Procedure of Tunable Metasurfaces

The device was measured using the setup shown schematically in Fig. 5.4a. A 915 nm fiber coupled semiconductor laser was used for illumination and a fiber collimation package (Thorlabs F220APC-780) used to collimate the incident beam. A 50X objective lens (Olympus LMPlanFL N, NA=0.5) and a tube lens (Thorlabs LB1945-B) with a focal distance of 20 cm were used to image intensity at different planes to a camera (CoolSNAP K4 from Photometrics). To adjust the light intensity and decrease the background noise captured by the camera, ND filters (Thorlabs ND filters, B coated) were used. A calibration sample with known feature sizes was also imaged with the setup to find the overall magnification. The sample was first mounted on a glass substrate, for characterization under no strain. The device with highest focusing efficiency (lowest systematic fabrication error) was found under no strain, because the current measurement setup does not enable translational movement of devices under strain. Then, for measurements under strain, it was manually clamped between two machined Teflon rings, such that the microlens of interest with lowest systematic fabrication error was placed near the center of the rings. Then the clamped sample mounted on a translation stage was pushed toward a machined Teflon tube, such that the microlens of interest was stretched radially. To measure the focusing efficiencies under a specific strain, an additional lens with a focal length of 10 cm (Thorlabs LB1676-B) was used to partially focus the collimated beam. The beam radius was changed by adjusting the relative distance between the lens and the device under the test, such that more than 99% of the beam power falls inside the device under the test. A pinhole with a diameter ~3 times the measured FWHM was placed in the focal plane of the microlens to only let the light inside the pinhole pass through. This value is chosen because assuming a Gaussian beam profile, more than 99% of the beam power falls inside a pinhole with a diameter ~3 times the FWHM. The pinhole was fabricated by evaporating a thick layer of chrome on a fused silica substrate, and defining holes in it by wet etching. A power meter (Thorlabs PM100D) with a photodetector (Thorlabs S122C) was used to measure efficiencies at 915 nm. The focusing efficiency was calculated as the ratio of the power in focus (measured optical power after the pinhole) to the incident power (measured power before the sample). The focusing efficiency at 15% strain was measured in this manner. Focusing efficiencies at other strains were calculated relative to the focusing efficiency at 15% strain in the following manner: first, light intensity captured with the camera in the plane of focus was integrated

inside a circle with a diameter ~3 times of the measured FWHM at each strain value including the 15% strain. Then, the integrated power for each strain was divided by the integrated power at 15% strain. Moreover, the ratio of the input power at 15% strain to the input power at other strains was calculated (the input power of the beam hitting the device increases as the device area increases). The focusing efficiency at other strains was then found by multiplying these two normalization factors by the directly measured efficiency at 15% strain. The measurement setup used for the efficiency characterization is shown in Fig. 5.9.

5.6 Characterization of Tunable Elastic Metasurfaces

For characterization of the fabricated tunable metasurface microlens, a custom built microscope was used to image the transmitted light intensity at different distances from the metasurface (Fig. 5.4a). First, the sample was mounted on a flat glass substrate and characterized in the relaxed mode, and then it was clamped between two Teflon rings. A radial force was applied by pushing another Teflon tube from the backside and stretching the metasurface (see Fig. 5.10). An array of microlenses mounted between the rings and under ~30% strain is shown in Fig. 5.4b. Measured optical intensities in the axial plane (Fig. 5.4c, left) and the focal plane (Fig. 5.4c, right) at 6 different strain values (0% to 50%) show a large focal distance tunability while keeping a nearly diffraction limited focus at all strains. For comparison, and to investigate the effect of the weak dependence of the transmission coefficients on the lattice size, the performance of the metasurface at different strains is simulated in two different cases. First, we use the actual intensity and phase of the transmission coefficients shown in Figs. 5.2c and 5.2d, which take into account the effect of lattice constant changing with strain (see Fig. 5.6 for results). Second, neglecting the strain dependence, we use the transmission coefficients calculated at 25% strain (plotted in Fig. 5.2b), for all strain values. Simulated intensity profiles for this case are plotted in Fig. 5.7. In both cases, the simulated intensity profiles and the corresponding focal distances and full width at half maximums (FWHMs) are in good agreement with their measured counterparts. This confirms that the weak dependence on lattice constant does not affect the functionality and the diffraction limited performance of the device. Figure 5.4d shows a good agreement between the measured and the analytically predicted focal distances, which are plotted versus $(1+\epsilon)^2$. Measured FWHM of the focal spots for different strains and their corresponding diffraction limited values are shown in Fig. 5.4e as a function of the NA of the microlens. The

results show nearly diffraction limited operation of the microlens under strain values up to above 50%. As expected, NA decreases and the focal spot enlarges as strain is increased.

Focusing efficiency is defined as the ratio of the optical power focused by the device to the incident power, and is measured and plotted in Fig. 5.4f for various strains. The measured 75% focusing efficiency in the relaxed state, shows the high optical quality of the device. The efficiency decreases gradually with increasing the strain; however, it remains above 50% for strain values up to 50%. To further understand the effect of the weak dependence of the transmission coefficients on the lattice strain, focusing efficiencies are calculated in two different cases considering and neglecting this dependence. In the first case, we have used the actual transmission coefficients for each strain value (plotted in Figs. 5.2c and 5.2d), and in the second case we have used the transmission coefficients calculated at 25% strain (Fig. 5.2b). These two simulated focusing efficiencies are plotted in Fig. 5.4f along with the measured values. It is observed that the small dependence of the transmission coefficients on strain results in a reduction of the focusing efficiency at strains other than the design value. At small strains, the measured focusing efficiencies agree well with their simulated values, but the measured efficiencies are lower at large strain values. We attribute the lower measured efficiency to possible mechanical deformations and misalignments of the nano-posts under strain, and the non-uniformity of the strain across the microlens. In addition, device characterizations were performed on the lens with the highest efficiency at 0% strain among the fabricated set (several lenses with all nano-post widths biased at different values were fabricated in order to compensate for the systematic fabrication errors.). Therefore, the measured focusing efficiencies in the relaxed state and at small strains could be higher than the simulated values for the lens designed for optimal performance at 25% strain. Also, the measured values are lower than the simulated focusing efficiencies obtained using ideal strain-independent transmission coefficients (Fig. 5.4f).

The reliability of the tuning process was tested by measuring the focal spot and focusing efficiency of the tunable metasurface microlens after multiple straining cycles. No changes in the focusing efficiency and focal spot shape of the microlens were observed after more than 10 cycles of stretching and releasing the device (see Fig. 5.11 in Sec. 6.7).

The demonstrated metasurface lenses are transmissive over a broad wavelength range (see Fig. 5.12 for simulated transmittance and reflection spectra). Although they

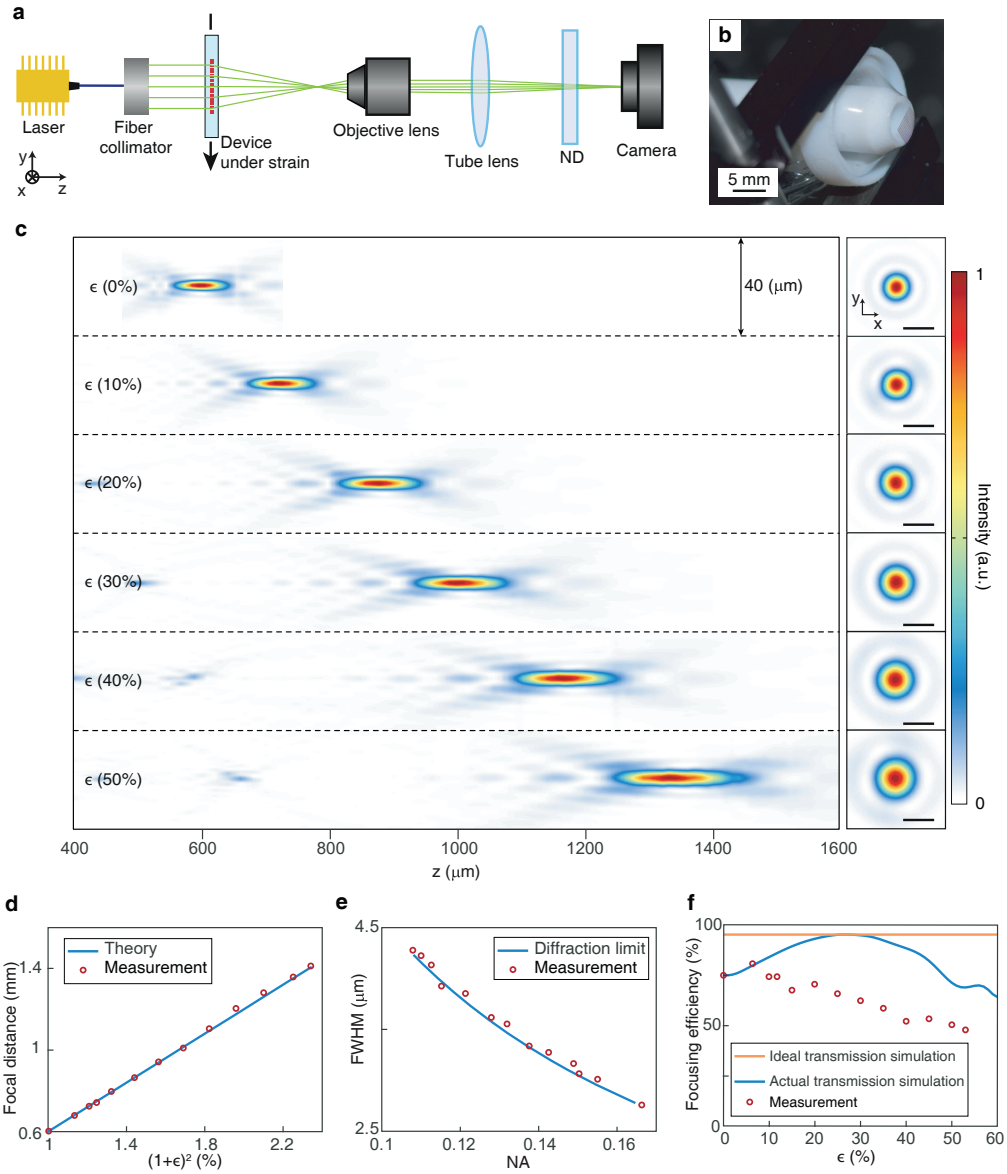

Figure 5.4: **Measurement results.** **a**, Schematic of the measurement setup, ND: neutral density filter. **b**, An array of elastic metasurface microlenses clamped between two Teflon rings, under ~30% strain. **c**, Measured optical intensity profiles of a radially strained metasurface microlens (ϵ = 0% to 50%) in the axial plane (left) and the focal plane (right). Scale bars: 5 μm. **d**, Measured and analytically predicted focal distances (i. e. $(1+\epsilon)^2 f$) for different strain values versus square of the stretch ratio ($(1+\epsilon)^2$). Focal distance is tuned from 600 μm to more than 1400 μm (more than 952 diopters change in optical power). **e**, Measured and diffraction limited FWHM spot size in the focal plane for different strain values as a function of the NA of the microlens. **f**, Measured and the two simulated focusing efficiencies as a function of strain. Measurements and simulations are performed at the wavelength of 915 nm. See Sec. 6.7 for the measurement and simulation details.

suffer from chromatic aberrations similar to the other diffractive meta-lenses on rigid substrates [66, 255], multiwavelength tunable operation can readily be achieved by combining the current platform with the multiwavelength metasurface concept [146, 255–257].

5.7 Summary and Outlook

In conclusion, we demonstrated highly tunable dielectric metasurfaces based on elastic substrates. As proof of concept, a microlens with more than 952 diopters change in optical power was demonstrated. The proposed platform can be applied to other devices based on metasurfaces thus adding tunability over a thin layer without increasing the complexity of the system. For instance, it can be integrated with the recently demonstrated lithographically staked metasurfaces for correcting large angle aberrations [138] to enable ultra-compact wide field adjustable NA tunable objectives. Tunable metasurfaces can also be fabricated on high speed electrically tunable elastomers in order to decrease their response time to less than a millisecond [258]. Moreover, integration of the proposed platform with flexible and wearable electronics [259] can also lead to versatile tunable optoelectronic technologies.

5.8 Appendix

Sampling frequency of the phase profile

The lattice constant should be chosen such that the lattice remains non-diffractive and satisfies the Nyquist sampling criterion. From a signal processing point of view, the locally varying transmission coefficient of a flat microlens can be considered as a spatially band-limited signal with a $2\mathrm{NA}k_0$ bandwidth (ignoring the effect of the edges), where NA is the microlens numerical aperture, and k_0 is the vacuum wavenumber. A hypothetical one dimensional band-limited spectrum is depicted in Fig. 5.5 (solid blue curve). By sampling the microlens phase profile with sampling frequency of K_s, the images (dashed blue curves in Fig. 5.5) are added to the spectrum. Therefore, for the perfect reconstruction of the microlens' transmission coefficient, the Nyquist criterion should be satisfied: $K_s > 2\mathrm{NA}k_0$. On the other hand, the lattice should remain subwavelength; the higher order diffractions (dashed blue curves in Fig. 5.5) should remain non-propagating. Propagation in free space can be considered as a low pass filter with $2nk_0$ bandwidth (solid red curve in Fig. 5.5), where n is the refractive index of the surrounding medium. Therefore, in order to have perfect reconstruction of phase and non-propagating higher order diffractions,

the following relation should be satisfied:

$$K_s > nk_0 + \mathrm{NA}k_0. \tag{5.2}$$

Note that the sampling frequency (K_s) is a reciprocal lattice vector. For the square lattice $K_s = 2\pi/\Lambda$, where Λ is the lattice constant. Therefore Eq. (5.2) would be simplified as follows:

$$\Lambda < \frac{\lambda}{n + \mathrm{NA}}, \tag{5.3}$$

where λ is the free space wavelength. Note that the maximum value of numerical aperture is $\mathrm{NA}_{\mathrm{max}} = n$, which simplifies Eq. (5.3) to $\Lambda < \lambda/(2n)$. For designing tunable microlenses, Eq. (5.3) should be satisfied for all the strains of interest, and $\Lambda = (1 + \epsilon)a$, where a is the unstrained lattice constant. For the parameters used in the main text, the unstrained lattice constant should be smaller than 401 nm in order to have tunable microlens up to 50% strains. The unstrained lattice constant was chosen to be 380 nm.

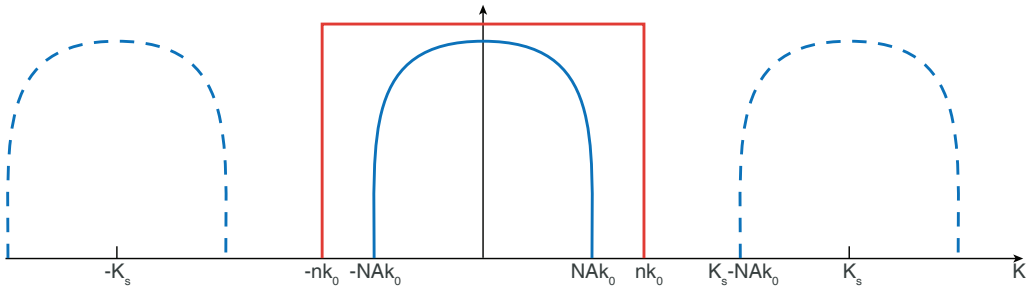

Figure 5.5: **Sampling frequency of the phase profile for perfect reconstruction of the wavefront.** The locally varying transmission coefficient spectrum of a flat microlens can be considered as a band-limited signal with $2\mathrm{NA}k_0$ bandwidth (solid blue curve). By sampling the transmission coefficient with sampling frequency of K_s, displaced copies of the band-limited signal are added to the spectrum (dashed blue curves). In order to avoid undesirable diffractions, the free space low pass filter (solid red curve) should only filter the zeroth order diffraction (solid blue curve).

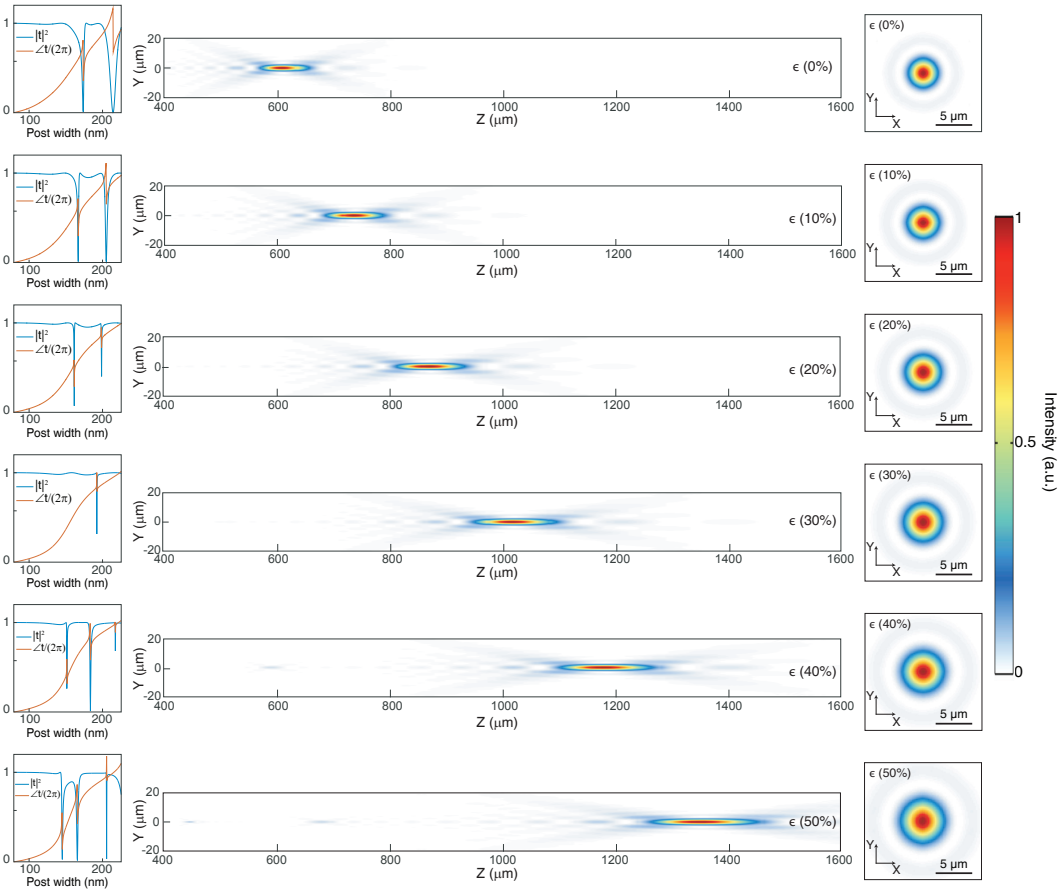

Figure 5.6: **Simulation results of the tunable microlens using the actual nanoposts' transmission coefficients, extracted from Figs. 5.2b and 5.2c.** Intensity profiles of the tunable microlens are simulated at different strains (ϵ = 0% to 50%) using the actual transmission coefficients at each strain value. Intensity and phase of the transmission coefficient at respective strain values are shown in the left, and their corresponding intensity profiles in the axial plane and in the focal plane are shown in the middle and right, respectively.

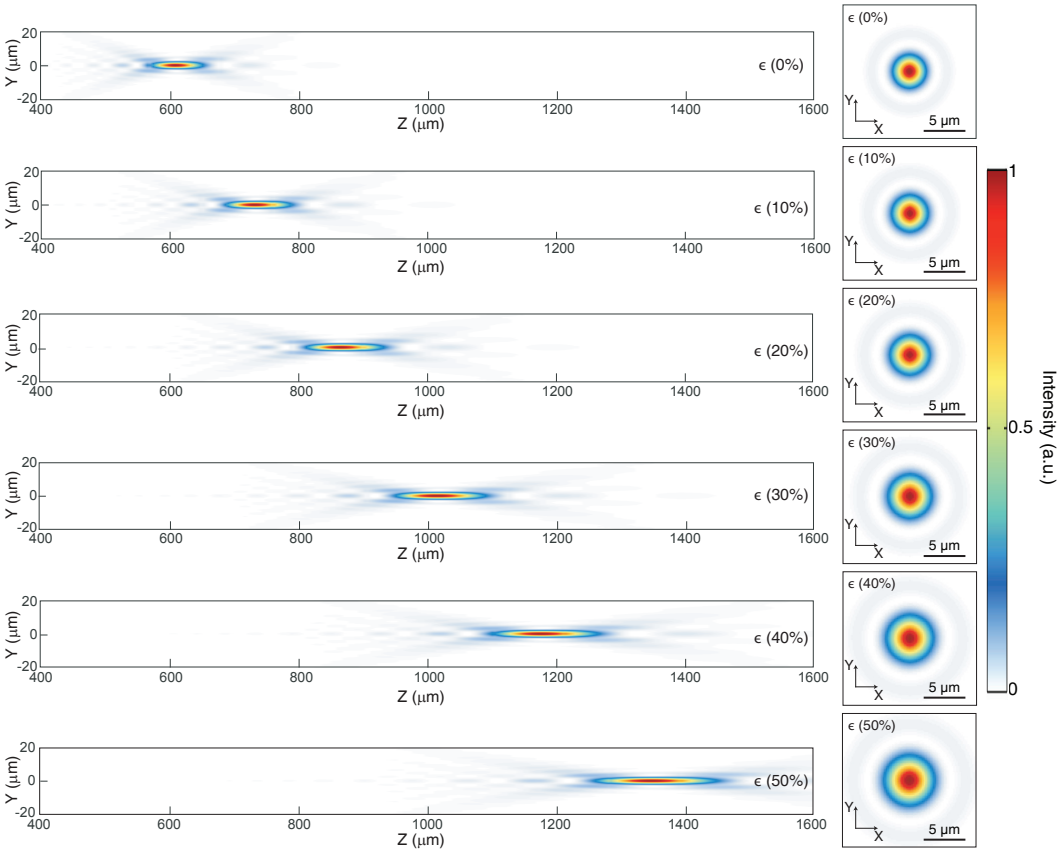

Figure 5.7: **Simulation results of the tunable microlens assuming transmission coefficients that do not change with strain.** We have used the simulated nano-post transmission coefficients at the strain value of 25% (main text, Fig. 2d) for all strains. Simulated intensity profiles for different strains (ϵ = 0% to 50%) are shown in the axial plane (left) and in the focal plane (right).

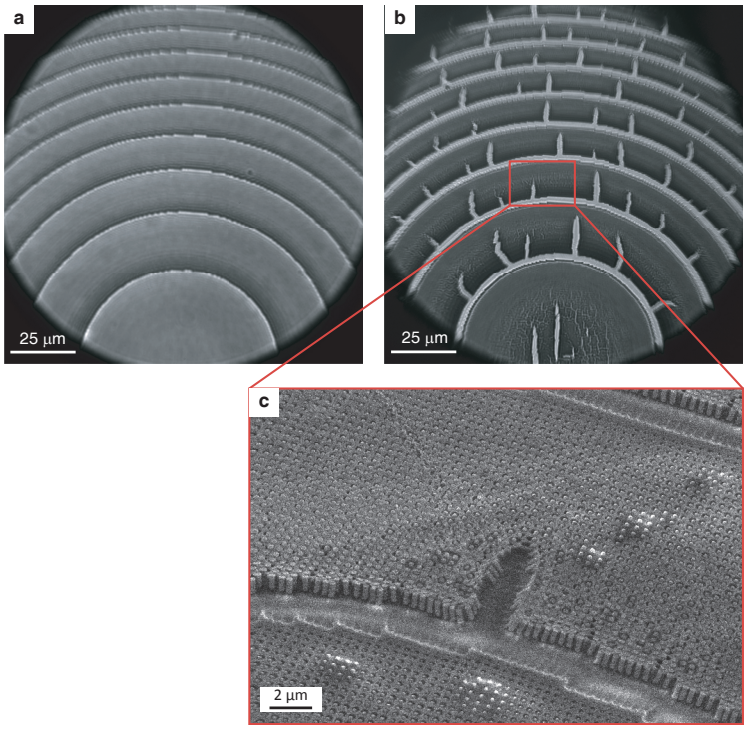

Figure 5.8: **Importance of PDMS cladding in the performance of the elastic metasurface under high strains.** Optical images of the nano-posts in PDMS with **a** and without the PDMS claddings **b**, under ~50% radial strain. The images are taken using the same measurement setup shown in Fig. 4**a** under green laser illumination. Elastic metasurface without the PDMS cladding stretches non-uniformly, and some cracks are formed at the borders of the small and large nano-posts starting at ~25% strain. By increasing the strain, these cracks spread in the elastic metasurface and some of the nano-posts stick out of the PDMS. **c**, Scanning electron micrograph of the nano-posts without the PDMS cladding under ~50% radial strain, taken at a tilt angle of 30 degrees. a ~10-nm-thick gold layer was deposited on the sample to dissipate charge accumulation during the scanning electron imaging. The metasurface microlens presented in the main manuscript has PDMS cladding, and its nano-posts are completely encapsulated inside a thin PDMS layer. In this manner, the cracks do not show up between the nano-posts even at very high strains (as shown in **a**).

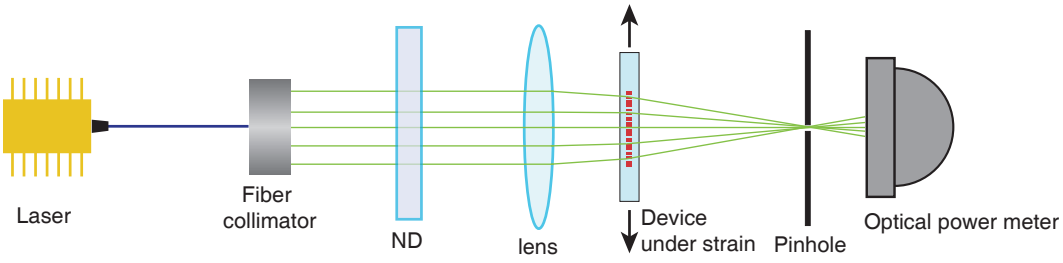

Figure 5.9: **Schematic illustration of the measurement setup used for measuring the efficiencies of the tunable microlens.** ND: neutral density filter.

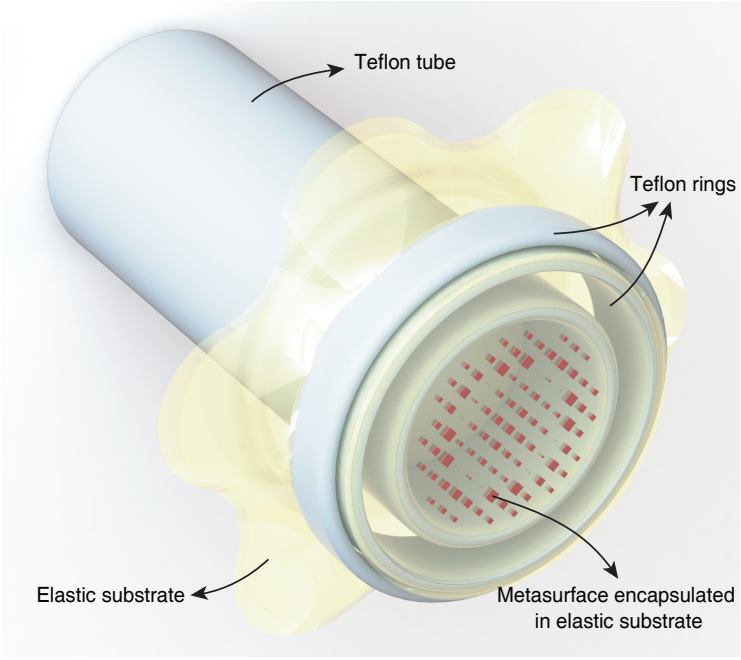

Figure 5.10: **Schematic illustration of the method used for radially stretching the elastic metasurface.** The elastic metasurface is fixed between the Teflon rings and is stretched radially by pushing the Teflon tube against it from the backside.

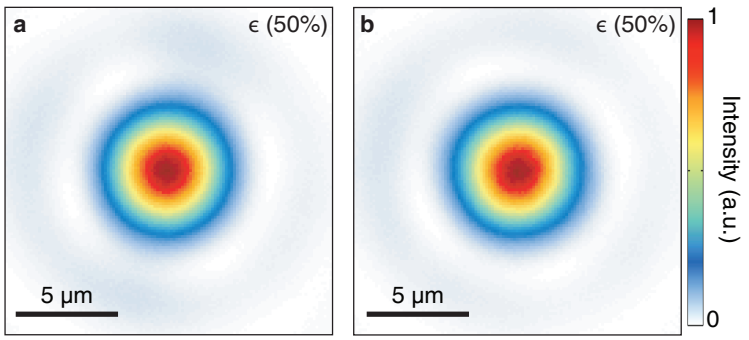

Figure 5.11: **Reliability measurement of the microlens under strain.** Measured optical intensity profile of the tunable microlens in the plane of focus under 50% strain after one **a**, and more than ten times of stretching and releasing the device **b**.

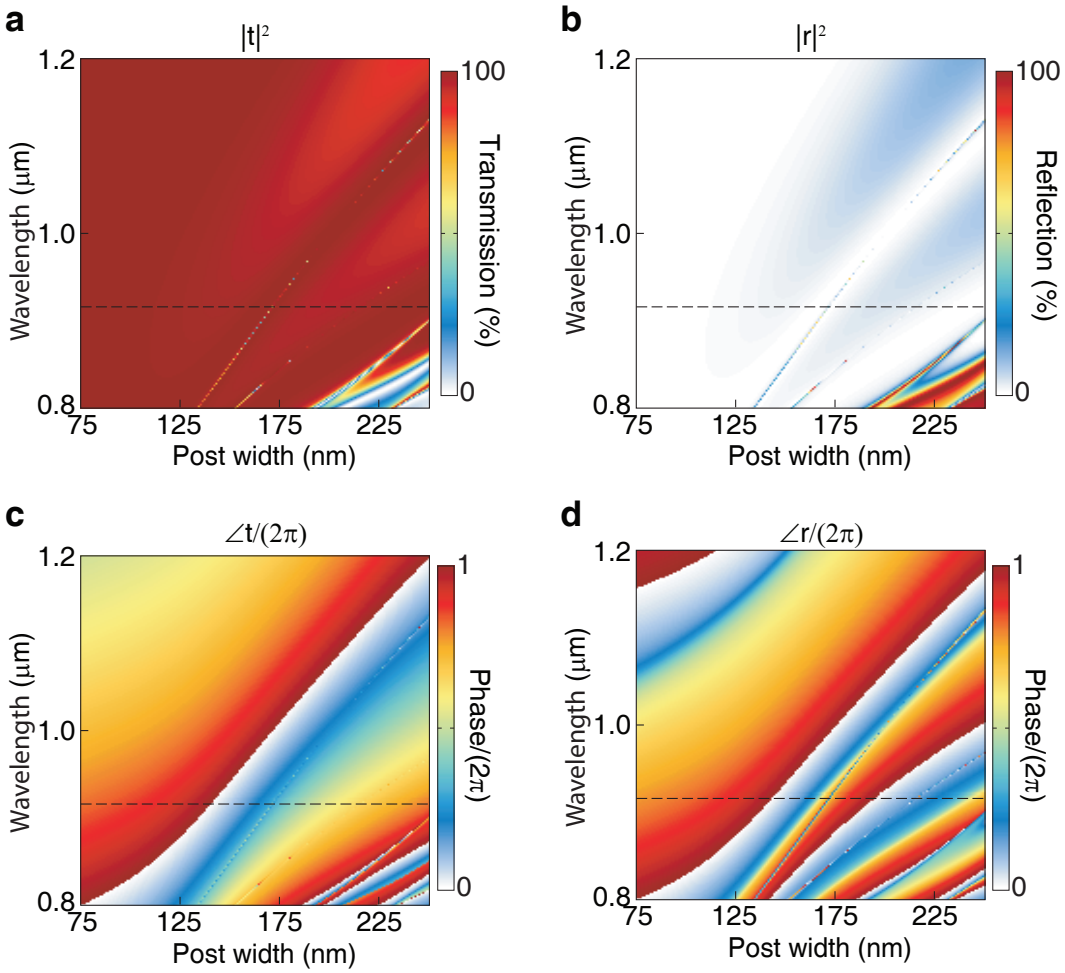

Figure 5.12: **Simulated transmittance and reflection spectra of uniform array of nano-posts.** **a**, Simulated intensity and **c**, phase of the transmission coefficient for the array shown in Fig. 2**a** as a function of the nano-post width at 25% strain. **b**, Reflection intensity and **d**, phase of the reflection coefficient for the same structure. Black dashed lines indicate the simulation wavelength of 915 nm, which is used in this manuscript.

Chapter 6

METASURFACE ASSISTED 3D BEAM SHAPING

The material in this chapter was in part presented in

> S. M. Kamali, E. Arbabi, H. Kwon, and A. Faraon, "Metasurface-mask-assisted 3d beam shaping: a new route for 3d fabrication of exotic periodic structures", Submitted,

Fast, large scale, and robust three-dimensional (3D) fabrication techniques for patterning a variety of structures with nanometer resolution are important in many areas of science and technology such as photonics, electronics, and mechanics with a wide range of applications from tissue engineering [260] to nano-architected materials [261, 262]. Although there are several promising 3D manufacturing techniques for realizing different classes of structures suitable for various applications [263–265], each has limitations mainly in the speed, geometries, and resolution of the final 3D structure. To overcome some of these limitations, in this chapter, we introduce the metasurface-mask-assisted 3D fabrication technique which provides great freedom in patterning various periodic structures through single photon interference lithography, thus enabling large scale, fast, and robust 3D fabrication. To showcase the versatility of this platform, we demonstrate metasurface masks that generate exotic periodic lattices like gyroid, rotated cubic, and diamond structures. As a proof of concept, we experimentally demonstrate generation of the diamond lattice for the first time under green laser illumination through the proposed platform.

6.1 Motivation

There is a huge interest in the fast fabrication of large scale 3D lattices with nanoscale resolution in various areas including novel engineered materials [265], micro-electromechanical systems [266], nano-architected materials [261, 262], microelectronics [267], tissue engineering and biomedical engineering [260], micro fuel cell development [268], optics [264], and micro- and nano-fluidics [269]. Different 3D manufacturing techniques have been proposed for different applications, including approaches based on self-assembly methods [270, 271], holographic lithography [272–275], multiple exposures lithography [276], controlled chemical

etching [277], and various additive manufacturing methods [278] like stereolithography [279], laser or ink-based direct writing [280] among many others. Each of these techniques provides new capabilities for fabricating different classes of 3D structures for different applications beyond traditional 2D photolithography steppers. Nevertheless, none could compete with traditional steppers in simultaneously providing a high speed, large scale and scalable lithography, simple and robust experimental setup, varieties of 3D structures, high yield, and defect free structures. Here, we introduce the concept of large scale metasurface assisted 3D lithography, schematically shown in Fig. 6.1, to circumvent some of these shortcomings. The method is based on using metasurfaces as photolithography masks to generate exotic 3D structures, and also take advantage of the traditional stepper technique in fabricating fast, large scale, 3D patterns with nanometer resolution through a relatively simple and robust process. The metasurface mask (which we call meta-mask from here on) provides control over the complex coefficients of the two orthogonal polarizations for various diffraction orders, resulting in the realization of exotic 3D patterns like the gyroid, diamond, or cubic patterns. As a proof of concept, for the first time, we experimentally demonstrate the diamond pattern through design and fabrication of a meta-mask. We should note that conformal masks have been used before for fabricating 3D patterns in photoresists [281, 282]. However, they suffer from low diffraction efficiencies (which result in low contrast 3D structures) and have very limited degree of freedom in generating desired 3D patterns.

Optical metasurfaces are 2D arrangements of scatterers that are designed to modify different characteristics of light such as its wavefront, polarization, intensity distribution, or spectrum with subwavelength resolution [1, 3, 7, 10, 11]. By proper design of the scatterers, different characteristics of the incident light can be engineered, and therefore different optical elements like gratings, lenses, holograms, waveplates, polarizers, and spectral filters can be realized [101, 118, 119, 138, 139, 283]. Furthermore, a single metasurface can provide novel functionalities, which if at all possible, would require a combination of complex optical elements to implement [14, 15, 35, 124]. Here, we demonstrate for the first time that by exploiting the metasurface capabilities in modifying the phase, intensity, and polarization of the optical wavefront, different meta-masks can be designed to generate novel 3D patterns like the gyroid, cubic, or diamond structures.

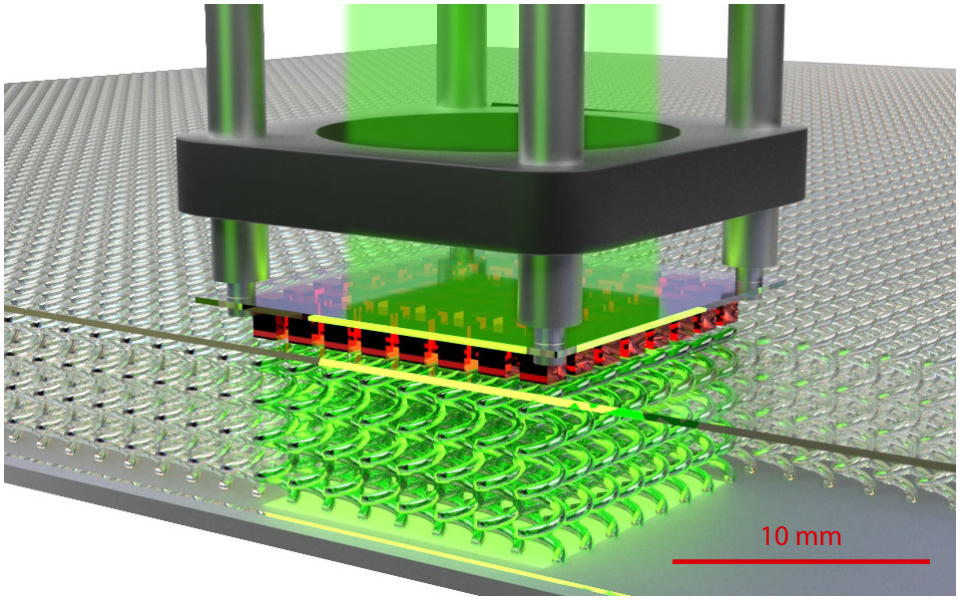

Figure 6.1: **Concept of large-scale meta-mask assisted 3D fabrication**. Schematic illustration of large-scale metasurface assisted 3D printing. A large meta-mask (~1 cm^2) is designed and used as a photo-lithography mask to create the desired 3D pattern in the photoresist. The large (~1 cm^2 wide and ~10 μm thick) 3D pattern is generated inside the photoresist through single photon lithography. Similar to a stepper, a linear stage could be used here to create large-scale 3D periodic patterns.

6.2 Meta-mask assisted 3D beam shaping platform

Figure 6.2a schematically shows a meta-mask, and how it generates different diffraction orders that interfere to realize a specific desired intensity pattern inside a transparent photoresist. It was previously shown that all fourteen Bravais lattices can be formed by interference of four noncoplanar beams [284]. Therefore, the meta-mask is in principle capable of generating all Bravias lattices in the resist. In Fig. 6.2, the illumination is assumed to be a 532-nm laser with linear polarization. The photoresist is assumed to be a sensitized SU-8, with the ability to form a solid structure under 532-nm photoexposure. The meta-mask is assumed to provide the desired amplitude and phase masks for the x- and y-polarized incident light.

The meta-mask basically generates different plane-waves (diffraction orders) with different propagation directions that are determined by its lateral periods. The electric field associated with the n^{th} planewave can be written as $\vec{E}_n e^{-j\vec{k}_n.\vec{r}}$. The overal electric field resulting from the interference of these planewaves can be written as

$$\vec{E} = E_x\vec{x} + E_y\vec{y} + E_z\vec{z}, \tag{6.1}$$

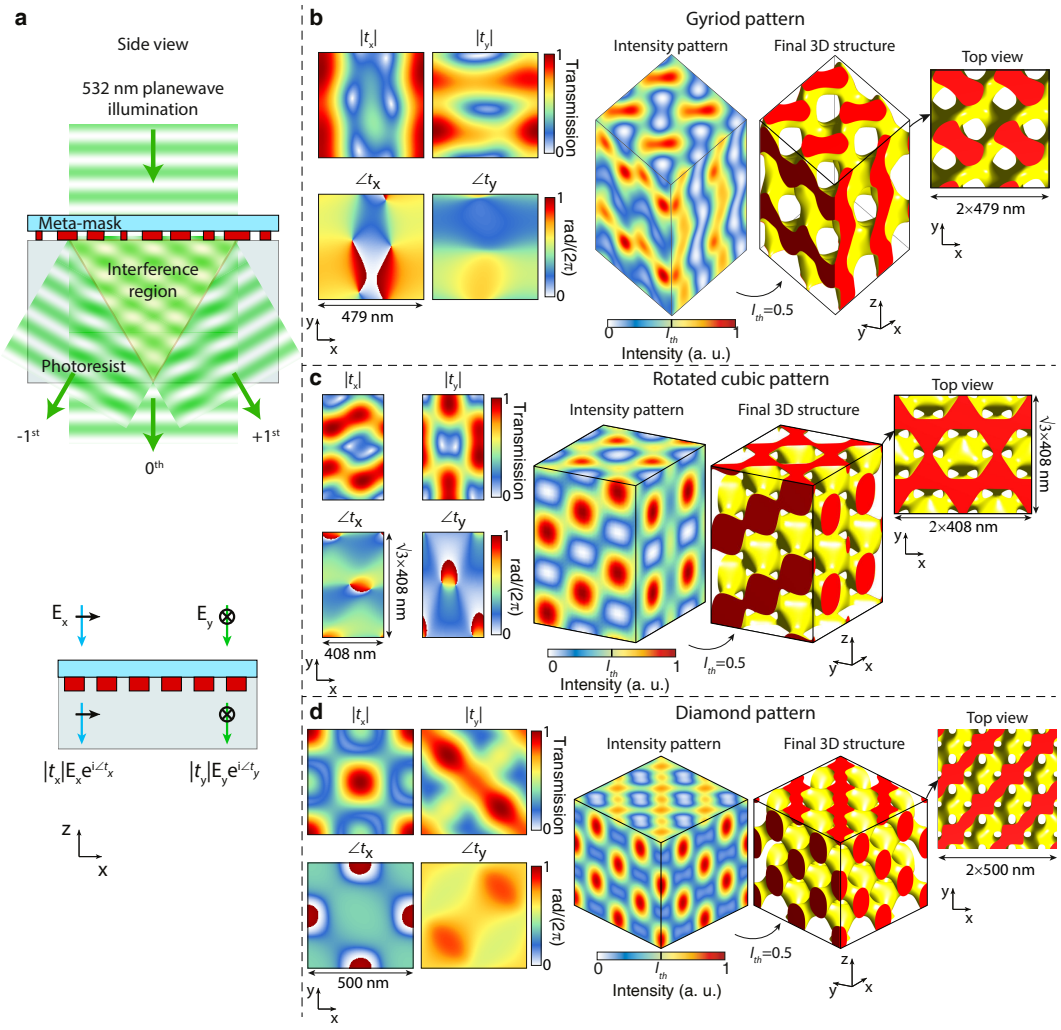

Figure 6.2: **Design of meta-masks for generating desired 3D periodic patterns through interference**. **a**, Schematic illustration of a meta-mask generating specific diffraction orders with designed complex coefficients to make a desired 3D pattern in the photoresist (top). Schematic of a meta-mask with amplitude, polarization, and phase control to make a desired 3D pattern (bottom).**b**-**d**, X- and y-polarized transmission amplitudes and phases of different meta-masks designed to create the gyroid, rotated cubic, and diamond patterns in the photoresist. The input light is assumed to be linearly polarized with $|E_x|/|E_y| = 0.85$, $|E_x|/|E_y| = 0.97$, and $|E_x|/|E_y| = 1$ for the three different patterns, respectively. Left (**b**-**d**): transmission amplitude and phases of the designed meta-masks. Middle (**b**-**d**): generated 3D intensity patterns in the sensitized SU-8 photoresist under 532-nm laser illumination. Right (**b**-**d**): Birds eye view and top view of the expected 3D structures formed in the negative photoresist (sensitized SU-8) assuming a specific intensity threshold. Here, it is assumed that the regions with intensity values above 0.5 will be polymerized in the resist, and areas below this level are developed.

where

$$
\begin{aligned}
E_x &= \sum_{n=1}^{N} E_{nx} e^{-j\vec{k}_n.\vec{r}} \\
E_y &= \sum_{n=1}^{N} E_{ny} e^{-j\vec{k}_n.\vec{r}} \\
E_z &= \sum_{n=1}^{N} \frac{-\vec{k}_n.\vec{x}}{\vec{k}_n.\vec{z}} E_{nx} e^{-j\vec{k}_n.\vec{r}} + \frac{-\vec{k}_n.\vec{y}}{\vec{k}_n.\vec{z}} E_{ny} e^{-j\vec{k}_n.\vec{r}}.
\end{aligned}
\tag{6.2}
$$

The 3D intensity profile is defined as

$$
I = \frac{1}{2\eta} |\vec{E}|^2, \tag{6.3}
$$

where $\eta = \sqrt{\mu/\epsilon}$ is the characteristic impedance of the propagating medium. In single photon lithography the photoresist polymerization is proportional to the exposure intensity, and therefore the 3D structure is generally formed for intensities above a specific threshold value, defined here as I_{th}.

The main advantage of using meta-masks is that the complex coefficients of different x- and y-polarized diffraction orders (E_{nx} and E_{ny}) can be controlled independently and at will. Therefore, it provides more degrees of freedom to define more exotic 3D structures like the gyroid and diamond patterns.

6.3 Operation principle and design procedure

The design process of the meta-mask to generate a specific 3D periodic lattice is as follows: First, the lateral periods of the 3D structure must be properly selected such that the intensity interference pattern is fully periodic in all three dimensions. These lateral dimensions play a critical role as they define the number of diffraction orders and their directions, as well as the in-depth periodicity. After selecting the appropriate lattice constants, the corresponding diffraction order coefficients are optimized to generate the desired 3D pattern. Finally, the meta-mask is designed and implemented through HCA metasurface platform. To showcase the capability of meta-masks, we demonstrate meta-masks that generate different lattices like the gyroid, cubic, and diamond patterns. The in-plane dimensions, and the corresponding in-depth periods are noted for these structures in Sec. 6.7 and Fig. 6.5.

The level set representation of the three structures is given in Sec. 6.7, in the form of $f(x, y, z) - t > 0$. In these equations, the parameter t is used to control the volume

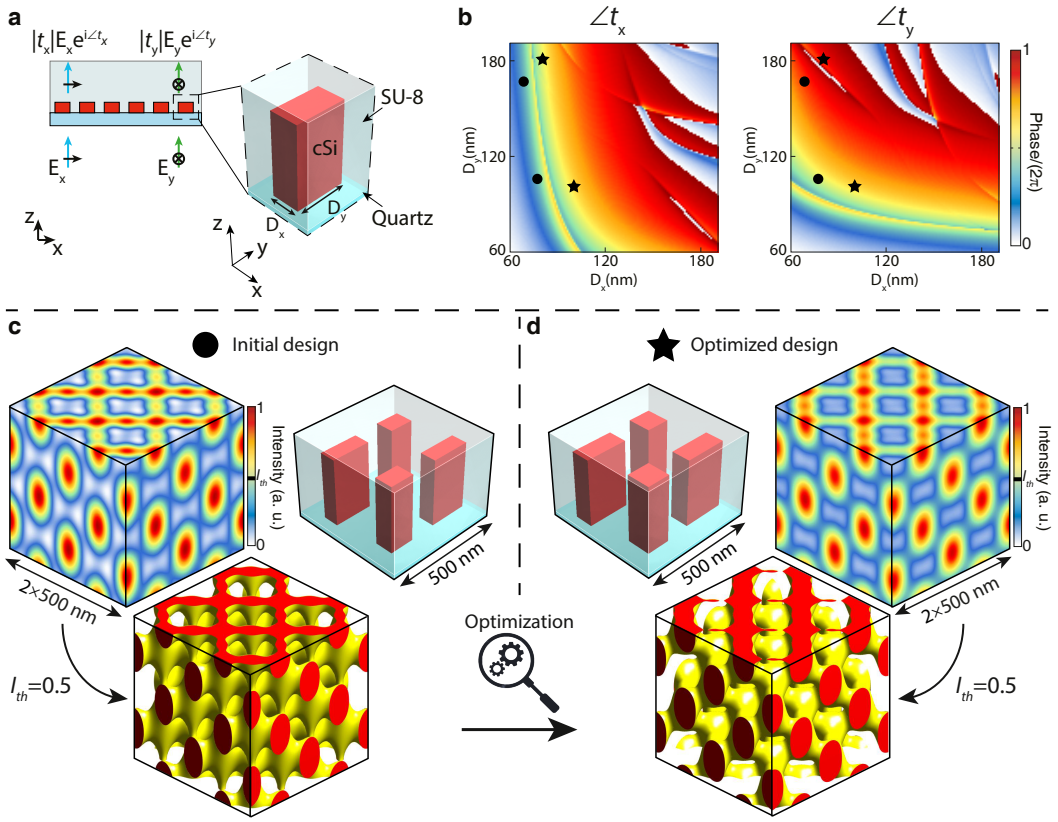

Figure 6.3: **Realization of the diamond pattern meta-mask with nano-posts. a**, Schematic drawing of different views of a uniform array of rectangular cross-section cSi nano-posts arranged in a square lattice resting on a quartz substrate and covered by an SU-8 layer. Tuning the in-plane dimensions of nano-posts, D_x and D_y, allows for independent control of the transmission phases of x- and y-polarized light at 532 nm. **b**, Transmission phases of the x- and y-polarized light at 532 nm for the uniform array shown in **a**, as functions of the nano-post widths. The nano-posts height is 291 nm and the lattice constant is 250 nm. **c**, The initial diamond meta-mask is designed through sampling the phase diagrams shown in Fig. 6.2d at four points. The corresponding nano-post dimensions are shown in Fig. 6.3b with black circles. The full-wave simulated 3D intensity pattern and the corresponding 3D structure demonstrate an 84% similarity compared to the target diamond pattern. **d**, The nano-post dimensions are further optimized to realize a 90% similarity with the target diamond pattern. The optimized nano-post dimensions are shown in Fig. 6.3b with black stars. All simulations are performed at the wavelength of 532 nm. cSi: crystalline silicon. See Sec. 6.7 for simulation details.

fraction of the structure, as it is assumed to be solid for $f(x, y, z) - t > 0$. This parameter can be controlled experimentally by adjusting the exposure threshold of the photoresist. Here, we have assumed it to be 0.25, 0.15, and 0.3 for defining the gyroid, rotated cubic, and diamond patterns respectively. See Fig. 6.6 for the defined

target patterns. For realizing the patterns with amplitude and phase masks, we used a global optimization technique to find the complex coefficients of different diffraction orders, E_{nx} and E_{ny}, which are given in Fig. 6.6. The optimized amplitude and phase masks for each pattern, shown in the left column of Figs. 6.2b, c, and d , are calculated from the optimized diffraction order coefficients using Equation 6.2 at $z = 0$ plane. The 3D intensity patterns are then calculated using Equation 6.2, and are shown in the middle column of Figs. 6.2b, c, and d. The corresponding 3D structures, assuming $I_{th} = 0.5$, are shown in the right column of Figs. 6.2b, c, and d. To determine the degree of similarity between the achieved and desired patterns, we used a fitness factor defined as the fraction of voxels in one unit cell that match the 3D target structure. The fitness factors for the gyroid, rotated cubic, and diamond patterns are 97 %, 82 %, and 93 %, respectively (see Sec. 6.7 for simulation details).

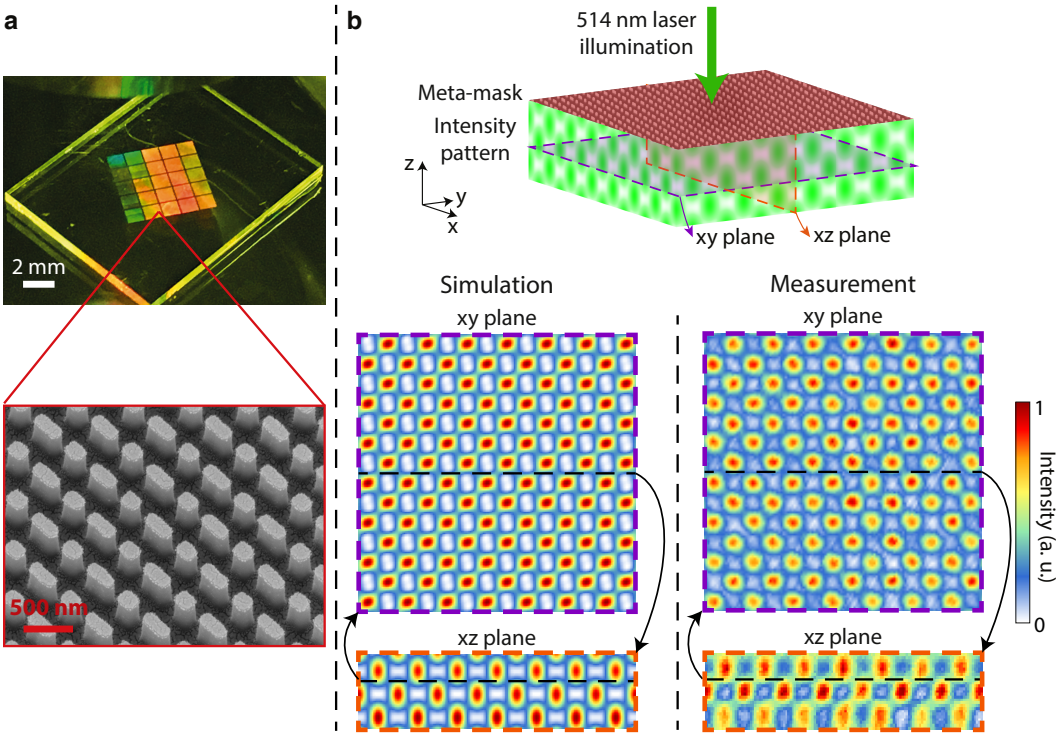

Figure 6.4: **Experimental characterization of the diamond meta-mask. a**, Optical image of the fabricated optimized diamond meta-mask (top). A 5×5 array of masks is fabricated and shown on top. SEM image of a portion of the mask before spin coating the SU-8 layer is shown on the bottom. **b**, The meta-mask is characterized under 514-nm laser illumination using a confocal microscopy setup (514-nm laser was the closest available laser line to 532 nm in the confocal microscopy setup). Two measured cross-sections of the captured 3D intensity pattern (right) are in good agreement with the simulated results (left).

To realize the diamond meta-mask for 532 nm wavelength, we used a matasurface platform composed of cuboid shaped crystalline silicon (cSi) nanoposts embedded in an SU-8 protecting layer and resting on a quartz substrate. A schematic of the metasurface platform is shown in Fig. 6.3a. Transmission phases of the x- and y-polarized light can be fully and independently controlled from 0 to 2π by changing the in-plane dimensions of the nanoposts [14]. The cSi nanoposts are 291 nm tall and fully embedded in the SU-8 layer, and the lattice constant is 250 nm. A periodic array of such cuboid shaped nanoposts was simulated to find the transmission phases, which are plotted in Fig. 6.3b (see Sec. 6.7 for simulation details and Fig. 6.7b for transmission powers). The diamond pahse-masks shown in Fig. 6.2d, are sampled at four points with a 250-nm period, and the corresponding nanoposts are shown in Fig. 6.3b with black circles (see Fig. 6.7a for the sampling points). Since the nano-posts have high transmissions for both x and y polarizations, we have incorporated the desired difference between their powers into the input polarization. In other words, the input polarization is chosen such that $|E_x|/|E_y|$ is equal to $< |t_x| > / < |t_y| >$, where $< \cdot >$ denotes averaging over a unit cell area. The full-wave simulated 3D intensity distribution and the corresponding periodic 3D structure are shown in Fig. 6.3c for this initial design. The fitness factor of this initial design is 84% and the total simulated transmission efficiency is 74% (see Sec. 6.7 for full-wave simulation details and Fig. 6.8a for the phase and amplitude masks). To improve the degree of similarity of the achieved and desired structures, we then used this design as an initial point and further optimized the nanoposts' widths through a global optimization method. Considering the diagonal symmetry of the diamond meta-mask, the optimization parameters were reduced to four values (widths of the two different nanoposts). The optimized values are shown in Fig. 6.3b with black stars. The full-wave simulated 3D intensity profile and the resulting structure are shown in Fig. 6.3d in a volume equal to $2 \times 2 \times 2$ periods (see Fig. 6.8b for the corresponding phase and amplitude masks). The fitness factor of the final optimized structure is 90 % and the total simulated transmission efficiency is 82 %. It is worth-noting that the optimized meta-mask solution is not unique and various initial points or optimization techniques can result in different optimized designs. Details of the simulation and optimization steps are discussed in Sec. 6.7.

6.4 Fabrication and characterization of the meta-mask

The meta-mask is fabricated using standard nanofabrication techniques (see Sec. 6.7 for fabrication details). Figure 6.4a shows an optical image of the final fabricated device. A scanning electron micrograph of a part of the fabricated meta-mask before being capped with the SU-8 protecting layer is shown in Fig. 6.4a as well.

To characterize the fabricated meta-mask we used a confocal microscopy setup with an oil immersion objective lens that captures all the excited diffraction orders. The sample was illuminated by a 514-nm laser beam, which was the closest available laser line to 532 nm in the microscopy setup. The optical intensity distribution was captured in multiple parallel planes with ~45-nm depth steps. The right column of Fig. 6.4b shows the measured intensity profiles at two sample cross-sections (xy and xz planes as schematically shown in Fig. 6.4b). See Sec. 6.7 for details of the measurement procedure, and see Fig. 6.9 for measurement results over a larger area. The measured intensity profiles are in good agreement with the simulated results (simulated with the same illumination wavelength of 514 nm) as shown in the left column of Fig. 6.4b. We attribute nonuniformities and small drifts in the z stack to sample vibrations, and sample mount tilt angles.

6.5 Discussion

The meta-mask assisted 3D fabrication platform enables a fast, large-scale, and robust system for realizing exotic 3D structures. In this paper, we focused on fully periodic lattices, while a wider category of aperiodic structures can also designed and fabricated using the same concept. Some limited previous efforts for pattering aperiodic structures through conformal masks demonstrate the proof of concept [281]. Moreover, it is worth noting that high diffraction efficiencies provided by the meta-masks result in high contrast well defined 3D structures in the photoresist even under fast single photon lithography. Therefore, the use of meta-mask assisted platforms could eliminate the limited intensity contrast issue faced in single-photon lithography that has previously been addressed through multi-photon lithography [285, 286]. Furthermore, here we showcased the capability of this platform through a single layer metasurface, while cascaded metasurface layers could also be designed to provide full and precise control over the complex coefficients of the two orthogonal polarization diffraction orders, or provide additional control degrees of freedom like wavelength or illumination angle.

6.6 Conclusion and outlook

In conclusion, we introduced the concept of meta-mask assisted 3D fabrication, which provides a fast and robust technique for fabrication of exotic 3D periodic patterns at large scales. We demonstrated the versatility of this platform through designing different exotic 3D patterns like the gyroid, rotated cubic, and diamond patterns. Moreover, as a proof of concept, we experimentally demonstrate the diamond pattern through design and fabrication of the meta-mask. The meta-mask assisted 3D fabrication platform paves the road for fabricating large scale novel and exotic 3D patterns with nanoscale resolution.

6.7 Appendix

Simulation and Optimization Procedure

To find the optimized complex coefficients of different diffraction orders and the input polarization for generating the target 3D periodic pattern, we used a global particle swarm optimization method. For the diamond and rotated cubic structures, we forced the coefficients of unwanted diffraction orders to be zero. The target 3D patterns were defined with voxel sizes of $\sim$10 nm^3 and $\sim$13 nm^3 for the rectangular (gyroid and diamond) and triangular (rotated cubic) lattices, respectively.

To find the transmission powers and phases of a uniform array of nanoposts under x- and y-polarized illumination, RCWA technique was used [148]. X- and y-polarized incident plane waves at 532 nm wavelength were used as the excitation, and the transmission powers and phases of the x- and y-polarized transmitted waves were extracted. The subwavelength 250 nm lattice constant in the SU-8 propagating medium results in the excitation of only the zeroth order diffracted light. The cSi layer was assumed to be 291 nm thick. Refractive indices at 532 nm wavelength were assumed as follows: cSi: $4.136 - 1j0.01027$, SU-8: 1.595, and quartz: 1.4607. The nanopost in-plane dimensions (D_x and D_y) were swept such that the minimum feature size and the gap size remain larger than 60 nm for relieving fabrication constraints.

We used the finite-difference time-domain method (Lumerical) for simulating the meta-masks realized with cSi nanoposts. The electric fields were extracted on a xy-plane $\sim$ 20 nm above the nanoposts. We used the plane wave expansion (PWE) technique [226] to generate the 3D intensity profiles and the 3D structures.

To optimized the nano-posts in-plane dimensions for the diamond meta-mask, we used a global particle swarm optimization method with the fitness factor target

function. In order to find the 3D structure, we used the same Lumerical simulation package with the PWE technique.

Sample fabrication

to define the pattern in cSi on quartz wafers, a Vistec EBPG5200 e-beam lithography system and a ~300 nm thick layer of ZEP-520A positive electron-beam resist was used (spin coated at 5000 rpm for 1 min). The pattern was developed in the resist developer (ZED-N50 from Zeon Chemicals) for 3 minutes. The pattern was then transferred into a ~ 50-nm-thick deposited Al_2O_3 layer, by a lift off process. The patterned Al_2O_3 hard mask was then used to dry etch the cSi layer in a mixture of SF_6 and C_4F_8 plasma. Finally, the Al_2O_3 mask was removed in a 1:1 solution of ammonium hydroxide and hydrogen peroxide at 80°C. Finally, a 2-μm-thick layer of SU-8 protecting layer was spin coated on the meta-mask.

Measurement procedure

The diamond meta-mask was measured using a confocal microscopy setup (Zeiss LSM 710). A 100X oil immersion objective lens (alpha Plan-Apochromat Oil DIC M27, NA= 1.46) was used to capture all the excited diffraction orders, as the diamond mask has NA~1.45 at 514 nm wavelength. We used Zeiss Immersol^{TM} 518 F with a refractive index of 1.518, which was the closest allowed oil in the microscopy setup to the refractive index of SU-8 (1.595). We captured 3D image stacks with in-plane pixel sizes of ~ 28 nm^2 and in-depth pixel sizes of ~ 45 nm. We captured in-plane images as large as 15μm^2, shown in Fig. 6.9. We should note that the resolution of the system is set by the objective lens and is ~ 176 nm and ~ 482 nm in-plane and in-depth, respectively.

Fully periodic 3D structures

According to the grating equation, to have a fully periodic structure, the gyroid and diamond patterns should have square in-plane lattices with lattice constants of 479 nm and 500 nm, which result in in-depth periods of 1184 nm and 500 nm, respectively. The rotated cubic pattern has a triangular in-plane lattice with a lattice constant of 408 nm, resulting in an in-depth period of 500 nm. Figure 6.5 demonstrates in-plane and in-depth periods of interference patterns of different diffraction orders for square and triangular lattices.

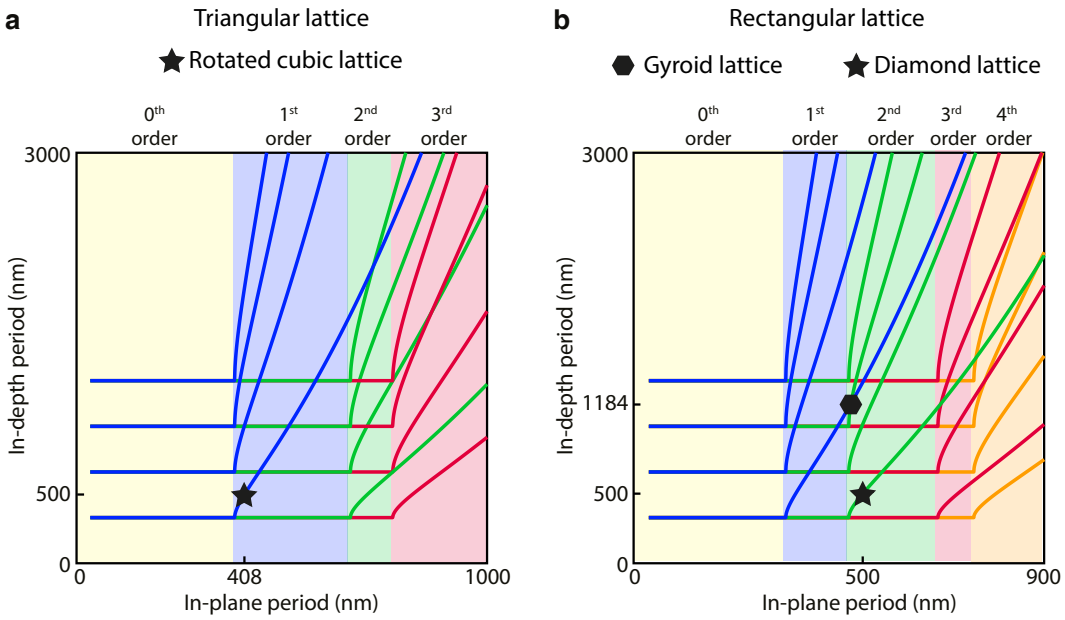

Figure 6.5: **Square and triangular lattice diffraction orders and their corresponding in-plane and in-depth periods.** **a**, Different excited diffraction orders and the corresponding in-depth periods in a triangular lattice as a function of in-plane periods. The designed rotated cubic lattice is shown with black star **b**, Same as **a**, but for rectangular lattice. The designed gyroid and diamond lattices are shown with black hexagon and black star, respectively. Here the lattices are two dimensional and the number of diffraction orders are only referring to the order of their excitations.

The level set representation of 3D structures

The gyroid (F_G), rotated cubic (F_C), and diamond (F_D) lattices are defined with the level set approximations as follows:

$$\begin{aligned} F_G(x,y,z) = &\sin 2\pi(\frac{x}{P_x})\cos 2\pi(\frac{y}{P_y}) + \sin 2\pi(\frac{y}{P_y})\cos 2\pi(\frac{z}{P_z}) \\ &+ \sin 2\pi(\frac{z}{P_z})\cos 2\pi(\frac{x}{P_x}) - t, \end{aligned} \tag{6.4}$$

where $P_x = 479$ nm, $P_y = 479$ nm, $P_z = 1184$ nm,

$$F_C(x,y,z) = \cos 2\pi(\frac{x'}{P_x}) + \cos 2\pi(\frac{y'}{P_y}) + \cos 2\pi(\frac{z'}{P_z}) - t, \tag{6.5}$$

where $P_x = P_y = P_z = 408$ nm, and

$$\begin{aligned} x' &= -0.71x - 0.41y - 0.58z, \\ y' &= 0.71x - 0.41y - 0.58z, \\ z' &= 0.81y - 0.58z, \end{aligned} \tag{6.6}$$

$$F_D(x,y,z) = \sin 2\pi\left(\frac{x}{P_x} + \frac{y}{P_y} + \frac{z}{P_z}\right) + \sin 2\pi\left(\frac{x}{P_x} - \frac{y}{P_y} + \frac{z}{P_z}\right) + \sin 2\pi\left(\frac{x}{P_x} + \frac{y}{P_y} - \frac{z}{P_z}\right) + \sin 2\pi\left(-\frac{x}{P_x} + \frac{y}{P_y} + \frac{z}{P_z}\right) - t, \tag{6.7}$$

where $P_x = P_y = P_z = 500$ nm.

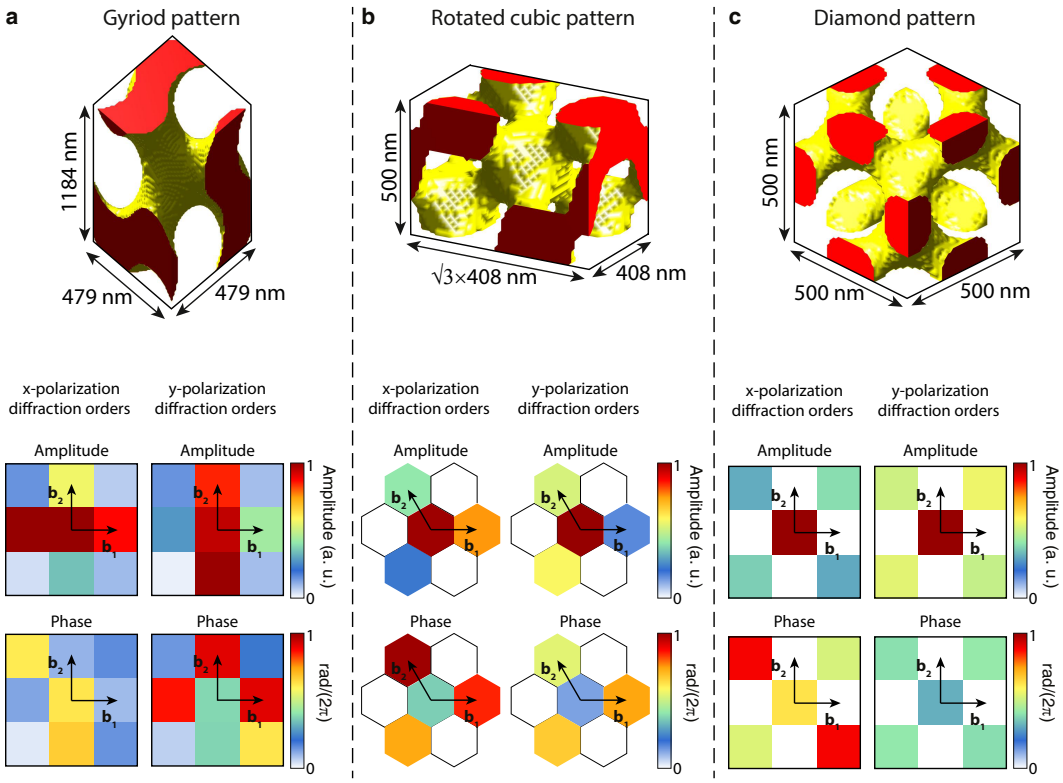

Figure 6.6: **Target 3D structures and their corresponding optimized diffraction order coefficients. a**, Target gyroid pattern defined with the level set approximation with $t = 0.25$ (top). The optimized diffraction order coefficients for the x and y polarizations for gyroid structure with square lattice (bottom). **b**, Same as **a**, but for rotated cubic pattern with triangular lattice and $t = 0.15$. **b**, Same as **a**, but for diamond pattern with square lattice and $t = 0.3$.

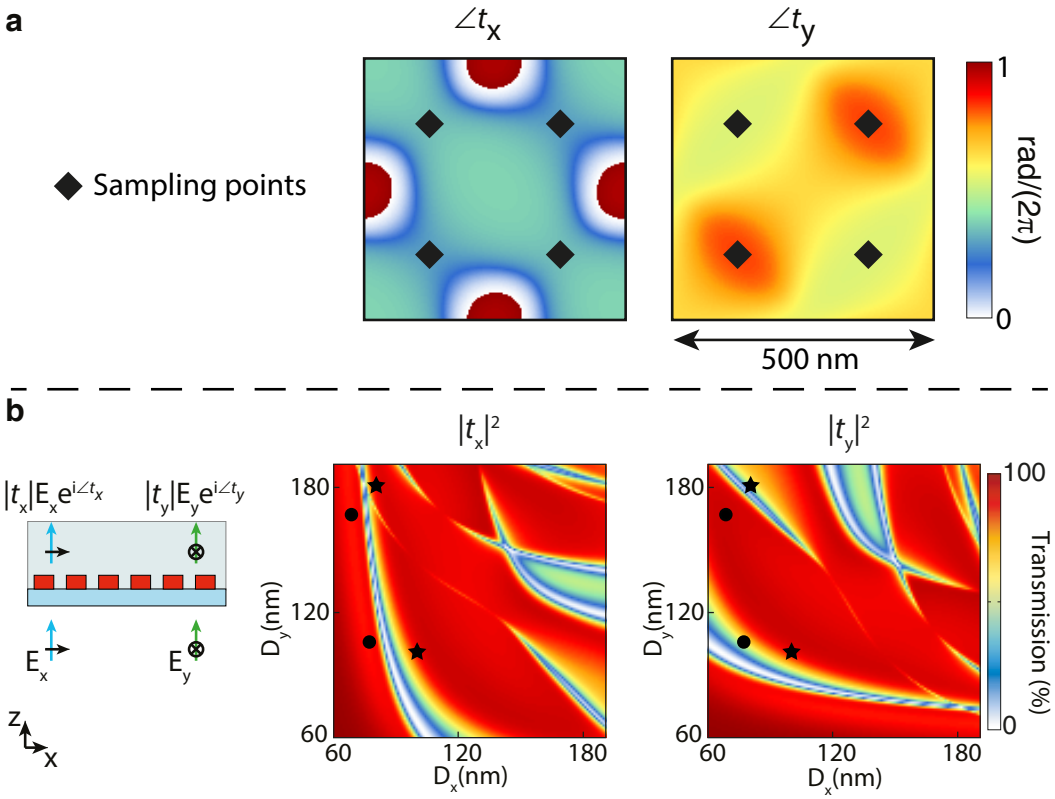

Figure 6.7: **Diamond meta-mask sampling points and transmission powers of uniform nanoposts. a**, The desired diamond phase-masks are sampled at four points with with a 250-nm period. Position of the sampling points are shown with black squares. **b**, Transmission powers of the x- and y-polarized light at 532 nm for the uniform array of nanoposts as functions of the nano-post widths.

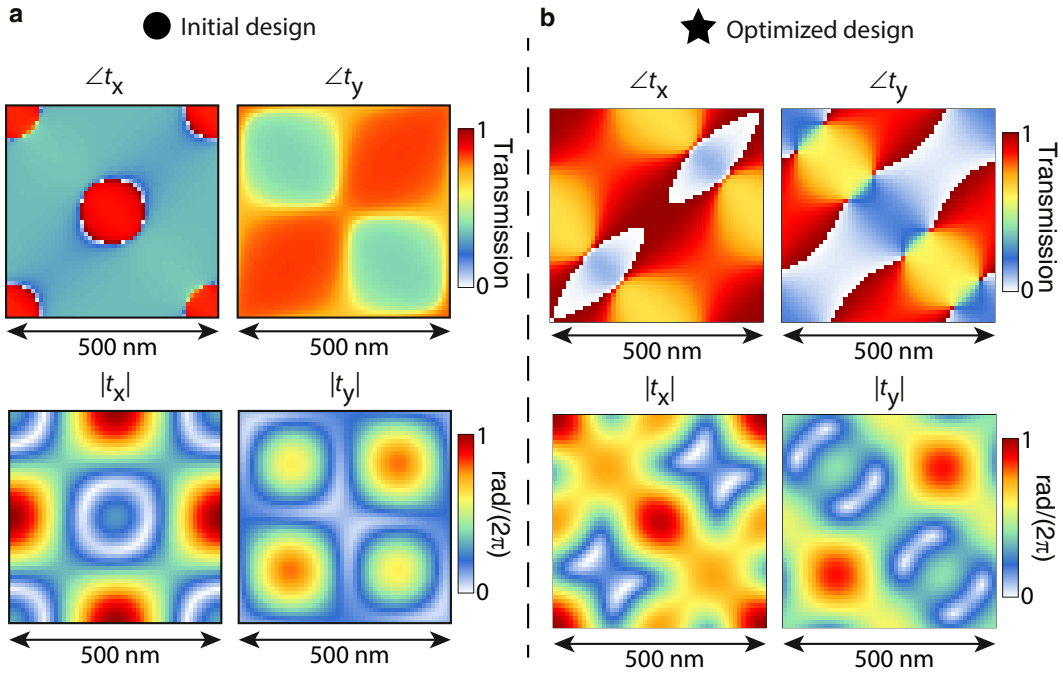

Figure 6.8: **Transmission amplitudes and phases of the initial and optimized diamond meta-masks.** **a**, X- and y-polarized transmission phases (top row) and amplitudes (bottom row) of the initial design. The input polarization is chosen to be linearly polarized with $|E_x|/|E_y| = 0.84$. **b**, Same as **a**, but for the optimized design. The input polarization is chosen to be linearly polarized with $|E_x|/|E_y| = 0.5$.

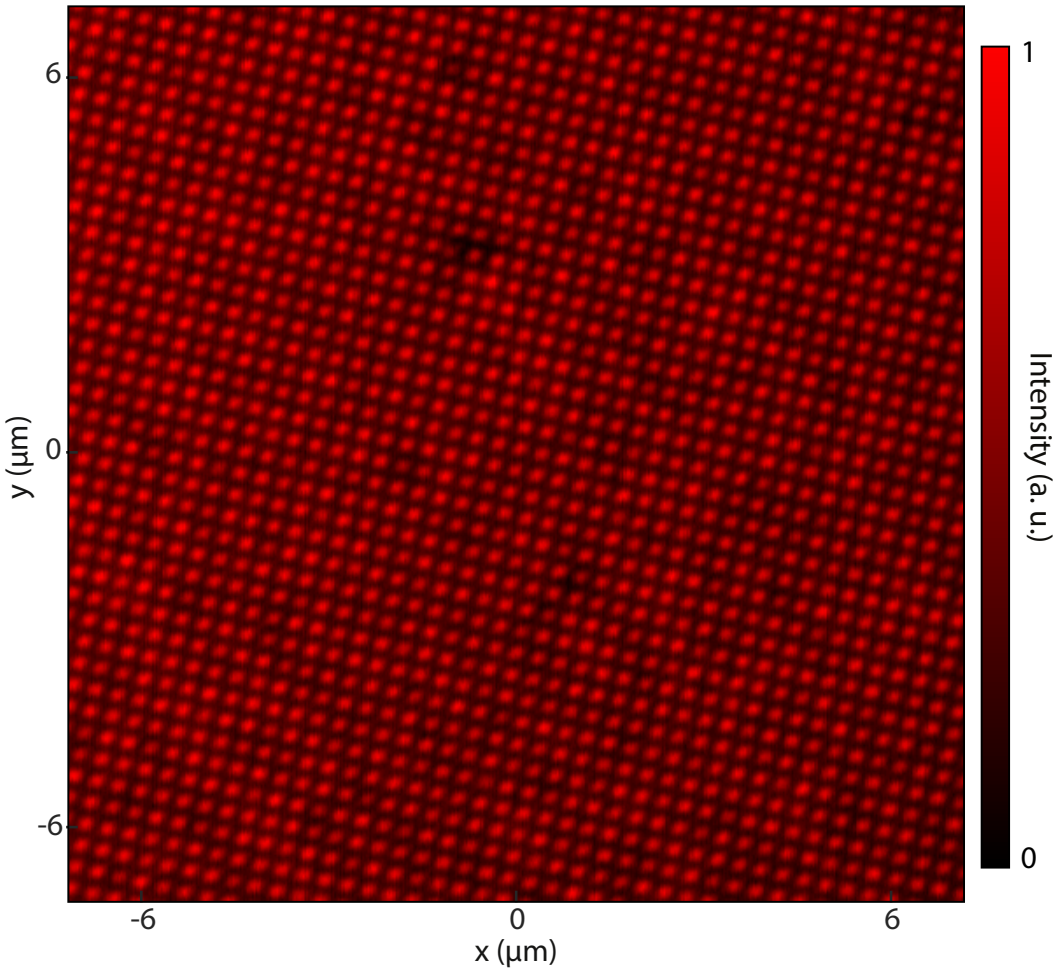

Figure 6.9: **Larger area of measured in-plane intensity profile of the diamond meta-mask.**

Chapter 7

METASYSTEMS: INTEGRATED METASURFACES

The material in this chapter was in part presented in

> S. M. Kamali*, E. Arbabi*, and A. Faraon, "Metasurface-based compact light engine for ar headsets", in Spie photon. west (2019), p. 11040, DOI: doi.org/10.1117/12.2523720.

Fabrication of metasurfaces with conventional nano-fabrication techniques allows for their vertical [138, 287] and in-plane [140] integration, enabling various types of unique optical systems like wide-field-of-view lenses and compact spectrometers. Like conventional optical systems, multiple metasurfaces can be co-designed and combined to make *metasystems*. In this chapter, we showcase this capability of metasurfaces through an example of ultra-compact projection optics for augmented reality (AR) headsets [287].

7.1 Motivation

Despite the great advances, potentials of AR to fundamentally transform the way people use computers is partially hindered by the size and weight of the AR headsets. In waveguide-based devices, the light engine constitutes a significant portion of the total volume and weight. Dielectric metasurfaces have in recent years been used to demonstrate various high performance optical elements like blazed gratings and wide field of view lenses with small thicknesses, high efficiencies, and little stray light. In this chapter, we present the proposal and design of a compact light engine based on multi-metasurface optical systems with wide fields of view, integrated with three monochrome μ-light emitting diode (LED) displays for red, green, and blue. The metasurfaces image the μ-light emitting diodes (LEDs) on the prism or grating couplers. This design avoids an important shortcoming of μ-LEDs and metasurface lenses, i.e., each works well for a single wavelength. As an example, we present a design for 532 nm, with over 3000 resolved angular points in an 8-mm-diameter field of view, and a total volume less than 0.65 cc (<2 cc for the three wavelengths). Limited by the total internal reflection region inside a waveguide with a 1.78 refractive index, the light engine can produce an image with over 1500×1500 points over a

field of view slightly larger than 85°×85° in air. To the best of our knowledge, this is the first proposal and demonstration of such a system and therefore opens the path towards exploring the potentials of the metasurface optical systems for compact AR headsets with enhanced optical capabilities.

Powered by the great advancements in electronics, computer science, and compact refractive and diffractive micro-optics [288], headmounted AR displays have in recent years become a new category of consumer electronics. With many great proposals and demonstrations based on various technologies including visor and waveguide based systems [289–292], many products from different companies are now hitting the market. Among various designs, waveguide-based designs seem more suitable for compact AR headsets with wide fields of view. In these devices, the light engine constitutes a significant portion of the volume and weight of the device, and can even limit its performance by not providing the whole field of view and resolution supported by the waveguide optics.

Here we present the proposal and design of a compact light engine based on three monochrome μ-LED displays imaged using multi-metasurface integrated optical systems corrected for wide fields of view. Since each μ-LED display has its own metasurface optics, this design significantly avoids the main challenge facing both μ-LEDs and metasurfaces, that is, they each work well when designed for a single color. This shortcoming has so far prevented the use of μ-LEDs in AR headsets because the pixel size is significantly increased when μ-LEDs of different colors are combined to provide full red-green-blue (RGB) coverage on the same chip. On the other hand, hindered by the size and weight of optical elements, it has not been practical to use three separate μ-LED displays as each of them would require its own imaging optics.

The proposed design overcomes this issue since the imaging optics for each color can be separate, while keeping the total volume and weight of the optics low (i.e., to lower than 2 cubic centimeters and less than 3 grams for the optics of the three colors combined). More specifically, we demonstrate a five layer metasurface design with a corrected FOV of 8 mm (close to 90° inside a glass with a refractive index of 1.78) to provide near diffraction-limited focusing with about 3000 resolved points. The optics has a collection NA of 0.25, and delivers the collimated beams with root mean square (RMS) wavefront errors lower than 0.25 across its field to an aperture with a diameter of 2.1 mm. Capped by the total internal reflection region of the waveguide (i.e., 35°-80°, for an index of 1.78) the optics can deliver over 1500×1500

points for each color, within a FOV just above 85°×85° in air. If the use of glass substrates with ultra-high indices (e.g., n≈1.95) is possible, it is possible to make the device even more compact with a larger FOV in air, as we show in a secondary design with FOV=105°×105°, and collection NA=0.4. We also present metasurface designs based on HCA platform using cSi nano-scatterers that can implement the proposed metasurfaces at all wavelengths of interest (480 nm, 532 nm, and 635 nm). In the end, we discuss the main challenges faced by this technology including the chromatic dispersion and point potential methods of mitigation. While the concept of metasurfaces has previously been proposed for use in AR devices [293, 294], it has generally been limited to their application as periodic grating couplers. Being the first proposal and demonstration of its kind, we believe that this work will pave the way and encourage the exploration of potentials of metasurface optical elements for integration into compact optical systems used in AR headsets.

7.2 Concept of ultra-compact μ-LED and metasurface-based light engines

Figure 7.1 schematically shows the concept of the metasurface based light engine AR display. As shown in Fig. 7.1**a**, light from monochrome μ-LED displays is collimated and directed to the waveguide, using the multi-metasurface optical systems. Based on whether the eye box expanders and the out-coupling gratings can be combined for different colors or not (e.g., using volumetric Bragg gratings), one, two, or three waveguides might be used in the actual design. Here, for the sake of simplicity, we assume that the waveguides can be combined and therefore show only one waveguide. As seen in Fig. 7.1**b**, light engines for the three colors combined can be smaller than 3 cubic centimeters (with about 2 mm of thickness reserved for the μ-LED displays and their electrical circuitry). Figure 7.1**c** schematically shows a zoomed-in view of the light engine for the red color μ-LED display. The multiple metasurface system images each pixel of the μ-LED display into the grating coupler aperture with a corrected wavefront. To better visualize the compactness of the proposed platform, a schematic illustration of the whole metasurface-based light engine mounted on a typical pair of glasses is shown in Fig. 7.1**d**.

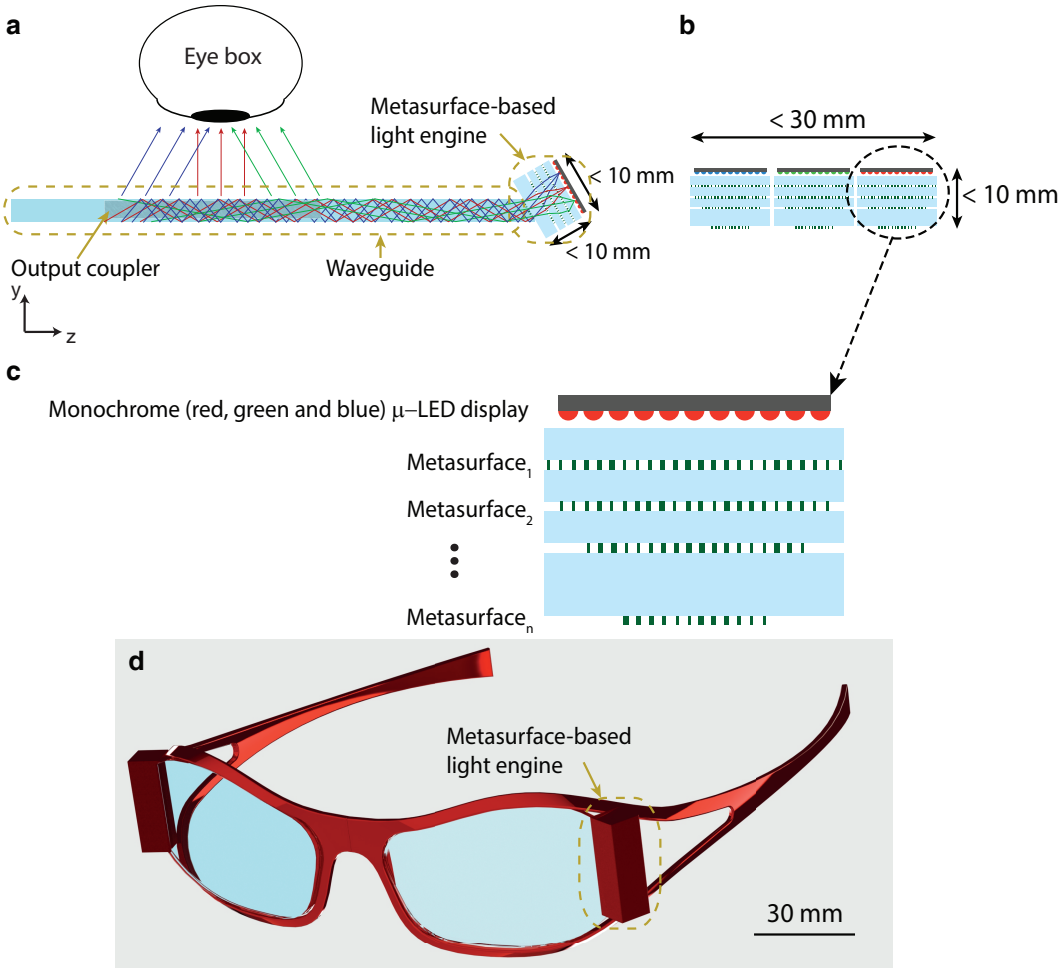

Figure 7.1: **Concept of μ-LED and metasurface-based light engines for AR glasses based on waveguides. a**, Schematic top-view of the glass, showing relative locations of the waveguide, light engine, and the eye box. The metasurface-based optics collimates light from the monochrome μ-LED displays and directs it to the prism coupler. Inside the waveguide, light is expanded by the eye box expander and is finally out-coupled using holographic volume gratings that could increase the FOV. **b**, Schematics of the side view of the μ-LED displays and the metasurface based optics, showing all three colors at the same time. The whole light engine is smaller than 30mm × 10mm × 10mm, with the total volume of the optics smaller than 2 cubic centimeters. **c**, Zoomed-in view of the μ-LED display and typical metasurfaces forming the light engine optics for the red color. **d**, Schematic illustration of the whole metasurface-based light engine mounted on a typical pair of glasses.

7.3 Metasurface design

The HCA based metasurface platform that can be used to implement the metasurfaces is shown in Fig. 7.2**a**. In order to better suppress higher order diffractions and

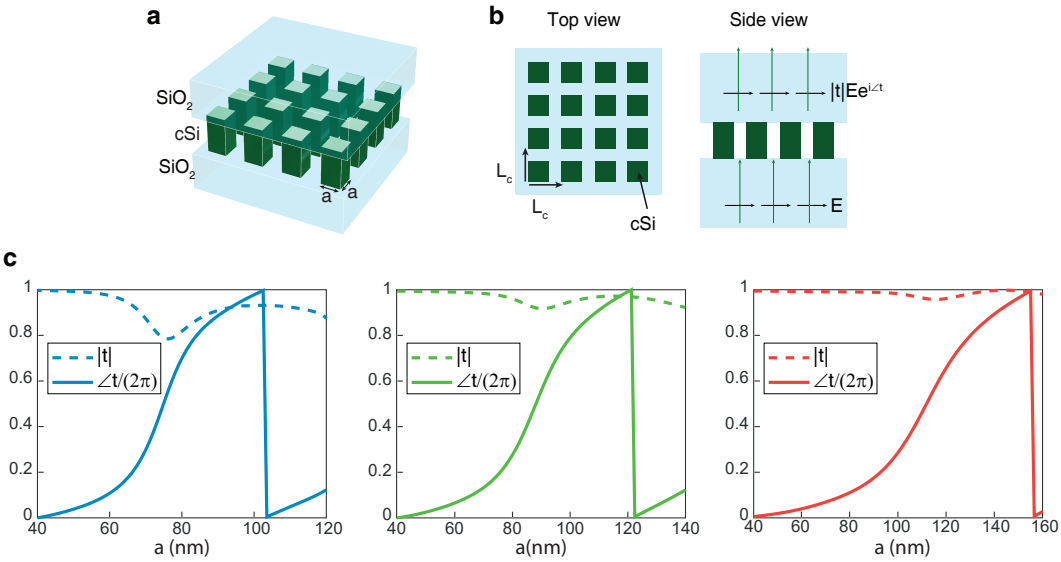

Figure 7.2: **Schematics and design graphs for dielectric metasurfaces based on cSi. a**, Schematic illustration of the proposed metasurface structure that is composed of cSi nano-posts with square cross sections, sandwiched between two low-index substrates. For fabrication considerations, one of the substrates can actually be fabricated by spin coating a thick spin-on glass or polymer layer that does not fill in the nano-post gaps. **b**, Top and side views of the proposed metasurface structure, showing the lattice constant L_c, and the complex transmission t. The optimal metasurface structure will have different thicknesses and lattice constants for the three different colors. **c**, The simulated transmission amplitudes and phases for metasurfaces designed for blue (left, 480 nm), green (middle, 532 nm), and red (right, 635 nm). The metasurfaces have thicknesses of 224 nm, 270 nm, and 340 nm, and lattice constants of 180 nm, 200 nm, and 240 nm for blue, green, and red, respectively. Measured refractive indices of cSi on quartz was used for the simulations. The used index values are $4.413 - 0.04033j$, $4.136 - 0.01027j$, and $3.874 - 0.008432j$ at wavelengths of 480 nm, 532 nm, and 635 nm, respectively. The graphs ensure full 2π phase coverage at all required wavelengths with high transmission. In addition, the high refractive index of cSi ensures the ability to optimize metasurfaces for large deflection angles with high diffraction efficiencies.

unwanted scattering, the nano-posts are generally patterned on a uniform lattice, for instance a square lattice like Fig. 7.2**b**. In addition, the lattice should be subwavelength and satisfy the Nyquist sampling rate for the used material systems and transmission functions that are implemented [35]. With proper design, the nano-post array can have very high transmission efficiencies (80%-100%, depending on the material losses), while at the same time providing full 0-2π phase coverage with changing the nano-post dimensions [65, 66, 75]. Figure 7.2**c** shows the transmission phases and amplitudes for three arrays with different lattice constants and nano-post thicknesses

designed for blue, green, and red (480 nm, 532 nm, and 635 nm, respectively). In order to use the same material system for all colors, all metasurfaces are designed using cSi. This way, the metasurfaces for all three colors can be fabricated on the same substrates, increasing the mechanical robustness and decreasing the required packaging volume and weight significantly. The three graphs in Fig. 7.2**c** show the clear ability of the designed nano-post arrays to provide full phase coverage with high transmission. One important property of this type of metasurface is the very low coupling between adjacent nano-posts as the the high index contrast between the nano-posts and the surrounding media results in almost all of the optical energy being confined inside the nano-posts [66, 75]. As a result, sizes of the nano-posts can be changed without significantly altering the transmission phases and amplitudes of its neighbors. This enables high efficiency beam deflection to large angles, which in turn results in thin high-efficiency lenses with large NAs [32, 66].

7.4 Ray optics design of the light engine

While a single-layer metasurface lens has the ability to focus light to a point without spherical aberrations [40, 221], multiple metasurface layers are required in order to correct for other monochromatic aberrations [29, 138]. Figure 7.3 summarizes the results of one such design, where 5 metasurface layers are cascaded to provide near-diffraction-limited imaging of the green μ-LED to the input aperture of the waveguide (i.e., the prism edge). As seen in Fig. 7.3**a**, the first four metasurfaces have radii of 4.5 mm, and are each separated 1 mm from the previous surface, where the spacing glasses each have a refractive index of ~1.5. The fifth glass layer is 4 mm thick and has an index of ~1.78, to match that of the waveguide. The fifth metasurface has a diameter of 2.1 mm, resulting in an input aperture of 2.1 mm at the coupling prism. The total thickness of the device is 8 mm, and it could be fitted inside a 9mm × 9mm × 8mm cube, and thus it will occupy a volume of less than 0.65 cubic centimeters (i.e., <2 cubic centimeters for the three wavelengths combined). In addition, the total glass volume is about $3 \times 0.4 = 1.2$ cubic centimeters, so the total weight of the glass would be about 3 grams (assuming a density of 2.5 grams/cc).

As seen from the spot diagram simulations of Fig. 7.3**b**, the system has a near-diffraction-limited focusing up to a FOV of 4 mm, corresponding to an angle of ~44 degrees (0.77 Rad). Considering the ~1.5 Rad FOV, the optics has more than 3000 resolvable points along the diagonal (corresponding to more than 2000×2000 points). The light at the object plane is telecentric and is collected up to an NA of 0.25 for most

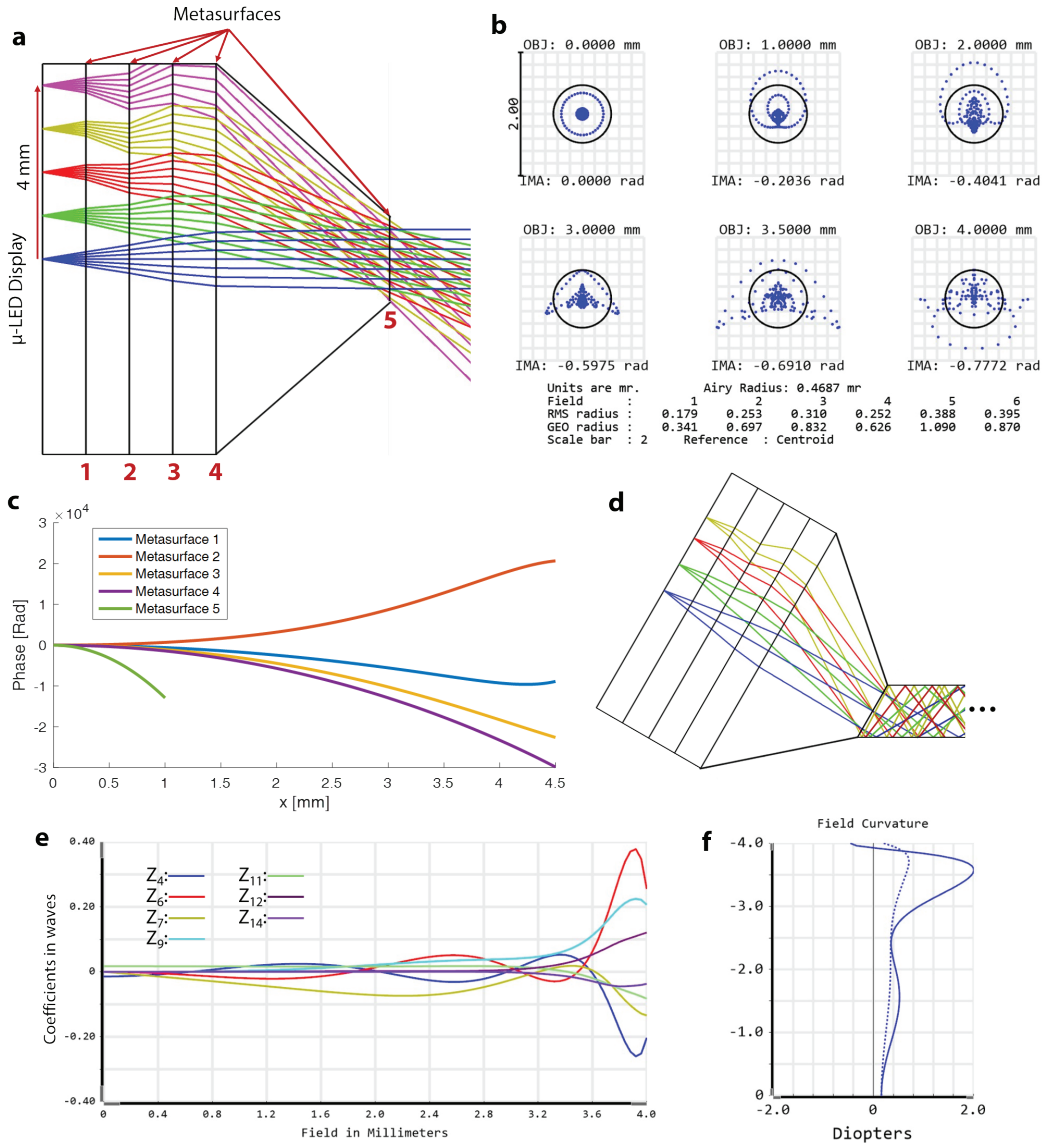

Figure 7.3: **Design of a 5-layer metasurface based light engine.** **a**, A five-layer metasurface design with a FOV of 8 mm (diameter) and collection NA of 0.25. Locations of the metasurfaces are denoted with the numbered vertical lines. The system includes 4 glass layers of 1 mm thickness each, and a fifth layer that is 4 mm thick (the conical layer). The first 4 layers have refractive indices of ~1.5, and the fifth layer has an index of ~1.78 to match that of the prism and the waveguide. **b**, Spot diagram simulations for six different points in the FOV. **c**, Optimized phase profiles for the five metasurfaces, numbered from left to the right according to panel **a**. **d**, Schematic of the light engine mounted on a 57.5-degree prism-coupled waveguide. **e**, Nonzero standard Zernike coefficients 4-14 versus the FOV, calculated for an aperture diameter of 2.1 mm. **f**, The field curvature versus FOV, showing less than 2 diopters of curvature, and also showing that the dominant aberration is astigmatism.

of the surface, except very close to 4 mm where the effective collection NA is slightly less. The optimized phase profiles for the five metasurfaces are plotted in Fig. 7.3**c**. It is worth noting that for two of the metasurfaces the maximum required OPD is about 5000 waves, which corresponds to a thickness of more than 3 mm (assuming a glass with an index of 1.78). Figure 7.3**d** schematically shows the light engine integrated with a waveguide that has a prism with a 57.5-degree edge, and therefore a thickness just below 1.8 mm. Assuming a waveguide index of 1.78 (similar to the one used here), angles from 35 to 80 degrees can be used for coupling as they are bounded by total internal reflection inside the waveguide. This means that an angular area of 45°×45° can be directly coupled inside the waveguide. Given the smaller than 0.5 mRad angular resolution, this corresponds to a resolution of more than 1500×1500 points for each color. With the three wavelengths combined, this means a total of more than 7 megapixels. On the μ-LED display, this roughly corresponds to a FOV of 4mm × 4mm. Given that μ-LED displays with pixel sizes of about 3 μm have already been demonstrated [295, 296], it seems reasonable to think that ones with pixel pitches of about 2.5 μm are feasible too. We should also note here that for such a smaller FOV, the metasurface optics can also have smaller diameter (about 7 mm) and smaller total volume (about 1.2 cc for the three wavelengths combined). In addition, the 45°×45° FOV inside the waveguide translates to a larger than 85°×85° FOV in air.

Figures 7.3**e** and 7.3**f** show the first nonzero standard Zernike coefficients (Z_4 to Z_{14}) and the field curvature, respectively. As seen from both graphs, the dominant aberration is astigmatism. Nevertheless, the RMS wavefront error (calculated from rays in reference to the centroid) is smaller than 0.25 waves over the whole FOV, and is smaller than 0.1 waves for field values below 3 mm. Calculated from the Zernike coefficients, the wavefront error peaks at slightly above 0.4 waves close to 3.9 mm, and is smaller than 0.25 waves below 3 mm.

7.5 Discussion

Like any other optical system, the design of the metasurface light engine optics involves various compromises. For instance, the collection NA and the angular resolution of the optics can be increased at the expense of FOV (with the same volume constraints). One example of such an alternative design is summarized in Fig. 7.4. If high-index glass substrates are available (e.g., n≈1.95) and smaller physical FOVs are desired, more compact designs are possible, similar to the one shown in Fig. 7.4.

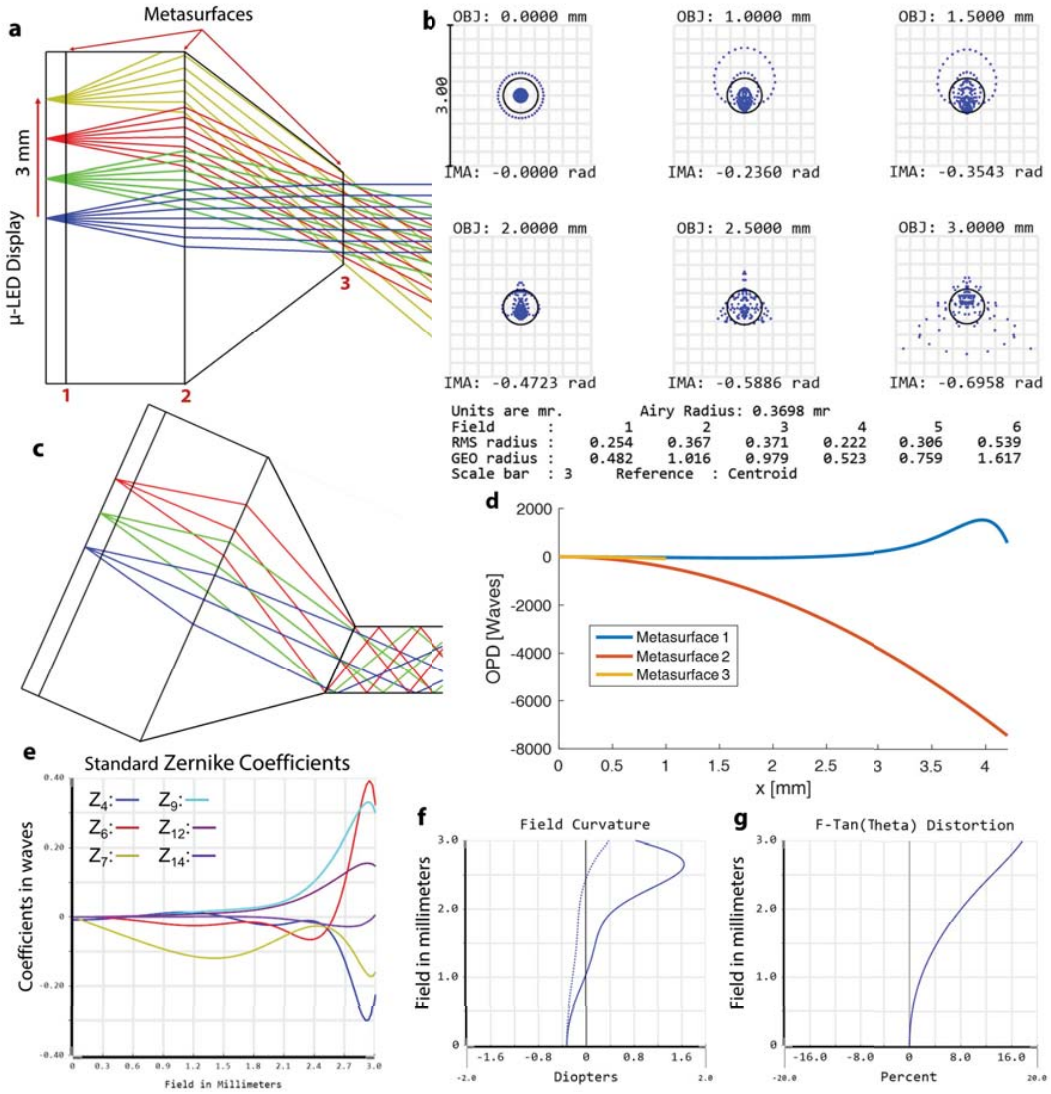

Figure 7.4: **Design of a more compact metasurface based light engine with 3 layers.** **a**, A three-layer metasurface design with a FOV of 6 mm (diameter) and collection NA of 0.4. The three glass substrates and the waveguide have refractive indices of ~1.95, and are 0.5, 3, and 4 mm thick from left to right, respectively. **b**, Spot diagram simulations for six different points in the FOV. **c**, Schematic of the light engine mounted on a 60-degree prism-coupled waveguide. **d**, Optimized phase profiles for the five metasurfaces, numbered from left to the right according to panel **a**. **e**, Nonzero standard Zernike coefficients 4-14 versus the FOV, calculated for an aperture diameter of 2 mm. **f**, The field curvature, and **g**, distortion versus FOV.

This design has three metasurface layers, and can support a diagonal FOV of 6 mm on the display. The total optics size is smaller than 6mm × 6mm × 7.5mm, and it can deliver over 2000×2000 resolved points over a 105°×105° FOV in air. Other designs that are closer to the perfect human eye resolution of 0.3 mRad are possible with a

FOV smaller than 6 mm diagonal. In addition, the number of metasurface layers is inversely proportional to the system efficiency, while it is possible to increase the collection NA with more layers. Therefore, a compromise should be made that maximizes the total system efficiency in this regard as well.

The main drawback of using metasurface optics is their large chromatic dispersion, which unlike refractive optics does not mainly originate from material dispersion and as such, unlike the case of refractive element, it cannot be solved using combination of different materials. While it is possible (and in fact relatively straightforward) to design metasurfaces that have high diffraction efficiencies over bandwidths of more than 10% [140, 297], similar to other diffractive devices [298], metasurfaces, have a large negative dispersion resulting from a phase profile that is almost constant with wavelength [135]. As a result, the regular chromatic dispersion of the metasurfaces can significantly decrease the achievable resolution and degrade the device performance. For instance, while the exact amount of degradation depends on the actual LED linewidth, for a typical value of 30-40 nm the resolution might drop by more than a factor of ten for the design in Fig. 7.4. Despite the modest success of the independent group delay-phase delay control method in addressing the chromatic dispersion issue in metasurfaces [118, 299, 300], its applicability is severely limited to devices with miniature sizes (i.e., a couple of hundred microns in diameter) because of the requirement for extremely high quality factor resonances in millimeter scale devices. As a result, the two main approaches for addressing the chromatic dispersion issue are using metasurface diffractive/refractive combinations [27, 288, 301], and decreasing the emission bandwidth of μ-LEDs. With these methods, it might be possible to decrease the effect of chromatic dispersion to levels that are acceptable for human eye.

The unique properties of metasurfaces enable a few platforms for tunable, conformal, and folded optical elements and systems that are more difficult to achieve with other technologies. For instance, various types of tunable metasurface devices, either based on stretchable substrates which is discussed in Chapter 5 [35, 124, 252], or micro-electro-mechanically tunable doublets [139] have been recently demonstrated that can potentially be integrated into the light engine optics to enable time-multiplexed multi-focus image rendering. Obviously, other types of flat tunable lenses, such as liquid crystal ones [210] can also be used for this purpose. Conformal metasurfaces discussed in Chapter 4 [124, 302] provide additional design degrees of freedom by allowing for the metasurface to be non-planar. In addition to higher diffraction

efficiencies and lower stray light, one of their main advantages over their conventional Fresnel counterparts is that the metasurface phase profile does not need to have the same symmetries of the underlying surface since the phase profile is defined lithographically in a different step. Finally, the folded metasurface optical platform can be used to reduce the total volume of the optics by using the metasurface substrate multiple times as propagation space [140]. While requiring more complicated design strategies (and potentially having a poorer optical quality), the folded metasurface platform can result in more compact devices with less complicated fabrication steps as most of the alignment steps can be eliminated.

Finally, while the use of low-throughput high-end patterning techniques like electron beam lithography is possible for proof of concept demonstrations and design rounds, it is essential to use low-cost high-throughput techniques such as nano-imprint lithography [303, 304] for mass production. Using such techniques and material systems like silicon for which high-quality etching processes are available can potentially reduce the fabrication cost of the optics.

7.6 Conclusion and outlook

In this chapter we introduced the optical metasystems as a new platform for making compact optical systems through integration of multiple co-designed metasurfaces. As an example, we proposed a design for a compact light engine composed of three monochrome μ-LED displays imaged using multi-metasurface optical systems corrected over a wide FOV. This design avoids the main challenge faced by both small μ-LED displays and metasurfaces, i.e., their operation is limited to one color range. As a proof of principle, we designed a five-layer and a three-layer metasurface optical system with a corrected FOV of 8 mm diagonal (close to 90° angular inside a glass with a refractive index of 1.78), with a close to diffraction-limited operation over the whole FOV. With a total size smaller than 2 cubic centimeters, the metasurface optics has the ability to generate 2000×2000 diffraction-limited points within its FOV. The same optics can be coupled to a waveguide delivery system and provide a wide FOV of >85°×85° in air. While several fundamental and technical challenges such as the chromatic dispersion, alignment of different colors, and fabrication tolerances need to be investigated, we believe that this work demonstrates a clear potential for metasurfaces to address some of the challenges faced in the design of compact light engines for headmounted AR displays.

Chapter 8

CONCLUSION AND OUTLOOK

HCAs outperform the other metasurface platforms in wavefront manipulation as they provide high efficiencies and novel functionalities such as control over the polarization, spectral, and angular degrees of freedom that are not available using other platforms. The development and study of optical metasurfaces have been a rapidly growing field of research in the past few years, because of their capabilities to mimic the functionality of conventional diffractive optical elements with higher efficiencies and resolutions, and more importantly for their advantages in providing new functionalities not achievable with conventional diffractive optics. Their subwavelength thickness, planar form factor, compatibility with conventional micro/nano-fabrication techniques, potentially low-cost batch fabrication, ability to replace a system of multiple bulky conventional elements with a miniature element, new capabilities to control different degrees of freedom of light, and prospects for a paradigm change in how optical systems are designed make them very promising for the realization of the next generation of compact high-performance optical systems.

Despite all the advancements made in the past few years, several challenges still remain unresolved both from fundamental and practical points of view. An important theoretical issue is the number of available degrees of freedom that exist in a single surface or a specific volume. This would determine the number of functionalities that can be encoded in such a device with negligible performance degradation. The importance of this issue becomes more clear as one considers the great interest in realizing multi-functional metasurfaces. Despite several such devices including multi-wavelength metasurfaces [135, 137, 305], multi-angle metasurfaces [15, 143], and metasurfaces with independent polarization and phase control [14, 132], the number of available degrees of freedom in such a device, and how exactly they can be utilized, is still mostly unknown. Although optimization techniques have been used to improve the performance of multi-functional devices [130, 306, 307], they still do not determine the possible number of functionalities. Another area which requires significant advancements is the modeling and design of non-periodic metasurfaces. Currently, almost all of the design methods are based on the results of simulation of periodic lattices of the meta-atoms. Although this approach works

well for slowly varying metasurfaces with small deflection angles, its underlying assumptions (namely locality, angle independence, and weak coupling of meta-atoms) cease to be valid for devices with large deflection angles. Therefore, more precise design methods that take all of these into account, and at the same time can be applied to large non-periodic structures are of great interest. In addition to enabling high-efficiency high-NA devices, such methods could also allow for the design and analysis of novel metasurfaces that are not bound by the assumption of locality. Finally, despite several attempts at realizing achromatic and dispersion-engineered metasurfaces, the operation bandwidths, sizes, and numerical apertures of devices that are possible with the existing platforms are very limited. The dependence of all of these limitations on the possible controllable quality factors that the platform provides makes the problem even more challenging. As a result, there is still a long way to the realization of achromatic and dispersion-engineered metasurfaces with practical sizes (i.e., aperture sizes of a few millimeters) and moderate to high numerical apertures.

In addition to fundamental challenges, there are also several unresolved practical issues hindering the realization of high-volume low-cost metasurface devices for real-life applications. One issue worth addressing is the absence of a low-loss high-index material for visible light. Although there have been several realization of dielectric metasurfaces in the visible [123, 219, 308, 309], their efficiency is still not as high as infrared metasurfaces where materials with low loss and high refractive index like silicon can be used. This is especially true for the cases of polarization independent metasurfaces, and devices with independent control of phase and polarization. In addition, for several applications, it is essential that the metasurface is capped by a low-index material (for instance for mechanical robustness, fabrication requirements, or realization of flexible and conformal metasurfaces). In such scenarios, the refractive index of currently available low-loss materials in the visible is not high enough to provide low-coupling between nanoposts and full phase coverage.

To have a significant industrial impact, the manufacturing processes of metasurfaces should be compatible with the existing low-cost large-scale foundry technology. Although this might already be possible for devices working in near and mid-IR (above 1.5 μm wavelength), it is challenging for devices that work below 1 μm, which are fabricated almost exclusively with EBL. In principle, large-scale fabrication techniques like DUV lithography, roll-to-roll nano-imprint, and soft lithography

could address this challenge; however, there still exist practical barriers that should be overcome before this becomes a reality.

Another category of highly desirable devices is the tunable metasurfaces. Despite several demonstrations of wavefront tuning using metasurfaces, none of them can still compete with the commercially available liquid crystal based SLMs. High-efficiency, ultra-fast, high-resolution wavefront tuning is of great need, and there is a lot of room for optimizing high-performance metadevices for beam steering applications, spatial light modulators, and dynamic holographic displays.

With the future advancements of metasurfaces in mind, we envision them at least as a complementary platform, if not a paradigm changing one, in optical element and system design for various applications.

BIBLIOGRAPHY

[1] S. M. Kamali*, E. Arbabi*, A. Arbabi, and A. Faraon, "A review of dielectric optical metasurfaces for wavefront control", Nanophotonics **7**, 1041–1068 (2018) DOI: 10.1515/nanoph-2017-0129, (cited on pp. 1, 40, 97).

[2] C. L. Holloway, E. F. Kuester, J. A. Gordon, J. O'Hara, J. Booth, and D. R. Smith, "An overview of the theory and applications of metasurfaces: the two-dimensional equivalents of metamaterials", IEEE Antennas Propag. Mag. **54**, 10–35 (2012) (cited on p. 1).

[3] A. V. Kildishev, A. Boltasseva, and V. M. Shalaev, "Planar photonics with metasurfaces", Science **339**, 1232009 (2013) (cited on pp. 1, 3, 97).

[4] N. Yu, and F. Capasso, "Flat optics with designer metasurfaces", Nat. Mater. **13**, 139–150 (2014) (cited on p. 1).

[5] N. M. Estakhri, and A. Alu, "Recent progress in gradient metasurfaces", J. Opt. Soc. Am. B **33**, A21–A30 (2016) (cited on p. 1).

[6] S. Jahani, and Z. Jacob, "All-dielectric metamaterials", Nat. Nanotechnol. **11**, 23–36 (2016) (cited on p. 1).

[7] P. Lalanne, and P. Chavel, "Metalenses at visible wavelengths: past, present, perspectives", Laser Photon. Rev. **11**, 1600295 (2017) (cited on pp. 1, 40, 97).

[8] I. Staude, and J. Schilling, "Metamaterial-inspired silicon nanophotonics", Nat. Photon. **11**, 274–284 (2017) (cited on p. 1).

[9] P. Genevet, F. Capasso, F. Aieta, M. Khorasaninejad, and R. Devlin, "Recent advances in planar optics: from plasmonic to dielectric metasurfaces", Optica **4**, 139–152 (2017) (cited on p. 1).

[10] H.-H. Hsiao, C. H. Chu, and D. P. Tsai, "Fundamentals and applications of metasurfaces", Small Methods **1**, 1600064 (2017) (cited on pp. 1, 97).

[11] P. Qiao, W. Yang, and C. J. Chang-Hasnain, "Recent advances in high-contrast metastructures, metasurfaces, and photonic crystals", Adv. Opt. Photonics **10**, 180–245 (2018) (cited on pp. 1, 40, 97).

[12] W. Zi Jing, W. Yuan, O. Kevin, R. Junsuk, Y. Xiaobo, Z. Shuang, F. Nicholas, Y. Ta-Jen, and Z. Xiang, "Optical and acoustic metamaterials: superlens, negative refractive index and invisibility cloak", J. Opt. **19**, 084007 (2017) (cited on p. 1).

[13] S. Kruk, and Y. Kivshar, "Functional meta-optics and nanophotonics governed by Mie resonances", ACS Photonics **4**, 2638–2649 (2017) (cited on p. 1).

[14] A. Arbabi, Y. Horie, M. Bagheri, and A. Faraon, "Dielectric metasurfaces for complete control of phase and polarization with subwavelength spatial resolution and high transmission", Nat. Nanotechnol. **10**, 937–943 (2015) (cited on pp. 1, 5, 10, 20, 28–33, 38, 40, 41, 64, 97, 103, 123).

[15] S. M. Kamali, E. Arbabi, A. Arbabi, Y. Horie, M. Faraji-Dana, and A. Faraon, "Angle-multiplexed metasurfaces: encoding independent wavefronts in a single metasurface under different illumination angles", Phys. Rev. X **7**, 041056 (2017) DOI: 10.1103/PhysRevX.7.041056, (cited on pp. 1, 10, 97, 123).

[16] J. Huang, and J. A. Encinar, *Reflectarray antennas* (John Wiley & Sons, Inc., 2007) (cited on p. 2).

[17] D. M. Pozar, and T. A. Metzler, "Analysis of a reflectarray antenna using microstrip patches of variable size", Electron. Lett. **29**, 657–658 (1993) (cited on p. 2).

[18] N. Yu, P. Genevet, M. A. Kats, F. Aieta, J.-P. Tetienne, F. Capasso, and Z. Gaburro, "Light propagation with phase discontinuities: generalized laws of reflection and refraction", Science **334**, 333–337 (2011) (cited on pp. 2–4).

[19] C. S. Malagisi, "Microstrip disc element reflect array", in Eascon '78; electronics and aerospace systems convention (1978), pp. 186–192 (cited on p. 2).

[20] J. Huang, and R. J. Pogorzelski, "A ka-band microstrip reflectarray with elements having variable rotation angles", IEEE Trans. Antennas Propag. **46**, 650–656 (1998) (cited on p. 2).

[21] R. C. Fairchild, and J. R. Fienup, "Computer-originated aspheric holographic optical elements", Opt. Eng. **21**, 211133–211140 (1982) (cited on p. 2).

[22] L. B. Lesem, P. M. Hirsch, and J. A. Jordan, "The kinoform: a new wavefront reconstruction device", IBM J. Res. Dev. **13**, 150–155 (1969) (cited on p. 2).

[23] D. C. O'Shea, T. J. Suleski, A. D. Kathman, and D. W. Prather, *Diffractive optics: design, fabrication, and test* (SPIE Press, 2004) (cited on pp. 2, 3).

[24] W. Stork, N. Streibl, H. Haidner, and P. Kipfer, "Artificial distributed-index media fabricated by zero-order gratings", Opt. Lett. **16**, 1921–1923 (1991) (cited on p. 2).

[25] M. W. Farn, "Binary gratings with increased efficiency", Appl. Opt. **31**, 4453–4458 (1992) (cited on p. 2).

[26] G. J. Swanson, *Binary optics technology: theoretical limits on the diffraction efficiency of multilevel diffractive optical elements*, tech. rep. (DTIC Document, 1991) (cited on p. 3).

[27] G. J. Swanson, *Binary optics technology: the theory and design of multi-level diffractive optical elements*, tech. rep. (DTIC Document, 1989) (cited on pp. 3, 121).

[28] W. T. Welford, "Aplanatic hologram lenses on spherical surfaces", Opt. Commun. **9**, 268–269 (1973) (cited on p. 3).

[29] D. A. Buralli, and G. M. Morris, "Design of a wide field diffractive landscape lens", Appl. Opt. **28**, 3950–3959 (1989) (cited on pp. 3, 117).

[30] "https://www.rpcphotonics.com/", (access date: 12/11/2017) (cited on p. 3).

[31] D. Fattal, J. Li, Z. Peng, M. Fiorentino, and R. G. Beausoleil, "Flat dielectric grating reflectors with focusing abilities", Nat. Photon. **4**, 466–470 (2010) (cited on pp. 3, 4, 6).

[32] D. Lin, P. Fan, E. Hasman, and M. L. Brongersma, "Dielectric gradient metasurface optical elements", Science **345**, 298–302 (2014) (cited on pp. 3, 4, 40, 117).

[33] C. Pfeiffer, and A. Grbic, "Metamaterial Huygens' surfaces: tailoring wave fronts with reflectionless sheets", Phys. Rev. Lett. **110**, 197401 (2013) (cited on pp. 3, 4).

[34] Y. F. Yu, A. Y. Zhu, R. Paniagua-Dominguez, Y. H. Fu, B. Luk'yanchuk, and A. I. Kuznetsov, "High-transmission dielectric metasurface with 2π phase control at visible wavelengths", Laser Photon. Rev. **9**, 412–418 (2015) (cited on pp. 4, 5, 8, 79).

[35] S. M. Kamali, E. Arbabi, A. Arbabi, Y. Horie, and A. Faraon, "Highly tunable elastic dielectric metasurface lenses", Laser Photon. Rev. **10**, 1062–1062 (2016) DOI: 10.1002/lpor.201600144, (cited on pp. 4–6, 10, 35, 97, 116, 121).

[36] F. Lu, F. G. Sedgwick, V. Karagodsky, C. Chase, and C. J. Chang-Hasnain, "Planar high-numerical-aperture low-loss focusing reflectors and lenses using subwavelength high contrast gratings", Opt. Express **18**, 12606–12614 (2010) (cited on pp. 3, 6).

[37] D. Fattal, J. Li, Z. Peng, M. Fiorentino, and R. G. Beausoleil, "A silicon lens for integrated free-space optics", in Advanced photonics, OSA Technical Digest (CD) (2011), ITuD2 (cited on pp. 3, 5, 6, 9).

[38] Y. Zhao, and A. Alu, "Manipulating light polarization with ultrathin plasmonic metasurfaces", Phys. Rev. B **84**, 205428 (2011) (cited on p. 3).

[39] Y. Zhao, N. Engheta, and A. Alu, "Homogenization of plasmonic metasurfaces modeled as transmission-line loads", Metamaterials **5**, 90–96 (2011) (cited on p. 3).

[40] F. Aieta, P. Genevet, M. A. Kats, N. Yu, R. Blanchard, Z. Gaburro, and F. Capasso, "Aberration-free ultrathin flat lenses and axicons at telecom wavelengths based on plasmonic metasurfaces", Nano Lett. **12**, 4932–4936 (2012) (cited on pp. 3, 117).

[41] L. Huang, X. Chen, H. Muhlenbernd, G. Li, B. Bai, Q. Tan, G. Jin, T. Zentgraf, and S. Zhang, "Dispersionless phase discontinuities for controlling light propagation", Nano Lett. **12**, 5750–5755 (2012) (cited on p. 3).

[42] A. Di Falco, Y. Zhao, and A. Alu, "Optical metasurfaces with robust angular response on flexible substrates", Appl. Phys. Lett. **99**, 163110 (2011) (cited on p. 3).

[43] N. Yu, F. Aieta, P. Genevet, M. A. Kats, Z. Gaburro, and F. Capasso, "A broadband, background-free quarter-wave plate based on plasmonic metasurfaces", Nano Lett. **12**, 6328–6333 (2012) (cited on p. 3).

[44] G. Li, M. Kang, S. Chen, S. Zhang, E. Y.-B. Pun, K. W. Cheah, and J. Li, "Spin-enabled plasmonic metasurfaces for manipulating orbital angular momentum of light", Nano Lett. **13**, 4148–4151 (2013) (cited on p. 3).

[45] X. Ni, A. V. Kildishev, and V. M. Shalaev, "Metasurface holograms for visible light", Nat. Commun. **4**, 2807 (2013) (cited on p. 3).

[46] A. Pors, and S. I. Bozhevolnyi, "Plasmonic metasurfaces for efficient phase control in reflection", Opt. Express **21**, 27438–27451 (2013) (cited on p. 3).

[47] A. Pors, M. G. Nielsen, R. L. Eriksen, and S. I. Bozhevolnyi, "Broadband focusing flat mirrors based on plasmonic gradient metasurfaces", Nano Lett. **13**, 829–834 (2013) (cited on p. 3).

[48] S. Datthanasombat, A. Prata, L. R. Arnaro, J. A. Harrell, S. Spitz, and J. Perret, "Layered lens antennas", in Antenn. propag. soc. symp. Vol. 2 (2001), pp. 777–780 (cited on p. 3).

[49] F. Monticone, N. M. Estakhri, and A. Alu, "Full control of nanoscale optical transmission with a composite metascreen", Phys. Rev. Lett. **110**, 203903 (2013) (cited on p. 3).

[50] A. Arbabi, and A. Faraon, "Fundamental limits of ultrathin metasurfaces", Sci. Rep. **7**, 43722 (2017) (cited on p. 3).

[51] E. Hasman, V. Kleiner, G. Biener, and A. Niv, "Polarization dependent focusing lens by use of quantized Pancharatnam-Berry phase diffractive optics", Appl. Phys. Lett. **82**, 328–330 (2003) (cited on pp. 3, 28).

[52] A. Epstein, and G. V. Eleftheriades, "Floquet-Bloch analysis of refracting Huygens metasurfaces", Phys. Rev. B **90**, 235127 (2014) (cited on p. 3).

[53] A. Epstein, and G. V. Eleftheriades, "Passive lossless Huygens metasurfaces for conversion of arbitrary source field to directive radiation", IEEE Trans. Antennas Propag. **62**, 5680–5695 (2014) (cited on p. 3).

[54] M. Kim, A. M. H. Wong, and G. V. Eleftheriades, "Optical Huygens' metasurfaces with independent control of the magnitude and phase of the local reflection coefficients", Phys. Rev. X **4**, 041042 (2014) (cited on p. 3).

[55] S. L. Jia, X. Wan, X. J. Fu, Y. J. Zhao, and T. J. Cui, "Low-reflection beam refractions by ultrathin Huygens' metasurface", AIP Adv. **5**, 067102 (2015) (cited on p. 3).

[56] A. Epstein, J. P. S. Wong, and G. V. Eleftheriades, "Cavity-excited Huygens' metasurface antennas for near-unity aperture illumination efficiency from arbitrarily large apertures", Nat. Commun. **7**, 10360 (2016) (cited on p. 3).

[57] A. Epstein, and G. V. Eleftheriades, "Huygens' metasurfaces via the equivalence principle: design and applications", J. Opt. Soc. Am. B **33**, A31–A50 (2016) (cited on p. 3).

[58] I. Staude, A. E. Miroshnichenko, M. Decker, N. T. Fofang, S. Liu, E. Gonzales, J. Dominguez, T. S. Luk, D. N. Neshev, and I. e. a. Brener, "Tailoring directional scattering through magnetic and electric resonances in subwavelength silicon nanodisks", ACS Nano **7**, 7824–7832 (2013) (cited on pp. 5, 8).

[59] S. Campione, L. I. Basilio, L. K. Warne, and M. B. Sinclair, "Tailoring dielectric resonator geometries for directional scattering and Huygens' metasurfaces", Opt. Express **23**, 2293–2307 (2015) (cited on p. 5).

[60] M. Decker, I. Staude, M. Falkner, J. Dominguez, D. N. Neshev, I. Brener, T. Pertsch, and Y. S. Kivshar, "High-efficiency dielectric Huygens' surfaces", Adv. Opt. Mater. **3**, 813–820 (2015) (cited on pp. 5, 8, 60, 79).

[61] V. Asadchy, M. Albooyeh, and S. Tretyakov, "Optical metamirror: all-dielectric frequency-selective mirror with fully controllable reflection phase", J. Opt. Soc. Am. B **33**, A16–A20 (2016) (cited on p. 5).

[62] W. Zhao, H. Jiang, B. Liu, J. Song, Y. Jiang, C. Tang, and J. Li, "Dielectric Huygens' metasurface for high-efficiency hologram operating in transmission mode", Sci. Rep. **6**, 30613 (2016) (cited on p. 5).

[63] A. Forouzmand, and H. Mosallaei, "All-dielectric c-shaped nanoantennas for light manipulation: tailoring both magnetic and electric resonances to the desire", Adv. Opt. Mater. **5**, 1700147 (2017) (cited on p. 5).

[64] A. Arbabi, M. Bagheri, A. J. Ball, Y. Horie, D. Fattal, and A. Faraon, "Controlling the phase front of optical fiber beams using high contrast metastructures", in Conference on lasers and electro-optics (cleo) (2014), STu3M.4 (cited on pp. 5, 6, 9).

[65] S. Vo, D. Fattal, W. V. Sorin, P. Zhen, T. Tho, M. Fiorentino, and R. G. Beausoleil, "Sub-wavelength grating lenses with a twist", IEEE Photon. Technol. Lett. **26**, 1375–1378 (2014) (cited on pp. 5–9, 60, 116).

[66] A. Arbabi, Y. Horie, A. J. Ball, M. Bagheri, and A. Faraon, "Subwavelength-thick lenses with high numerical apertures and large efficiency based on high-contrast transmitarrays", Nat. Commun. **6**, 7069 (2015) (cited on pp. 5–9, 29, 35, 59, 60, 63, 65, 79, 88, 116, 117).

[67] A. Arbabi, R. M. Briggs, Y. Horie, M. Bagheri, and A. Faraon, "Efficient dielectric metasurface collimating lenses for mid-infrared quantum cascade lasers", Opt. Express **23**, 33310–33317 (2015) (cited on pp. 5, 48).

[68] A. Zhan, S. Colburn, R. Trivedi, T. K. Fryett, C. M. Dodson, and A. Majumdar, "Low-contrast dielectric metasurface optics", ACS Photonics **3**, 209–214 (2016) (cited on pp. 5, 9).

[69] S. Kruk, B. Hopkins, I. I. Kravchenko, A. Miroshnichenko, D. N. Neshev, and Y. S. Kivshar, "Invited article: broadband highly efficient dielectric metadevices for polarization control", APL Photonics **1**, 030801 (2016) (cited on pp. 5, 9, 40).

[70] M. Khorasaninejad, W. T. Chen, R. C. Devlin, J. Oh, A. Y. Zhu, and F. Capasso, "Metalenses at visible wavelengths: diffraction-limited focusing and subwavelength resolution imaging", Science **352**, 1190–1194 (2016) (cited on pp. 5, 29).

[71] R. Paniagua-Dominguez, Y. F. Yu, E. Khaidarov, S. Choi, V. Leong, R. Bakker, X. Liang, Y. H. Fu, V. Valuckas, L. A. Krivitsky, and A. I. Kuznetsov, "A metalens with near-unity numerical aperture", Nano Lett. **18**, 2124–2132 (2018) (cited on pp. 5, 9, 29).

[72] B. H. Chen, P. C. Wu, V.-C. Su, Y.-C. Lai, C. H. Chu, I. C. Lee, J.-W. Chen, Y. H. Chen, Y.-C. Lan, and C.-H. e. a. Kuan, "GaN metalens for pixel-level full-color routing at visible light", Nano Lett. **17**, 6345–6352 (2017) (cited on p. 5).

[73] B. Wang, F. Dong, Q.-T. Li, D. Yang, C. Sun, J. Chen, Z. Song, L. Xu, W. Chu, and Y.-F. e. a. Xiao, "Visible-frequency dielectric metasurfaces for multiwavelength achromatic and highly dispersive holograms", Nano Lett. **16**, 5235–5240 (2016) (cited on p. 5).

[74] S. Astilean, P. Lalanne, P. Chavel, E. Cambril, and H. Launois, "High-efficiency subwavelength diffractive element patterned in a high-refractive-index material for 633 nm", Opt. Lett. **23**, 552–554 (1998) (cited on pp. 5, 29).

[75] P. Lalanne, S. Astilean, P. Chavel, E. Cambril, and H. Launois, "Blazed binary subwavelength gratings with efficiencies larger than those of conventional echelette gratings", Opt. Lett. **23**, 1081–1083 (1998) (cited on pp. 5, 6, 29, 60, 116, 117).

[76] P. Lalanne, "Waveguiding in blazed-binary diffractive elements", J. Opt. Soc. Am. A **16**, 2517–2520 (1999) (cited on pp. 5, 6, 59, 60).

[77] P. Lalanne, S. Astilean, P. Chavel, E. Cambril, and H. Launois, "Design and fabrication of blazed binary diffractive elements with sampling periods smaller than the structural cutoff", J. Opt. Soc. Am. A **16**, 1143–1156 (1999) (cited on pp. 5, 6, 9).

[78] H. Mosallaei, and K. Sarabandi, "A one-layer ultra-thin meta-surface absorber", in Antenn. propag. soc. symp. Vol. 1B (2005), pp. 615–618 (cited on p. 5).

[79] I. Martinez, A. H. Panaretos, D. H. Werner, G. Oliveri, and A. Massa, "Ultra-thin reconfigurable electromagnetic metasurface absorbers", in 7th european conference on antennas and propagation (eucap) (2013), pp. 1843–1847 (cited on p. 5).

[80] Y. Yao, R. Shankar, M. A. Kats, Y. Song, J. Kong, M. Loncar, and F. Capasso, "Electrically tunable metasurface perfect absorbers for ultrathin mid-infrared optical modulators", Nano Lett. **14**, 6526–6532 (2014) (cited on p. 5).

[81] J. Y. Jung, J. Lee, D. G. Choi, J. H. Choi, J. H. Jeong, E. S. Lee, and D. P. Neikirk, "Wavelength-selective infrared metasurface absorber for multispectral thermal detection", IEEE Photon. Jour. **7**, 1–10 (2015) (cited on p. 5).

[82] Z. Yang, B. O. Zhu, and Y. Feng, "Free space electromagnetic wave modulation using tunable metasurface absorber", in Asia-pacific microwave conference (apmc), Vol. 1 (2015), pp. 1–3 (cited on p. 5).

[83] Y. Ra'di, V. S. Asadchy, S. U. Kosulnikov, M. M. Omelyanovich, D. Morits, A. V. Osipov, C. R. Simovski, and S. A. Tretyakov, "Full light absorption in single arrays of spherical nanoparticles", ACS Photonics **2**, 653–660 (2015) (cited on p. 5).

[84] A. K. Azad, W. J. M. Kort-Kamp, M. Sykora, N. R. Weisse-Bernstein, T. S. Luk, A. J. Taylor, D. A. R. Dalvit, and H.-T. Chen, "Metasurface broadband solar absorber", Sci. Rep. **6**, 20347 (2016) (cited on p. 5).

[85] W. Guo, Y. Liu, and T. Han, "Ultra-broadband infrared metasurface absorber", Opt. Express **24**, 20586–20592 (2016) (cited on p. 5).

[86] S. J. Kim, J. Park, M. Esfandyarpour, E. F. Pecora, P. G. Kik, and M. L. Brongersma, "Superabsorbing, artificial metal films constructed from semiconductor nanoantennas", Nano Lett. **16**, 3801–3808 (2016) (cited on p. 5).

[87] Z. Luo, J. Long, X. Chen, and D. Sievenpiper, "Electrically tunable metasurface absorber based on dissipating behavior of embedded varactors", Appl. Phys. Lett. **109**, 071107 (2016) (cited on p. 5).

[88] C. Wan, Y. Ho, S. Nunez-Sanchez, L. Chen, M. Lopez-Garcia, J. Pugh, B. Zhu, P. Selvaraj, T. Mallick, and S. e. a. Senthilarasu, "A selective metasurface absorber with an amorphous carbon interlayer for solar thermal applications", Nano Energy **26**, 392–397 (2016) (cited on p. 5).

[89] J.-Y. Jung, K. Song, J.-H. Choi, J. Lee, D.-G. Choi, J.-H. Jeong, and D. P. Neikirk, "Infrared broadband metasurface absorber for reducing the thermal mass of a microbolometer", Sci. Rep. **7**, 430 (2017) (cited on p. 5).

[90] A. Li, S. Kim, Y. Luo, Y. Li, J. Long, and D. F. Sievenpiper, "High-power transistor-based tunable and switchable metasurface absorber", IEEE Trans. Microw. Theory Tech. **65**, 2810–2818 (2017) (cited on p. 5).

[91] Z. Sun, J. Zhao, B. Zhu, T. Jiang, and Y. Feng, "Selective wave-transmitting electromagnetic absorber through composite metasurface", AIP Adv. **7**, 115017 (2017) (cited on p. 5).

[92] B. Tang, Z. Li, E. Palacios, Z. Liu, S. Butun, and K. Aydin, "Chiral-selective plasmonic metasurface absorbers operating at visible frequencies", IEEE Photon. Technol. Lett. **29**, 295–298 (2017) (cited on p. 5).

[93] R. Magnusson, and S. Wang, "Optical guided-mode resonance filter", US Patent, 5, 216, 680 (1993) (cited on p. 5).

[94] D. Shin, S. Tibuleac, T. A. Maldonado, and R. Magnusson, "Thin-film optical filters with diffractive elements and waveguides", Opt. Eng. **37**, 2634–2646 (1998) (cited on p. 5).

[95] M. Shokooh-Saremi, and R. Magnusson, "Particle swarm optimization and its application to the design of diffraction grating filters", Opt. Lett. **32**, 894–896 (2007) (cited on p. 5).

[96] J. D. Ortiz, J. D. Baena, R. Marques, and F. Medina, "A band-pass/stop filter made of SRRs and C-SRRs", in Ieee international symposium on antennas and propagation (apsursi) (2011), pp. 2669–2672 (cited on p. 5).

[97] T. Ellenbogen, K. Seo, and K. B. Crozier, "Chromatic plasmonic polarizers for active visible color filtering and polarimetry", Nano Lett. **12**, 1026–1031 (2012) (cited on pp. 5, 29).

[98] J. D. Ortiz, J. D. Baena, V. Losada, F. Medina, R. Marques, and J. L. A. Quijano, "Self-complementary metasurface for designing narrow band pass/stop filters", IEEE Microw. Wirel. Compon. Lett. **23**, 291–293 (2013) (cited on p. 5).

[99] Y. Wang, D. Stellinga, A. B. Klemm, C. P. Reardon, and T. F. Krauss, "Tunable optical filters based on silicon nitride high contrast gratings", IEEE J. Sel. Top. Quantum Electron. **21**, 108–113 (2015) (cited on p. 5).

[100] Y. Horie, A. Arbabi, S. Han, and A. Faraon, "High resolution on-chip optical filter array based on double subwavelength grating reflectors", Opt. Express **23**, 29848–29854 (2015) (cited on p. 5).

[101] Y. Horie, A. Arbabi, E. Arbabi, S. M. Kamali, and A. Faraon, "Wide bandwidth and high resolution planar filter array based on DBR-metasurface-DBR structures", Opt. Express **24**, 11677–11682 (2016) DOI: 10.1364/OE.24.011677 (cited on pp. 5, 97).

[102] Y. Horie, S. Han, J.-Y. Lee, J. Kim, Y. Kim, A. Arbabi, C. Shin, L. Shi, E. Arbabi, S. M. Kamali, H.-S. Lee, S. Hwang, and A. Faraon, "Visible wavelength color filters using dielectric subwavelength gratings for backside-illuminated CMOS image sensor technologies", Nano Lett. **17**, 3159–3164 (2017) DOI: 10.1021/acs.nanolett.7b00636 (cited on p. 5).

[103] W. Yue, S. Gao, S.-S. Lee, E.-S. Kim, and D.-Y. Choi, "Subtractive color filters based on a silicon-aluminum hybrid-nanodisk metasurface enabling enhanced color purity", Sci. Rep. **6**, 29756 (2016) (cited on p. 5).

[104] K. Yamada, K. J. Lee, Y. H. Ko, J. Inoue, K. Kintaka, S. Ura, and R. Magnusson, "Flat-top narrowband filters enabled by guided-mode resonance in two-level waveguides", Opt. Lett. **42**, 4127–4130 (2017) (cited on p. 5).

[105] M. F. Limonov, M. V. Rybin, A. N. Poddubny, and Y. S. Kivshar, "Fano resonances in photonics", Nat. Photon. **11**, 543–554 (2017) (cited on p. 5).

[106] J. Lee, M. Tymchenko, C. Argyropoulos, P.-Y. Chen, F. Lu, F. Demmerle, G. Boehm, M.-C. Amann, A. Alu, and M. A. Belkin, "Giant nonlinear response from plasmonic metasurfaces coupled to intersubband transitions", Nature **511**, 65–69 (2014) (cited on p. 5).

[107] M. Tymchenko, J. S. Gomez-Diaz, J. Lee, N. Nookala, M. A. Belkin, and A. Alu, "Gradient nonlinear Pancharatnam-Berry metasurfaces", Phys. Rev. Lett. **115**, 207403 (2015) (cited on p. 5).

[108] O. Wolf, S. Campione, A. Benz, A. P. Ravikumar, S. Liu, T. S. Luk, E. A. Kadlec, E. A. Shaner, J. F. Klem, and M. B. e. a. Sinclair, "Phased-array sources based on nonlinear metamaterial nanocavities", Nat. Commun. **6**, 7667 (2015) (cited on p. 5).

[109] R. Camacho-Morales, M. Rahmani, S. Kruk, L. Wang, L. Xu, D. A. Smirnova, A. S. Solntsev, A. Miroshnichenko, H. H. Tan, and F. e. a. Karouta, "Nonlinear generation of vector beams from AlGaAs nanoantennas", Nano Lett. **16**, 7191–7197 (2016) (cited on p. 5).

[110] N. Nookala, J. Lee, M. Tymchenko, J. Sebastian Gomez-Diaz, F. Demmerle, G. Boehm, K. Lai, G. Shvets, M.-C. Amann, and A. e. a. Alu, "Ultrathin gradient nonlinear metasurface with a giant nonlinear response", Optica **3**, 283–288 (2016) (cited on p. 5).

[111] S. Jafar-Zanjani, J. Cheng, V. Liberman, J. B. Chou, and H. Mosallaei, "Large enhancement of third-order nonlinear effects with a resonant all-dielectric metasurface", AIP Adv. **6**, 115213 (2016) (cited on p. 5).

[112] S. Liu, M. B. Sinclair, S. Saravi, G. A. Keeler, Y. Yang, J. Reno, G. M. Peake, F. Setzpfandt, I. Staude, and T. e. a. Pertsch, "Resonantly enhanced second-harmonic generation using III-V semiconductor all-dielectric metasurfaces", Nano Lett. **16**, 5426–5432 (2016) (cited on p. 5).

[113] S. V. Makarov, M. I. Petrov, U. Zywietz, V. Milichko, D. Zuev, N. Lopanitsyna, A. Kuksin, I. Mukhin, G. Zograf, and E. e. a. Ubyivovk, "Efficient second-harmonic generation in nanocrystalline silicon nanoparticles", Nano Lett. **17**, 3047–3053 (2017) (cited on p. 5).

[114] A. E. Miroshnichenko, A. B. Evlyukhin, Y. F. Yu, R. M. Bakker, A. Chipouline, A. I. Kuznetsov, B. Luk'yanchuk, B. N. Chichkov, and Y. S. Kivshar, "Nonradiating anapole modes in dielectric nanoparticles", Nat. Commun. **6**, 8069 (2015) (cited on p. 5).

[115] P. C. Wu, C. Y. Liao, V. Savinov, T. L. Chung, W. T. Chen, Y.-W. Huang, P. R. Wu, Y.-H. Chen, A.-Q. Liu, and N. I. e. a. Zheludev, "Optical anapole metamaterial", ACS Nano **12**, 1920–1927 (2018) (cited on p. 5).

[116] A. B. Klemm, D. Stellinga, E. R. Martins, L. Lewis, G. Huyet, L. O'Faolain, and T. F. Krauss, "Experimental high numerical aperture focusing with high contrast gratings", Opt. Lett. **38**, 3410–3413 (2013) (cited on p. 6).

[117] Y. Yang, W. Wang, P. Moitra, I. I. Kravchenko, D. P. Briggs, and J. Valentine, "Dielectric meta-reflectarray for broadband linear polarization conversion and optical vortex generation", Nano Lett. **14**, 1394–1399 (2014) (cited on pp. 6, 8, 40).

[118] E. Arbabi, A. Arbabi, S. M. Kamali, Y. Horie, and A. Faraon, "Controlling the sign of chromatic dispersion in diffractive optics with dielectric metasurfaces", Optica **4**, 625–632 (2017) DOI: 10.1364/OPTICA.4.000625 (cited on pp. 6, 10, 15, 38, 97, 121).

[119] A. Arbabi, E. Arbabi, Y. Horie, S. M. Kamali, and A. Faraon, "Planar metasurface retroreflector", Nat. Photon. **11**, 415–420 (2017) DOI: 10.1038/nphoton.2017.96 (cited on pp. 6, 10, 15, 29, 97).

[120] A. Arbabi, Y. Horie, and A. Faraon, "Planar retroreflector", in Conference on lasers and electro-optics (cleo) (2014), pp. 1–2 (cited on p. 6).

[121] C. Hong, S. Colburn, and A. Majumdar, "Flat metaform near-eye visor", Appl. Opt. **56**, 8822–8827 (2017) (cited on p. 6).

[122] P. R. West, J. L. Stewart, A. V. Kildishev, V. M. Shalaev, V. V. Shkunov, F. Strohkendl, Y. A. Zakharenkov, R. K. Dodds, and R. Byren, "All-dielectric subwavelength metasurface focusing lens", Opt. Express **22**, 26212–26221 (2014) (cited on pp. 6, 7).

[123] M. Khorasaninejad, A. Y. Zhu, C. Roques-Carmes, W. T. Chen, J. Oh, I. Mishra, R. C. Devlin, and F. Capasso, "Polarization-insensitive metalenses at visible wavelengths", Nano Lett. **16**, 7229–7234 (2016) (cited on pp. 7–9, 124).

[124] S. M. Kamali, A. Arbabi, E. Arbabi, Y. Horie, and A. Faraon, "Decoupling optical function and geometrical form using conformal flexible dielectric metasurfaces", Nat. Commun. **7**, 11618 (2016) DOI: doi.org/10.1038/ncomms11618, (cited on pp. 7, 9, 10, 15, 40, 79, 80, 83, 97, 121).

[125] K. E. Chong, I. Staude, A. James, J. Dominguez, S. Liu, S. Campione, G. S. Subramania, T. S. Luk, M. Decker, and D. N. e. a. Neshev, "Polarization-independent silicon metadevices for efficient optical wavefront control", Nano Lett. **15**, 5369–5374 (2015) (cited on pp. 8, 79).

[126] M. I. Shalaev, J. Sun, A. Tsukernik, A. Pandey, K. Nikolskiy, and N. M. Litchinitser, "High-efficiency all-dielectric metasurfaces for ultracompact beam manipulation in transmission mode", Nano Lett. **15**, 6261–6266 (2015) (cited on p. 8).

[127] Z. Zhou, J. Li, R. Su, B. Yao, H. Fang, K. Li, L. Zhou, J. Liu, D. Stellinga, and C. P. e. a. Reardon, "Efficient silicon metasurfaces for visible light", ACS Photonics **4**, 544–551 (2017) (cited on p. 9).

[128] S. J. Byrnes, A. Lenef, F. Aieta, and F. Capasso, "Designing large, high-efficiency, high-numerical-aperture, transmissive meta-lenses for visible light", Opt. Express **24**, 5110–5124 (2016) (cited on p. 9).

[129] A. Arbabi, E. Arbabi, S. M. Kamali, Y. Horie, S. Han, and A. Faraon, "Increasing efficiency of high-NA metasurface lenses", in Spie photon. west, Vol. 10113 (2017), 101130K–1 (cited on pp. 9, 35).

[130] D. Sell, J. Yang, S. Doshay, R. Yang, and J. A. Fan, "Large-angle, multifunctional metagratings based on freeform multimode geometries", Nano Lett. **17**, 3752–3757 (2017) (cited on pp. 9, 38, 123).

[131] M. P. Backlund, A. Arbabi, P. N. Petrov, E. Arbabi, S. Saurabh, A. Faraon, and W. E. Moerner, "Removing orientation-induced localization biases in single-molecule microscopy using a broadband metasurface mask", Nat. Photon. **10**, 459–462 (2016) DOI: 10.1038/nphoton.2016.93 (cited on pp. 10, 40, 48).

[132] E. Arbabi, S. M. Kamali, A. Arbabi, and A. Faraon, "Full-stokes imaging polarimetry using dielectric metasurfaces", ACS Photonics **5**, 3132–3140 (2018) DOI: 10.1021/acsphotonics.8b00362, (cited on pp. 10, 40, 123).

[133] E. Arbabi, S. M. Kamali, A. Arbabi, and A. Faraon, "Vectorial holograms with a dielectric metasurface: ultimate polarization pattern generation", Submitted, (cited on p. 10).

[134] S. M. Kamali, E. Arbabi, A. Arbabi, Y. Horie, and A. Faraon, "Metasurfaces with controlled angular phase dispersion", in Spie photon. west (2017), 101130Q (cited on p. 10).

[135] E. Arbabi, A. Arbabi, S. M. Kamali, Y. Horie, and A. Faraon, "Multiwavelength polarization-insensitive lenses based on dielectric metasurfaces with meta-molecules", Optica **3**, 628–633 (2016) DOI: 10.1364/OPTICA.3.000628 (cited on pp. 10, 121, 123).

[136] E. Arbabi, A. Arbabi, S. M. Kamali, Y. Horie, and A. Faraon, "Multiwavelength metasurfaces through spatial multiplexing", Sci. Rep. **6**, 32803 (2016) DOI: 10.1038/srep32803 (cited on pp. 10, 20, 38).

[137] E. Arbabi, A. Arbabi, S. M. Kamali, Y. Horie, and A. Faraon, "High efficiency double-wavelength dielectric metasurface lenses with dichroic birefringent meta-atoms", Opt. Express **24**, 18468–18477 (2016) DOI: 10.1364/OE.24.018468 (cited on pp. 10, 20, 123).

[138] A. Arbabi, E. Arbabi, S. M. Kamali, Y. Horie, S. Han, and A. Faraon, "Miniature optical planar camera based on a wide-angle metasurface doublet corrected for monochromatic aberrations", Nat. Commun. **7**, 13682 (2016) DOI: 10.1038/ncomms13682 (cited on pp. 10, 29, 38, 88, 97, 112, 117).

[139] E. Arbabi, A. Arbabi, S. M. Kamali, Y. Horie, M. Faraji-Dana, and A. Faraon, "Mems-tunable dielectric metasurface lens", Nat. Commun. **9**, 812 (2018) DOI: 10.1038/s41467-018-03155-6 (cited on pp. 10, 29, 97, 121).

[140] M. Faraji-Dana*, E. Arbabi*, A. Arbabi, S. M. Kamali, H. Kwon, and A. Faraon, "Compact folded metasurface spectrometer", Nat. Commun. **9**, 4196 (2018) DOI: 10.1038/s41467-018-06495-5 (cited on pp. 10, 112, 121, 122).

[141] M. Faraji-Dana, E. Arbabi, H. Kwon, S. M. Kamali, A. Arbabi, J. G. Bartholomew, and A. Faraon, "Miniaturized metasurface hyperspectral-imager", Submitted (cited on p. 10).

[142] A. F. Oskooi, D. Roundy, M. Ibanescu, P. Bermel, J. D. Joannopoulos, and S. G. Johnson, "Meep: a flexible free-software package for electromagnetic simulations by the FDTD method", Comput. Phys. Commun. **181**, 687–702 (2010) (cited on p. 18).

[143] J. Cheng, S. Inampudi, and H. Mosallaei, "Optimization-based dielectric metasurfaces for angle-selective multifunctional beam deflection", Sci. Rep. **7**, 12228 (2017) (cited on pp. 19, 123).

[144] V. S. Asadchy, A. Díaz-Rubio, S. N. Tcvetkova, D. H. Kwon, A. Elsakka, M. Albooyeh, and S. A. Tretyakov, "Flat engineered multichannel reflectors", Phys. Rev. X **7**, 031046 (2017) (cited on p. 19).

[145] J. P. Balthasar Mueller, N. A. Rubin, R. C. Devlin, B. Groever, and F. Capasso, "Metasurface polarization optics: independent phase control of arbitrary orthogonal states of polarization", Phys. Rev. Lett. **118**, 113901 (2017) (cited on pp. 20, 40).

[146] F. Aieta, M. A. Kats, P. Genevet, and F. Capasso, "Multiwavelength achromatic metasurfaces by dispersive phase compensation", Science **347**, 1342–1345 (2015) (cited on pp. 20, 88).

[147] D. Lin, A. L. Holsteen, E. Maguid, G. Wetzstein, P. G. Kik, E. Hasman, and M. L. Brongersma, "Photonic multitasking interleaved Si nanoantenna phased array", Nano Lett. **16**, 7671–7676 (2016) (cited on pp. 20, 38).

[148] V. Liu, and S. Fan, "S4 : a free electromagnetic solver for layered periodic structures", Comput. Phys. Commun. **183**, 2233–2244 (2012) (cited on pp. 20, 48, 54, 66, 80, 105).

[149] X. Zhu, Z. Ge, T. X. Wu, and S.-T. Wu, "Transflective liquid crystal displays", J. Display Technol. **1**, 15 (2005) (cited on p. 27).

[150] D.-K. Yang, *Fundamentals of liquid crystal devices* (John Wiley & Sons, 2014) (cited on p. 27).

[151] Q. Zhan, "Trapping metallic rayleigh particles with radial polarization", Opt. Express **12**, 3377–3382 (2004) (cited on p. 27).

[152] Y. Kozawa, and S. Sato, "Optical trapping of micrometer-sized dielectric particles by cylindrical vector beams", Opt. Express **18**, 10828–10833 (2010) (cited on p. 27).

[153] M. Meier, V. Romano, and T. Feurer, "Material processing with pulsed radially and azimuthally polarized laser radiation", Appl. Phys. A **86**, 329–334 (2007) (cited on p. 27).

[154] R. Weber, A. Michalowski, M. Abdou-Ahmed, V. Onuseit, V. Rominger, M. Kraus, and T. Graf, "Effects of radial and tangential polarization in laser material processing", Physics Procedia **12**, 21–30 (2011) (cited on p. 27).

[155] G. S. Duesberg, I. Loa, M. Burghard, K. Syassen, and S. Roth, "Polarized raman spectroscopy on isolated single-wall carbon nanotubes", Phys. Rev. Lett. **85**, 5436–5439 (2000) (cited on p. 27).

[156] J. M. Benevides, S. A. Overman, and G. J. Thomas Jr, "Raman, polarized raman and ultraviolet resonance raman spectroscopy of nucleic acids and their complexes", J. Raman Spectrosc. **36**, 279–299 (2005) (cited on p. 27).

[157] L. Nikolova, and T. Todorov, "Diffraction efficiency and selectivity of polarization holographic recording", Optica Acta **31**, 579–588 (1984) (cited on pp. 27, 40).

[158] J. Tervo, and J. Turunen, "Paraxial-domain diffractive elements with 100% efficiency based on polarization gratings", Opt. Lett. **25**, 785–786 (2000) (cited on p. 27).

[159] C. Oh, and M. J. Escuti, "Achromatic diffraction from polarization gratings with high efficiency", Opt. Lett. **33**, 2287–2289 (2008) (cited on pp. 27, 40).

[160] Z. Bomzon, V. Kleiner, and E. Hasman, "Computer-generated space-variant polarization elements with subwavelength metal stripes", Opt. Lett. **26**, 33–35 (2001) (cited on p. 28).

[161] Z. Bomzon, V. Kleiner, and E. Hasman, "Pancharatnam-Berry phase in space-variant polarization-state manipulations with subwavelength gratings", Opt. Lett. **26**, 1424–1426 (2001) (cited on pp. 28, 40).

[162] E. Hasman, Z. Bomzon, A. Niv, G. Biener, and V. Kleiner, "Polarization beam-splitters and optical switches based on space-variant computer-generated subwavelength quasi-periodic structures", Opt. Commun. **209**, 45–54 (2002) (cited on p. 28).

[163] G. Biener, A. Niv, V. Kleiner, and E. Hasman, "Formation of helical beams by use of Pancharatnam-Berry phase optical elements", Opt. Lett. **27**, 1875–1877 (2002) (cited on pp. 28, 40).

[164] Z. Bomzon, G. Biener, V. Kleiner, and E. Hasman, "Space-variant Pancharatnam-Berry phase optical elements with computer-generated subwavelength gratings", Opt. Lett. **27**, 1141–1143 (2002) (cited on p. 28).

[165] C.-H. Tsai, U. Levy, L. Pang, and S. Fainman, "Fabrication and characterization of GaAs-based space-variant inhomogeneous media for polarization control at 10.6 μm", in Spie optical science and technology, Vol. 5515 (2004), p. 8 (cited on p. 28).

[166] U. Levy, C.-H. Tsai, L. Pang, and Y. Fainman, "Engineering space-variant inhomogeneous media for polarization control", Opt. Lett. **29**, 1718–1720 (2004) (cited on pp. 28, 40).

[167] C.-I. Chang, *Hyperspectral imaging: techniques for spectral detection and classification*, Vol. 1 (Springer Science & Business Media, 2003) (cited on p. 28).

[168] D.-W. Sun, *Hyperspectral imaging for food quality analysis and control* (Elsevier, 2010) (cited on p. 28).

[169] J. S. Tyo, D. L. Goldstein, D. B. Chenault, and J. A. Shaw, "Review of passive imaging polarimetry for remote sensing applications", Appl. Opt. **45**, 5453–5469 (2006) (cited on pp. 28–30).

[170] N. M. Garcia, I. de Erausquin, C. Edmiston, and V. Gruev, "Surface normal reconstruction using circularly polarized light", Opt. Express **23**, 14391–14406 (2015) (cited on p. 28).

[171] D. L. Coffeen, "Polarization and scattering characteristics in the atmospheres of earth, venus, and jupiter", J. Opt. Soc. Am. **69**, 1051–1064 (1979) (cited on p. 28).

[172] R. Walraven, "Polarization imagery", in Spie opt. eng. Vol. 20 (1981), p. 200114 (cited on p. 28).

[173] W. G. Egan, W. R. Johnson, and V. S. Whitehead, "Terrestrial polarization imagery obtained from the space shuttle:characterization and interpretation", Appl. Opt. **30**, 435–442 (1991) (cited on p. 28).

[174] Y. Liu, T. York, W. Akers, G. Sudlow, V. Gruev, and S. Achilefu, "Complementary fluorescence-polarization microscopy using division-of-focal-plane polarization imaging sensor", J. Biomed. Opt. **17**, 116001 (2012) (cited on p. 28).

[175] N. W. Roberts, M. J. How, M. L. Porter, S. E. Temple, R. L. Caldwell, S. B. Powell, V. Gruev, N. J. Marshall, and T. W. Cronin, "Animal polarization imaging and implications for optical processing", Proceed. IEEE **102**, 1427–1434 (2014) (cited on p. 28).

[176] T. Charanya, T. York, S. Bloch, G. Sudlow, K. Liang, M. Garcia, W. J. Akers, D. Rubin, V. Gruev, and S. Achilefu, "Trimodal color-fluorescence-polarization endoscopy aided by a tumor selective molecular probe accurately detects flat lesions in colitis-associated cancer", J. Biomed. Opt. **19**, 14 (2014) (cited on p. 28).

[177] M. Garcia, C. Edmiston, R. Marinov, A. Vail, and V. Gruev, "Bio-inspired color-polarization imager for real-time in situ imaging", Optica **4**, 1263–1271 (2017) (cited on pp. 28, 29).

[178] J. Johnson, "Infrared polarization signature feasibility tests", US Army Mobility Equipment Research and Development Center **TR-EO-74-1 (AD COO1-133)** (1974) (cited on p. 28).

[179] S. A. Chin-Bing, "Infrared polarization signature analysis", Defense Technical Information Center **Rep. ADC008418** (1976) (cited on p. 28).

[180] J. E. Solomon, "Polarization imaging", Appl. Opt. **20**, 1537–1544 (1981) (cited on p. 28).

[181] J. L. Pezzaniti, and R. A. Chipman, "Mueller matrix imaging polarimetry", in Opt. eng. Vol. 34 (1995), p. 11 (cited on p. 28).

[182] G. P. Nordin, J. T. Meier, P. C. Deguzman, and M. W. Jones, "Micropolarizer array for infrared imaging polarimetry", J. Opt. Soc. Am. A **16**, 1168–1174 (1999) (cited on pp. 28, 29).

[183] J. Guo, and D. Brady, "Fabrication of thin-film micropolarizer arrays for visible imaging polarimetry", Appl. Opt. **39**, 1486–1492 (2000) (cited on pp. 28, 29).

[184] V. Gruev, J. V. d. Spiegel, and N. Engheta, "Image sensor with focal plane extraction of polarimetric information", in 2006 ieee international symposium on circuits and systems (2006), pp. 214–216 (cited on p. 28).

[185] D. Rust, "Integrated dual imaging detector", US Patent, 5, 438, 414 (1995) (cited on p. 29).

[186] A. G. Andreou, and Z. K. Kalayjian, "Polarization imaging: principles and integrated polarimeters", IEEE Sens. Jour. **2**, 566–576 (2002) (cited on p. 29).

[187] V. Gruev, A. Ortu, N. Lazarus, J. V. d. Spiegel, and N. Engheta, "Fabrication of a dual-tier thin film micropolarization array", Opt. Exp. **15**, 4994–5007 (2007) (cited on p. 29).

[188] V. Gruev, R. Perkins, and T. York, "Ccd polarization imaging sensor with aluminum nanowire optical filters", Opt. Express **18**, 19087–19094 (2010) (cited on p. 29).

[189] P. C. Deguzman, and G. P. Nordin, "Stacked subwavelength gratings as circular polarization filters", Appl. Opt. **40**, 5731–5737 (2001) (cited on p. 29).

[190] G. Myhre, W.-L. Hsu, A. Peinado, C. LaCasse, N. Brock, R. A. Chipman, and S. Pau, "Liquid crystal polymer full-Stokes division of focal plane polarimeter", Opt. Express **20**, 27393–27409 (2012) (cited on p. 29).

[191] W.-L. Hsu, G. Myhre, K. Balakrishnan, N. Brock, M. Ibn-Elhaj, and S. Pau, "Full-stokes imaging polarimeter using an array of elliptical polarizer", Opt. Express **22**, 3063–3074 (2014) (cited on p. 29).

[192] W.-L. Hsu, J. Davis, K. Balakrishnan, M. Ibn-Elhaj, S. Kroto, N. Brock, and S. Pau, "Polarization microscope using a near infrared full-stokes imaging polarimeter", Opt. Express **23**, 4357–4368 (2015) (cited on p. 29).

[193] B. Groever, W. T. Chen, and F. Capasso, "Meta-lens doublet in the visible region", Nano Lett. **17**, 4902–4907 (2017) (cited on p. 29).

[194] D. Wen, F. Yue, S. Kumar, Y. Ma, M. Chen, X. Ren, P. E. Kremer, B. D. Gerardot, M. R. Taghizadeh, and G. S. e. a. Buller, "Metasurface for characterization of the polarization state of light", Opt. Express **23**, 10272–10281 (2015) (cited on p. 29).

[195] M. Khorasaninejad, W. Zhu, and K. B. Crozier, "Efficient polarization beam splitter pixels based on a dielectric metasurface", Optica **2**, 376–382 (2015) (cited on p. 29).

[196] A. Pors, M. G. Nielsen, and S. I. Bozhevolnyi, "Plasmonic metagratings for simultaneous determination of stokes parameters", Optica **2**, 716–723 (2015) (cited on p. 29).

[197] W. T. Chen, P. Torok, M. R. Foreman, C. Y. Liao, W. Y. Tsai, P. R. Wu, and D. P. Tsai, "Integrated plasmonic metasurfaces for spectropolarimetry", Nanotechnology **27**, 224002 (2016) (cited on p. 29).

[198] J. P. Balthasar Mueller, K. Leosson, and F. Capasso, "Ultracompact metasurface in-line polarimeter", Optica **3**, 42–47 (2016) (cited on p. 29).

[199] F. Ding, A. Pors, Y. Chen, V. A. Zenin, and S. I. Bozhevolnyi, "Beam-size-invariant spectropolarimeters using gap-plasmon metasurfaces", ACS Photonics **4**, 943–949 (2017) (cited on p. 29).

[200] E. Maguid, I. Yulevich, M. Yannai, V. Kleiner, M. L. Brongersma, and E. Hasman, "Multifunctional interleaved geometric-phase dielectric metasurfaces", Light: Sci. Appl. **6**, e17027 (2017) (cited on p. 29).

[201] S. Wei, Z. Yang, and M. Zhao, "Design of ultracompact polarimeters based on dielectric metasurfaces", Opt. Lett. **42**, 1580–1583 (2017) (cited on p. 29).

[202] S. Huard, *Polarization of light*, Vol. 1 (Wiley-VCH, 1997) (cited on p. 30).

[203] R. C. Jones, "A new calculus for the treatment of optical systems. i. description and discussion of the calculus", J. Opt. Soc. Am. **31**, 488–493 (1941) (cited on p. 32).

[204] B. Bayer, "Color imaging array", US Patent, 3, 971, 065 (1976) (cited on p. 38).

[205] J. Hu, C.-H. Liu, X. Ren, L. J. Lauhon, and T. W. Odom, "Plasmonic lattice lenses for multiwavelength achromatic focusing", ACS Nano **10**, 10275–10282 (2016) (cited on p. 38).

[206] O. Bryngdahl, "Polarizing holography", J. Opt. Soc. Am. **57**, 545–546 (1967) (cited on p. 40).

[207] M. Nakajima, H. Komatsu, Y. Mitsuhashi, and T. Morikawa, "Computer generated polarization holograms: phase recording by polarization effect in photodichroic materials", Appl. Opt. **15**, 1030–1033 (1976) (cited on p. 40).

[208] T. Todorov, L. Nikolova, and N. Tomova, "Polarization holography. 2: polarization holographic gratings in photoanisotropic materials with and without intrinsic birefringence", Appl. Opt. **23**, 4588–4591 (1984) (cited on p. 40).

[209] J. Kim, Y. Li, M. N. Miskiewicz, C. Oh, M. W. Kudenov, and M. J. Escuti, "Fabrication of ideal geometric-phase holograms with arbitrary wavefronts", Optica **2**, 958–964 (2015) (cited on p. 40).

[210] A. Jamali, D. Bryant, Y. Zhang, A. Grunnet-Jepsen, A. Bhowmik, and P. J. Bos, "Design of a large aperture tunable refractive fresnel liquid crystal lens", Appl. Opt. **57**, B10–B19 (2018) (cited on pp. 40, 121).

[211] M. Fratz, P. Fischer, and D. M. Giel, "Full phase and amplitude control in computer-generated holography", Optics Letters **34**, 3659–3661 (2009) (cited on p. 40).

[212] M. Fratz, D. M. Giel, and P. Fischer, "Digital polarization holograms with defined magnitude and orientation of each pixel's birefringence", Opt. Lett. **34**, 1270–1272 (2009) (cited on p. 40).

[213] P. Lalanne, J. Hazart, P. Chavel, E. Cambril, and H. Launois, "A transmission polarizing beam splitter grating", J. Opt. A Pure Appl. Opt. **1**, 215 (1999) (cited on p. 40).

[214] W. Yu, T. Konishi, T. Hamamoto, H. Toyota, T. Yotsuya, and Y. Ichioka, "Polarization-multiplexed diffractive optical elements fabricated by subwavelength structures", Appl. Opt. **41**, 96–100 (2002) (cited on p. 40).

[215] I. Kim, G. Yoon, J. Jang, P. Genevet, K. T. Nam, and J. Rho, "Outfitting next generation displays with optical metasurfaces", ACS Photonics **5**, 3876–3895 (2018) (cited on p. 40).

[216] V.-C. Su, C. H. Chu, G. Sun, and D. P. Tsai, "Advances in optical metasurfaces: fabrication and applications [invited]", Opt. Express **26**, 13148–13182 (2018) (cited on p. 40).

[217] Q. He, S. Sun, S. Xiao, and L. Zhou, "High-efficiency metasurfaces: principles, realizations, and applications", Adv. Opt. Mater. **6**, 1800415 (2018) (cited on p. 40).

[218] X. Zang, F. Dong, F. Yue, C. Zhang, L. Xu, Z. Song, M. Chen, P.-Y. Chen, G. S. Buller, and Y. e. a. Zhu, "Polarization encoded color image embedded in a dielectric metasurface", Adv. Mater. **30**, 1707499 (2018) (cited on p. 40).

[219] N. K. Emani, E. Khaidarov, R. Paniagua-Dominguez, Y. H. Fu, V. Valuckas, S. Lu, X. Zhang, S. T. Tan, H. V. Demir, and A. I. Kuznetsov, "High-efficiency and low-loss gallium nitride dielectric metasurfaces for nanophotonics at visible wavelengths", Appl. Phys. Lett. **111**, 221101 (2017) (cited on pp. 40, 124).

[220] S. Kruk, F. Ferreira, N. Mac Suibhne, C. Tsekrekos, I. Kravchenko, A. Ellis, D. Neshev, S. Turitsyn, and Y. Kivshar, "Transparent dielectric metasurfaces for spatial mode multiplexing", Laser Photon. Rev. **12**, 1800031 (2018) (cited on p. 40).

[221] E. Arbabi, J. Li, R. J. Hutchins, S. M. Kamali, A. Arbabi, Y. Horie, P. Van Dorpe, V. Gradinaru, D. A. Wagenaar, and A. Faraon, "Two-photon microscopy with a double-wavelength metasurface objective lens", Nano Lett. **18**, 4943–4948 (2018) DOI: 10.1021/acs.nanolett.8b01737 (cited on pp. 40, 48, 117).

[222] H. Kwon, E. Arbabi, S. M. Kamali, M. Faraji-Dana, and A. Faraon, "Computational complex optical field imaging using a designed metasurface diffuser", Optica **5**, 924–931 (2018) DOI: 10.1364/OPTICA.5.000924 (cited on p. 40).

[223] Z.-L. Deng, J. Deng, X. Zhuang, S. Wang, K. Li, Y. Wang, Y. Chi, X. Ye, J. Xu, and G. P. e. a. Wang, "Diatomic metasurface for vectorial holography", Nano Lett. **18**, 2885–2892 (2018) (cited on p. 40).

[224] R. Zhao, B. Sain, Q. Wei, C. Tang, X. Li, T. Weiss, L. Huang, Y. Wang, and T. Zentgraf, "Multichannel vectorial holographic display and encryption", Light Sci. Appl. **7**, 95 (2018) (cited on p. 40).

[225] N. A. Rubin, A. Zaidi, M. Juhl, R. P. Li, J. P. B. Mueller, R. C. Devlin, K. Leósson, and F. Capasso, "Polarization state generation and measurement with a single metasurface", Optics Express **26**, 21455–21478 (2018) (cited on p. 48).

[226] M. Born, and E. Wolf, *Principles of optics: electromagnetic theory of propagation, interference and diffraction of light*, 7th (Cambridge University Press, Cambridge, 1999) (cited on pp. 55, 105).

[227] K. P. Thompson, and J. P. Rolland, "Freeform optical surfaces: a revolution in imaging optical design", Opt. Photon. News **23**, 30–35 (2012) (cited on p. 55).

[228] R. R. Shannon, "Overview of conformal optics", in, Vol. 3705 (1999), pp. 180–189 (cited on p. 55).

[229] D. J. Knapp, "Overview of conformal optics", in, Vol. 4832 (2002), pp. 394–409 (cited on pp. 55, 56).

[230] P. Fan, U. K. Chettiar, L. Cao, F. Afshinmanesh, N. Engheta, and M. L. Brongersma, "An invisible metal–semiconductor photodetector", Nat. Photon. **6**, 380 (2012) (cited on p. 56).

[231] X. Ni, Z. J. Wong, M. Mrejen, Y. Wang, and X. Zhang, "An ultrathin invisibility skin cloak for visible light", Science **349**, 1310–1314 (2015) (cited on p. 56).

[232] J. Valentine, J. Li, T. Zentgraf, G. Bartal, and X. Zhang, "An optical cloak made of dielectrics", Nat. Mater. **8**, 568 (2009) (cited on p. 56).

[233] T. Ergin, N. Stenger, P. Brenner, J. B. Pendry, and M. Wegener, "Three-dimensional invisibility cloak at optical wavelengths", science **328**, 337–339 (2010) (cited on p. 56).

[234] G. Zheng, H. Mühlenbernd, M. Kenney, G. Li, T. Zentgraf, and S. Zhang, "Metasurface holograms reaching 80% efficiency", Nat. Nanotechnol. **10**, 308–312 (2015) (cited on p. 56).

[235] J. Y. H. Teo, L. J. Wong, C. Molardi, and P. Genevet, "Controlling electromagnetic fields at boundaries of arbitrary geometries", Phys. Rev. A **94**, 023820 (2016) (cited on p. 56).

[236] L. Josefsson, and P. Persson, *Conformal array antenna theory and design*, Vol. 29 (John wiley & sons, 2006) (cited on p. 56).

[237] J. He, R. G. Nuzzo, and J. A. Rogers, "Inorganic materials and assembly techniques for flexible and stretchable electronics", Proc. IEEE **103**, 619–632 (2015) (cited on p. 65).

[238] D.-H. Kim, J.-H. Ahn, W. M. Choi, H.-S. Kim, T.-H. Kim, J. Song, Y. Y. Huang, Z. Liu, C. Lu, and J. A. Rogers, "Stretchable and foldable silicon integrated circuits", Science **320**, 507–511 (2008) (cited on p. 65).

[239] C. Wang, D. Hwang, Z. Yu, K. Takei, J. Park, T. Chen, B. Ma, and A. Javey, "User-interactive electronic skin for instantaneous pressure visualization", Nat. Mater. **12**, 899 (2013) (cited on p. 65).

[240] J. Sauro, and J. R. Lewis, "Estimating completion rates from small samples using binomial confidence intervals: comparisons and recommendations", in Proceedings of the human factors and ergonomics society annual meeting, Vol. 49, 24 (SAGE Publications Sage CA: Los Angeles, CA, 2005), pp. 2100–2103 (cited on p. 69).

[241] L. Zhu, J. Kapraun, J. Ferrara, and C. J. Chang-Hasnain, "Flexible photonic metastructures for tunable coloration", Optica **2**, 255–258 (2015) (cited on p. 77).

[242] P. Gutruf, C. Zou, W. Withayachumnankul, M. Bhaskaran, S. Sriram, and C. Fumeaux, "Mechanically tunable dielectric resonator metasurfaces at visible frequencies", ACS Nano **10**, 133–141 (2016) (cited on pp. 77, 79).

[243] J. S. Donner, J. Morales-Dalmau, I. Alda, R. Marty, and R. Quidant, "Fast and transparent adaptive lens based on plasmonic heating", ACS Photonics **2**, 355–360 (2015) (cited on p. 77).

[244] J. Sautter, I. Staude, M. Decker, E. Rusak, D. N. Neshev, I. Brener, and Y. S. Kivshar, "Active tuning of all-dielectric metasurfaces", ACS Nano **9**, 4308–4315 (2015) (cited on p. 77).

[245] Y. Chen, X. Li, Y. Sonnefraud, A. I. Fernandez-Dominguez, X. Luo, M. Hong, and S. A. Maier, "Engineering the phase front of light with phase-change material based planar lenses", Sci. Rep. **5**, 8660 (2015) (cited on p. 77).

[246] Q. Wang, E. T. F. Rogers, B. Gholipour, C.-M. Wang, G. Yuan, J. Teng, and N. I. Zheludev, "Optically reconfigurable metasurfaces and photonic devices based on phase change materials", Nat. Photon. **10**, 60–65 (2016) (cited on p. 77).

[247] Y. Yao, R. Shankar, M. A. Kats, Y. Song, J. Kong, M. Loncar, and F. Capasso, "Electrically tunable metasurface perfect absorbers for ultrathin mid-infrared optical modulators", Nano Lett. **14**, 6526–6532 (2014) (cited on p. 77).

[248] Y.-W. Huang, H. W. H. Lee, R. Sokhoyan, R. A. Pala, K. Thyagarajan, S. Han, D. P. Tsai, and H. A. Atwater, "Gate-tunable conducting oxide metasurfaces", Nano Lett. **16**, 5319–5325 (2016) (cited on p. 77).

[249] A. Simonov, O. Akhzar-Mehr, and G. Vdovin, "Light scanner based on a viscoelastic stretchable grating", Opt. Lett. **30**, 949–951 (2005) (cited on p. 77).

[250] S. Olcum, A. Kocabas, G. Ertas, A. Atalar, and A. Aydinli, "Tunable surface plasmon resonance on an elastomeric substrate", Opt. Express **17**, 8542–8547 (2009) (cited on p. 77).

[251] X. Li, L. Wei, S. Vollebregt, R. Poelma, Y. Shen, J. Wei, P. Urbach, P. Sarro, and G. Zhang, "Tunable binary fresnel lens based on stretchable pdms/cnt composite", in 2015 transducers-2015 18th international conference on solid-state sensors, actuators and microsystems (transducers) (IEEE, 2015), pp. 2041–2044 (cited on p. 77).

[252] H.-S. Ee, and R. Agarwal, "Tunable metasurface and flat optical zoom lens on a stretchable substrate", Nano Lett. **16**, 2818–2823 (2016) (cited on pp. 77, 121).

[253] J. W. Goodman, *Introduction to fourier optics* (Roberts and Company Publishers, 2005) (cited on p. 78).

[254] A. F. Oskooi, D. Roundy, M. Ibanescu, P. Bermel, J. D. Joannopoulos, and S. G. Johnson, "Meep: a flexible free-software package for electromagnetic simulations by the FDTD method", Comput. Phys. Commun. **181**, 687–702 (2010) (cited on p. 81).

[255] E. Arbabi, A. Arbabi, S. M. Kamali, Y. Horie, and A. Faraon, "Multiwavelength polarization-insensitive lenses based on dielectric metasurfaces with meta-molecules", Optica **3**, 628–633 (2016) (cited on p. 88).

[256] E. Arbabi, A. Arbabi, S. M. Kamali, Y. Horie, and A. Faraon, "High efficiency double-wavelength dielectric metasurface lenses with dichroic birefringent meta-atoms", Opt. Express **24**, 18468–18477 (2016) (cited on p. 88).

[257] E. Arbabi, A. Arbabi, S. M. Kamali, Y. Horie, and A. Faraon, "Multiwavelength metasurfaces through spatial multiplexing", Sci. Rep. **6**, 32803 (2016) (cited on p. 88).

[258] R. Pelrine, R. Kornbluh, Q. Pei, and J. Joseph, "High-speed electrically actuated elastomers with strain greater than 100%", Science **287**, 836–839 (2000) (cited on p. 88).

[259] J. A. Rogers, T. Someya, and Y. Huang, "Materials and mechanics for stretchable electronics", Science **327**, 1603–1607 (2010) (cited on p. 88).

[260] S. V. Murphy, and A. Atala, "3d bioprinting of tissues and organs", Nat. biotechnol. **32**, 773 (2014) (cited on p. 96).

[261] T. A. Schaedler, A. J. Jacobsen, A. Torrents, A. E. Sorensen, J. Lian, J. R. Greer, L. Valdevit, and W. B. Carter, "Ultralight metallic microlattices", Science **334**, 962–965 (2011) (cited on p. 96).

[262] D. W. Yee, M. D. Schulz, R. H. Grubbs, and J. R. Greer, "Functionalized 3d architected materials via thiol-michael addition and two-photon lithography", Adv. Mater. **29**, 1605293 (2017) (cited on p. 96).

[263] E. MacDonald, and R. Wicker, "Multiprocess 3d printing for increasing component functionality", Science **353**, aaf2093 (2016) (cited on p. 96).

[264] K. A. Arpin, A. Mihi, H. T. Johnson, A. J. Baca, J. A. Rogers, J. A. Lewis, and P. V. Braun, "Multidimensional architectures for functional optical devices", Adv. Mater. **22**, 1084–1101 (2010) (cited on p. 96).

[265] J. R. Tumbleston, D. Shirvanyants, N. Ermoshkin, R. Janusziewicz, A. R. Johnson, D. Kelly, K. Chen, R. Pinschmidt, J. P. Rolland, A. Ermoshkin, et al., "Continuous liquid interface production of 3d objects", Science **347**, 1349–1352 (2015) (cited on p. 96).

[266] J. B. Reeves, R. K. Jayne, L. Barrett, A. E. White, and D. J. Bishop, "Fabrication of multi-material 3d structures by the integration of direct laser writing and mems stencil patterning", Nanoscale (2019) (cited on p. 96).

[267] H. Ning, J. H. Pikul, R. Zhang, X. Li, S. Xu, J. Wang, J. A. Rogers, W. P. King, and P. V. Braun, "Holographic patterning of high-performance on-chip 3d lithium-ion microbatteries", PNAS **112**, 6573–6578 (2015) (cited on p. 96).

[268] T.-S. Wei, B. Y. Ahn, J. Grotto, and J. A. Lewis, "3d printing of customized li-ion batteries with thick electrodes", Adv. Mater. **30**, 1703027 (2018) (cited on p. 96).

[269] H. Gong, B. P. Bickham, A. T. Woolley, and G. P. Nordin, "Custom 3d printer and resin for 18 μm$\times$ 20 μm microfluidic flow channels", Lab on a Chip **17**, 2899–2909 (2017) (cited on p. 96).

[270] Y. A. Vlasov, X.-Z. Bo, J. C. Sturm, and D. J. Norris, "On-chip natural assembly of silicon photonic bandgap crystals", Nature **414**, 289 (2001) (cited on p. 96).

[271] S. Vignolini, N. A. Yufa, P. S. Cunha, S. Guldin, I. Rushkin, M. Stefik, K. Hur, U. Wiesner, J. J. Baumberg, and U. Steiner, "A 3d optical metamaterial made by self-assembly", Adv. Mater. **24**, OP23–OP27 (2012) (cited on p. 96).

[272] M. Campbell, D. Sharp, M. Harrison, R. Denning, and A. Turberfield, "Fabrication of photonic crystals for the visible spectrum by holographic lithography", Nature **404**, 53 (2000) (cited on p. 96).

[273] J.-H. Jang, C. K. Ullal, M. Maldovan, T. Gorishnyy, S. Kooi, C. Koh, and E. L. Thomas, "3d micro-and nanostructures via interference lithography", Adv. Funct. Mater. **17**, 3027–3041 (2007) (cited on p. 96).

[274] S.-K. Lee, S.-G. Park, J. H. Moon, and S.-M. Yang, "Holographic fabrication of photonic nanostructures for optofluidic integration", Lab on a Chip **8**, 388–391 (2008) (cited on p. 96).

[275] I. Wathuthanthri, Y. Liu, K. Du, W. Xu, and C.-H. Choi, "Simple holographic patterning for high-aspect-ratio three-dimensional nanostructures with large coverage area", Adv. Funct. Mater. **23**, 608–618 (2013) (cited on p. 96).

[276] B. E. Kelly, I. Bhattacharya, H. Heidari, M. Shusteff, C. M. Spadaccini, and H. K. Taylor, "Volumetric additive manufacturing via tomographic reconstruction", Science, eaau7114 (2019) (cited on p. 96).

[277] S. Matthias, and F. Müller, "Asymmetric pores in a silicon membrane acting as massively parallel brownian ratchets", Nature **424**, 53 (2003) (cited on p. 97).

[278] M. Vaezi, H. Seitz, and S. Yang, "A review on 3d micro-additive manufacturing technologies", Int. J. Adv. Manuf. Technol. **67**, 1721–1754 (2013) (cited on p. 97).

[279] F. P. Melchels, J. Feijen, and D. W. Grijpma, "A review on stereolithography and its applications in biomedical engineering", Biomaterials **31**, 6121–6130 (2010) (cited on p. 97).

[280] J. Mueller, J. R. Raney, K. Shea, and J. A. Lewis, "Architected lattices with high stiffness and toughness via multicore–shell 3d printing", Adv. Mater. **30**, 1705001 (2018) (cited on p. 97).

[281] S. Jeon, J.-U. Park, R. Cirelli, S. Yang, C. E. Heitzman, P. V. Braun, P. J. Kenis, and J. A. Rogers, "Fabricating complex three-dimensional nanostructures with high-resolution conformable phase masks", PNAS **101**, 12428–12433 (2004) (cited on pp. 97, 104).

[282] S. Jeon, Y.-S. Nam, D. J.-L. Shir, J. A. Rogers, and A. Hamza, "Three dimensional nanoporous density graded materials formed by optical exposures through conformable phase masks", Appl. phys. lett. **89**, 253101 (2006) (cited on p. 97).

[283] M. L. Solomon, J. Hu, M. Lawrence, A. Garcıa-Etxarri, and J. A. Dionne, "Enantiospecific optical enhancement of chiral sensing and separation with dielectric metasurfaces", ACS Photon. **6**, 43–49 (2018) (cited on p. 97).

[284] L. Cai, X. Yang, and Y. Wang, "All fourteen bravais lattices can be formed by interference of four noncoplanar beams", Opt. Lett. **27**, 900–902 (2002) (cited on p. 98).

[285] S. Jeon, V. Malyarchuk, J. A. Rogers, and G. P. Wiederrecht, "Fabricating three dimensional nanostructures using two photon lithography in a single exposure step", Opt. Express **14**, 2300–2308 (2006) (cited on p. 104).

[286] D. Shir, E. Nelson, Y. Chen, A. Brzezinski, H. Liao, P. Braun, P. Wiltzius, K. Bogart, and J. Rogers, "Three dimensional silicon photonic crystals fabricated by two photon phase mask lithography", Appl. Phys. Lett. **94**, 011101 (2009) (cited on p. 104).

[287] S. M. Kamali*, E. Arbabi*, and A. Faraon, "Metasurface-based compact light engine for ar headsets", in Spie photon. west (2019), p. 11040, DOI: doi.org/10.1117/12.2523720 (cited on p. 112).

[288] B. C. Kress, and P. Meyrueis, *Applied digital optics: from micro-optics to nanophotonics* (John Wiley & Sons, Ltd, 2009) (cited on pp. 113, 121).

[289] B. Kress, and T. Starner, "A review of head-mounted displays HMD technologies and applications for consumer electronics", in Spie defense, security, and sensing, Vol. 8720 (2013), p. 13 (cited on p. 113).

[290] X. Hu, and J. Carollo, "Head mounted display device with multiple segment display and optics", US Patent App., 14/923, 144 (2017) (cited on p. 113).

[291] A. Travis, J. S. Kollin, and A. Georgiou, "Virtual image display with curved light path", US Patent, 9, 759, 919 (2017) (cited on p. 113).

[292] A. Maimone, A. Georgiou, and J. S. Kollin, "Holographic near-eye displays for virtual and augmented reality", ACM Trans. Graph. **36**, 1–16 (2017) (cited on p. 113).

[293] D. Lin, M. Melli, E. Poliakov, P. S. Hilaire, S. Dhuey, C. Peroz, S. Cabrini, M. Brongersma, and M. Klug, "Optical metasurfaces for high angle steering at visible wavelengths", Sci. Rep. **7**, 2286 (2017) (cited on p. 114).

[294] Z. Shi, W. T. Chen, and F. Capasso, "Wide field-of-view waveguide displays enabled by polarization-dependent metagratings", in Spie photonics europe, Vol. 10676 (2018), p. 6 (cited on p. 114).

[295] "http://www.eenewseurope.com/news/leti-solves-stacking-issue-micro-led-displays", (access date: 01/22/2019) (cited on p. 119).

[296] "Https://www.ledinside.com/news/2018/3/jbd_devises_new_micro_led_technology_to_make_ultra_compact_micro_led_microdisplays", (access date: 01/22/2019) (cited on p. 119).

[297] L. Wang, S. Kruk, H. Tang, T. Li, I. Kravchenko, D. N. Neshev, and Y. S. Kivshar, "Grayscale transparent metasurface holograms", Optica **3**, 1504–1505 (2016) (cited on p. 121).

[298] D. Faklis, and G. M. Morris, "Spectral properties of multiorder diffractive lenses", Appl. Opt. **34**, 2462–2468 (1995) (cited on p. 121).

[299] W. T. Chen, A. Y. Zhu, V. Sanjeev, M. Khorasaninejad, Z. Shi, E. Lee, and F. Capasso, "A broadband achromatic metalens for focusing and imaging in the visible", Nat. Nanotechnol. **13**, 220–226 (2018) (cited on p. 121).

[300] S. Wang, P. C. Wu, V.-C. Su, Y.-C. Lai, M.-K. Chen, H. Y. Kuo, B. H. Chen, Y. H. Chen, T.-T. Huang, and J.-H. e. a. Wang, "A broadband achromatic metalens in the visible", Nat. Nanotechnol. **13**, 227–232 (2018) (cited on p. 121).

[301] K. Miyamoto, "The phase fresnel lens", J. Opt. Soc. Am. **51**, 17–20 (1961) (cited on p. 121).

[302] J. Burch, and A. Di Falco, "Surface topology specific metasurface holograms", ACS Photonics **5**, 1762–1766 (2018) (cited on p. 121).

[303] C. Peroz, V. Chauveau, E. Barthel, and E. Sondergard, "Nanoimprint lithography on silica sol–gels: a simple route to sequential patterning", Adv. Mater. **21**, 555–558 (2009) (cited on p. 122).

[304] C. Pina-Hernandez, V. Lacatena, G. Calafiore, S. Dhuey, K. Kravtsov, A. Goltsov, D. Olynick, V. Yankov, S. Cabrini, and C. Peroz, "A route for fabricating printable photonic devices with sub-10 nm resolution", Nanotechnology **24**, 065301 (2013) (cited on p. 122).

[305] M. Khorasaninejad, F. Aieta, P. Kanhaiya, M. A. Kats, P. Genevet, D. Rousso, and F. Capasso, "Achromatic metasurface lens at telecommunication wavelengths", Nano Lett. **15**, 5358–5362 (2015) (cited on p. 123).

[306] D. Sell, J. Yang, S. Doshay, and J. A. Fan, "Periodic dielectric metasurfaces with high-efficiency, multiwavelength functionalities", Adv. Opt. Mater. **5**, 1700645 (2017) (cited on p. 123).

[307] Z. Lin, B. Groever, F. Capasso, A. W. Rodriguez, and M. Loncar, "Topology optimized multi-layered meta-optics", https://arxiv.org/abs/1706.06715 (2017) (cited on p. 123).

[308] Y. Ren, L. Li, Z. Wang, S. M. Kamali, E. Arbabi, A. Arbabi, Z. Zhao, G. Xie, Y. Cao, N. Ahmed, Y. Yan, C. Liu, A. J. Willner, S. Ashrafi, M. Tur, A. Faraon, and A. E. Willner, "Orbital angular momentum-based space division multiplexing for high-capacity underwater optical communications", Sci. Rep. **6**, 33306 (2016) DOI: doi.org/10.1038/srep33306 (cited on p. 124).

[309] Z.-L. Deng, S. Zhang, and G. P. Wang, "Wide-angled off-axis achromatic metasurfaces for visible light", Opt. Express **24**, 23118–23128 (2016) (cited on p. 124).